High harmonic generation and attosecond dynamics in small organic molecules and biomolecules

A thesis presented upon application for
admission to the degree of

Doctor of Philosophy

in the Faculty of Engineering and Physical Sciences
by

Peter Philip Mulholland
MSci (Hons) 2014

School of Mathematics and Physics
Queen's University Belfast
Northern Ireland

May 2019

Abstract

Developments in laser technology over the past 60 years have enabled experimentalists to study a number of interesting processes that can occur during laser-molecule interactions. Study of such processes can help to shed light on ultrafast electronic and molecular processes, and aid with the development of a range of technologies. However, theoretically describing interactions of molecules with intense laser pulses is challenging. Traditionally, describing such interactions requires the solution of the time-dependent Schrödinger equation, but this approach is only feasible for the smallest molecular systems. An alternative approach is to use time-dependent density functional theory (TDDFT). In this thesis we report on calculations of ionization and high harmonic generation (HHG) in a number of small molecules, using the EDAMAME code, which combines a TDDFT description of electronic dynamics with a classical treatment of ionic dynamics. The work is divided into two main areas.

In the first area, we study the response of acetylene to a linearly polarized, mid infrared (mid-IR) laser pulse. The alignment of the molecule relative to the laser polarization direction is shown to have a large influence on HHG in the system. With the molecular axis aligned parallel to the laser polarization direction, we observe a double plateau in the harmonic spectrum, with an inner plateau that arises due to ionization from and recombination back to an excited state. This mechanism is investigated through use of a pump-probe scheme, in which the molecule is excited by a vacuum ultraviolet (VUV) pump pulse before HHG is driven by the mid-IR probe pulse. With the wavelength of the pump pulse suitably chosen, we observe a dramatic enhancement of the inner plateau harmonics, while the outer plateau is relatively unaffected.

In the second area of work, we study the interaction of a mid-IR pulse with three biologically relevant molecules: the nucleobases uracil and thymine, and the radiosensitiser

molecule 5-fluorouracil. We firstly compare differences in ionization and HHG between the two nucleobases, and between different molecular orientations relative to the laser polarization direction. On average we observe greater ionization from thymine than from uracil, but comparable HHG. Comparing the responses of the nucleobase thymine and the radiosensitiser 5-fluorouracil, we again see greater ionization from thymine, but larger differences in HHG between thymine and 5-fluorouracil than between uracil and thymine. In all three molecules we find that ionization and HHG are significantly reduced when the laser is polarized perpendicular to the plane of the molecule.

Acknowledgements

Firstly, I must thank my supervisor, Dr Daniel Dundas, for all of his support and guidance throughout my PhD project. Throughout my 4 years working on the PhD, Dan never failed to make time to see me, and was always very helpful in answering my many questions. I consider myself extremely fortunate to have been able to work with such a pleasant and knowledgeable supervisor.

A great deal of thanks must also go to the members of the Atomistic Simulation Centre. It was a privilege to spend 4 years working among such a welcoming, funny and intelligent group of people. I don't think I will ever work somewhere again that has quite as odd tea-break conversations as we had in the ASC! Particular thanks to my officemates throughout my time in the group, for the craic they provided and for the camaraderie developed through shared PhD struggles. I hope that the friendships I have made during my time in the ASC will continue on in the future. Thanks also to the many staff members in the School of Mathematics and Physics who have helped me throughout my time at Queen's.

I would also like to thank EPSRC/RCUK for giving me the opportunity to take part in their Policy Internship scheme, which allowed me to spend three enjoyable months working in the Research Service in the National Assembly for Wales. Thanks also to the very welcoming staff in the Research Service, as well as my fellow policy interns and Welsh housemates.

Writing a thesis involves many long days (and nights) in the office, and so I am lucky to have had a number of fine food establishments near QUB, with special mentions going to Boojum and Umi for keeping me well fed with burritos and falafel over a number

of years. Writing this thesis would have been considerably more difficult without the accompaniment of a good soundtrack; there are too many artists and composers to thank individually for contributing to this soundtrack, but special mentions must go to Lucy Rose and Lin-Manuel Miranda.

On a more serious note, I am forever grateful to all of my family and friends for their support, and for putting up with me during some stressful and less than enthusiastic moments over the last few years. I am greatly appreciative to them for providing me with distraction and perspective when I needed it. Finally, my greatest thanks must go to my parents, for their tireless support and encouragement over the past 27 years, but particularly throughout my PhD; I am immensely grateful. As a small token of my appreciation, this thesis is dedicated to them.

Financial support from the Engineering and Physical Sciences Research Council (EPSRC) is gratefully acknowledged.

Contents

List of Figures

List of Tables

Introduction

Effective design or control of any system requires an understanding of the dynamic response of individual components of the system to changing conditions. At the atomic and molecular scale, these dynamics can occur on extremely short timescales. Understanding such dynamics is important for scientific and technological advancement in a number of areas, for example for the development of more efficient solar cells, more sensitive electronic devices, and more effective radiotherapy treatments. Due to the extremely short timescales of electronic processes in molecules (on the order of attoseconds to femtoseconds), their study requires the use of specialized techniques.

Intense, ultrashort, laser pulses are an effective tool for studying such processes, allowing for sufficient precision and sufficiently short temporal resolution. Since the demonstration of the first working laser in 1960, laser technology has improved radically thanks to a number of important innovations. Some of these developments were recently recognised in the 2018 Nobel Prize in Physics, which was awarded "for groundbreaking inventions in the field of laser physics". As the maximum intensity of laser pulses has increased dramatically, so too has the minimum pulse duration decreased. State of the art laser systems can now produce controlled pulses with durations comparable to the characteristic timescales of electronic motion. Such short pulses are essential for imaging, and potentially controlling, the dynamics of electrons, for example during chemical reactions.

The huge increase in laser intensities in recent years has allowed experimentalists to study a number of interesting physical processes that do not occur in laser-molecule interactions when lower intensity pulses are used. One such process is high harmonic generation (HHG). In this process, an electron is ionized from an atom or molecule by

an intense laser field, and can gain a large amount of kinetic energy while propagating in the presence of the field, before returning to the parent system when the direction of the applied field reverses. Upon return, the ionized electron may recombine with the atom or molecule, with the kinetic energy gained in the field emitted as a high energy photon. This kinetic energy can be substantial, and so the emitted photon can have an energy many times the energy of a photon in the applied laser field. HHG is a particularly interesting process due to its applications as both a sensitive probe of electronic and molecular dynamics and a means of producing attosecond duration pulses.

While the improvements in laser technology have enabled the study of interesting processes such as HHG, they have also made the description of laser-molecule interactions more complicated, and the interpretation of experimental results more challenging. For this reason, new theoretical approaches are required to model the interactions of molecules with high intensity laser fields, in order to aid the interpretation of the experimental results, and to study systems and regimes that are difficult to realise experimentally.

The electronic and ionic dynamics of a non-relativistic molecular system exposed to an intense laser pulse can in principle be obtained through direct solution of the time-dependent Schrödinger equation (TDSE). In practice however, this approach is only feasible for the smallest molecular systems, due to the dramatic increase in computational cost as the system size is increased. Alternative approaches are therefore required in order to study strong-field dynamics in molecules more generally. A common simplification is to separate the dynamics of the electrons and ions, since the electrons will in general adapt to changes on a much faster timescale than the ions. Even with this approximation however, we still require the solution of the TDSE for a many-electron system; an impossible task for all but the simplest of systems.

An alternative to solving the TDSE directly is to use time-dependent density functional theory (TDDFT). While in the TDSE the evolving state of the electronic system can be completely described by the time-dependent electronic wavefunction, in TDDFT the state of the system is instead described in terms of the time-dependent single-particle electronic density. Based on the ideas of density functional theory (DFT), which has be-

come one of the most widely used methods for electronic structure calculations, TDDFT was shown in 1984 to be in principle an exact theory. While in practice this exactness is unachievable due to the necessity of invoking several approximations, TDDFT has grown in popularity over the past 20 years due to its useful balance between accuracy and efficiency.

The general aim of this project is to use TDDFT to study the interaction of intense, short laser pulses with a number of small molecules. Of particular interest will be the degree to which HHG varies between molecules and between molecular orientations relative to the applied laser field. In the work described in this thesis, four molecules are studied using the EDAMAME (Ehrenfest DynAMics on Adaptive MEshes) code. Written in Fortran2008, this is a highly parallelized computer code suitable for large-scale calculations on supercomputers, making use of thousands of processors. EDAMAME employs a mixed quantum-classical description of laser-molecule interactions, in which the electronic dynamics are described using TDDFT, while the motion of the ions is treated classically. Using EDAMAME, we are able to study the interaction of a range of molecules with intense laser pulses, and can investigate, for example, the effect of molecular orientation, ionic motion, and choice of laser parameters on the response of the molecule. The project is divided into two main areas of work.

In the first area of work, the molecule of interest is acetylene, which is a small, linear, hydrocarbon. The relative simplicity of acetylene, along with the fact that it is cheaply available in the gas phase at room temperature, has made it a popular molecule for both experimental and theoretical studies for many years. In recent years, a number of experimental studies have studied HHG in acetylene, investigating how the HHG signal varies as the molecule is rotated, as well as how the maximum energy of the emitted harmonics can be increased by using longer wavelength laser pulses. Theoretically however, studies of HHG in acetylene have been much more limited. This is due in part to the fact that accurately describing HHG theoretically is a challenging task. The difficulty arises from the fact that although the HHG process occurs over a very short timescale, the ionized electron can travel a large distance away from the atom or molecule during that time. As such, accurately describing HHG requires calculations with both large spatial extents and fine temporal resolution. Taken together these two requirements make the theoretical description of HHG in molecules computationally

demanding. The purpose of this area of work is to perform one of the first in-depth theoretical studies of HHG in acetylene, using a mid-infrared driving laser pulse, as was used in recent experimental HHG studies in acetylene. Of particular interest in this study will be the effect of the alignment of the molecule (relative to the laser polarization direction) on both the ionization and HHG in the molecule, and the effect that exciting the molecule ahead the application of the driving laser pulse has on the response of the system (i.e. the effect of different pump-probe laser pulse setups).

The other three molecules studied in this thesis are uracil, thymine and 5-fluorouracil, which are of interest due to their biological relevance. Thymine and uracil are nucleobases in DNA and RNA respectively, while 5-fluorouracil is a radiosensitiser molecule, which can be used in radiotherapy treatments to enhance lethal damage to cancerous cells. These three molecules are much more complex than acetylene, and more challenging to work with both experimentally and computationally. A number of previous studies on these molecules have focused on the fragmentation and relaxation dynamics of the molecules, following interaction with a low intensity, high frequency, pump pulse. Studies of the interaction of these molecules with intense laser pulses, however, are few in number, especially in terms of HHG studies. On the experimental side, this is due in part to technical challenges in preparing a suitable gas-phase sample of molecules, since uracil, thymine and 5-fluorouracil are all solid at room temperature. From a theoretical point of view, describing the interaction of these molecules with an intense laser pulse raises the same challenges that describing such an interaction for acetylene does, but these are exasperated due to the significantly larger size and complexity of these biological molecules. This area of work has three main aims. Firstly, to determine the extent to which EDAMAME can accurately and efficiently describe larger and more complicated molecules than those previously studied with the code. Secondly, to perform the first calculations of HHG in these biologically-relevant molecules, and investigate the effect of the molecular alignment relative to the laser polarization direction on the harmonic response. Thirdly, to compare ionization and HHG in uracil and thymine on the one hand (and how the calculated harmonic responses compare with the results of the only experimental study of HHG in these molecules to date), and in thymine and 5-fluorouracil on the other (and whether there are significant differences between the responses of the nucleobase and the radiosensitiser).

Thesis structure

This thesis is arranged as follows. We begin, in Chapter 1, by introducing a number of key aspects of strong-field physics, with a focus on the ionization and harmonic generation processes that can occur during the interaction of a molecule with a short, intense, applied laser field. In Chapter 2 we introduce a number of the theoretical approaches used to describe such an interaction, with a particular focus on the time-dependent density functional theory (TDDFT) and quantum-classical molecular dynamics methods used in the work described in this thesis. These methods are implemented in a Fortran2008 code called EDAMAME, which is the subject of Chapter 3. This code is used to study the interaction of a number of different molecules with intense laser pulses; the results of these calculations are presented in Chapters 4 and 5.

In Chapter 4, we investigate the response of acetylene to mid-infrared (mid-IR) laser pulses. In this study we focus on the high harmonic spectra produced during interactions with various choices of laser parameters and molecular orientations (relative to the laser polarization direction). Of particular interest is the presence of a double plateau structure in the high harmonic spectrum when the molecular axis is aligned parallel to the laser polarization direction. We investigate the origin of the inner plateau region in this spectrum, and propose that it arises due to ionization from and recombination back to an excited state. This mechanism is investigated using a pump-probe laser setup, in which we excite the molecule with a lower intensity, higher frequency, pump pulse before applying the mid-IR probe pulse.

In Chapter 5, we compare the responses of uracil, thymine and 5-fluorouracil to a mid-IR laser pulse, as well as the effect of the molecular orientation relative to the laser polarization direction. The more complicated structure of these molecules compared to acetylene required the implementation of new finite difference methods into the EDAMAME code. Using these new methods, we study ionization and high harmonic generation in the three molecules, for three different orientations of each. Firstly we compare the responses of the two nucleobases, uracil and thymine, and consider how our results compare with a previous experimental study of HHG in ablation plumes of uracil and thymine. We then consider differences between the responses of the nucleobase in DNA, thymine, and its radiosensitising replacement, 5-fluorouracil. To

conclude the thesis, we summarise the main results of Chapters 4 and 5, and outline a number of possible directions for future work.

Unless otherwise stated, atomic units will be used throughout this thesis. In this system of units, the electronic mass, electronic charge and reduced Planck constant are defined as $m_e = e = \hbar = 1$. Some important conversions between atomic units and other common units are given in Table 1.

Quantity	Name/Symbol	Value in SI units	Value in common units
Length	Bohr radius (a_0)	5.29177×10^{-11} m	0.529177 Å
Energy	Hartree (Ha)	4.35975×10^{-18} J	27.2114 eV
Time		2.41888×10^{-17} s	2.41888×10^{-2} fs
Velocity		2.18769×10^{6} ms^{-1}	(1/137) c
E-field		5.14221×10^{11} V/m	5.14221×10^{9} V/cm
B-field		2.35371×10^{5} T	2.35371×10^{9} G
Intensity		3.50945×10^{20} W/m^2	3.50945×10^{16} W/cm^2

Table 1: A number of important conversion factors for switching between atomic units, SI units, and other common units. In the entry for velocity, c is the speed of light in ms^{-1} ($c = 2.99792\times10^{8}$ ms^{-1}).

Peer-reviewed publications

- Peter Mulholland and Daniel Dundas, *"High-order harmonic generation from highly excited states in acetylene"*, Physical Review A, Volume 97, Issue 4, 043428, 2018.

- Daniel Dundas, Peter Mulholland, Abigail Wardlow and Alejandro de la Calle, *"Probing the role of excited states in ionization of acetylene"*, Physical Chemistry Chemical Physics, Volume 19, Issue 30, 19619-19630, 2017.

- Peter Mulholland and Daniel Dundas, *"High-order harmonic generation in uracil, thymine and 5-fluorouracil"*, Manuscript in preparation.

Relevant conference proceedings

- Peter Mulholland and Daniel Dundas, *"Resonant enhancement of high harmonic generation in acetylene using a VUV pump pulse"*, Poster session presented at: 4th COST XLIC General Meeting, 14–16 March 2017, Prague, Czech Republic.

- Peter Mulholland and Daniel Dundas, *"Ionization and high harmonic generation in acetylene"*, Poster session presented at: 2nd COST XLIC Working Group 1 Meeting, "Ultrafast electron dynamics in molecules", 29–30 August 2016, Edinburgh, United Kingdom.

- Peter Mulholland, Alejandro de la Calle, Abigail Wardlow and Daniel Dundas, *"Dynamics of diatomic molecules in intense laser fields"*, Poster session presented at: 2nd COST XLIC Working Group 3 Meeting, "Control of chemical reactivity", 4–5 April 2016, Belfast, United Kingdom.

Chapter 1

Strong-field laser-matter interactions

1.1 Introduction

The series of photographs shown in Fig. 1.1 are iconic in the history of photography, and were made into one of the earliest examples of a motion picture. Produced in 1878, these photos were the result of a photographic experiment that aimed to determine whether a galloping horse ever completely lifts all four of its feet off the ground; this involves motion that is too fast for the human eye to resolve. In order to answer this question, Eadweard Muybridge set up a series of cameras, each connected to a tripwire that would trigger the camera when the horse galloped past. The resulting photographs showed that all four feet do indeed leave the ground at once.

While having a large number of cameras spread out along the path of the horse allowed Muybridge to photograph the horse at different stages of its gallop, resolving the motion of the horse at all required cameras with fast shutter speeds. Without this, the rapid movement of the horse and its hooves would have been blurred out in every photograph. The importance of the shutter speed is illustrated in Fig. 1.2. In Fig. 1.2(a), a slow shutter speed is used, and the resulting photograph is so blurry that the subjects (pigeons) are almost unrecognisable. In Fig. 1.2(b), the shutter speed is increased, and

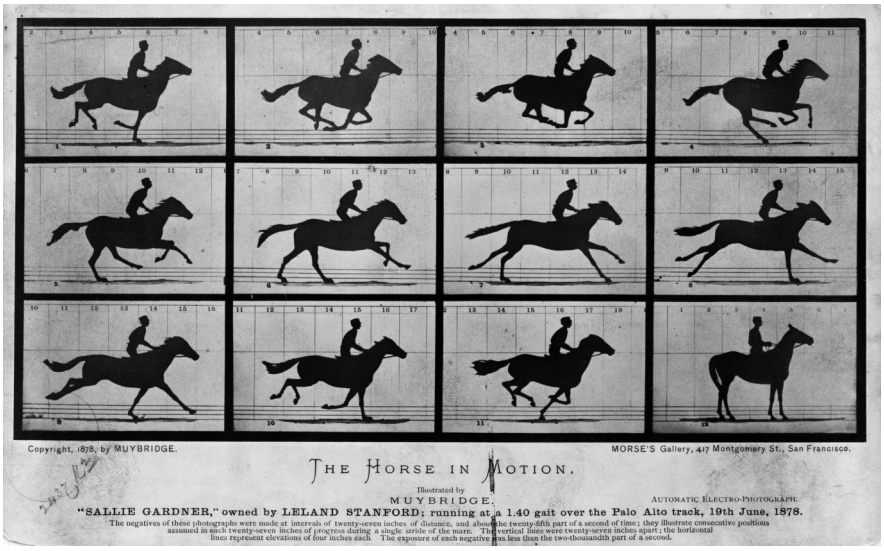

Figure 1.1: Series of photographs by Eadweard Muybridge: *The Horse in motion. "Sallie Gardner," owned by Leland Stanford; running at a 1:40 gait over the Palo Alto track, 19th June 1878*. Figure reproduced from the Library of Congress Prints and Photographs Division repository [1].

the birds on the ground are well imaged, but the wings of those in flight are still blurry. Finally, in Fig. 1.2(c) the shutter speed is increased further still, and the motions of all the birds are well resolved, with the blurring that was seen with slower shutter speeds eliminated.

In the years since Muybridge's experiment, improvements in camera technology have made photographing fast motion in everyday life an almost trivial task, for example in sports or wildlife photography. The crucial point here is that obtaining a sharp image that is free from blurring requires the ability to probe the system with controllable temporal resolution that is at least as fast as the duration of the process being imaged.

This same principle applies to the study of processes in atoms, molecules and nanostructures. The processes occurring in these systems are orders of magnitude faster than the motions captured in Figs. 1.1 and 1.2 however, as illustrated in Fig. 1.3. The spatial extent of structures on the molecular scale is connected, through quantum mechanics, to the speed of the dynamics occurring, with the oscillation period of a wavepacket in a superposition of states being inversely proportional to the energy separation between the states. In other words, the larger the gap between energy levels, the faster the motion of a particle in the superposition state [3]. In a molecule there are three main types of motion; in order of increasing speed these are molecular rotations, molecular

(a) Slow shutter speed (1/8 s) (b) Medium shutter speed (1/125 s) (c) Fast shutter speed (1/500 s)

Figure 1.2: Effect of camera shutter speed on resolving fast motion. (a) The shutter speed (1/8 s) is too slow to capture the birds in flight. (b) With a faster shutter speed (1/125 s), the birds on the ground are now recognisable, but the wings of those in flight are still blurry. (c) With an even fast shutter speed (1/500 s), the motion of the birds is completely frozen, and the wings are sharply defined. Figure adapted from [2].

vibrations, and electronic motion.

Generally speaking, the separation between electronic energy levels is on the order of 1 eV, while between vibrational energy levels the separation is ≈ 1 meV, and $\approx 1\,\mu$eV for rotational energy levels. The associated timescales for these three types of motion are:

- rotational motion: nanosecond–picosecond (10^{-9} – 10^{-12} s),
- vibrational motion: picosecond–femtosecond (10^{-12} – 10^{-15} s), and
- electronic motion: femtosecond–attosecond (10^{-15} – 10^{-18} s).

To put these timescales in context, note that light travels approximately 0.3 mm in 1 picosecond (ps), 0.3 μm in 1 femtosecond (fs), and 0.3 nm in 1 attosecond (as). In the Bohr model of the atom, the orbital period of an electron in the ground state of hydrogen is around 150 as. The ratio of an attosecond to one second is roughly the same as the ratio of one second to the age of the universe (~ 13.8 billion years $\sim 4 \times 10^{17}$ s).

With timescales as short as these, sophisticated techniques are clearly required to capture, and ultimately control, the ultrafast processes occurring in molecules. An effec-

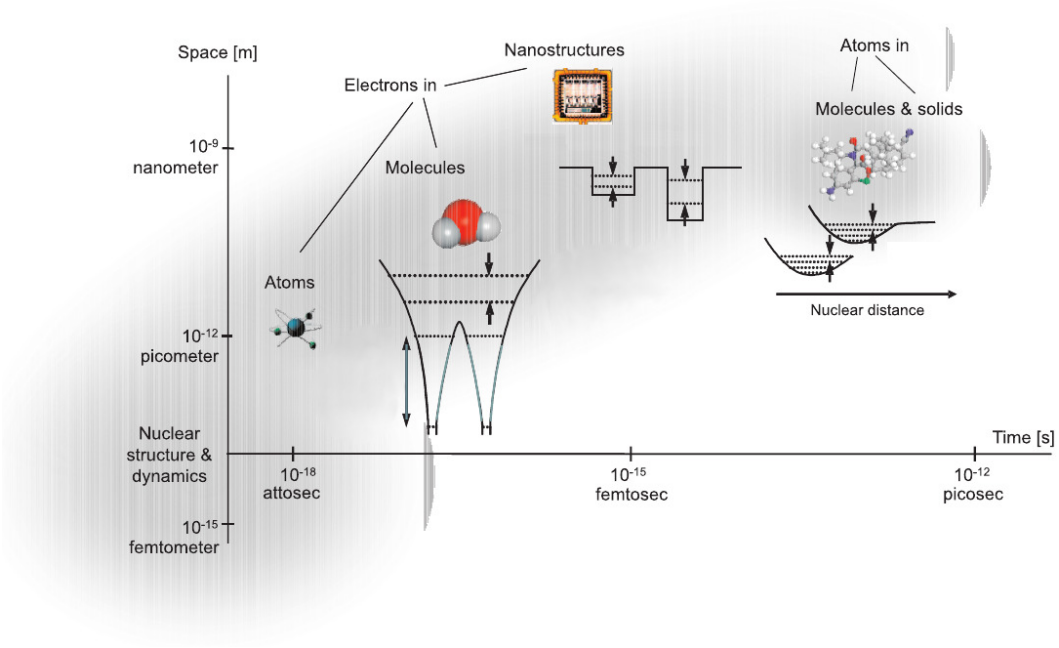

Figure 1.3: Characteristic length and time scales for a range of structures and dynamics. Figure adapted from [3].

tive way to do this is through the use of intense, ultrashort, laser pulses. As we will see in the next section, since its invention in the 1960s, laser technology has advanced dramatically, with orders of magnitude improvements in the maximum achievable intensity and minimum achievable duration. Considering pulse duration in particular, in recent years the use of a non-linear process known as high harmonic generation (HHG) has enabled the production of laser pulses with durations < 1 fs, i.e. attosecond pulses.

These developments brought with them their own ongoing challenges (such as the need for methods to accurately measure the duration of attosecond pulses, and technical refinements to enable production of pulses of sufficient intensity to perform attosecond-pump-attosecond-probe experiments [4]), but have enabled the production of pulses as short as 43 as [5]. With time resolution as short as this, experimentalists are beginning to be able to directly observe electronic dynamics, and even exert some control over them [3, 6, 7]. For such experiments to be successful, and the results understandable, advancements in the theoretical description of molecules under the influence of strong laser fields are also required; this will be the topic of Chapter 2.

Before that however, in this chapter we will introduce some of the main aspects of laser-molecule interactions, with a particular focus on the physical processes that can occur

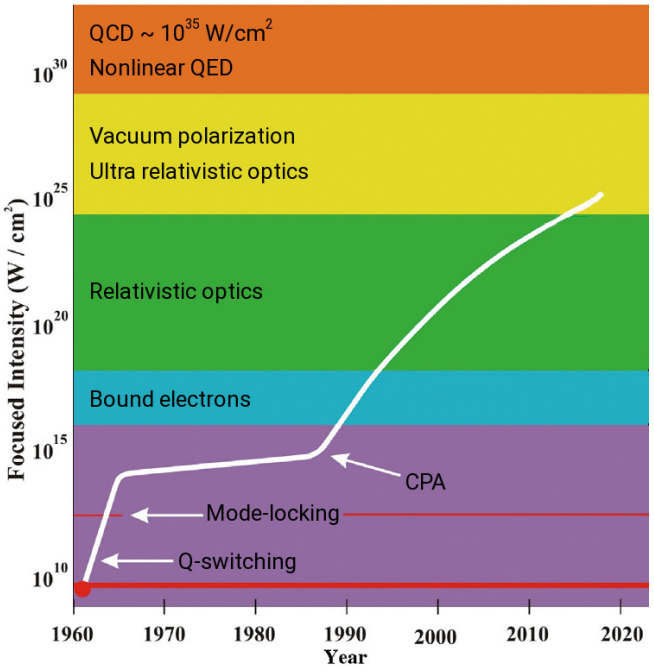

Figure 1.4: Increase in focused laser intensity since 1960. Three significant advances in laser technology (described in main text) are indicated with arrows. Figure adapted from [9].

when high intensity laser pulses are used. The chapter is arranged as follows. In Section 1.2 we provide a brief overview of the development of laser technology over the past 60 years, by highlighting three key advances that have enabled tabletop femtosecond laser sources to become readily available in university laboratories. Widespread access to these intense, ultrashort sources of light has allowed researchers to study a range of strong-field phenomena; we introduce a number of these in Sections 1.3 and 1.4. Section 1.3 is concerned with ionization processes, and how the transition from a low intensity, high frequency laser field to a high intensity, low frequency field is associated with a change in the dominant ionization mechanism. In Section 1.4 we discuss the topic of high harmonic generation, showing how the mechanism can be described by a semiclassical three-step model. Finally, in Section 1.5, we introduce a number of important applications of HHG, as well as some experimental considerations.

1.2 Femtosecond laser technology

The basic physics behind the operation of a laser can be found in any undergraduate physics textbook. Put simply, a laser enables the production of a beam of coherent light,

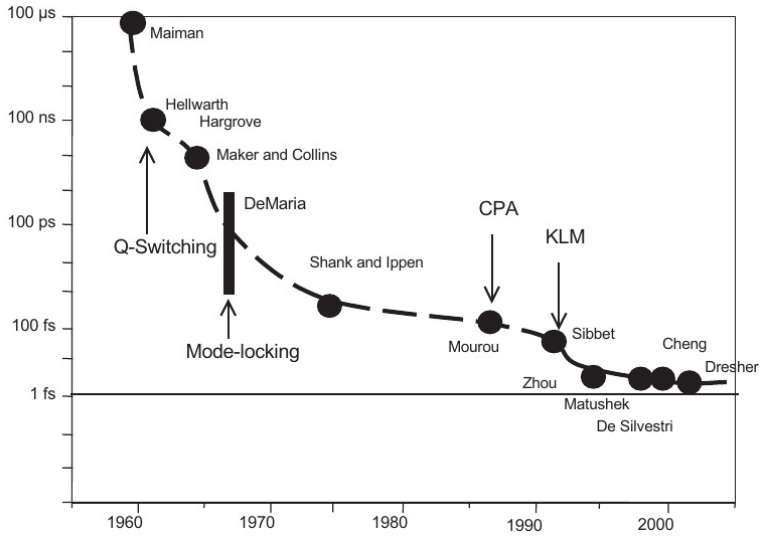

Figure 1.5: Developments in laser technology from 1960 to the early 2000s and the associated reductions in the shortest achievable pulse duration. Some important advancements (described in main text) and contributors are marked with arrows and circles. Figure reproduced from [10].

through population inversion and subsequent stimulated emission in a lasing medium. However, since the discussion of the concept in the late 1950s and the subsequent demonstration of the first working laser by Theodore Maiman in 1960 [8], laser technology has made great advances. Since that time, the maximum power that can be produced by a laser has increased by many orders of magnitude (Fig. 1.4), while the shortest laser pulse duration has decreased by similarly impressive amounts (Fig. 1.5[1]). Several technological developments have been central to these advancements; these will be briefly outlined below. The general aim of all these advances was to squeeze increasingly large amounts of energy into increasingly short periods of time, therefore increasing the intensity of the laser pulse. Considering a laser system as consisting of an optical resonator (surrounding the lasing medium) and an amplifier [11], the first two developments we consider are related to the resonator, while the third is related to the amplifier.

[1]Note that this figure does not show the more recent reductions in pulse duration achieved through the use of high harmonic generation, which enabled the production of pulses of sub-femtosecond duration; these are discussed in Section 1.5.4.

1.2.1 Q-switching

A laser operating in its most basic form is known as a continuous wave laser, in which the output power remains almost constant over time. This is in contrast to a pulsed mode of operation, in which the power is released as a series of finite duration pulses. While continuous wave lasers find many applications in industry, for example, for the purposes of ultrafast laser spectroscopy, pulsed lasers are the tool of choice. One of the first major developments in pulsed laser technology was the development of Q-switching in the late 1950s and early 1960s [12]. The Q value of a laser refers to the quality factor of the optical resonator, and is a measure of the resonator losses per oscillation. With Q-switching, a low Q value is used while the laser medium is being pumped, to suppress stimulated emission and the lasing process. In this way the level of population inversion, and consequently the energy stored, in the medium increases, until some maximum level is reached. At this point the Q value is quickly switched from low to high, allowing stimulated emission to begin. The energy gained in the medium is released in a short period of time, resulting in a short, intense laser pulse.

With Q-switching, pulses on the order of a few nanoseconds can be produced [11]. The production of sub-ns pulses would require a further technological development: mode-locking.

1.2.2 Mode-locking

In a standard laser cavity setup of two mirrors on either side of the laser gain medium, interference between the light waves that are reflecting back and forth in the cavity will give rise to a number of modes with discrete frequencies that are supported by the laser cavity. In general these modes will oscillate independently of each other with different phases, which can lead to fluctuations in output as the different modes constructively and destructively interfere with each other. The goal of mode-locking is to create a fixed phase between the modes, using one of a number of techniques [13]. The effect of this is that the modes will constructively interfere with each other periodically, and interfere destructively the rest of the time, resulting in a series of short, intense pulses. The development of mode-locking technology in the 1960s, and subsequently Kerr-lens mode-locking (KLM) in the early 1990s [14], enabled laser pulses with durations of

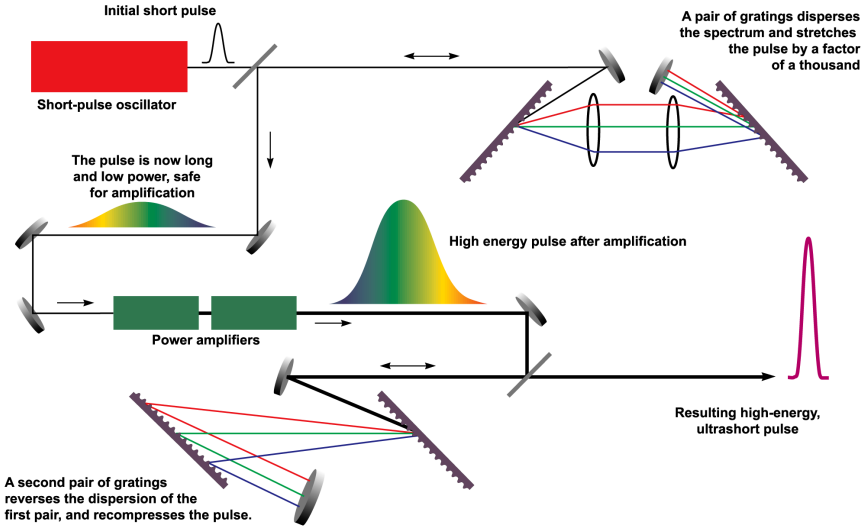

Figure 1.6: Schematic representation of the chirped pulse amplification technique. Starting in the upper left corner of the diagram, an ultrashort pulse is produced by the oscillator, and is passed through a pair of diffraction gratings. These add a "chirp" to the pulse, increasing the pulse duration and reducing the pulse intensity to a level at which it can safely pass through the amplifiers. The amplified pulse is then recompressed by another pair of diffraction gratings, resulting in a high intensity, ultrashort pulse. Figure reproduced from Wikipedia [17], and adapted from [18].

picoseconds down to 10s of femtoseconds to be routinely produced.

Both Q-switching and mode-locking are improvements that reduce the duration of output pulses. However, in order to reach high intensities, a reduction in pulse duration must be accompanied by an increase in the energy per pulse. Amplifying the energy of short pulses is the purpose of the next technological advancement we consider: chirped pulse amplification.

1.2.3 Chirped Pulse Amplification (CPA)

The pulses produced by a typical laser oscillator are capable of delivering a relatively small amount of energy. In order to produce large intensity pulses, the energy of each pulse must be increased by many orders of magnitude; i.e. the pulses must be amplified. This is done by passing the pulses through some amplification medium, of which there are multiple options, including gases, dyes and solid state media [13]. Intense, short pulses, however, can cause serious damage to the amplification medium. One method of avoiding such damage is to increase the diameter of the laser beam, to reduce the pulse intensity prior to amplification. A significant drawback of this approach

however is that a large beam requires large optical components (mirrors, amplification media etc.) which would be prohibitively expensive to all except large, specialist, laser facilities. The route to affordable tabletop laser systems capable of producing intense, femtosecond pulses therefore required a different approach: chirped pulse amplification (CPA) [15, 16].

With CPA the short pulse is expanded in time rather than in space. This is achieved by using, for example, two diffraction gratings as shown in Fig. 1.6. The diffraction gratings separate out different frequency components of the short pulse to produce a "chirped" pulse (one that is stretched in time, with long wavelength components of the pulse arriving ahead of short wavelength components). This lower intensity pulse can then be safely amplified, before passing through another set of diffraction gratings to remove the chirp (i.e., recompress the pulse in time), resulting in a short, high intensity laser pulse.

Using chirped pulse amplification, femtosecond pulses with peak intensities of 10^{18} W/cm^2 and beyond became accessible in university laboratories. This opened up the field of femtochemistry, for which Ahmed Zewail would go on to win the Nobel Prize in Chemistry in 1999 [19]. More recently, Gérard Mourou and Donna Strickland shared in the Nobel Prize in Physics in 2018 for the development of CPA itself [20].

1.2.4 Summary

In this section we have highlighted three key developments in laser technology over the past 60 years. The invention of Q-switching and mode-locking led to a massive reduction in the duration of easily producible pulses, while chirped pulse amplification overcame difficulties with amplifying short pulses. Together these developments have allowed femtosecond pulses with electric fields comparable to (or larger than) the Coulomb field in atoms and molecules to become readily available in laboratories around the world. Such high intensity pulses allow experimentalists to study the range of processes that can occur when molecules are driven far from equilibrium.

Breaking the "femtosecond barrier" would require yet another development: harnessing the potential of high harmonic generation to produce attosecond pulses. This technique, and the high harmonic generation process itself, will be discussed later in this

chapter. Before that however, in the next section we will introduce the ionization processes that can occur in molecules exposed to the intense laser pulses discussed above.

1.3 Ionization processes

In the picture of ionization introduced by Einstein to describe the photoelectric effect [21], an electron can only be ionized from a system exposed to light if the energy of individual incident photons is greater than the ionization potential of the system. When the intensity of the incident light is high however, it was predicted as early as the 1930s, and later observed experimentally, that ionization is possible via other processes. In this section we introduce and discuss these processes.

1.3.1 Multiphoton ionization (MPI) and above-threshold ionization (ATI)

We begin by considering ionization of atoms or molecules in the presence of laser fields of moderate intensity, i.e., not large enough to significantly perturb the Coulomb potential felt by bound electrons.

The idea of multiphoton ionization (MPI) was first proposed by Maria Goeppert-Mayer (who later went on to become a Nobel laureate for her work on nuclear shell structure) in her 1931 PhD thesis [22], in which she demonstrated how time-dependent perturbation theory predicts the possibility of a two-photon absorption process. MPI more generally is the process in which an electron is ionized by a number of photons, each of which would have insufficient energy to cause ionization by itself (Fig. 1.7(a)). In other words, ionization can occur provided that

$$n\omega_L \geq I_p, \tag{1.1}$$

where n is the number of absorbed photons, ω_L is the frequency of the laser pulse (which is equal to the photon energy when working in atomic units), and I_p is the ionization potential of the system. Multiphoton ionization is a highly non-linear process; by using lowest-order perturbation theory (LOPT) it can be shown that, assuming the laser intensity I is low enough and that resonance effects aren't at play, the n-photon ionization rate, Γ_n, scales as

$$\Gamma_n \propto I^n. \tag{1.2}$$

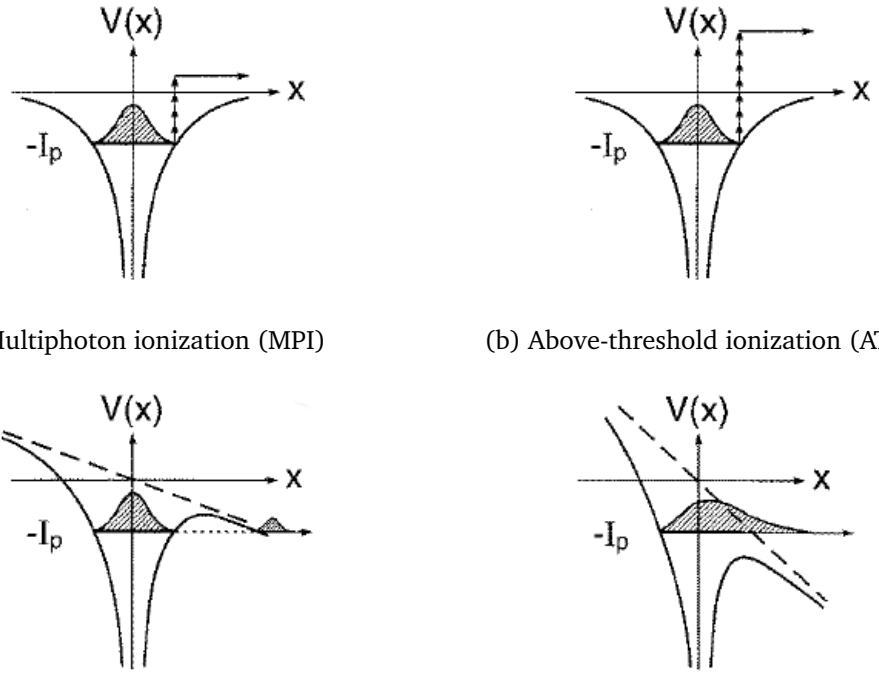

(a) Multiphoton ionization (MPI)

(b) Above-threshold ionization (ATI)

(c) Tunnel ionization (TI)

(d) Over-the-barrier ionization (OTBI)

Figure 1.7: Schematic diagram showing different ionization regimes, for increasing intensity of applied field. (a) MPI: absorption of four photons of individual energy $\omega_L < I_p$ is large enough to ionize an electron (i.e., $4\omega_L \geq I_p$). (b) ATI: as MPI, but the escaping photoelectron absorbs an extra three photons as it is ionizing, gaining kinetic energy. (c) TI: at higher intensities, the applied electric field distorts the Coulomb potential enough that a potential barrier is formed, through which an electronic wavepacket can tunnel ionize. (d) OTBI: at even higher intensities, the applied field is strong enough that the potential barrier is suppressed to such a degree that the electron is free to ionize without tunnelling. Figure adapted from [11].

When MPI was first proposed, there were no light sources of sufficient intensity available to test Goeppert-Mayer's theory. However, experimental validation did come several decades later [23, 24], following the invention of the laser. Subsequent measurements of multiphoton ionization rates across a range of intensities showed that the simple relationship given in Eq. (1.2) holds for a range of intensities, but breaks down if the laser intensity is increased beyond a certain limit, known as the saturation intensity. Beyond this point, further increases in intensity produce smaller increases in ionization rate, due to saturation as the ionization probability approaches 1 throughout the sample.

The simple scaling of Eq. (1.2) also becomes more complicated if there exists an excited state in the system that is in resonance with some multiple of the photon energy. In

this situation, one may observe resonantly-enhanced multiphoton ionization (REMPI), in which the multiphoton transition from the initial state to the final (continuum) state is mediated by a transition to an excited state, resulting in an increased ionization rate.

The description of MPI (and REMPI) can be further complicated by the onset of ac-Stark shifts at higher intensities. The ac-Stark shift is an effect in which the energies of the states of the system are shifted due to the strong oscillating electric field of the laser pulse. At low laser intensities these shifts are small, but as the intensity increases the energy shifts become so large that they can no longer be described by LOPT (although they can be included at higher orders of perturbation theory [11]). The ac-Stark shift can lead to increases in the ionization potential, as well as shifts away from resonant transitions. This is due to the difference in the Stark shift felt by different states. The level of Stark shifting caused by an applied field can be described in terms of the so-called ponderomotive energy, U_p, associated with the laser field. A free electron in a laser field will oscillate in time. The ponderomotive energy is the cycle-averaged kinetic energy of this electron, and is given by

$$U_p = \frac{E_0^2}{4\omega_L^2}, \tag{1.3}$$

where E_0 is the peak electric field strength of the laser pulse, and ω_L is the laser frequency. A related quantity to the ponderomotive energy is the quiver amplitude. This is the amplitude of the oscillations of a free electron in a laser field, and is given by

$$\alpha_0 = \frac{E_0}{\omega_L^2}. \tag{1.4}$$

Both the quiver amplitude and the ponderomotive energy are important quantities in strong-field physics, and will be referred to throughout this thesis.

Returning now to ac-Stark shifts, in the presence of a strong field, loosely bound states (highly excited, Rydberg and continuum states) will experience an energy shift very close to the ponderomotive energy. Conversely, the tightly bound states will experience a negligible shift in energy. Therefore the effective ionization potential is increased, by approximately U_p [11].

So far we have considered MPI in which the system absorbs just enough energy from

incoming photons to overcome the ionization potential. We can also consider the situation in which the system absorbs more photons than necessary, resulting in an emitted photoelectron with some amount of kinetic energy, which can be much greater than zero. This process is known as above-threshold ionization (ATI), and can be considered at the perturbative level as MPI by more photons than the minimum number required for ionization (Fig. 1.7(b)) [11]. ATI was first observed experimentally by Agostini *et al.* in 1979 [25], with a perturbative theory to describe the experimental observations developed shortly after [26]. As with MPI, a perturbative approach can be used to determine an expression for the ionization rate as a function of intensity, namely

$$\Gamma_{n+s} \propto I^{n+s}, \tag{1.5}$$

where n is the minimum number of photon required for ionization (as before), and s is the number of excess photons absorbed. The energy of the emitted photoelectron is then simply given by

$$E_{\text{elec}} = (n+s)\omega_L - I_p. \tag{1.6}$$

A typical ATI spectrum in the perturbative regime will therefore consist of a series of peaks separated by the photon energy ω_L, decreasing in intensity with increasing s. At higher intensities, the perturbative picture begins to break down, and additional features appear in the ATI spectrum, such as suppression of low-order peaks due to the ac-Stark shifting of energy levels.

While various orders of perturbation theory can be used to describe MPI, REMPI, ac-Stark shifts, and ATI spectra in the perturbative regime, as the laser intensity is increased further the perturbative picture of Goeppert-Mayer breaks down, and ionization no longer proceeds via multiphoton ionization. Instead, a process known as tunnel (or tunnelling) ionization becomes the dominant mechanism.

1.3.2 Tunnel ionization

Shortly after laser sources were developed to the point that the predictions surrounding multiphoton ionization could be experimentally tested, it was observed that ionization rates did not always follow the power law dependence of Eq. (1.2); instead an exponential dependence was observed. These observations led Leonid Keldysh to propose

an alternative ionization mechanism to the perturbative MPI theory described previously. This mechanism is based on the distortion of the Coulombic potential by the strong electric field of the applied laser pulse, as shown in Fig. 1.7(c). This distortion causes the formation of a potential barrier, through which the electron will have some probability of tunnelling.

In Keldysh's 1965 paper [27], he postulated that as the frequency of an applied field decreases (or as the field strength increases), there is a transition from the multiphoton regime to the so-called tunnelling regime, in which the ionization probability has an exponential dependence on the strength of the applied field. The transition between these two regimes is characterised by the ratio

$$\gamma = \sqrt{\frac{I_p}{2U_p}}, \tag{1.7}$$

where I_p is the ionization potential and U_p the ponderomotive energy. This ratio, derived by considering the ratio of the optical frequency to the tunnelling frequency, is known as the Keldysh parameter. The value of γ indicates which ionization mechanism is dominant. In the tunnelling regime, $\gamma \ll 1$; this is the case for an intense applied field with a low frequency. At the other extreme, in the multiphoton regime $\gamma \gg 1$; this is the case for a relatively low intensity, high frequency field.

To derive an expression for the tunnelling ionization rate, Keldysh's theory makes two key assumptions: (i) the frequency of the field is low enough that it can be considered as a dc-field; (ii) the final state of the electron can be described as a Volkov state [28] (i.e., the final state takes into account the interaction of the electron with the field only, not with the ion). In the limiting case of tunnelling ionization, the rate derived by Keldysh can be expressed as [29]

$$\Gamma \propto \exp\left[-\frac{2\gamma}{3\omega_L}\right]. \tag{1.8}$$

Subsequent works by other authors derived more generally applicable expressions for the tunnelling ionization rate. See for example, the Keldysh-Faisal-Reiss (KFR) approximation [30, 31], the Ammosov-Delone-Kraĭnov (ADK) model for atoms [32], and the extension of the ADK model to molecules (the MO-ADK model) [33]. Due to the strong

dependence of the ionization rate on the electric field strength, ionization due to an oscillating laser pulse is highly localised around the peaks and troughs of the laser field, resulting in short bursts of ionization, as will be evident in the results presented in this thesis.

From the schematic representation of tunnelling ionization shown in Fig. 1.7(c), it is clear that increasing the applied field strength will eventually lead to a point in which the potential barrier is reduced so much that the electron is no longer bound (Fig. 1.7(d)). An electron escaping in this manner is known as over-the-barrier ionization (OTBI).

As will be seen in the next subsection and in Section 1.4, Keldysh's picture of ionization proceeding via tunnelling is an essential first step towards understanding a number of other non-perturbative processes that can occur during strong-field laser-matter interactions.

1.3.3 ATI and the three-step recollision model

In Section 1.3.1 we introduced ATI as MPI by more photons than required for ionization, with the resulting ATI spectra consisting of a series of peaks separated by the photon energy, ω_L, whose intensity decreases rapidly with increasing peak energy. Later experiments involving higher intensity fields measured ATI spectra with shapes similar to those shown in Fig. 1.8, consisting of two distinct regions. The first of these is a series of low energy peaks, with a cutoff around $2U_p$. This region is then followed by a plateau region of peaks with higher energy but lower intensity, which extends to a cutoff around $10U_p$. This is the typical structure of ATI spectra. Significantly, the intensities of the peaks in the plateau region decrease much more slowly with increasing energy than predicated by the perturbative description. A number of non-perturbative pictures were produced to explain this observed structure of ATI spectra. The most notable of these was the semiclassical three-step recollision model, introduced by Corkum in 1993 [35].

In the first step of this model, an electron is tunnel ionized, with a probability given by the ADK model [32]. Once the electron is ionized, it is treated as a classical particle in the presence of the laser field. In the original formulation of the recollision model,

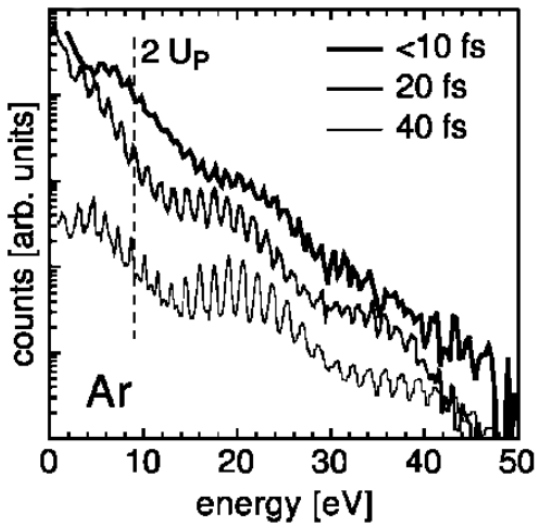

Figure 1.8: Above-threshold ionization (ATI) spectra of argon for different pulse durations, with a laser intensity of 0.8×10^{14} W/cm^2. Each spectrum consists of a low energy region extending to $2U_p$ in which the number of counts decreases sharply with energy, followed by a plateau region in which the number of counts decrease slowly with energy. The plateau regions extends to a cutoff around $10U_p$. Note that the spectra have been separated from each other vertically for clarity. Figure adapted from [34].

the effect of any Coulomb potential from the parent ion (also referred to as the core) is neglected in this second step. Additionally, it is assumed that the electron is "born" into the continuum at the origin and with zero initial velocity (i.e., $x(t_0) = v(t_0) = 0$ in a one-dimensional picture, where t_0 is the time at which the electron tunnel ionizes). In the final step the electron can either be driven back towards the parent ion and recollide in some way, or propagate away from the parent ion without recollision. For the case of ATI in this three-step model, the recolliding electron elastically scatters from the core.

This three-step model allows us to explain the origin of the $2U_p$ and $10U_p$ cutoffs in the ATI spectra. The trajectory of an electron in the continuum under the influence of a strong laser field is strongly dependent on the laser phase at which it is tunnel ionized. By considering the different possible classical trajectories, it can be shown that for electrons that drift away from the core without recollision (so-called "direct electrons"), the maximum kinetic energy that can be gained is $2U_p$. On the other hand, considering the trajectories in which the ionized electron is driven back towards the core and backscatters, it can be shown that electrons can gain up to as much as $10U_p$

in kinetic energy [29, 35].

As we will see in Section 1.4, the three-step recollision model is not limited to describing ATI. By considering recollision processes other than elastic scattering, the three-step model can be applied to other non-perturbative processes; most notably, high harmonic generation.

1.3.4 Summary

In this section we have given a brief introduction to a number of ionization processes that can occur during the interaction of a strong laser field with an atomic or molecular system. At low intensities ($< 10^{14}\,\mathrm{W/cm^2}$), perturbation theory can be used to describe ionization, in the form of MPI and ATI. At higher intensities, the perturbative picture breaks down, and Keldysh's tunnelling model of ionization becomes more applicable. The transition between the perturbative regime and the tunnelling regime can be understood in terms of the Keldysh parameter.

The semiclassical three-step recollision model of Corkum was introduced, which has been used to explain experimental observations of features in ATI spectra that cannot be explained with a perturbative description. In the next section we will see how the three-step recollision model can also be applied to another process, and the one of the most interest in this thesis: high harmonic generation.

1.4 Harmonic generation and high harmonic generation

In the previous section we introduced a number of ionization mechanisms, in which the interaction of a laser pulse with a system (e.g., a molecule) leads to the emission of one or more electrons. Harmonic generation, in basic terms, is an alternative process that results in the emission of photons rather than electrons, whose energy is higher than that of the photons of the incident laser field. As with ionization, there are different mechanisms for the production of harmonics with different intensities of laser pulse. In this section we will describe the two separate processes of harmonic generation (HG) and high harmonic generation (HHG), and discuss how HHG can be described in terms of the three-step recollision model.

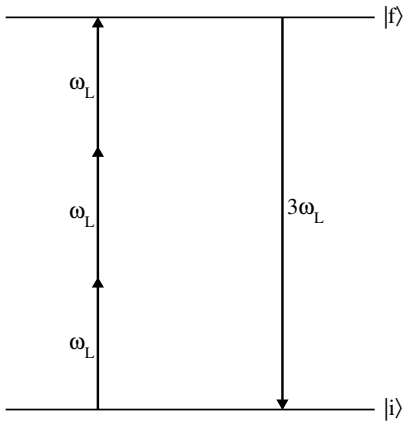

Figure 1.9: Schematic diagram of the harmonic generation process. In this example the system is excited from some initial state, $|i\rangle$, to some final (excited) state, $|f\rangle$, by the absorption of three photons, each of energy ω_L. The system then relaxes back to its initial state, resulting in the emission of a single photon of energy $3\omega_L$.

1.4.1 Harmonic generation at low intensities

In the perturbative regime, harmonic generation (HG) proceeds via the mechanism shown in Fig. 1.9, in which the absorption of N photons of energy ω_L leads to the emission of a single photon of energy $N\omega_L$. For media that possess inversion symmetry (for example, noble gases, which are commonly used in experiments), conservation of parity means that only odd harmonics (harmonics with frequencies that are odd multiples of the incident laser frequency) are produced. This is due to the fact that in systems with inversion symmetry the eigenstates have a defined parity, and the de-excitation of the system that leads to the emission of a single photon of energy $N\omega_L$ must be a transition between two states of different parity. Consequently, the excitation of the system cannot be due to absorption of an even number of photons [36].

The conversion efficiencies of the emitted harmonics in this process are strongly dependent on laser intensity, since the probability of absorbing N photons decreases rapidly as N increases. As was the case with MPI and ATI, the development of higher intensity lasers led to the experimental observation in the 1980s of the production of harmonics which could not be explained by this perturbative description.

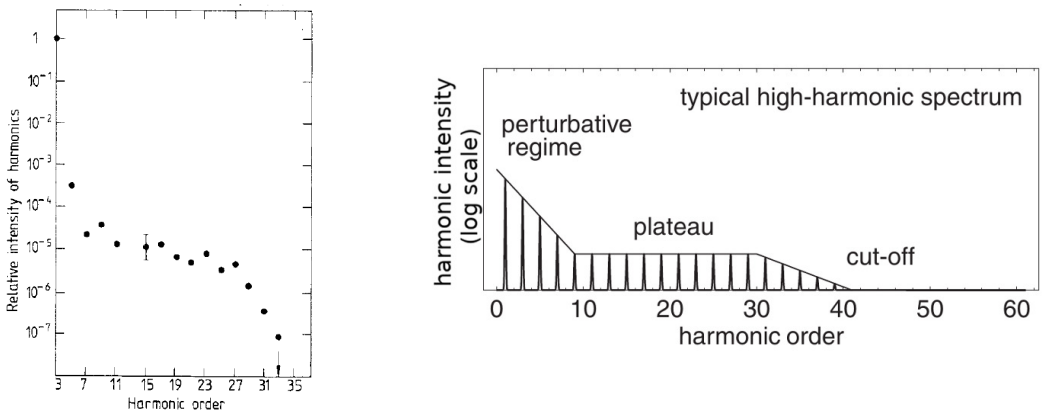

(a) Experimental HHG spectrum (b) Typical structure of a HHG spectrum

Figure 1.10: Typical structure of high harmonic spectra. Note that the energy of emitted photons is given as a harmonic order; i.e., harmonic number = 1 means that emitted photons have the same energy as incident photons. (a) Harmonics generated in Ar with a 30 ps, infrared laser of intensity 3×10^{13} W/cm^2. Figure reproduced from [38]. (b) General structure of a high harmonic spectrum (harmonic intensities plotted on a logarithmic scale). Figure adapted from [39].

1.4.2 High harmonic generation (HHG): the three-step model

Measuring the intensity of photons produced in a harmonic generation experiment as a function of photon energy allows one to plot a harmonic spectrum. The harmonic spectra obtained in early experiments involving high intensity (10^{13}–10^{14} W/cm^2) laser pulses [37, 38], such as the spectrum shown in Fig. 1.10(a), exhibited a dependence of harmonic intensity on harmonic order that did not fit with the perturbative picture. Subsequent measurements confirmed that the general shape of such harmonic spectra is that of Fig. 1.10(b). These spectra have three main features. Firstly, there are a number of low-order harmonics, whose intensity decreases rapidly with increasing harmonic order. These peaks arise from transitions between bound levels (described within the perturbative picture), with a rapid decrease in intensity with increasing harmonic order, as expected from the perturbative description. This region of low-order harmonics is followed by a (potentially extensive) plateau region in which the intensity varies little between harmonic order. Finally, there is a sharp cut-off at the end of the plateau region, beyond which no harmonics are emitted. The peaks in this plateau region are produced by an altogether different mechanism than the lowest-order harmonics; this process is known as high harmonic generation (HHG). We also note from Fig. 1.10 that, in general, HHG results in the emission of odd harmonics only, for the

reasons of parity conservation described in Section 1.4.1 above.

In Section 1.3.3, the non-perturbative aspect of ATI with intense laser pulses was understood in terms of the semiclassical three-step recollision model of Corkum *et al.*, with the recolliding electron scattering elastically from the core. This three-step model has also been applied to explain the HHG process [35], in which the recolliding electron recombines to the parent atom or molecule, emitting a high energy photon in the process. For HHG, the three steps of this semiclassical model, illustrated in Fig. 1.11, can be summarised as

1. An electron is ionized via tunnel ionization and appears in the continuum with zero velocity;
2. The free electron is then accelerated by the electric field of the laser pulse, following a classical trajectory;
3. Depending on the polarization of the laser field and the ionization time of the electron, the oscillating electric field may then cause the accelerated electron to return to the parent ion, where it can recombine to the ground state, giving up the kinetic energy it gained in the continuum in the form of a high energy photon (a high-order harmonic).

Just as with ATI spectra, the position of the cutoff in the harmonic spectrum can be estimated by solving classical equations of motion for an electron in the presence of the oscillating laser field. For a monochromatic, linearly polarized laser field described by

$$E(t) = E_0 \cos(\omega_L t), \tag{1.9}$$

where E_0 and ω_L are the amplitude and frequency of the field respectively, the equation of motion of the electron following ionization is

$$\frac{d^2x}{dt^2} = \ddot{x}(t) = E_0 \cos(\omega_L t), \tag{1.10}$$

where we have assumed that the motion of the electron is entirely along the laser polarization direction, since the field is linearly polarized. Integrating this equation and applying the the initial condition $v(t_0) = 0$ (i.e., the electron has zero velocity

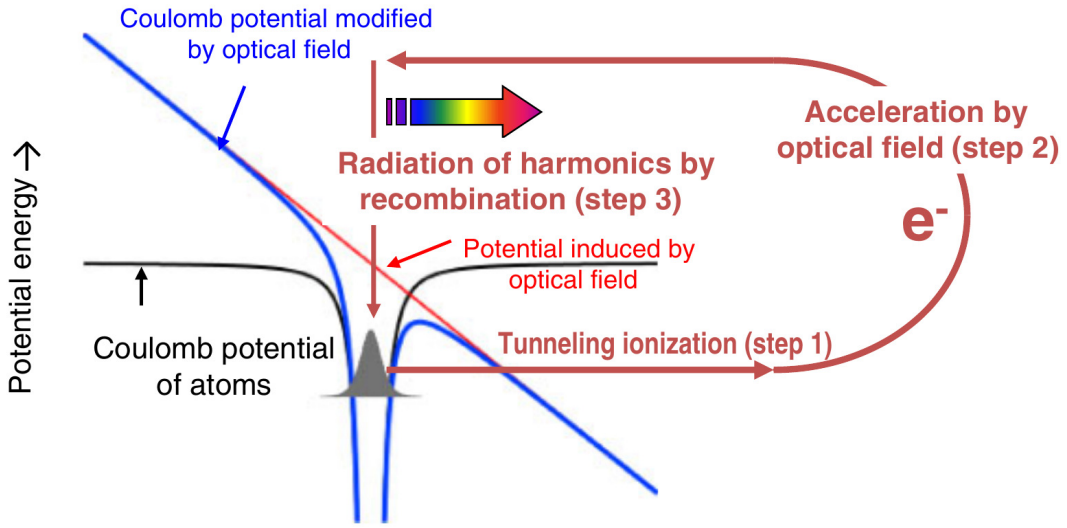

Figure 1.11: Schematic representation of the three-step model of high harmonic generation. In the first step, the applied laser field distorts the Coulomb potential enough that a potential barrier is formed, through which an electron tunnel ionizes. In the second step, the newly ionized electron is accelerated by the applied laser field, gaining kinetic energy. When the sign of the applied field reverses, the electron is driven back to the parent ion. Recombination can then occur (step three), with the electron's kinetic energy being emitted in the form of a high energy photon. Figure reproduced from [40].

immediately following ionization), the velocity of the electron at time t is given by

$$\dot{x}(t) = \frac{E_0}{\omega_L}\Big[\sin(\omega_L t) - \sin(\omega_L t_0)\Big], \tag{1.11}$$

where t_0 is the time at which the electron ionizes ($t > t_0$). The position of the electron at time t is then given by a further integration, namely

$$x(t) = -\frac{E_0}{\omega_L^2}\Big[\cos(\omega_L t) - \cos(\omega_L t_0) + \omega_L(t - t_0)\sin(\omega_L t_0)\Big], \tag{1.12}$$

where we have assumed that the position of the electron immediately following ionization is $x(t_0) = 0$. The recollision times may be found by solving Eq. (1.12) for $x(t) = 0$, for which there are no analytical solutions. Solving this equation numerically, it can be shown that the kinetic energy of the electron upon recollision, given by

$$E_k = \frac{1}{2}\dot{x}^2(t) = 2U_p\left[\sin(\omega_L t) - \sin(\omega_L t_0)\right]^2, \tag{1.13}$$

has a maximum value of $3.17U_p$. The recolliding electron may scatter off the core, or

it may recombine, giving up its kinetic energy in the form of a high energy photon. In the case of recombination, the maximum energy of emitted photons is therefore

$$E_c = n_{\mathrm{c}}\omega_L \simeq I_p + 3.17U_p, \tag{1.14}$$

where n_{c} is the maximum (cutoff) harmonic produced and I_p is the ionization potential of the system. This prediction from the semiclassical approximation of Corkum *et al.* was in good agreement with empirical scaling laws from earlier experimental works [41, 42], and Eq. (1.14) is now widely used to calculate expected HHG cutoffs (although an alternative cutoff law, based on a fully quantum treatment, also exists; this will be introduced below).

1.4.3 Electron trajectories

One advantage of working with the semiclassical three-step model of HHG is the conceptual and mathematical simplicity of associating the energy of emitted harmonics with the trajectories taken by the ionized electrons. Solution of the classical equations of motion given above allows the trajectories of electrons ionized at different phases of the laser field to be investigated. For a number of these possible trajectories, the electron will in fact never return to the core; in the following discussion it should be assumed that we are only interested in those trajectories that do result in a recollision.

For each electron recollision energy (with the exception of the cutoff energy), there are two possible trajectories that will result in a recolliding electron with that energy: these trajectories are referred to as either short or long trajectories. As illustrated in Fig. 1.12, electrons ionized within the first $\sim 1/20$ of a laser cycle after the peak of the laser field will follow a so-called long trajectory, and recombine with the core $> 2/3$ of a laser cycle after ionization. On the other hand, electrons ionized between $\sim 1/20$ and $\sim 1/4$ of a laser cycle after the peak will follow a short trajectory, spending much less time in the continuum, and recombining within 2/3 of a laser cycle. As indicated by the shading in Fig. 1.12(a), and shown more explicitly in Fig. 1.12(b), the shortest short trajectories and the longest long trajectories will have very little kinetic energy on recollision. The short and long trajectories overlap for electrons ionized $\sim 1/20$ of a cycle after the peak. This cutoff trajectory leads to recombination at $\sim 2/3$ of a cycle

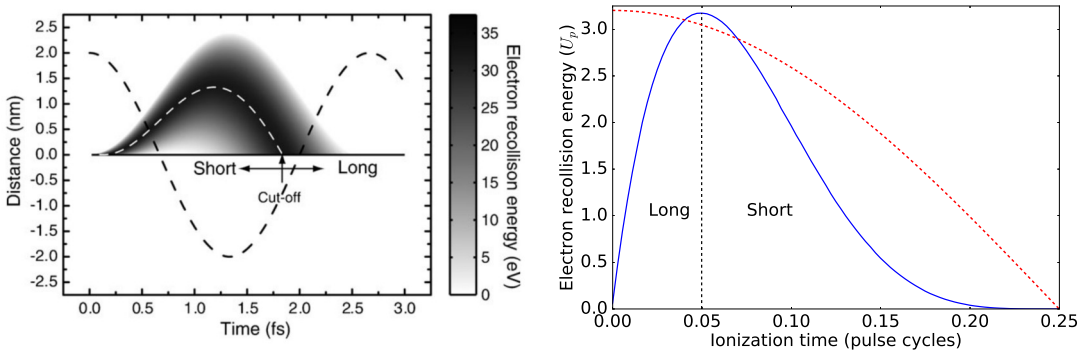

(a) Electron trajectories

(b) Electron recollision energies

Figure 1.12: Relationship between an electron's ionization phase and its recollision energy in the semiclassical three-step model. (a) Electron trajectories following ionization in the presence of an 800 nm laser field with intensity 2×10^{14} W/cm^2. The electric field of the laser is indicated by the dashed black line, and is defined to peak at $t = 0$. The electron's displacement is plotted on the vertical scale, while the shading indicates the electron's kinetic energy upon recollision. The dotted white line indicates the trajectory associated with the highest recollision energy (i.e., the trajectory associated with the cutoff harmonic). Figure reproduced from [43]. (b) Electron recollision energy as a function of ionization time. The red dashed line indicates the electric field of the laser, which is defined to peak at $t = 0$. The vertical dashed line indicates the ionization phase that results in the maximum recollision energy of $3.17\,U_p$, at the crossover between long and short trajectories.

after the peak, with the maximum possible recollision energy of $3.17U_p$.

As a final point regarding HHG trajectories, it should be noted that in the discussion so far we have assumed that the laser field is linearly polarized, meaning that an electron ionized in one direction will be driven back along the same direction when the sign of the laser field changes. If instead the field is elliptically or circularly polarized, HHG will generally be suppressed compared to the linearly polarized case. This suppression can be understood in terms of the electron trajectories: with an elliptically or circularly polarized laser field, the ionized electron will trace out a spiral-like trajectory, possibly missing the core and therefore avoiding recombination. Clearly this is particularly relevant for the description of HHG from atoms and small molecules; with larger molecules in non-linearly polarized fields there is the possibility of ionization from one atomic site on the molecule and recombination at a different site [44–46]. As we will see in Section 1.5.4, the strong dependence of HHG on the ellipticity of the laser field has been exploited to enable the production of isolated attosecond pulses [47].

While the three-step model described above is invaluable as a conceptual description

of high harmonic generation, describing the ionized electron's motion in the laser field by classical mechanics is of course an approximation, and one that neglects several important features. For this reason, a number of other models have been developed that aim to improve upon the semiclassical three-step model while still retaining its conceptual attractiveness. We shall introduce two of these models below.

1.4.4 Beyond the semiclassical three-step model

Shortly after the introduction of the semiclassical three-step model by Corkum and others, a fully quantum model along the same lines was developed based on the strong-field approximation (SFA) of Keldysh, Faisal and Reiss [27, 30, 31] (the KFR theory for strong-field ionization). This approximation was extended to describe high harmonic generation by Lewenstein *et al.* [48], with the main assumptions being that the dynamics of a continuum electron are dominated by the laser field, and that the only bound state involved in the dynamics of the system is the ground state. These assumptions are generally most valid when the Keldysh parameter $\gamma \ll 1$, i.e., in the tunnelling or over-the-barrier ionization regimes [48].

The Lewenstein model is closely related to the semiclassical three-step model (indeed, in their original paper Lewenstein *et al.* make a point of showing how their model justifies the assumptions at the heart of the semiclassical model), but captures additional features such as wavepacket diffusion. In addition, the SFA-based model leads to an altered version of the cutoff law derived with the three-step model, namely

$$E_{\mathrm{c}}^{q} = n_{\mathrm{c}}\omega_L = 3.17U_p + I_p F(I_p/U_p), \tag{1.15}$$

where the factor $F(I_p/U_p) = 1.32$ for $I_p \ll U_p$ and decreases slowly towards 1 as I_p grows. The difference between the two cutoff laws is due to two effects. Firstly, in the Lewenstein model, the electron cannot appear at the origin after tunnel ionization as is assumed in the three-step model, but can recombine at the origin. Therefore the electron is able to gain additional kinetic energy as it travels this extra distance before recombination. Secondly, this gain of kinetic energy in the Lewenstein model is decreased for larger values of I_p due to diffusion effects [48].

The Lewenstein model has proven to be a very successful model of HHG, and has been

invaluable in comparing with and interpreting experimental results [49–51]. However, it too contains a number of striking approximations. These include the neglect of electron-electron interactions, as well as ignoring laser-induced depletion of the ground state population. The use of plane waves to describe the continuum wavepacket also neglects the effect that the Coulomb potential has on it.

Various modifications to the SFA have been proposed since the original 1994 paper; an overview of some of these can be found in a recent review [52]. Here we highlight just one of the most successful extensions to the SFA: quantitative rescattering theory (QRS) [53]. The central idea of this theory is the replacement of the plane-wave approximation normally used in the recombination step of the SFA by scattering waves. In the QRS, HHG spectra are expressed in terms of the product of a returning electron wavepacket and the exact photorecombination transition dipole. In essence the QRS keeps an SFA description of the ionization and propagation steps of the three-step model (which the Lewenstein model describes fairly accurately), while treating the recombination step more accurately. In this way the QRS offers a compromise between the efficiency of the SFA on one hand, and the accuracy of *ab initio* approaches (see Chapter 2) on the other. For further discussion around the QRS, see [52–54].

The SFA and the QRS are powerful techniques, which have provided qualitative and quantitative understanding of HHG in many systems. However, they are based on the single active electron approximation, and as such are unsuited to general application to multielectron systems where a number of orbitals contribute to the dynamics. For these systems, more computationally demanding, *ab initio* theoretical treatments are required; we will introduce some of these in Chapter 2.

1.4.5 Summary

In this section we have introduced the key concepts around high harmonic generation. We have seen how the typical shape of a harmonic spectrum for a strong-field laser-molecule interaction consists of several distinct regions, originating from a combination of bound-bound and bound-continuum transitions. The semiclassical three-step model of HHG (and its fully quantum analogue based on the SFA) were introduced, and the link between harmonic orders and electron trajectories was discussed.

The production of high harmonics has attracted much interest in recent years, largely due to the potential of HHG in a number of applications. In the final section of this chapter, we will briefly highlight two of these applications, as well as noting some of the experimental techniques and challenges associated with HHG.

1.5 Applications of HHG and experimental considerations

To conclude this chapter, we wish to briefly highlight two of the most exciting applications of HHG in recent years, namely the use of HHG for attosecond pulse production and for imaging molecular orbitals (with the possibility of dynamic probing of molecular structure). Firstly though, we will briefly mention a few experimental considerations related to HHG. These are important to be aware of when considering comparisons between experimental and theoretical results.

1.5.1 HHG in experiments

The description of HHG given in the previous section is based on experiments involving gas or plasma HHG targets. As well as allowing for samples to be studied free from any effects from the environment, these types of targets have the advantage over solid targets that the atoms or molecules in the interaction area can be replenished more easily. Performing HHG experiments on molecules that only occur naturally as solids therefore requires specialised techniques to produce samples suitable for HHG studies, for example heating of the solid sample [55, 56] or laser ablation [57, 58]. A challenge with these techniques is getting the correct balance between producing a high enough sample density to give a measurable HHG signal, and minimising the amount of molecular fragmentation that occurs during the creation of the sample; a prepared sample containing too large a number of fragments of the parent molecule could lead to misleading results.

In the three-step model introduced in Section 1.4.2, HHG is described in terms of the single-atom (or microscopic) response. This will also be what is considered in the results presented in Chapters 4 and 5. In experiments, on the other hand, the measured harmonics are the result of both the microscopic and macroscopic responses of the sample. Capturing macroscopic (propagation) effects in theoretical descriptions of

HHG is challenging, and will not be attempted in the work described in this thesis. For this reason, direct quantitative comparison of experimental results with the results presented in later chapters is difficult. While some comparisons with experimental results are possible (for example considering how HHG efficiency changes as the molecular alignment is varied, as will be seen in Chapter 4, or considering the relative intensities of HHG in different molecules, as in Chapter 5), making quantitative comparisons with experimental results more generally would require several additional non-trivial steps [59]; two of these are highlighted below.

Firstly, in our calculations the molecule under investigation is initially aligned in one of several ways with respect to the laser polarization direction. In experiments, the sample gas is made up of a large number of molecules, each with their own alignment. Comparison with experiment would in general require the use of some type of orientation averaging technique [60–62] to account for the random alignment of molecules in the experimental sample (this is less of an issue when making comparisons with experiments employing one of the alignment techniques that will be described in Section 1.5.2). Such averaging techniques require single-molecule calculations to be performed for a relatively large number of different molecular alignments, which would be time-consuming and computationally expensive for calculations of the type presented in Chapters 4 and 5.

Secondly, since HHG is a non-linear, coherent process, obtaining a strong harmonic signal depends strongly on how well in phase the harmonic emission is throughout the whole interaction volume. Experiments studying HHG have to deal with a number of effects that contribute to phase mismatch in the sample, which can significantly reduce the efficiency of HHG in the system. A microscopic phase (also known as an atomic or dipole phase) arises from the fact that a specific harmonic can be produced by an electron following one of two possible trajectories (long or short). Since the kinetic energy gained by the ionized electron is dependent on U_p, which is proportional to the laser intensity, there will also be a phase associated with variations in the laser intensity throughout the interaction volume (due to the necessity of focusing the laser beam). Macroscopic effects associated with the propagation of the driving laser beam and the high harmonic beam also introduce potential phase mismatch. These include gas and plasma dispersion effects (changes of refractive index with wavelength), and

the geometric Guoy phase arising from focusing of the driving laser beam. For further details on all of these effects, as well as the techniques used to reduce phase mismatch, the reader is referred to relevant reviews found in, for example, [13, 63, 64]. By their very nature, these macroscopic phase-matching effects do not enter in to the single-molecule calculations presented in later chapters. They are simply mentioned here to make the reader aware of some of the differences between HHG calculations and experiments, and consequently some of the effects that would need to be included in a calculation of HHG if detailed quantitative comparison with experiment was required.

1.5.2 Molecular alignment

Unlike HHG in atoms, HHG in molecules can exhibit a strong dependence on the orientation of the molecule with respect to the laser polarization direction [65–68]. This alignment-dependence is essential for some of the applications of HHG highlighted in Section 1.5.3. In these applications, and more generally, interpreting the results of a molecular HHG experiment often requires some knowledge of the molecular alignment with respect to the field. Therefore it is often beneficial to attempt to create some degree of uniform alignment throughout the sample of molecules.

Alignment can be induced in a sample of molecules using one of a number of techniques. For polar molecules (molecules with a permanent dipole moment), a degree of alignment can be induced by applying a static electric field. For molecules more generally, if the applied field is strong enough ($\sim 10^{12}$–10^{13} W/cm^2) an induced dipole moment can be set up in the molecule, and alignment can be achieved via either adiabatic alignment or non-adiabatic (impulsive) alignment. In the adiabatic case, the applied pulse has a duration that is longer than the rotational period of the molecule, meaning that the molecule has time to come into equilibrium with the laser field. Typically nano–picosecond duration pulses are used for adiabatic alignment. In non-adiabatic alignment, a laser pulse with duration much shorter than the rotational period of the molecule is applied, giving the system a “kick”, which creates a superposition of rotational states in the molecule. The subsequent (field-free) evolution of this rotational wavepacket results in periodic transitions between alignment and anti-alignment within the sample. Non-adiabatic alignment requires the use of femtosecond pulses, and has the advantage that the resulting system can be be studied in field-free condi-

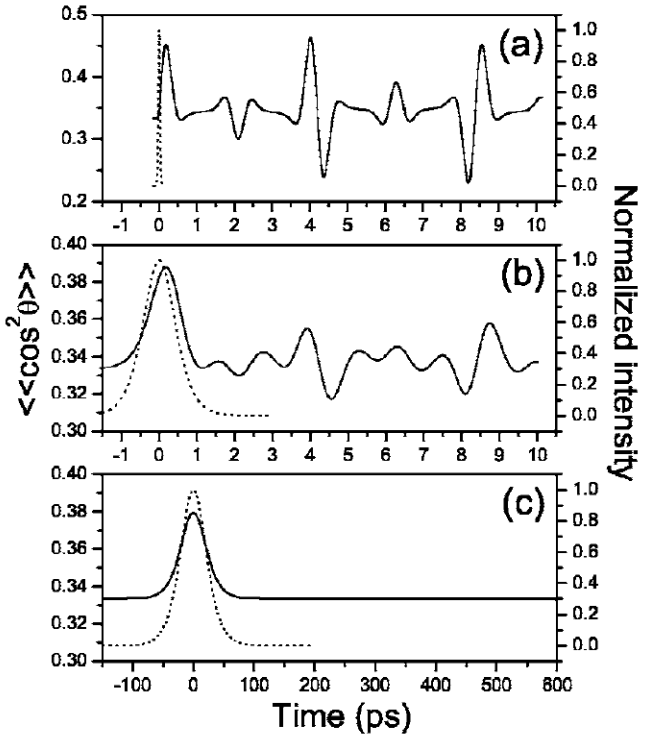

Figure 1.13: Examples of the difference between adiabatic and non-adiabatic alignment. Calculated values for the degree of alignment in N_2 at 50 K with different pulse durations T and peak intensities I_0 (pulse profile indicated by dotted curves). (a) $T = 50$ fs, $I_0 = 2.5\times10^{13}$ W/cm^2: non-adiabatic alignment. Following a short aligning pulse, the molecules are brought into alignment. Due to the number of rotational states excited by the pulse however, they quickly de-phase and alignment is lost. Beating between rotational states causes revivals of alignment every ~ 4 ps. (b) $T = 1$ ps, $I_0 = 2.5\times10^{12}$ W/cm^2: intermediate case between non-adiabatic and adiabatic alignment. (c) $T = 50$ ps, $I_0 = 2.5\times10^{12}$ W/cm^2: adiabatic alignment. The degree of alignment increases and decreases in line with changes in the pulse intensity. Once the pulse has ended there are no revivals of alignment (i.e., the molecules revert to a random distribution). Figure reproduced from [69].

tions (which is not the case if a static field or adiabatic alignment is used).

The degree of alignment obtained is generally given in terms of the parameter $\langle\cos^2\theta\rangle$, where θ is the angle between the molecular symmetry axis and the laser polarization direction. A value of $\langle\cos^2\theta\rangle = 1/3$ represents a randomly orientated sample of molecules, while values of 1 and 0 indicates perfect alignment and anti-alignment respectively. The difference between adiabatic and non-adiabatic alignment is illustrated in Fig. 1.13. A detailed review of aligning molecules with strong laser pulses can be found in [70].

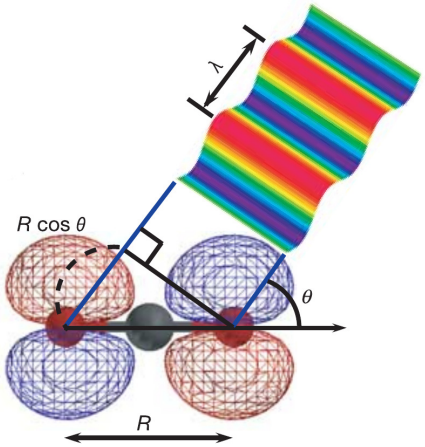

Figure 1.14: Schematic representation of a technique for using HHG to probe molecular structure. By treating a CO_2 molecule as an elongated diatomic molecule, with the two O nuclei (red spheres) acting as point emitters, a two-centre interference model can be applied. Here λ is the de Broglie wavelength of the recolliding electron, θ is the angle between the molecular axis and the laser polarization direction, and R is the separation between the two O atoms. Depending on the values of these parameters, destructive or constructive interference may occur during the recombination step of HHG. Measurement of the harmonic spectra at a range of values of θ then in principle allows R to be determined using the interference conditions given in the text. Figure adapted from [72].

The alignment techniques described above are essential for experiments studying the orientation-dependence of ionization and HHG in molecules, as well as for the first application of HHG we will consider: HHG as a tool for imaging molecular structure and dynamics.

1.5.3 HHG for ultrafast imaging

The recolliding electron in HHG has two characteristics that make it a potentially powerful probe of molecular structure and dynamics. Firstly, depending on the laser parameters, the returning electron may have gained substantial kinetic energy during its excursion in the laser field, and therefore have a correspondingly short de Broglie wavelength ($\approx$1 Å). Secondly, since the entire HHG process takes place in less than one optical cycle of the driving laser pulse, the recolliding electron can act as a probe pulse of very short duration ($\approx$1 fs). These two properties, combined with sophisticated experimental techniques, mean that use of HHG offers the potential for imaging molecular structure and dynamics with sub-angstrom spatial resolution and sub-femtosecond temporal resolution [43, 71].

Some of the earliest experimental studies on the use HHG for imaging were those of Kanai *et al.* [72] and Itatani *et al.* [73]. Kanai *et al.* reported in 2005 on the first experimental confirmation of intramolecular two-centre interference, which they measured in aligned samples of CO_2. By simultaneously measuring the ionization yield and the harmonic intensity, the authors were able to show that in CO_2 HHG is enhanced when ionization is suppressed due to molecular alignment, and vice versa. The consequence of this observation is that observed minima in the HHG spectra of CO_2 must be due to interference during the recombination step, rather than any effect during the ionization step. Since the rotational period of the molecule is known, measurement of the harmonic intensity as a function of time (i.e., as a function of orientation angle, θ, for an aligned sample of molecules; see Fig. 1.14) allows the distance between oxygen atoms to be determined using simple interference conditions [72, 74]

$$R\cos\theta = n\lambda \qquad \text{(destructive interference)}, \tag{1.16}$$

$$R\cos\theta = (n-1/2)\lambda \qquad \text{(constructive interference)}. \tag{1.17}$$

Two-centre interference has since been observed in a number of other molecules, including H_2 [75], N_2O [76] and C_2H_2[68]. A challenging aspect of this technique however is that the derivation of the simple interference formulae above requires that the initial state of the molecule can be approximated by a linear combination of atomic orbitals (LCAO), with one atomic orbital per site. When this is not the case, the interpretation of the observed interferences is not obvious.

As well as measuring bond lengths, HHG can also be used to image the structure of molecular orbitals, as demonstrated by Itatani *et al.* in 2004 [73]. In the tomographic reconstruction method employed in this experiment, the high harmonic spectrum was measured from an aligned sample of N_2 molecules, for 19 different alignments. Tomographic inversion of these spectra then allowed the highest occupied molecular orbital (HOMO) of N_2 to be reconstructed (Fig. 1.15(a)), in good agreement with *ab initio* calculations (Figs. 1.15(b), 1.15(c)). This technique takes advantage of the fact that harmonic generation is highly sensitive to both the alignment angle and the spatial structure of the electronic wavefunction, as well as the fact that in N_2, tunnel ionization occurs predominantly from the HOMO (the orbital with the lowest ionization

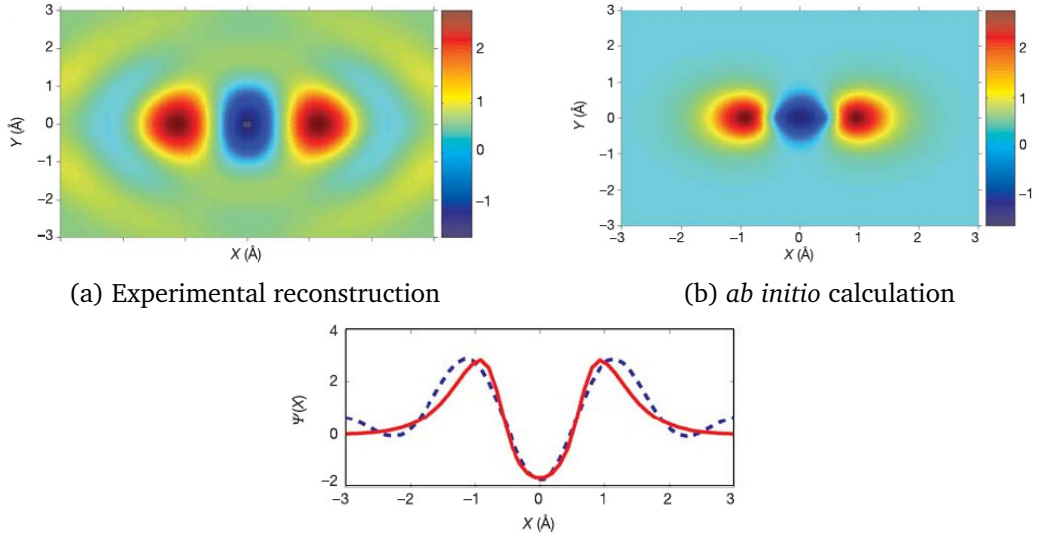

(a) Experimental reconstruction

(b) *ab initio* calculation

(c) Cuts along x-axis for (a) and (b)

Figure 1.15: Wavefunction of the highest occupied molecule orbital of N_2. (a) Reconstruction of the wavefunction, obtained through tomographic inversion of experimental HHG spectra taken at 19 different molecular alignment angles. (b) *ab initio* calculation of the wavefunction. (c) Cuts along the internuclear axis for the reconstructed (dashed blue curve) and *ab initio* (solid red curve) wavefunctions. Figure adapted from [73].

potential). Although this was a reconstruction of a static molecular orbital, it was envisaged that the concept could be extended to image dynamics using a pump-probe setup (i.e., a pump pulse initiates some dynamics, and a subsequent probe pulse generates harmonics which are measured; the pump-probe delay then gives information about the dynamics).

The experiment and analysis of Itatani *et al.* worked from the assumption that the harmonic spectra contained information about the structure of the HOMO alone. Subsequent experiments however showed that orbitals below the HOMO also contribute to HHG [77, 78]. In experiments on aligned CO_2 molecules, Smirnova *et al.* demonstrated that measurement of both the phases and amplitudes of high harmonics allows for study of these multielectron dynamics [79].

Rather than using two time-delayed laser pulses as is usual for pump-probe schemes, it is also possible to conduct pump-probe experiments using HHG itself as both the pump and the probe. This is the technique used in the PACER (probing attosecond dynamics by chirp encoded recollision) method [49, 80, 81], in which the tunnel ionization step of HHG acts as the pump and the recollision of the electron acts as the probe. By first

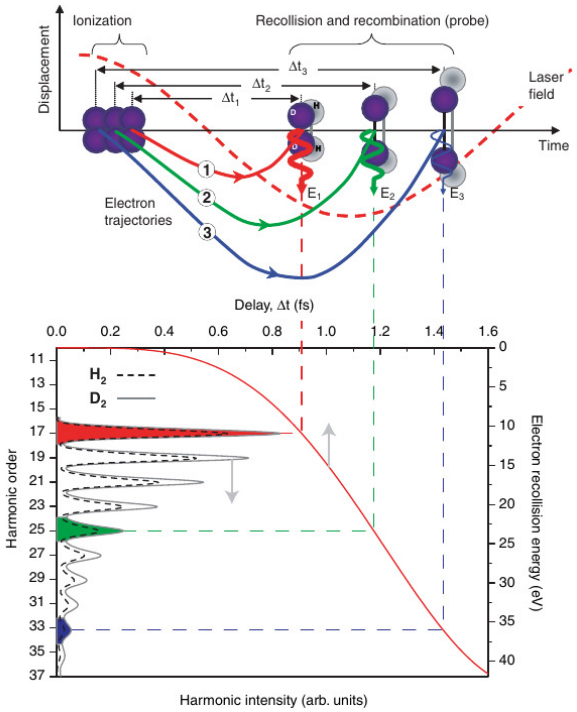

Figure 1.16: Principle behind the PACER technique. Electrons ionized at different phases of the laser field follow different trajectories (1, 2, 3) after ionization, and recollide with the core after different time delays (Δt_1, Δt_2, Δt_3). The different kinetic energies (E_1, E_2, E_3) associated with these trajectories result in the emission of different harmonic orders when the electron recombines. This allows a range of pump-probe delays to be accessed from the measurement of a single harmonic spectrum. Measuring the ratio of harmonics generated in different isotopes (in this case H_2 and D_2) then allows the effect of nuclear dynamics to be isolated. Figure reproduced from [49].

filtering out the long trajectory contributions to HHG, the PACER method takes advantage of the one-to-one mapping between the duration of short electron trajectories and the associated high harmonic order (Fig. 1.16). This allows a range of pump-probe delays to be studied by measuring the harmonic spectrum from a single laser pulse. The PACER technique has been experimentally demonstrated by studying nuclear motion in H_2 and D_2 molecules approximately 1 fs after ionization, with a temporal resolution of ≈ 100 as [49].

The examples given here are just a sample of the applications of HHG for imaging. More comprehensive reviews of the subject can be found in [43, 71, 82, 83].

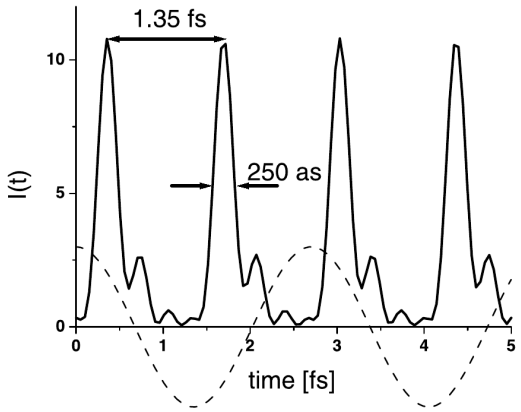

Figure 1.17: Train of attosecond pulses produced via HHG. The dashed line represents the IR probe field, which has a period equal to twice the delay time between successive attosecond pulses. Note that this reconstruction of temporal intensity profiles for the attosecond pulses is based on the assumption that all pulses are identical; in reality there may be some variation between the pulses. Figure reproduced from [84].

1.5.4 HHG for attosecond pulse production

Since the period of an electromagnetic field is inversely proportional to the associated photon energy, producing increasingly short pulses will clearly require higher frequency radiation. By filtering a high harmonic spectrum to select only a small number of the highest energy harmonics, it is possible to produce attosecond duration pulses. As was seen in Fig. 1.12, in HHG the most energetic harmonics are emitted in very narrow windows of time due to ionization near the peak field strengths of the driving laser pulse. For a multicycle driving pulse, this results in the production of a train of attosecond pulses; one produced every half cycle of the driving pulse (Fig. 1.17) [84–86].

To facilitate a greater degree of control in observing or controlling ultrafast processes, a single, isolated, attosecond pulse would be preferable to an attosecond pulse train. This requires high harmonics to only be emitted in a single half-cycle of the driving pulse. While reducing the duration of the driving pulse to just a few cycles will reduce the number of attosecond pulses in the pulse train, it will not, by itself, enable the production of an isolated attosecond pulse, since the shortest possible driving pulse duration is one cycle, which will result in two attosecond pulses. Therefore one of a number of techniques, known as gating techniques, must be employed to preferentially select the high harmonics produced in a single half cycle.

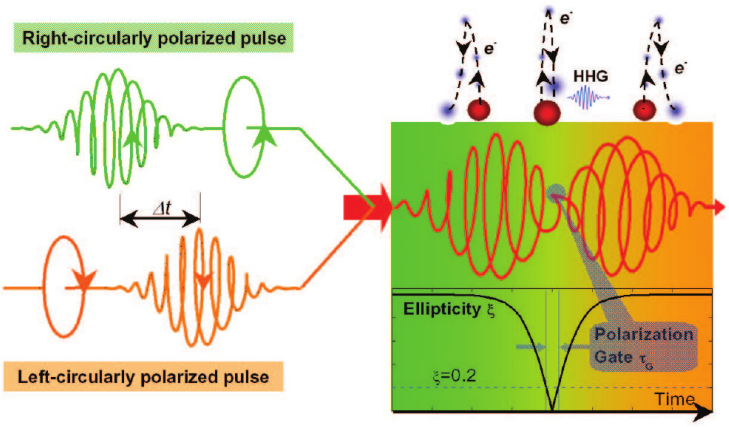

Figure 1.18: Schematic of the polarization gating technique used for producing isolated attosecond pulses. A right circularly polarized pulse and a left circularly polarized pulse are combined, with some delay time Δt between them, with the resulting pulse having an ellipticity that varies over time. Initially, the ellipticity is high, and no HHG can occur. In the middle of the pulse, the ellipticity drops to near zero for a very short time (less than half a pulse cycle), during which time HHG can occur. The ellipticity quickly increases again following this, and HHG is suppressed once more. Figure reproduced from [87].

One such technique is polarization gating, illustrated in Fig. 1.18. In this technique, the driving pulse is composed of a right circularly polarized pulse and a left circularly polarized pulse. When these two circularly polarized pulses are brought together with a suitable time delay, the resulting pulse has an ellipticity that varies over time: at the beginning and end of the pulse it is circularly polarized, but linearly polarized at some time in the middle. Crucially, the duration of the linear polarization region can be made shorter than one cycle by varying the durations of the circularly polarized pulses and the delay between them [87]. Due to the strong dependence of HHG on ellipticity referenced in Section 1.4.3, emission of harmonics is suppressed during the circularly polarized regions, and only allowed when the ellipticity briefly drops to near zero (the linearly polarized region). In this way HHG can be confined to a single half-cycle of the driving pulse, enabling the production of an isolated attosecond pulse.

Using polarization gating and other gating techniques [88], experimentalist have managed to produced isolated attosecond pulses as short as 47 as [5, 47, 89, 90], approaching one atomic unit of time (24 as). For more details on attosecond pulse production techniques, as well as the techniques required to characterize such short pulses, the reader is referred to [91, 92] and the references within.

1.5.5 Summary

In this section we have looked at HHG from a practical perspective. A number of experimental techniques and considerations have been introduced, and the differences between microscopic and macroscopic harmonic response have been highlighted. Two areas in which HHG has found practical applications were also discussed, namely the production of attosecond pulses and the use of HHG for imaging molecular structure and dynamics.

1.6 Conclusions

In this chapter we have given a brief overview of some of the aspects of strong-field physics that are most relevant to the work presented in this thesis. By analogy with photography of fast moving objects, we discussed how the study of processes occurring on the fast timescales of motion at the molecular scale requires specialised techniques. Lasers were then introduced as a tool that provided the necessary temporal resolution. By highlighting a few specific examples, we have seen how improvements to laser technology over the past half a century have greatly reduced the minimum duration of laser pulses while increasing the maximum pulse intensity. The resulting femtosecond and attosecond duration pulses, with electric field strengths comparable to or greater than the Coulomb field in molecules, led to the emergence of the fields of femtochemistry and, more recently, attoscience.

With such intense laser fields, a range of physical processes can occur in the atom, molecule or nanostructure under investigation. A number of these processes were introduced in this chapter, beginning with ionization mechanisms in Section 1.3. The transition from multiphoton ionization in low intensity fields to tunnelling ionization in high intensity fields was described, as well as how this transition can be understood in terms of the Keldysh parameter. The semiclassical three-step recollision model was then introduced, which can be used to explain experimental observations of non-perturbative effects in above-threshold ionization.

In Section 1.4 we introduced high harmonic generation, and discussed how it can be described by the semiclassical three-step model or its quantum analogue. The relation-

ship between electron trajectories and harmonic order was also discussed. In the final section of this chapter, we briefly introduced a number of challenges and considerations associated with HHG experiments, as well as two interesting applications of HHG.

The strong-field processes introduced in this chapter are challenging to describe theoretically, since a perturbative approach can in general no longer be applied. Approximations such as the SAE and SFA have enjoyed a great deal of success and popularity, but are challenging to apply to accurately describe multielectron effects in strong-field laser-molecule interactions. Describing such effects in general requires a full, multielectron, *ab initio* description. A number of the methods available for applying such a description will be discussed in the next chapter.

Chapter 2

Theoretical descriptions of strong-field laser-molecule interactions

---

2.1 Introduction

The improvements in laser technology over the past half a century that were outlined in the previous chapter brought with them a serious theoretical challenge: namely, how to accurately (quantum mechanically) describe the dynamics of molecules exposed to intense laser pulses, when the strength of the laser field renders a perturbative approach inadequate. Accurately and efficiently describing the dynamics of molecules during interactions with these new generations of laser pulses has required both the tailoring of existing theoretical methods as well as the development of new techniques. As we shall see in this chapter, describing the interaction of molecules with strong laser pulses is no easy task, and certain assumptions or restrictions almost always have to be made. One such assumption, the single active electron (SAE) approximation, is assumed in both the three-step and Lewenstein models described in the previous chapter. This approximation, as the name implies, assumes that only one electron is involved in the dynamics of the system. While these SAE-based models have been hugely successful in

providing qualitative understanding, a number of results demonstrating the role of several electrons, in high harmonic generation for example [78, 79, 93], have made clear the need to go beyond the SAE approximation. In this chapter we will introduce some of the most commonly used theoretical methods for treating multielectron systems, and highlight their relative advantages and disadvantages.

The chapter is arranged as follows: in Section 2.2 we will introduce how laser-matter interactions are described by theory in the most general sense, followed by a brief description of a number of the most widely used approximations and most popular theoretical methods used to describe time-dependent laser interactions with multielectron systems. In Section 2.3 we present the theory that is the basis of the work presented in this thesis: time-dependent density functional theory (TDDFT). The key concepts behind TDDFT, as well as its strengths and limitations, will be outlined in this section. In Section 2.4 we show how the electronic description provided by time-dependent density functional theory can be supplemented with a classical treatment of nuclear motion, in a quantum-classical molecular dynamics method. Finally in Section 2.5 we show how laser fields can be incorporated semi-classically into the theory described in the previous sections.

2.2 Describing the dynamics of multielectron systems

In this section we will discuss how the dynamics of a general multielectron system can be described theoretically. We begin by introducing the time-dependent Schrödinger equation, and then show how a number of approximations can reduce the complexity of the problem to a manageable level. Finally we introduce a number of the most commonly used wavefunction-based theoretical approaches to treating the time-dependent electronic structure problem. Note that since we are interested in studying systems interacting with very short laser pulses ($\approx 25\,$fs and shorter), we focus only on time-dependent methods; time-independent methods such as Floquet theory [94–96] will not be discussed since they are not applicable for describing such short pulses. In addition, it is assumed throughout that we are interested in describing a highly perturbed system (i.e., one in which perturbative approaches cannot be applied), since the intensities of the laser pulses considered in Chapters 4 and 5 are well outside the perturbative regime [97].

2.2.1 Time-Dependent Schrödinger Equation for molecular systems

The dynamics of any non-relativistic system are described by the time-dependent Schödinger equation (TDSE)

$$H(t)\Psi(t) = i\frac{\partial}{\partial t}\Psi(t), \tag{2.1}$$

where Ψ and H are the wavefunction and Hamiltonian of the system, respectively. For a general system of N_e electrons with positions vectors denoted by $\boldsymbol{r} = \{\boldsymbol{r}_1, \ldots, \boldsymbol{r}_{N_e}\}$, and N_n ions with position vectors denoted by $\boldsymbol{R} = \{\boldsymbol{R}_1, \ldots, \boldsymbol{R}_{N_n}\}$, the TDSE is

$$H(\boldsymbol{r}, \boldsymbol{R}, t)\Psi(\boldsymbol{r}, \boldsymbol{R}, t) = i\frac{\partial}{\partial t}\Psi(\boldsymbol{r}, \boldsymbol{R}, t). \tag{2.2}$$

The Hamiltonian of the system, $H(\boldsymbol{r}, \boldsymbol{R}, t)$, can be written as a sum of kinetic and potential terms, as

$$H(\boldsymbol{r}, \boldsymbol{R}, t) = T_e(\boldsymbol{r}, t) + T_N(\boldsymbol{R}, t) + V(\boldsymbol{r}, \boldsymbol{R}, t) + U(\boldsymbol{r}, \boldsymbol{R}, t), \tag{2.3}$$

where $T_e(\boldsymbol{r}, t)$ and $T_N(\boldsymbol{R}, t)$ are the kinetic energies of the electrons and ions of the system respectively, and $V(\boldsymbol{r}, \boldsymbol{R}, t)$ is the total potential energy of the system. Any time-dependent external potential (e.g., an applied laser field) is introduced through the general term $U(\boldsymbol{r}, \boldsymbol{R}, t)$, the form of which is assumed to be known. The other three terms in the Hamiltonian are given by

$$T_e(\boldsymbol{r}, t) = -\sum_{i=1}^{N_e} \frac{1}{2}\nabla_i^2, \tag{2.4}$$

$$T_N(\boldsymbol{R}, t) = -\sum_{I=1}^{N_n} \frac{1}{2M_I}\nabla_I^2, \tag{2.5}$$

and

$$V(\boldsymbol{r}, \boldsymbol{R}, t) = \frac{1}{2}\sum_{i=1}^{N_e}\sum_{\substack{j=1 \\ j\neq i}}^{N_e} \frac{1}{|\boldsymbol{r}_i - \boldsymbol{r}_j|} - \sum_{i=1}^{N_e}\sum_{J=1}^{N_n} \frac{Z_J}{|\boldsymbol{r}_i - \boldsymbol{R}_J|} + \frac{1}{2}\sum_{I=1}^{N_n}\sum_{\substack{J=1 \\ J\neq I}}^{N_n} \frac{Z_I Z_J}{|\boldsymbol{R}_I - \boldsymbol{R}_J|}, \tag{2.6}$$

where M_K and Z_K are respectively the mass and charge of ion K. The three terms on the right hand side of Eq. (2.6) correspond to electron-electron, electron-ion, and

ion-ion interactions respectively.

In principle, the full dynamics of the system could be found by solving Eq. (2.2), with the Hamiltonian defined in Eqs. (2.3) – (2.6), and assuming the initial state of the system is known (which could be found by solving the time-independent Schödinger equation, $H\Psi = E\Psi$). However, in practice solving Eq. (2.2) directly is impossible for all but the simplest of systems, as we will see below.

The simplest molecular system is the hydrogen molecular ion, H_2^+. For this system, Eq. (2.2) becomes

$$H(\boldsymbol{r}, \boldsymbol{R}_1, \boldsymbol{R}_2, t)\Psi(\boldsymbol{r}, \boldsymbol{R}_1, \boldsymbol{R}_2, t) = i\frac{\partial}{\partial t}\Psi(\boldsymbol{r}, \boldsymbol{R}_1, \boldsymbol{R}_2, t), \tag{2.7}$$

where $\boldsymbol{r}$ and $\boldsymbol{R}_1$, $\boldsymbol{R}_2$ are the vector positions of the single electron and the two ions respectively. Here we have a system with just one electron and two protons, and already an analytical solution is impossible, meaning that numerical methods must be employed. Attempting to solve this problem directly using numerical methods is a very computationally demanding task, due to the dimensionality of this equation. As it is written here, Eq. (2.7) would in essence be a (9 + 1)-dimensional TDSE in Cartesian coordinates (3 spatial coordinates for each particle, plus time). In practice this dimensionality can be reduced considerably if only the vibrational motion of the nuclei is taken into account. Examples of this approach for describing the dynamics of H_2^+ include references [98–101].

Even for small systems however, solving the TDSE directly with electronic and ionic degrees of freedom treated equally is prohibitively expensive (extending the approach used in the works referenced above to the hydrogen molecule would be approaching the limit of what is possible with current supercomputing facilities). Therefore some approximations are generally made to enable easier study of the dynamics of multielectron systems. In the next section we will introduce two of the most widely used approximations, which take advantage of the difference in masses between electrons and ions, and the consequent difference in their characteristic timescales.

2.2.2 Separating the electronic and nuclear degrees of freedom

One of the most commonly used approximations in simplifying the solution of the TDSE is the Born-Oppenheimer (BO) approximation [102], in which the motions of the electrons and ions are separated. In the BO approximation, the wavefunction is recast as

$$\Psi(\boldsymbol{r}_1,\ldots,\boldsymbol{r}_{N_e},\boldsymbol{R}_1,\ldots,\boldsymbol{R}_{N_n},t)=\sum_n \chi_n(\boldsymbol{R}_1,\ldots,\boldsymbol{R}_{N_n},t)\Phi_n(\boldsymbol{r}_1,\ldots,\boldsymbol{r}_{N_e},\boldsymbol{R}_1,\ldots,\boldsymbol{R}_{N_n}), \tag{2.8}$$

where χ_n and ϕ_n are nuclear and electronic wavefunctions respectively, with n indicating the electronic state. The dynamics of the system are then studied by first solving the time-independent Schödinger equation for the electronic part of the wavefunction, for a number of different nuclear configurations, i.e., different $\boldsymbol{R}_1,\ldots,\boldsymbol{R}_{N_n}$. The result is a set of potential energy surfaces (PES), along which the nuclei can then evolve over time. The idea behind the Born-Oppenheimer approximation stems from the large difference in mass between nuclei and electrons (the mass of the lightest nucleus, a proton, is 1836 times that of an electron) and consequently the difference in the timescales of nuclear and electronic motion, meaning that the electrons can be considered to respond instantaneously to any changes in the arrangement of the nuclei. In the original work by Born and Oppenheimer, the (time-independent) Hamiltonian was studied perturbatively, obtaining a perturbation series defined in terms of powers of the mass ratio $\kappa=(m/M)^{1/4}$, where m is the mass of the electron ($m=1$ in atomic units) and M is the average value of M_K. Following through the derivation, the Born-Oppenheimer approximation then involves neglecting off-diagonal terms in the resulting equations. It can be shown that the error in the BO approximation from neglecting these terms is proportional to $\kappa^4=m/M$ [114]. Examples of the BO approximation applied to describe small molecules include those in references [103–106]. The highly successful RMT (R-matrix with time-dependence) method for describing strong-field effects in atoms [107–110] has also recently been extended to describe the hydrogen molecular ion within the BO approximation [111, 112]. The Born-Oppenheimer approximation is now ubiquitous in the vast majority of static and dynamic molecular structure calculations, and is inherently assumed in the majority of the theoretical methods described in the remainder of this chapter.

In the Born-Oppenheimer picture the nuclei are described quantum mechanically, as wavepackets evolving along sets of potential energy surfaces. We can draw a connection between the evolution of these nuclear wavepackets and the (Newtonian) motion of classical nuclei using Ehrenfest's theorem [113], which relates the expectation values of the position and momentum operators with the expectation value of the force. Ehrenfest's theorem implies that in cases in which the ionic density matrix is localised (approximating a δ-function), the average values of the position and momentum of the ion will be approximately the same as those of a classical particle located at the centre of the approximate δ-function. Identifying the mean values of the position and momentum operators with the position and momentum of a classical particle in this way is known as the classical nuclei approximation. Since nuclear wavepackets are in general fairly localised (i.e., approaching δ-like) functions, provided that the curvature of the potential in which they move is sufficiently large [114], this classical nuclei approximation is a valid approximation in many situations, especially when considering heavy nuclei.

Even when the Born-Oppenheimer or classical nuclei approximations are employed, describing the dynamics of a many-electron system is still a formidable challenge. Therefore a wide range of theoretical techniques have been developed over the years in an attempt to accurately and efficiently describe the electronic dynamics. In the next section we will give a brief overview of some of these. As these are not the techniques implemented in the work presented in this thesis (Sections 2.3 – 2.5 of this chapter are dedicated to describing these techniques), this overview is not intended to provide a comprehensive description of each of the theoretical approaches mentioned. Instead, the aim is to provide the reader with a general idea of some of the alternative methods available.

2.2.3 Approximate solutions to the electronic wavefunction

One of the simplest approximations for describing a system of many interacting electrons is the Hartree-Fock approximation. This approximation is a more complete version of the self-consistent field approach developed by Hartree and Slater in 1928 [115, 116], in which the assumption is that the many-electron wavefunction, $\Phi(\boldsymbol{r}, t)$,

can be written simply as a product of one-electron orbitals, $\phi_i(\boldsymbol{r}_i, t)$, [114], i.e.

$$\Phi(\boldsymbol{r}, t) = \prod_{i=1}^{N_e} \phi_i(\boldsymbol{r}_i, t), \tag{2.9}$$

where N_e is the number of electrons as before. Applying a variational principle then leads to a set of coupled one-electron equations, the solution of which yields the Hartree wavefunctions and energies. A major failing of the Hartree approximation is that it treats electrons as distinguishable rather than indistinguishable particles. The consequence of this is that a wavefunction of the form given in Eq. (2.9) does not satisfy Pauli's exclusion principle, since such a wavefunction is not antisymmetric upon particle exchange, as Pauli's principle requires.

Introducing the required antisymmetry can be achieved by replacing the wavefunction proposed by Eq. (2.9) with one in the form of a Slater determinant

$$\boldsymbol{\Phi}_{\text{HF}}(\boldsymbol{x}_1, \boldsymbol{x}_2, \ldots, \boldsymbol{x}_{N_e}, t) = \frac{1}{\sqrt{N_e!}} \begin{vmatrix} \phi_1(\boldsymbol{x}_1, t) & \phi_2(\boldsymbol{x}_1, t) & \ldots & \phi_{N_e}(\boldsymbol{x}_1, t) \\ \phi_1(\boldsymbol{x}_2, t) & \phi_2(\boldsymbol{x}_2, t) & \ldots & \phi_{N_e}(\boldsymbol{x}_2, t) \\ \vdots & \vdots & \ddots & \vdots \\ \phi_1(\boldsymbol{x}_{N_e}, t) & \phi_2(\boldsymbol{x}_{N_e}, t) & \ldots & \phi_{N_e}(\boldsymbol{x}_{N_e}, t) \end{vmatrix}, \tag{2.10}$$

where the spatial and spin coordinates have been written as a single variable $\boldsymbol{x}_i = (\boldsymbol{r}_i, \sigma_i)$ and the ϕ_i ($i = 1, \ldots, N_e$) are therefore one-electron spin orbitals, composed of both spatial and spin components. This theoretical framework is known as the (time-dependent) Hartree-Fock approximation, and provides an attractive and intuitive picture of electrons as one-electron wavefunctions in the mean field of all other electrons. The dynamics of the system are then described by the time-dependent Hartree-Fock (TDHF) equations

$$\begin{aligned} i\frac{\partial}{\partial t}\phi_i(\boldsymbol{x}_i, t) =& F(t)\phi_i(\boldsymbol{x}_i, t), \\ =& \left[-\frac{1}{2}\nabla_i^2 - \sum_{J=1}^{N_n} \frac{Z_J}{|\boldsymbol{x}_i - \boldsymbol{R}_J|} + 2J - K + U(\boldsymbol{x}_i, t) \right] \phi_i(\boldsymbol{x}_i, t), \end{aligned} \tag{2.11}$$

for $i = 1, \ldots, N_e$, where $F(t)$ is the time-dependent Fock operator, and J and K are the

Coulomb and exchange operators respectively, defined as [117]

$$J\phi_i(\boldsymbol{x}_i,t) = \sum_j \left[\int \frac{|\phi_j(\boldsymbol{x}_j,t)|^2}{|\boldsymbol{x}_j-\boldsymbol{x}_i|}\mathrm{d}\boldsymbol{x}_j\right]\phi_i(\boldsymbol{x}_i,t), \tag{2.12}$$

and

$$K\phi_i(\boldsymbol{x}_i,t) = \sum_j \left[\int \frac{\phi_j^*(\boldsymbol{x}_j,t)\phi_i(\boldsymbol{x}_j,t)}{|\boldsymbol{x}_j-\boldsymbol{x}_i|}\mathrm{d}\boldsymbol{x}_j\right]\phi_j(\boldsymbol{x}_i,t). \tag{2.13}$$

The Hartree-Fock approximation can provide a reasonable description of many systems, but does have a serious failing, namely that it does not include electronic correlation. This is due to the fact that the true electronic wavefunction may not be well represented by a single Slater determinant. Use of a single configuration can also lead to an unrealistic inhibition of autoionization from doubly excited states. In addition, and importantly, the dependence of both the Coulomb and exchange operators on different orbitals (ϕ_i, ϕ_j) means that, unlike the TDSE, the TDHF equations are nonlinear, which in turn means that the principle of superposition is no longer valid, and the TDHF wavefunction is in essence an averaged representation of the exact wavefunction [118]. Despite these failings, the time-independent Hartree-Fock approximation has enjoyed a great deal of popularity within the quantum chemistry community, through its implementation in various software packages. Time-dependent Hartree-Fock has been applied to the study of ionization mechanics in atoms [118–120] and molecules [121, 122], although it is increasingly being supplanted by more sophisticated methods, including those discussed below.

A large number of methods exist that aim to improve upon the approximation given by Hartree-Fock; these are often referred to as post-Hartree-Fock (post-HF) methods. These methods seek to address the issue of electronic correlation being missing from the standard HF picture in one of a number of ways. Broadly speaking, this issue is addressed by either a perturbative approach (e.g., coupled cluster [114, 123], Møller-Plesset perturbation theory [114, 124]) or by combining several Slater determinants. We will not discuss the first of these approaches any further (the interested reader is referred to the references provided) but will briefly consider the second approach in more detail, and provide some examples of its use in calculations of laser-molecule interactions.

Perhaps the most intuitive approach for moving beyond HF is to describe the wavefunction not just as a single Slater determinant, as in Eq. (2.10), but instead as a linear combination of Slater determinants

$$\Psi(t) = \sum_k c_k(t)\Phi_k, \tag{2.14}$$

where the expansion coefficients c_k are such that $\sum_k c_k^2 = 1$. This method is known as the configuration interaction (CI) method [125, 126]. Here, Φ_0 is usually chosen to be the HF ground state Slater determinant, Φ_{HF}, since this is the best single determinant that can be obtained [114]. Additional Slater determinants then correspond to different excitations of the system, and are normally grouped into singly excited determinants (for a single electron excited from an occupied to an unoccupied orbital), doubly excited determinants (two electrons excited from occupied to unoccupied orbitals), and so on.

For performing practical time-dependent calculations, the number of additional Φ_k terms used in the above expansion, Eq. (2.14), and how these determinants are constructed, is the crux of the problem and the matter of much debate. Ideally all available determinants would be used in a CI calculation; this type of calculation is known as "full-CI", and is exact within the chosen basis set. In practice however this is only possible for the smallest systems, since the number of possible determinants depends on the factorials of both the number of electrons and the number of orbitals [114], and can reach as many as a million in systems with just tens of electrons and orbitals. Instead of full-CI, a cutoff on the number of determinants used is usually chosen so that all the singly, and possibly doubly, excited determinants are included in the calculation, while higher-order excitations are neglected (or included perturbatively). These type of calculations are referred to as configuration interaction singles (CIS/TD-CIS) or configuration interaction singles and doubles (CISD/TD-CISD) calculations (where "TD" $\equiv$ "time-dependent"). In the time-dependent examples referenced below, the number of determinants included is typically on the order of hundreds or thousands.

Since the number of available states grows rapidly with the size of a system, CI calculations including higher than double excitations are limited to the very smallest of systems. A number of groups have however performed simulations at the level of single or

double excitations (TD-CIS, TD-CISD) to calculate, for example, dipole response [127–129], high harmonic spectra [130–132], and photoelectron spectra [132]. However, use of time-dependent configuration interaction methods is not without its challenges. Ensuring that enough determinants are included to accurately describe the system can be challenging, and is exasperated by the need to include continuum or pseudocontinuum states in order to model ionization. The poor scaling of CI with system size drove the search to develop alternative methods which require the inclusion of smaller numbers of determinants; we will highlight a number of such methods below.

In the CI method, the additional Slater determinants, Φ_k, used in the expansion are constructed from the occupied and unoccupied one-electron orbitals of the HF Hamiltonian [114], and are fixed while the coefficients are variationally optimized to minimize the total energy of the system. An alternative approach is to allow both the determinants and the expansion coefficients to be optimized; such an approach is known as a multi-configuration method. Typically such an approach requires a much smaller number of determinants to be included than in a CI calculation. One of the most popular multi-configuration approaches is the multi-configuration time-dependent Hartree-Fock (MCTDHF) method [133–135]. In this method the wavefunction is given by

$$\Psi(t) = \sum_k c_k(t)\Phi_k(t). \tag{2.15}$$

A review of the MCTDHF method, and how it relates to other theoretical methods, can be found in [136]. MCTDHF has been successfully applied to describe a number of systems and processes, such as photoionization in atoms, diatomic molecules and model linear molecules [137–140], as well as photoexcitation, in lithium hydride and methane molecules [141] and in sodium clusters [142]. A limited number of HHG studies using MCTDHF have also been carried out [143–145], and extensions of the method beyond the Born-Oppenheimer approximation have been investigated [146, 147].

The closely related multi-configuration time-dependent Hartree (MCTDH) method [148, 149], in which the wavefunction is expressed by a superposition of time-dependent Hartree products (Eq. (2.9)) rather than Slater determinants [136], has also proven to be a highly successful approach for describing a range of physical processes. Exam-

ple applications include photodissociation of a range of small molecules such as NO_2 [150], vibrational predissociation dynamics of molecules and clusters [151], and intramolecular vibrational energy redistribution in small molecules [152]. A review of the MCTDH approach can be found in [153].

Another wavefunction-based approach that is typically more compact than configuration interaction is the algebraic diagrammatic construction (ADC) method [154, 155]. This approach involves the construction of so-called correlated excited states (CES) by applying a set of excitation operators (representing different physical excitations) to the exact correlated ground state of the system. The ADC method has the advantage that ground state correlation (described via Møller-Plesset perturbation theory) is built into every basis vector. Following on from a number of calculations of photoionization and X-ray cross sections [156, 157], this method has recently been applied to study HHG in aligned CO_2 molecules, focusing on the effect of multi-channel contributions to the harmonic response [158].

A number of other time-dependent post-HF methods exist, but these are beyond the scope of this thesis. The interested reader will find a review of some of these methods in [159]. As mentioned previously however, the scaling of these methods with system size presents a significant challenge to applying them more generally to time-dependent studies of laser-molecule interactions.

2.2.4 Summary

In this section we have shown how the dynamics of a general system are described by the time-dependent Schrödinger equation, but how solution of this is impossible in practice for all but the smallest of systems. Some of the approximations required to study the dynamics of larger systems have been introduced, as well a number of the most popular approaches to describing the electronic dynamics of molecular systems.

The approaches discussed in this section are all wavefunction methods; in other words, the wavefunction is the key quantity that needs to be calculated, with all observables expressed in terms of the wavefunction. In the next section we will see how an alternative approach exists in the form of density functional theory and its time-dependent analogue, in which the electronic density replaces the electronic wavefunction as the

basic variable.

2.3 Time-dependent density functional theory (TDDFT)

In the previous section we saw a number of methods for describing the dynamics of a multielectron system in the presence of a strong laser field. An alternative approach to these methods is time-dependent density functional theory (TDDFT). This is the time-dependent extension of an older theory, density functional theory (DFT), which we will refer to on occasion as "static" or "ground state" DFT. In (TD)DFT, the (time-dependent) many-body wavefunction is replaced as the central quantity of interest by the (time-dependent) single-particle electronic density. This change in focus allows a huge increase in the maximum system size that can be reasonably studied in a calculation.

In this section we will introduce the basic theorems and principles underlying TDDFT, state some of the central equations, and then present some successful applications of the theory, as well as some of its shortcomings and outstanding limitations. First however, we will briefly introduce the more mature ground state density functional theory, since the two theories share many of the same underlying principles.

2.3.1 Density functional theory (DFT)

Since its development more than 50 years ago, density functional theory (DFT) has grown in popularity amongst physicists, chemists and material scientists, and is now one of the most widely used methods for electronic structure calculations. One of the leading figures in the development of the theory, Walter Kohn, was jointly awarded the 1998 Nobel Prize in Chemistry for his work [160]. As a well-established theory, there are a number of excellent reviews of the history of DFT, its formalism, and its nuances, such as [114, 161, 162]. In the following we do not seek to provide an in-depth description of DFT; for this the reader is referred to one of these reviews, and the references therein.

At the heart of density functional theory are the two Hohenberg-Kohn theorems [163]. The first theorem states that there is a one-to-one correspondence between the potential and the single-particle electronic density of a given system. This density, $n(\boldsymbol{r})$, is

related to the many-body electronic wavefunction Ψ through

$$n(\boldsymbol{r}) = N_e \int \Psi^*(\boldsymbol{r}, \boldsymbol{r}_2, \ldots, \boldsymbol{r}_{N_e}) \Psi(\boldsymbol{r}, \boldsymbol{r}_2, \ldots, \boldsymbol{r}_{N_e}) \mathrm{d}\boldsymbol{r}_2 \ldots \mathrm{d}\boldsymbol{r}_{N_e}. \tag{2.16}$$

As a consequence of this one-to-one correspondence, all properties of the system (including the energy) are completely determined by the electronic density alone. This vital result allows a many-body problem with N_e electrons to be reduced from one with $3N_e$ coordinates to one with only 3. The second Hohenberg-Kohn theorem (sometimes called the Hohenberg-Kohn Variational Principle) defines an energy functional, which is minimized when the density is the ground state density of the system.

While the Hohenberg-Kohn theorem proves that a system can be described solely by its density, it provides no procedure for actually determining the ground state density. In their seminal paper in 1965 [164], Walter Kohn and Lu Jeu Sham developed a framework that overcame this deficiency and established DFT as a practical tool for tackling electronic structure problems.

In the Kohn-Sham picture, we consider a fictitious system of non-interacting electrons whose electronic density is identical to that of the system of interacting electrons. The advantage of working with this non-interacting auxiliary system is that the problem is reduced from dealing with an N_e-electron Schrödinger equation to a set of N_e one-electron Schrödinger-like equations, which we refer to as the Kohn-Sham equations. We will deal with the exact form of these Kohn-Sham equations in the next section, in the context of TDDFT.

Due to the enormous computational advantage associated with working with a non-interacting rather than an interacting system, density functional theory has been, and continues to be, an enormously successful theory, finding applications in a wide range of disciplines, from solid state physics [165] to biological science [166]. Like all methods it has its challenges and failings, many of which also affect TDDFT and will be discussed shortly. However, a search for publications involving DFT or a look through one of the many reviews of the current state of the field [167–169] will make it apparent how, despite its problems, DFT has become one of the most important computational tools available for modelling electronic structure.

2.3.2 Time-dependent DFT: the Runge-Gross theorem

Almost two decades after the publication of the Hohenberg-Kohn theorem, Erich Runge and Eberhard Gross developed an analogous theorem for time-dependent systems: the Runge-Gross theorem [170]. Only the result, not the proof, of this theorem will be presented here; for the proof see the original Runge-Gross paper [170] or the review in [171]. Similarly to the Hohenberg-Kohn theorem, the Runge-Gross theorem proved the existence of a one-to-one mapping between the (time-dependent) potential and the (time-dependent) density of the system. Just as in the static case, the Kohn-Sham approach can be applied to this time-dependent case, allowing the time-dependent density (and therefore, in principle, all properties of the system) to be calculated by considering a system of non-interacting electrons.

Since the electrons are non-interacting, the total N_e-electron wavefunction can be written as a single determinant of one-particle orbitals, and the problem is reduced to solving a set of N_e one-electron Schödinger-like equations: the time-dependent Kohn-Sham (TDKS) equations. Neglecting spin for brevity, the TDKS equations can be written as

$$\begin{aligned} i\frac{\partial}{\partial t}\psi_j(\boldsymbol{r},t) =& H_{\text{KS}}\psi_j(\boldsymbol{r},t) \\ =& \left[-\frac{1}{2}\nabla^2 + V_{\text{KS}}[n](\boldsymbol{r},t)\right]\psi_j(\boldsymbol{r},t), \qquad j=1,\ldots,N_e. \end{aligned} \tag{2.17}$$

Here $\psi_j(\boldsymbol{r},t)$ are the Kohn-Sham orbitals, from which the electronic density is given by

$$n(\boldsymbol{r},t) = \sum_{j=1}^{N_e} |\psi_j(\boldsymbol{r},t)|^2, \tag{2.18}$$

and is defined to be equal to the density of the real (interacting) system. In Eq. (2.17), H_{KS} and V_{KS} are the effective or Kohn-Sham Hamiltonian and potential respectively; i.e., the Hamiltonian and potential which yield, through Eqs. (2.17)–(2.18), a density equivalent to that of the interacting system. The square brackets $[n]$ indicate that $V_{\text{KS}}[n](\boldsymbol{r},t)$ is a functional of the electronic density. The potential $V_{\text{KS}}[n]$ is usually split into several parts, namely

$$V_{\text{KS}}[n](\boldsymbol{r},t) = V_{\text{H}}[n](\boldsymbol{r},t) + V_{\text{ext}}(\boldsymbol{r},\boldsymbol{R},t) + V_{\text{xc}}[n](\boldsymbol{r},t). \tag{2.19}$$

The three terms on the right hand side of this equation will now be considered individually.

The first term, V_{H}, is the Hartree potential for a time-dependent density

$$V_{\mathrm{H}}(\boldsymbol{r}, t) = \int \frac{n(\boldsymbol{r'}, t)}{|\boldsymbol{r} - \boldsymbol{r'}|} d\boldsymbol{r'}, \tag{2.20}$$

and accounts for the electrostatic potential without exchange or correlation effects.

The external potential, $V_{\text{ext}}(\boldsymbol{r}, \boldsymbol{R}, t)$, accounts for all the electron-ion interactions as well as the interactions between electrons and the laser field, i.e.

$$V_{\text{ext}}(\boldsymbol{r}, \boldsymbol{R}, t) = V_{\text{ions}} + U_{\text{elec}}. \tag{2.21}$$

These two terms, V_{ions} and U_{elec}, will be discussed in later sections.

The final potential term in Eq. (2.19) is the exchange-correlation potential, which accounts for all many-body effects not captured by V_{H} and V_{ext}. Since the one-to-one correspondence means that there is a unique Kohn-Sham potential V_{KS} which yields the density of the interacting system, Eq. (2.19) in fact defines the exchange-correlation potential V_{xc}. The exchange-correlation potential can formally be expressed as the functional derivative of the exchange-correlation action functional $A_{\text{xc}}[n]$ [172], i.e.

$$V_{\text{xc}}[n] = \frac{\delta A_{\text{xc}}[n]}{\delta n}. \tag{2.22}$$

In practice however, the exact form of $A_{\text{xc}}[n]$ (and therefore $V_{\text{xc}}[n]$) is generally unknown. Despite efforts to calculate exact time-dependent exchange-correlation potentials for specific systems (see, for example, [173]), this means that in general $V_{\text{xc}}[n]$ must be approximated. Some of the most common approximations will be discussed in the next section.

With the Kohn-Sham potential defined by Eqs. (2.19) – (2.22), describing the electronic dynamics of some system then requires solving the TDKS equations for the Kohn-Sham orbitals ψ_j, from which the electronic density can be obtained, and then extracting the desired observables, which themselves are functionals of the density. Since the Kohn-Sham potential, through the Hartree and exchange-correlation potentials, is a

functional of the density, the TDKS equations must be solved self-consistently.

Before we move to the next section, it should be noted that although TDDFT bears a similarity to TDHF in that they both involve representing the wavefunction as a single Slater determinant of one-particle orbitals, TDDFT (unlike TDHF) is in principle an exact theory. The approximate nature of practical implementations of TDDFT arises from the complexity of the exchange-correlation potential, and the failings of current exchange-correlation approximations to capture all the many-body effects contained in V_{xc}; the formalism of TDDFT itself is exact. Clearly then the accuracy of the exchange-correlation approximation is a key factor in determining the accuracy of a TDDFT calculation. A number of such approximations will be seen in the next section.

2.3.3 Exchange-correlation potential approximations

The work of Runge and Gross showed that TDDFT is in principle an exact theory. However, the exchange-correlation potential, $V_{\text{xc}}(\boldsymbol{r}, t)$, in the time-dependent Kohn-Sham equations is an unknown and highly complex object, which must be approximated in some way. By definition, and provided that the initial wavefunctions (both the interacting and noninteracting Kohn-Sham wavefunctions) are nondegenerate ground states, the exchange-correlation potential $V_{\text{xc}}(\boldsymbol{r}, t)$ is a functional of the entire history of the density $n(\boldsymbol{r}, t)$. In other words, $V_{\text{xc}}(\boldsymbol{r}, t)$ has a functional dependence not just on $n(\boldsymbol{r}, t)$, but on all $n(\boldsymbol{r}', t')$ for $0 \leq t' \leq t$ and for all arbitrary points $\boldsymbol{r}'$ in space, i.e., it is non-local in both space and time [171]. This dependence of $V_{\text{xc}}(\boldsymbol{r}, t)$ on the entire history of the density is referred to as the memory of the exchange-correlation potential.

In practice, non-locality in time is almost always neglected through the use of the adiabatic approximation, in which the dependence of the exchange-correlation potential on the density is restricted to the instantaneous density, i.e.,

$$V_{\text{xc}}^{\text{adia}}[n](\boldsymbol{r}, t) = V_{\text{xc}}^{\text{approx}}[n(t)](\boldsymbol{r}). \tag{2.23}$$

Such an approximation is valid for systems in which the potential varies slowly with time, which will not always be the case. However, including memory effects in the approximation of the exchange-correlation potential is far beyond the scope of this work; we refer the reader to [174] and the references therein for a review of the problems

posed by memory dependence and some of the attempts to develop functionals that address them.

In static DFT, the most basic exchange-correlation approximation is the local density approximation (LDA). In this approximation the exchange-correlation energy density at every point is approximated by the exchange-correlation energy density of a homogeneous electron gas, $\epsilon_{\text{xc}}^{\text{HEG}}$. The exchange-correlation action functional is then given by

$$A_{\text{xc}}[n] = E_{\text{xc}}^{\text{LDA}}[n] = \int n(\boldsymbol{r})\epsilon_{\text{xc}}^{\text{HEG}}(n(\boldsymbol{r}))\mathrm{d}\boldsymbol{r}. \tag{2.24}$$

The exchange and correlation parts of $\epsilon_{\text{xc}}^{\text{HEG}}(n(\boldsymbol{r}))$ are treated separately. For a homogeneous electron gas, the exchange energy has a known analytic form, and so the approximation to the exchange term in LDA is simply [175]

$$\epsilon_{\text{x}}^{\text{HEG}}(n(\boldsymbol{r})) = -\frac{3}{4}\left(\frac{3}{\pi}\right)^{1/3} n^{1/3}(\boldsymbol{r}). \tag{2.25}$$

Analytical forms of the correlation term are only available in high- and low-density limits. However a number of accurate parameterizations have been calculated, for example by Perdew and Wang [176] (this is the parameterization used in the work described in this thesis, but others are available - see Chapter 5 of [114] for references to some of these).

The local density approximation is attractive as it depends solely on the density at each point in space, unlike other approximations which depend on derivatives of the density, e.g., the generalized gradient approximation (GGA) [177], or on individual orbitals, e.g., the optimized effective potential (OEP) [178, 179]. This makes application of LDA a relatively straightforward task when compared to other, more complex, exchange-correlation approximations (for details of some of these approximations see, for example, Chapter 5 of [114] (for static DFT) and Part II of [180] (for TDDFT)). Such computational efficiency combined with (surprisingly) good accuracy for most systems [160] established LDA as a popular choice of exchange-correlation approximation, at least as a first approximation.

Due to its simplicity however, the local density approximation contains a number of errors. One of the most serious of these is that LDA contains self-interaction errors,

due to its handling of the exchange term. Self-interaction results in incorrect asymptotic behaviour of the exchange-correlation potential (an exponential decay instead of the correct Coulombic decay), and can lead to a number of non-physical effects, such as incorrect dissociation limits, underestimation of ionization potentials, instability of negatively charged ions, and absence of Rydberg series [114, 181, 182].

There are a range of schemes available for correcting the self-interaction error inherent in LDA. One of the most frequently used schemes is that introduced by Perdew and Zunger [183], in which the self-interaction-correction (SIC) is applied at the level of the energy functional and which yields a separate SIC potential for each Kohn-Sham state. This method of self-interaction-correction has problems however, in that the explicit orbital-dependence of the SIC functional poses practical problems and means that the orbitals are not guaranteed to be orthogonal, while the Kohn-Sham equations are no longer invariant under a unitary transformation of the orbitals [181, 184]. Some alternative approaches to SIC remove the explicit orbital dependence found in the Perdew-Zunger approach by constructing an optimized effective potential (OEP), which is state-independent. A popular example of an OEP-based method is that proposed by Krieger, Li and Iafrate (KLI) [185]. However, these methods still require dealing with a Coulomb term in the potential for each state individually; a computational burden that will grow with the size of the system.

A much simpler and computationally cheaper approach to correcting the self-interaction problem is the average-density self-interaction-correction (ADSIC) [182, 186]. In this orbital-independent scheme, a globally averaged subtraction method is used, in which the self-interaction is removed by simply subtracting the interaction due to the average density. Further details on ADSIC and its applicability, along with a comparison between different SIC schemes can be found in [182]. Briefly, the authors note that ADSIC will be most applicable in metal clusters (in which the spatial and energetic ranges of electrons are fairly small) and less applicable in all-electron calculations in atoms (in which there may be large spatial and energetic variations) or in molecular systems involving large degrees of fragmentation. However they also note the impressive performance of ADSIC, both in terms of accuracy and computationally efficiency, when used in the correct situation. For the systems studied in this work, we expect ADSIC to be reasonably accurate, especially since there will not be significant frag-

mentation on the timescales considered in our simulations. ADSIC also benefits from a number of formal advantages that other SIC schemes lack; these are discussed in [182]. One such benefit is that the exchange-correlation potential can be obtained as the functional derivative of the exchange-correlation functional; this allows the forces acting on the ions to be calculated using the Hellmann-Feynman theorem.

The two approximations discussed above (adiabatic and local density) come together in TDDFT as the adiabatic local density approximation (ALDA), in which the exchange-correlation potential is approximated as the ground state potential of a uniform gas, with an instantaneous, local density. Aside from the problems mentioned above, ALDA suffers from a number of other drawbacks. It has been shown that despite capturing autoionizing resonances that arise from single excitations, ALDA fails to capture those resonances arising from double excitations [187]. ALDA also has problems describing double ionization, for example failing in reproducing the famous "knee structure" indicative of non-sequential multiple ionization processes [173, 188].

While there are a number of alternative, more sophisticated, approximations available, they are all invariably much more computationally demanding than ALDA. The extra computational expense associated with these other approximations becomes particularly cumbersome when dealing with systems with many electrons. Therefore all work presented in this thesis uses ALDA, with the Perdew-Wang parameterization referenced above, supplemented by the average-density self-interaction-correction; we refer to this combined approximation as LDA-PW92-ADSIC.

2.3.4 Additional challenges and difficulties within TDDFT

As the previous section has shown, the lack of knowledge concerning the exact form of the exchange-correlation potential is a significant challenge facing TDDFT. While this is probably the biggest drawback to a TDDFT description of laser-molecule interactions, there are also a number of other difficulties.

As will become apparent in the next chapter, while some observables, e.g., the dipole moment, can be expressed in terms of the time-dependent electronic density, not all observables are as readily accessible. For some observables (e.g., ionization yields), a geometric approximation that depends on the density can easily be used in place of

the exact (unknown) functional of the density [189]. Calculating other observables however (e.g., ATI spectra) requires alternative techniques, which may require use of the Kohn-Sham orbitals directly rather than the density [190]. Some authors have raised concerns with this orbital-based approach, since the Kohn-Sham orbitals do not themselves have a strict physical meaning [191]; however this is the only currently feasible approach.

In addition, in comparison to some wavefunction-based approaches, understanding the role of individual states and channels can be challenging in TDDFT, due to the switch from the wavefunction to the density as the central quantity. Calculating individual ionization probabilities to differently-charged ionic states also requires special treatment, and a number of further approximations [192, 193].

Despite these challenges however, the efficiency and scalability of TDDFT compared to other methods makes it an important technique for studying laser-molecule interactions. While the use of TDDFT in the non-linear regime is still somewhat in its infancy (compared to TDDFT calculations in the linear response regime, or static DFT calculations), there have already been many successful applications. A small number of these will be highlighted in the next section.

2.3.5 Examples of use of TDDFT from literature

Having introduced some of the main failures and difficulties associated with TDDFT in the previous two subsections, we now wish to paint a more optimistic picture by highlighting some of the many successful applications of TDDFT over the past decades. TDDFT has been applied in a number of diverse fields, including the study of transport effects in molecular wires [194, 195] and of collision processes [196–198]. A large number of studies of the response of systems to applied fields have been performed in the linear regime, to calculate for example absorption spectra [199]; reviews of linear response applications can be found in [172, 200], and Part IV of [180]. Here we focus solely on applications in the non-linear regime, as this is where the work described in this thesis is based. In addition to the references given below, a review of relevant studies published before 2006 can be found in [191].

In order to investigate how the results from TDDFT compare with those from direct

solution of the TDSE, a number of calculations were performed in the early 2000s in which small systems such as H_2^+ were studied using both techniques. For example, in [201, 202] a basis-set-based TDDFT approach was combined with classical molecular dynamics (similar to the quantum-classical molecular dynamics approach described in Section 2.4) and used to study the dynamics of H_2^+ exposed to different laser pulses. The results of these calculations were compared with a set of TDSE calculations [203], and in general showed fair agreement. In particular, comparisons between snapshots of the probability distributions during the laser pulse obtained with the two techniques were in qualitative agreement, with some noticeable quantitative differences. The dissociation and ionization probabilities on the other hand showed fair qualitative and quantitative agreement between the TDDFT and TDSE calculations.

Dissociation of heavier molecules has also been studied, for example in [204, 205]. In these calculations, a mixed quantum-classical approach incorporating TDDFT was used to study the dynamics of a dimer (Na_2^+) and two trimers (He_3^+ and LiCN/LiNC). These systems were propagated for several hundred femtoseconds following irradiation by short, linearly-polarized laser pulses with intensities on the order of 10^{10} - 10^{12} W/cm^2, and frequencies chosen relative to the resonant frequencies of the system. In the case of Na_2^+, by varying the laser frequency the authors were able to show that, for a number of intensities, the expected behaviour took place: dissociation of the molecule was induced when the system was excited to an anti-bonding potential energy surface, and suppressed when the laser frequency excited electronic population to a bonding surface. For the trimer He_3^+, a dissociative picture was obtained that corresponded to that seen in a previous experimental study [206]. The LiCN calculations were less successful, with the dissociation dynamics of the molecule affected by artefacts of the exchange-correlation approximation that was used, which had the incorrect asymptotic behaviour.

The above study, [205], also included calculations of the high harmonic response of the dimers HD and H_2. The production of even harmonics is forbidden for symmetric diatomics like H_2, but may occur for a heteronuclear diatomic like HD. This effect had previously been investigated through one-dimensional solution of the TDSE [36]. By applying TDDFT with classical nuclear motion to the same problem, the authors were able to qualitatively reproduce the results obtained with quantum nuclear motion; i.e.,

they observed even harmonics in HD, but with much smaller harmonic intensities than observed with the quantum description.

A number of TDDFT studies have also made comparisons with experimental results; this is not a trivial comparison to make in general. For example, in [207] ionization from helium and argon atoms due to a two-colour laser field (attosecond XUV pulses in the presence of an IR pulse) was studied by performing TDDFT calculations, and comparing the results with those from experiment and those from TDSE calculations (within the single active electron approximation). By varying the delay time between the XUV pulses and the IR background pulse, the TDDFT calculations were able to reproduce the regular modulation in ionization signal observed in both experimental and TDSE results. Photoelectron spectra from the Ar atom obtained with the three different methods were also in qualitative agreement. Other systems included in this investigation included a carbon chain (C_3) and sodium clusters (Na_9^+, Na_{21}^+, Na_{41}^+), again considering the ionization yield as a function of XUV-IR delay time.

The study of high harmonic generation (HHG) in small molecules has been a popular use of TDDFT in recent years. For example, high harmonic spectra from a range of diatomic molecules have been calculated, including homonuclear diatomics like N_2 and F_2 [189, 208–211] and heteronuclear diatomics likes CO, BF and HF [212]. Comparisons with experimental data have shown that TDDFT calculations are capable of reproducing features in the harmonic spectra such as Cooper minima and shape resonances [211], as well as changes in high harmonic intensity as the angle between the laser polarization direction and the molecular axis is varied [209]. Other linear molecules such as OCS and CS_2 have also been studied [213]. These calculations collectively have shown the importance of multielectron and orientation effects in strong field ionization and high harmonic generation. As we will see in Chapter 4, both of these effects are also important for high harmonic generation in another linear molecule: acetylene.

In recent years, the applications of TDDFT in the non-linear regime have moved into and beyond the limits of what is possible with other theoretical methods. Recent examples include calculation of energy-, angle- and time-resolved photoelectron spectra of ethylene in a pump-probe setup (a UV pump followed by an XUV probe) [214] and the study of high harmonic generation in benzene during interactions with both linearly

and circularly polarized laser pulses [46]. One of the largest TDDFT calculations of a strong-field laser-molecule interaction was presented in [190]. In this work, energy- and angle-resolved photoelectron spectra were calculated for the C_{60} fullerene (the so-called "buckyball") exposed to a strong laser pulse. The results of these calculations were in good agreement with predictions made using the strong field approximation and quantitative rescattering theory.

The studies described above represent just a small fraction of the current wealth of TDDFT-based literature. Much as the use of static DFT rapidly grew (and continues to grow) in the years following the initial work of Hohenberg, Kohn and Sham, usage of TDDFT has been increasing year on year, and this trend looks set to continue into the future. As the topics of the studies discussed above indicate, the range of systems that TDDFT is being applied to continues to expand, with molecules and clusters that were previously inaccessible to theoreticians now being investigated as confidence of working with TDDFT grows.

2.3.6 Summary

In this section we have introduced time-dependent density functional theory, a theory in which the electronic-wavefunction-based description of a many-body system is replaced by a description in terms of the electronic density. The theorems underpinning TDDFT were introduced, and the Schrödinger-like time-dependent Kohn-Sham equations were presented and discussed.

While TDDFT is in principle an exact theory, the exact form of the exchange-correlation potential is unknown and so must be approximated. The adiabatic local density approximation (ALDA) is the simplest exchange-correlation approximation in TDDFT. Although it has some known errors, the balance afforded by ALDA between efficiency and accuracy, especially when supplemented by a self-interaction-correction such as ADSIC, makes it a popular choice of exchange-correlation approximation for studying laser-molecule interactions in the non-linear regime.

Similarly, while TDDFT itself comes with some challenging aspects (the lack of knowledge concerning the exchange-correlation potential being perhaps the most important), the level of efficiency and scalability it possesses compared to other methods while re-

taining reasonable accuracy makes it a powerful tool for studying strong-field effects in multielectron systems.

In the form described above, TDDFT accounts only for the electronic dynamics; it says nothing about the behaviour of the nuclei. In the next section we shall see how the nuclear dynamics can be incorporated classically alongside the quantum treatment of the electrons provided by TDDFT, in a quantum-classical molecular dynamics method.

2.4 Quantum-classical molecular dynamics

In the previous section we saw how time-dependent density functional theory allows the dynamics of a many-electron system to be studied without requiring solution of the full time-dependent Schrödinger equation. The TDDFT formulation presented above, however, includes no description of the motion of the ions. In some cases, neglecting ionic motion can be a reasonable assumption (for example considering very heavy ions evolving along non-dissociative potential energy surfaces). In many other cases however, the motion of the ions is an integral element of the dynamics of the molecule, and therefore accurately capturing the ionic motion is crucial in accurately describing the laser-molecule interaction. Furthermore, study of certain physical processes, for example fragmentation processes, by definition requires the inclusion of ionic motion.

One option for incorporating nuclear effects into a TDDFT description of a system is to reformulate the traditional TDDFT formalism into the so-called time-dependent multi-component density functional theory [215–218]. In this method the basic variables are the electron density (defined in a suitable body-fixed coordinate frame [215]) and the diagonal of the nuclear density matrix. For these variables an analogue of the Runge-Gross theorem can be proved, and Kohn-Sham equations for the electrons and nuclei derived. While this approach is attractive since it treats both the electrons and the nuclei fully quantum mechanically, it has the added complication of the need for the development of accurate approximations to the electron-nuclear correlation functional.

An alternative method for accurately and efficiently modelling both electronic and ionic dynamics is to couple a quantum treatment of the electrons (such as that given by TDDFT) with a classical treatment of the ions. The resulting quantum-classical molecular dynamics method is an example of the more general non-adiabatic quantum molec-

ular dynamics (NAQMD) approach. In this section we will outline an implementation of this method based on the Ehrenfest theorem [113], and derive the equations of motion for a system of quantum mechanical electrons and classical ions, firstly for a general quantum mechanical treatment of the electrons, and then considering specifically a TDDFT treatment.

Here we follow, in general, the derivation given in [219] and [220].

2.4.1 General formulation of the approach

We consider a system of N_e quantum mechanical electrons and N_n classical ions. The electrons are described (ignoring spin for brevity) by their many-body wavefunction $\Psi(\boldsymbol{r}, t)$, where $\boldsymbol{r}$ refers to their position vectors, $\boldsymbol{r} = \{\boldsymbol{r}_1, \ldots, \boldsymbol{r}_{N_e}\}$. The ions are described by their trajectories $\boldsymbol{R} = \{\boldsymbol{R}_1(t), \ldots, \boldsymbol{R}_{N_n}(t)\}$. The mass and charge of ion K are denoted by M_K and Z_K respectively.

We will derive the equations of motion for the electrons and ions by using a Lagrangian formalism. To find the equations of motion, we consider variations of the wavefunction and ion trajectories that leave the action, $\mathcal{A}$, stationary, i.e.

$$\delta\mathcal{A} = \delta \int_{t_0}^{t_1} \mathcal{L}\mathrm{d}t = 0. \tag{2.26}$$

Here $\mathcal{L}$ is the Lagrangian of the system, which is given by [221]

$$\begin{aligned}\mathcal{L} = \mathrm{i}\int \Psi^*(\boldsymbol{r}, t)\dot{\Psi}(\boldsymbol{r}, t)\mathrm{d}\boldsymbol{r} - \int \Psi^*(\boldsymbol{r}, t)H(\boldsymbol{r}, \boldsymbol{R}, t)\Psi(\boldsymbol{r}, t)\mathrm{d}\boldsymbol{r} \\ + \frac{1}{2}\sum_{K=1}^{N_n} M_K\dot{\boldsymbol{R}}_K^2(t) - V_{nn}(\boldsymbol{R}) - Z_K\boldsymbol{R}_K \cdot \boldsymbol{E}(t),\end{aligned} \tag{2.27}$$

where $\dot{\Psi}(\boldsymbol{r}, t) = \frac{\partial}{\partial t}\Psi(\boldsymbol{r}, t)$, and where the integration over $\boldsymbol{r}$ refers to integration over all electron coordinates, i.e.

$$\int \mathrm{d}\boldsymbol{r} = \int \mathrm{d}\boldsymbol{r}_1 \cdots \int \mathrm{d}\boldsymbol{r}_{N_e}. \tag{2.28}$$

For this mixed quantum-classical system, the action consists of a quantum part and a classical part [201]

$$\mathcal{A} = \mathcal{A}_q + \mathcal{A}_c, \tag{2.29}$$

where

$$\mathcal{A}_q = \int_{t_0}^{t_1} \left\langle \Psi(\boldsymbol{r},t) \left| \mathrm{i}\frac{\partial}{\partial t} - H(\boldsymbol{r},\boldsymbol{R},t) \right| \Psi(\boldsymbol{r},t) \right\rangle \mathrm{d}t, \tag{2.30}$$

and

$$\mathcal{A}_c = \int_{t_0}^{t_1} \left[\frac{1}{2}\sum_{K=1}^{N_n} M_K \dot{\boldsymbol{R}}_K^2(t) - V_{nn}(\boldsymbol{R}) - Z_K \boldsymbol{R}_K \cdot \boldsymbol{E}(t) \right] \mathrm{d}t, \tag{2.31}$$

where the bra-kets $\langle \ldots \rangle$ denote integration over all coordinates $\boldsymbol{r}_1, \ldots, \boldsymbol{r}_{N_e}$.

In Eqs. (2.27) and (2.30), $H(\boldsymbol{r},\boldsymbol{R},t)$ is the time-dependent Hamiltonian for the electrons, which depends parametrically on the ion coordinates, and is written as

$$H(\boldsymbol{r},\boldsymbol{R},t) = \sum_{i=1}^{N_e} \left[-\frac{1}{2}\nabla_i^2 + V_{\text{ext}}(\boldsymbol{r}_i,\boldsymbol{R},t) \right] + V_{ee}(\boldsymbol{r}). \tag{2.32}$$

Here ∇_i^2 is the Laplacian with respect to the electronic coordinates of electron i, and the electron-electron Coulomb repulsion term, $V_{ee}(\boldsymbol{r})$, is defined as

$$V_{ee}(\boldsymbol{r}) = \frac{1}{2}\sum_{i=1}^{N_e}\sum_{\substack{j=1 \\ j\neq i}}^{N_e} \frac{1}{|\boldsymbol{r}_i - \boldsymbol{r}_j|}. \tag{2.33}$$

The external potential term, $V_{\text{ext}}(\boldsymbol{r}_i,\boldsymbol{R},t)$, in the Hamiltonian consists of the interaction between electron i and the ions, $V_{\text{ions}}(\boldsymbol{r}_i,\boldsymbol{R},t)$, and the interaction between electron i and the applied laser field, $U_{\text{elec}}(\boldsymbol{r}_i,t)$, i.e.

$$V_{\text{ext}}(\boldsymbol{r}_i,\boldsymbol{R},t) = V_{\text{ions}}(\boldsymbol{r}_i,\boldsymbol{R},t) + U_{\text{elec}}(\boldsymbol{r}_i,t). \tag{2.34}$$

The electron-ion interaction term $V_{\text{ions}}(\boldsymbol{r}_i,\boldsymbol{R},t)$ is defined exactly as

$$\begin{aligned} V_{\text{ions}}(\boldsymbol{r}_i,\boldsymbol{R},t) &= \sum_{K=1}^{N_n} V_{\text{ion}}(\boldsymbol{r}_i,\boldsymbol{R}_K,t) \\ &= -\sum_{K=1}^{N_n} \frac{Z_K}{|\boldsymbol{r}_i - \boldsymbol{R}_K|}. \end{aligned} \tag{2.35}$$

Finally, the ion-ion Coulomb repulsion term, $V_{nn}(\boldsymbol{R})$, in Eq. (2.31) is defined as

$$V_{nn}(\boldsymbol{R}) = \frac{1}{2}\sum_{I=1}^{N_n}\sum_{\substack{J=1 \\ J\neq I}}^{N_n} \frac{Z_I Z_J}{|\boldsymbol{R}_I - \boldsymbol{R}_J|}, \tag{2.36}$$

while $Z_K \boldsymbol{R}_K \cdot \boldsymbol{E}(t)$ denotes the interaction between ion K and the applied laser field.

Returning to Eq. (2.26), we obtain the three Euler-Lagrange equations of motion

$$\frac{\partial \mathcal{L}}{\partial \Psi^*} = \frac{\mathrm{d}}{\mathrm{d}t}\left(\frac{\partial \mathcal{L}}{\partial \dot{\Psi}^*}\right), \tag{2.37}$$

$$\frac{\partial \mathcal{L}}{\partial \Psi} = \frac{\mathrm{d}}{\mathrm{d}t}\left(\frac{\partial \mathcal{L}}{\partial \dot{\Psi}}\right), \tag{2.38}$$

$$\frac{\partial \mathcal{L}}{\partial \boldsymbol{R}_K} = \frac{\mathrm{d}}{\mathrm{d}t}\left(\frac{\partial \mathcal{L}}{\partial \dot{\boldsymbol{R}}_K}\right). \tag{2.39}$$

Evaluating Eq. (2.37) for the Lagrangian defined in Eq. (2.27) results in the time-dependent Schrödinger equation

$$\mathrm{i}\frac{\partial}{\partial t}\Psi(\boldsymbol{r},t) = H(\boldsymbol{r},\boldsymbol{R},t)\Psi(\boldsymbol{r},t), \tag{2.40}$$

while evaluating Eq. (2.38) gives the complex conjugate of the TDSE. The remaining Euler-Lagrange equation, Eq. (2.39), leads to the equation of motion for the ions, namely

$$\begin{aligned} M_K \ddot{\boldsymbol{R}}_K = &- \int \Big(\Psi^*(\boldsymbol{r},t)\left(\boldsymbol{\nabla}_K H(\boldsymbol{r},\boldsymbol{R},t)\right)\Psi(\boldsymbol{r},t)\Big)\mathrm{d}\boldsymbol{r} \\ &- \boldsymbol{\nabla}_K\Big(V_{nn}(\boldsymbol{R}) + Z_K \boldsymbol{R}_K \cdot \boldsymbol{E}(t)\Big), \end{aligned} \tag{2.41}$$

where $\boldsymbol{\nabla}_K$ is the gradient operator with respect to the ionic coordinates of ion K.

In Eqs. (2.40) and (2.41) we have obtained a set of general equations of motion for a system of quantum mechanical electrons and classical ions. However, solution of these would still require direct solution of the TDSE, which as we have seen in previous sections is impossible for all but the simplest of systems. We therefore wish to derive an analogous set of equations to Eqs. (2.40) and (2.41), but in which the electronic dynamics are described by TDDFT.

2.4.2 Quantum-classical molecular dynamics with a TDDFT description of electrons

As we saw in Section 2.3, in the TDDFT method the full N_e-electron wavefunction is replaced by a Slater determinant of single particle orbitals, the Kohn-Sham orbitals ψ_j,

which reproduce the correct electron density through Eq. (2.18). With this treatment of the electrons, the Lagrangian can be written [220]

$$\begin{aligned}\mathcal{L} = \mathrm{i}\sum_{j=1}^{N_e}\int \psi_j^*(\boldsymbol{r},t)\dot{\psi}_j(\boldsymbol{r},t)\mathrm{d}\boldsymbol{r} + \frac{1}{2}\sum_{j=1}^{N_e}\int \psi_j^*(\boldsymbol{r},t)\nabla^2\psi_j(\boldsymbol{r},t)\mathrm{d}\boldsymbol{r} \\ - \int n(\boldsymbol{r},t)\left(V_{\text{ext}}(\boldsymbol{r},\boldsymbol{R},t) + \frac{1}{2}\int \frac{n(\boldsymbol{r'},t)}{|\boldsymbol{r}-\boldsymbol{r'}|}d\boldsymbol{r'}\right)\mathrm{d}\boldsymbol{r} \\ - A_{\text{xc}}[n] + \frac{1}{2}\sum_{K=1}^{N_n} M_K\dot{\boldsymbol{R}}_K^2(t) - V_{nn}(\boldsymbol{R}) - Z_K\boldsymbol{R}_K\cdot\boldsymbol{E}(t),\end{aligned} \tag{2.42}$$

where $A_{\text{xc}}[n]$ is the exchange-correlation action functional.

Rewriting the Euler-Lagrange equations, Eqs. (2.37) – (2.39), with the many-body wavefunction Ψ replaced by the Kohn-Sham orbitals ψ_j now leads analogously to the time-dependent Kohn-Sham equations

$$\mathrm{i}\frac{\partial}{\partial t}\psi_j(\boldsymbol{r},t) = H_{\text{KS}}(\boldsymbol{r},\boldsymbol{R},t)\psi_j(\boldsymbol{r},t), \tag{2.43}$$

and the ionic equation of motion

$$M_K\ddot{\boldsymbol{R}}_K = -\int\Big(n(\boldsymbol{r},t)\boldsymbol{\nabla}_K H_{\text{KS}}\Big)\mathrm{d}\boldsymbol{r} - \boldsymbol{\nabla}_K\Big(V_{nn}(\boldsymbol{R}) + Z_K\boldsymbol{R}_K\cdot\boldsymbol{E}(t)\Big), \tag{2.44}$$

where H_{KS} is the Kohn-Sham Hamiltonian defined in Eq. (2.17). In Eqs. (2.43) and (2.44) we have obtained a set of non-adiabatically coupled equations of motion describing the electronic and ionic dynamics of a general system. The solution of these equations will allow us to study the dynamics of the system, and to investigate the degree of coupling between the electronic and ionic motions. In the next chapter we will show how these equations are solved numerically on a real-space grid in our code, EDAMAME. Before that however, we will consider briefly the applicability of the classical treatment of the nuclei used in the quantum-classical method described above.

2.4.3 Applicability of classical description of ions

The approximation of treating nuclei as classical particles instead of describing them quantum mechanically both enables calculations to extend beyond the simplest systems and reduces the conceptual complexity of calculations and the interpretation of results.

It is, however, an approximation, and as such has limits to its applicability. For example, a full quantum treatment of the nuclei is required when describing zero-point motions or nuclear tunnelling effects [222, 223].

We have already seen in Section 2.3.5 an example of a case in which results from a classical treatment of the nuclear motion were in qualitative but not quantitative agreement with results from calculations incorporating quantum nuclear motion [205]. This example dealt with the interaction of a laser field with the diatomic HD molecule. A number of other studies have also highlighted how a proper quantum treatment of the nuclear motion is important in describing laser interactions with small molecules with light nuclei [74, 224].

In the Ehrenfest method for treating nuclear motion outlined above, the quantum mechanical nuclear dynamics are replaced by a single "mean-field" trajectory; i.e., the system evolves on a potential energy surface that is a weighted average of a number of the potential energy surfaces of the system [225]. Clearly such a mean-field approach will only be applicable in situations in which the classical trajectories associated with different states are not significantly different from each other, or in which the trajectory associated with a single state dominates the dynamics [226]. Situations in which there is substantial wavepacket splitting between significantly different classical trajectories are beyond the scope of Ehrenfest [225]. Effects such as this will become more prominent over longer timescales, and especially so when the difference between the timescales of nuclear and electronic motions is small (in molecules with light nuclei for example).

Since we are working with larger molecules with heavier nuclei than those considered in the references above, and considering the relatively short timescales that the dynamics of the systems studied in this thesis are propagated for ($\approx 25\,\text{fs}$), we expect that a classical treatment of the nuclear motion as outlined above will be a reasonable approximation.

2.4.4 Summary

In this section we have shown how a quantum description of electron dynamics (in particular, TDDFT) can be combined with a classical description of ionic motion in a

quantum-classical molecular dynamics method. By employing a Lagrangian formalism, we have derived equations of motion for the quantum mechanical electrons and the classical ions (Eqs. (2.43) and (2.44) respectively). In the next section we will complete our theoretical description of the laser-molecule interaction by showing how the interaction with the laser field can be treated in a semiclassical manner.

2.5 Semiclassical description of a laser-molecule system

In the previous sections, the applied laser field was included in the Hamiltonian as $U_{\text{elec}}(\boldsymbol{r}, t)$, but no details of the actual form of this term were given. In this section we show how a laser pulse can be introduced to the system as a classical field, resulting in a semiclassical treatment of the laser-molecule interaction. We begin by discussing when and why such a classical treatment of the laser field is appropriate, before showing how a description of the field in terms of a vector potential $\boldsymbol{A}(\boldsymbol{r}, t)$ can be obtained, starting from Maxwell's equations. An approximation known as the dipole approximation will then be introduced to simplify the description of the laser field, and the validity of this approximation discussed. Finally we will show how the laser interaction is included in the Hamiltonian, and how, with a suitable gauge transformation, we can obtain an expression for $U_{\text{elec}}(\boldsymbol{r}, t)$ in terms of the position vector $\boldsymbol{r}$ and the electric field vector $\boldsymbol{E}(t)$.

2.5.1 First quantization

In principle, the interaction of a laser pulse with a molecule will require the full relativistic and quantum mechanical description of both the molecule and the radiation field of the laser (i.e., describing individual photons). In practice however, a full quantum mechanical treatment may not be necessary, if the intensity of the laser pulse is large enough. To see why, consider the number of photons that would be present per unit volume in a laser beam of intensity I, wavelength λ, and frequency ω. The so-called photon density [227] in this case is given (in SI units) by

$$\rho = \frac{I}{\hbar \omega c}. \tag{2.45}$$

For a laser pulse with intensity $1.0\times10^{14}\,\mathrm{W/cm^2}$ and wavelength $\lambda = 1450\,\mathrm{nm}$, the photon density would therefore be $2.4\times10^{22}/\mathrm{cm^3}$ or 7.4×10^{10} per cubic wavelength. For a pulse with lower intensity and wavelength ($\mathrm{I} = 1.0\times10^{12}\,\mathrm{W/cm^2}$, $\lambda = 102\,\mathrm{nm}$), the photon density would be 1.8×10^{4} per cubic wavelength. Clearly in both cases the photon density per cubic wavelength is large, and so it is reasonable to use a semiclassical treatment of the laser-molecule interaction. In that case the molecule can be described quantum mechanically while the laser field is described as a classical field. Historically, this type of description is known as first quantization (in contrast to second quantization in which the electromagnetic field is also quantized).

2.5.2 Maxwell's equations and gauge transformations

Employing a semiclassical description greatly simplifies the treatment of our system, and allows us to draw on the well-known laws of classical electromagnetic theory. At the foundation of classical electromagnetism are Maxwell's equations. In atomic units (see Table 1 for conversions between systems of units), Maxwell's equations for electromagnetic waves in a vacuum may be written as

$$\boldsymbol{\nabla}\cdot\boldsymbol{E} = 0, \tag{2.46}$$

$$\boldsymbol{\nabla}\cdot\boldsymbol{B} = 0, \tag{2.47}$$

$$\boldsymbol{\nabla}\times\boldsymbol{E} = -\frac{\partial\boldsymbol{B}}{\partial t}, \tag{2.48}$$

$$\boldsymbol{\nabla}\times\boldsymbol{B} = \frac{1}{c^2}\frac{\partial\boldsymbol{E}}{\partial t}, \tag{2.49}$$

where $\boldsymbol{E} = \boldsymbol{E}(\boldsymbol{r},t)$ and $\boldsymbol{B} = \boldsymbol{B}(\boldsymbol{r},t)$ are the electric and magnetic field vectors, respectively. In Since the divergence of the curl of any vector field is zero [228], Eq. (2.47) implies that there must exist some vector potential $\boldsymbol{A} = \boldsymbol{A}(\boldsymbol{r},t)$ such that

$$\boldsymbol{B} = \boldsymbol{\nabla}\times\boldsymbol{A}. \tag{2.50}$$

Making this substitution for the magnetic field vector in Eq. (2.48) gives

$$\boldsymbol{\nabla}\times\left(\boldsymbol{E} + \frac{\partial\boldsymbol{A}}{\partial t}\right) = \boldsymbol{0}. \tag{2.51}$$

Noting the vector identity that the curl of the gradient of any scalar field gives the zero vector field (i.e., $\boldsymbol{\nabla}\times(\boldsymbol{\nabla}\phi) = \mathbf{0}$), we can express the electric field vector in terms of the vector potential $\boldsymbol{A} = \boldsymbol{A}(\boldsymbol{r}, t)$ and some scalar potential $\phi = \phi(\boldsymbol{r}, t)$ as [228]

$$\boldsymbol{E} = -\boldsymbol{\nabla}\phi - \frac{\partial \boldsymbol{A}}{\partial t}. \tag{2.52}$$

Using the expressions for $\boldsymbol{B}$ and $\boldsymbol{E}$ given by Eqs. (2.50) and (2.52) in Eq. (2.48), we can derive the following expression for $\boldsymbol{A}$ and ϕ

$$\nabla^2 \boldsymbol{A} - \frac{1}{c^2}\frac{\partial^2 \boldsymbol{A}}{\partial t^2} - \boldsymbol{\nabla}\left(\boldsymbol{\nabla}\cdot\boldsymbol{A} + \frac{1}{c^2}\frac{\partial \phi}{\partial t}\right) = \mathbf{0}. \tag{2.53}$$

These potentials $\boldsymbol{A}$ and ϕ are not unique, since a replacement of the form

$$\boldsymbol{A} \rightarrow \boldsymbol{A}' = \boldsymbol{A} + \boldsymbol{\nabla}\chi, \tag{2.54}$$

$$\phi \rightarrow \phi' = \phi - \frac{\partial \chi}{\partial t}, \tag{2.55}$$

will not alter the field strengths $\boldsymbol{E}$ and $\boldsymbol{B}$. Here $\chi = \chi(\boldsymbol{r}, t)$ is some arbitrary scalar field. Replacing $\boldsymbol{A}$ and ϕ with $\boldsymbol{A}'$ and ϕ' in this manner is known as a gauge transformation.

One particular gauge of interest is the Coulomb gauge, in which $\boldsymbol{\nabla}\cdot\boldsymbol{A} = 0$. Making a transformation to this gauge, and assuming that $\phi = 0$ [230], Eq. (2.52) reduces to

$$\nabla^2 \boldsymbol{A} - \frac{1}{c^2}\frac{\partial^2 \boldsymbol{A}}{\partial t^2} = \mathbf{0}. \tag{2.56}$$

One possible solution to this wave equation has the form

$$\boldsymbol{A}(\boldsymbol{r}, t) = \hat{\boldsymbol{\epsilon}} A_0 \cos(\boldsymbol{k}\cdot\boldsymbol{r} - \omega t + \delta), \tag{2.57}$$

where $\hat{\boldsymbol{\epsilon}}$ is the polarization vector of the field, A_0 is the peak value of $\boldsymbol{A}$, $\boldsymbol{k}$ is the wave vector, ω is the laser frequency, and δ is the phase of the field.

2.5.3 The dipole approximation

In Eq. (2.57) we have a fairly complicated expression for the vector potential $\boldsymbol{A}$; one that depends on both spatial coordinates and time. However, in certain circumstances we can reasonably approximate the laser field as being uniform across the small in-

teraction volume being considered. To see how this approximation is made, we first express Eq. (2.57) in terms of complex exponentials

$$\boldsymbol{A}(\boldsymbol{r},t) = \hat{\boldsymbol{\epsilon}}\frac{A_0}{2}\left[e^{i(\boldsymbol{k}\cdot\boldsymbol{r}-\omega t+\delta)} + e^{-i(\boldsymbol{k}\cdot\boldsymbol{r}-\omega t+\delta)}\right]. \tag{2.58}$$

Now expanding the spatial part of the first exponential term as a Taylor series, we have

$$e^{i\boldsymbol{k}\cdot\boldsymbol{r}} = 1 + (\boldsymbol{k}\cdot\boldsymbol{r}) + \frac{1}{2!}(\boldsymbol{k}\cdot\boldsymbol{r})^2 + \ldots, \tag{2.59}$$

and similarly for the second exponential term, where $\boldsymbol{k}$ is the wavevector. Clearly, if $|kr| \ll 1$, then the spatial dependence of $\boldsymbol{A}$ can reasonably be discarded, and we are left with a vector potential with no spatial dependence

$$\boldsymbol{A}(t) = \hat{\boldsymbol{\epsilon}}A_0\cos(\omega t + \delta). \tag{2.60}$$

This is known as the dipole approximation, and is considered a reasonable approximation to make when the wavelength of incident radiation is much greater than the characteristic size of the system being irradiated. Relating the magnitude of the wavevector to the wavelength as $|\boldsymbol{k}| = k = 2\pi/\lambda$, we can estimate typical values of $|kr|$ for the systems we will be considering. Taking an upper estimate of the size of the molecules considered in this work of 0.4 nm, $|kr|$ for a mid-IR wavelength of $\lambda = 1450$ nm is 0.0017, while for a VUV wavelength of $\lambda = 102$ nm it is 0.025. In both cases, the dipole approximation seems a reasonable approximation to make. If much shorter wavelengths were employed, the dipole approximation would no longer be valid, and the problem would become significantly more complex.

In addition, if the laser intensity was large enough that relativistic effects became important, the dipole approximation would again no longer be valid. These effects include, for example, relativistic mass shifts, break down of the effect of stabilization against ionization (an effect observed in atoms and molecules exposed to intense laser fields), and an increasing importance of the magnetic component of the laser field [229]. A relativistic treatment is considered necessary if

$$\frac{E_0/\omega}{c} \approx 1, \tag{2.61}$$

where E_0 is the maximum value of the electric field, ω is the laser frequency, c is the speed of light, and all quantities are expressed in atomic units [11]. For a mid-IR laser pulse with wavelength $\lambda = 1450$ nm and intensity 1.0×10^{14} W/cm^2, we have $\omega = 0.0314$ a.u. and $E_0 = 0.0534$, giving a value of the above ratio (noting that $c = 137$ in atomic units) of 0.0124. Therefore we do not expect relativistic effects to be important with these laser parameters. For more discussion on relativistic effects see section 10 of [11], [229], and the references within.

Beyond the dipole approximation, a first-order approximation (in which the $(\boldsymbol{k}\cdot\boldsymbol{r})^2$ and higher terms in Eq. (2.59) are neglected) or higher multipole approximations can be employed, at much greater computational cost [230–232]. Nondipole effects have been investigated and observed in a number of studies [233–235]. However, the laser intensities and photon energies employed in these studies are well beyond the laser parameters considered in this thesis. For the work presented in Chapters 4 and 5 we expect the dipole approximation to be adequate.

2.5.4 Electron-laser interaction

In the previous sections we have derived an expression for a time-dependent and spatially-independent vector potential

$$\boldsymbol{A}(t) = \hat{\boldsymbol{\epsilon}} A_0 \cos(\omega t + \delta), \tag{2.62}$$

which is related to the electric field vector (using Eq. (2.52) with $\phi = 0$) through

$$\boldsymbol{E} = -\frac{\partial \boldsymbol{A}}{\partial t}. \tag{2.63}$$

We now need to determine an expression for the electron-laser interaction potential $U_{\text{elec}}(\boldsymbol{r}, t)$.

The Hamiltonian for a particle of charge q and mass m moving in an electromagnetic field described by a vector potential $\boldsymbol{A}$ (and a scalar potential $\phi = 0$) is [236]

$$H_{\text{field}} = \frac{1}{2m}(\boldsymbol{p} - q\boldsymbol{A})^2, \tag{2.64}$$

where $\boldsymbol{p}$ is the canonical momentum of the particle.

In atomic units, considering an electron in particular (so that $m = 1$, $q = -1$), and replacing the canonical momentum with the momentum operator $\boldsymbol{p} \to -i\boldsymbol{\nabla}$, the Hamiltonian becomes

$$H_{\text{field}} = \frac{1}{2}(-i\boldsymbol{\nabla} + \boldsymbol{A})^2 \tag{2.65}$$

$$= -\frac{1}{2}\nabla^2 - i\boldsymbol{A}\cdot\boldsymbol{\nabla} + \boldsymbol{A}^2. \tag{2.66}$$

This form of the Hamiltonian is known as the velocity gauge or minimal coupling description.

The majority of the work described in this thesis was carried out in the length gauge, rather than the velocity gauge. The appropriate length gauge description can be obtained by performing the transformation [237]

$$\Psi_{\text{LG}}(\boldsymbol{r}, t) \to \exp\left[i\boldsymbol{A}\cdot\boldsymbol{r}\right]\Psi_{\text{VG}}(\boldsymbol{r}, t), \tag{2.67}$$

where LG and VG refer to the length and velocity gauges respectively. The Hamiltonian for an electron moving in the field described by $\boldsymbol{A}$ and $\boldsymbol{E}$ in the length gauge then becomes

$$H_{\text{field}} = -\frac{1}{2}\nabla^2 + \boldsymbol{r}\cdot\boldsymbol{E}. \tag{2.68}$$

Clearly the first term of H_{field} expressed in this way is simply the kinetic energy term already present in the Kohn-Sham Hamiltonian in Section 2.3. We therefore take the second term as the electron-laser interaction potential

$$U_{\text{elec}}(\boldsymbol{r}, t) = \boldsymbol{r}\cdot\boldsymbol{E}(t). \tag{2.69}$$

(In the velocity gauge, this term can be shown to be given by $U^{\text{V}}_{\text{elec}}(\boldsymbol{r}, t) = -i\boldsymbol{A}(t)\cdot\boldsymbol{\nabla}$ [237], since the $\boldsymbol{A}^2$ term in Eq. (2.66) can be removed by a different transformation).

In principle, with an exact description of the system the choice of gauge will have no impact on the results obtained, since quantum mechanics is gauge invariant. In practice, since approximations have been made, results obtained in different gauges are not guaranteed to be identical. However, previous comparisons of results obtained using length and velocity gauge descriptions of laser-matter interactions have shown

good agreement between the two gauges [219, 237]. The length gauge description is used in the majority of the work presented in this thesis as it is computationally more efficient for the systems being considered.

2.5.5 Summary

In this section we have seen how a laser field can be introduced to the theoretical description of a molecular system described in Sections 2.3 and 2.4. For the typical laser parameters used in the work described in this thesis, the photon density is considered large enough that the laser pulse can be described as a classical radiation field. It was shown how Maxwell's equations and gauge transformations lead to a description of the laser in terms of a vector potential $\boldsymbol{A}(\boldsymbol{r}, t)$. This description can be simplified to $\boldsymbol{A}(t)$ by employing the dipole approximation, which is generally a reasonable approximation to make when the laser wavelength is much greater than the size of the molecule. Finally, by considering the Hamiltonian for a charged particle moving in an electromagnetic field, we derived an expression for the electron-laser interaction potential in a length gauge description, namely $U_{\text{elec}}(\boldsymbol{r}, t) = \boldsymbol{r} \cdot \boldsymbol{E}(t)$.

2.6 Conclusions

In this chapter, we have described the formal theory required to model interactions of molecules with short, high intensity laser pulses. Describing the dynamics of a laser-molecule system in principle requires the solution of the full time-dependent Schrödinger equation. In practice however, this is impossible for all but the smallest of systems. In almost all cases, some approximations are required, for example the separation of the electronic and nuclear dynamics, as in the Born-Oppenheimer and classical nuclei approximations. Even with one of these approximations, describing the electronic dynamics of a multielectron system is an enormous challenge, and requires a specialist approach. There are a variety of methods available for tackling this problem, including time-dependent Hartree-Fock, post-Hartree-Fock approaches such as time-dependent configuration interaction, or the alternative method of time-dependent density functional theory.

In the latter of these methods (TDDFT), the wavefunction is replaced by the elec-

tronic density as the main quantity of interest, and solution of the time-dependent Schrödinger equation is no longer required. Instead, describing the electronic dynamics requires the self-consistent solution of a set of one-particle Schrödinger-like equations: the time-dependent Kohn-Sham (TDKS) equations. Solution of these will be, in principle, equivalent to solution of the full time-dependent Schrödinger equation. In practice however, a key quantity in the Hamiltonian of the TDKS equations, the exchange-correlation potential, is unknown, and must be approximated.

A number of approximations to the exchange-correlation potential are available, the simplest of which is the adiabatic local density approximation (ALDA). In this approximation the exchange-correlation potential is approximated as the ground state potential of a uniform gas, with instantaneous and local density. ALDA is the easiest exchange-correlation potential to implement, but does contain several errors, which can be significant depending on the system under investigation. One of the most significant of these is the self-interaction error inherent in ALDA; this leads to incorrect long-range behaviour with associated unphysical effects such as underestimated ionization potentials and incorrect dissociation limits. While a number of more complicated schemes for correcting the self-interaction error exist, the average-density self-interaction-correction (ADSIC) scheme provides a good compromise between accuracy and efficiency.

In the latter sections of this chapter, it was shown how a classical treatment of ionic motion can be combined with a quantum description of electronic dynamics, giving rise to a quantum-classical molecular dynamics approach, and finally how a laser field can be introduced classically to the system, resulting in a semiclassical treatment of the laser-molecule interaction.

In the next chapter, we will show how the theory described in this chapter is implemented in practice, in the Fortran2008 code EDAMAME.

Chapter 3

Numerical implementation of the quantum-classical molecular dynamics approach

---

3.1 Introduction

The theoretical formalism of quantum-classical molecular dynamics incorporating TDDFT, described in Chapter 2, is implemented in a Fortran2008 code named EDAMAME (Ehrenfest DynAMics on Adaptive MEshes). This software was developed in Queen's University Belfast [220] and has previously been used to study a number of molecular systems including nitrogen (N_2) and benzene (C_6H_6) [46, 220].

EDAMAME combines a TDDFT description of electronic dynamics with a classical description of the motion of the ions. It is a highly parallelized code, which allows it to take advantage of the computational power of high performance computing (HPC) systems, ranging from large national services such as ARCHER, the UK National Supercomputing Service [238], to small departmental clusters. The ability to spread a calculation over hundreds or thousands of cores is essential to the work described in this thesis; the large grid sizes needed for accurately describing the motion of ionized

wavepackets following ionization by a strong laser field mean that calculations on a desktop machine would be practically impossible.

This chapter will provide an overview of the design of EDAMAME, and is arranged as follows. In Section 3.2 we explain how the time-dependent Kohn-Sham equations are discretized and solved on a finite difference grid, describing how each of the potential terms appearing in the equations are calculated, as well as how the initial state is calculated and subsequently propagated in time. In Section 3.3 we consider the ionic dynamics, describing how the classical equations of motion are propagated in time, as well as how relaxed geometries are obtained. The parallelization of the code is discussed in Section 3.4. Finally, in Section 3.5, we describe how a number of observable quantities, such as ionization and high harmonic spectra, are calculated within EDAMAME.

3.2 Electronic Dynamics: TDDFT

Modelling the electronic dynamics of a system with N_e electrons within TDDFT requires the solution of the time-dependent Kohn-Sham (TDKS) equations. Since the systems studied in this work all have even numbers of electrons, and since we are interested in the effect of electric fields only (i.e., not magnetic fields), spin effects can be neglected. In this case the number of TDKS orbitals to be propagated is $N = N_e/2$, and the TDKS equations are

$$\begin{aligned} i\frac{\partial}{\partial t}\psi_j(\boldsymbol{r},t) =& H_{\text{KS}}\psi_j(\boldsymbol{r},t) \\ =& \left[-\frac{1}{2}\nabla^2 + V_{\text{KS}}(\boldsymbol{r},t)\right]\psi_j(\boldsymbol{r},t) \\ =& \left[-\frac{1}{2}\nabla^2 + V_{\text{H}}(\boldsymbol{r},t) + V_{\text{ext}}(\boldsymbol{r},\boldsymbol{R},t) + V_{\text{xc}}(\boldsymbol{r},t)\right]\psi_j(\boldsymbol{r},t), \end{aligned} \tag{3.1}$$

for $j = 1,\ldots,N$, where $V_{\text{H}}(\boldsymbol{r},t)$, $V_{\text{ext}}(\boldsymbol{r},\boldsymbol{R},t)$, and $V_{\text{xc}}(\boldsymbol{r},t)$ are the Hartree potential, external potential, and exchange-correlation potential introduced in Chapter 2. Each of these N time-dependent Kohn-Sham orbitals, $\psi_j(\boldsymbol{r},t)$, has an initial occupancy of 2, with the total density of the system being given by

$$n(\boldsymbol{r},t) = 2\sum_{j=1}^{N}|\psi_j(\boldsymbol{r},t)|^2. \tag{3.2}$$

Note that a small number of extra, unoccupied states (typically 5–10) are also included in EDAMAME calculations, as their inclusion generally helps with the convergence of the ground state (the calculation of which is described in Section 3.2.7). These orbitals have occupancies of 0, and do not contribute to the density or potential of the system.

In this section, we will describe how the TDKS equations are described and solved in EDAMAME.

3.2.1 Finite difference grid

Within EDAMAME, the Kohn-Sham orbitals are discretized on a finite difference grid in Cartesian coordinates. Use of finite difference grids rather than basis set techniques to solve the TDKS equations allows the extent of the grid to be increased more easily, and for the calculation to be parallelized across large numbers of processors (see Section 3.4). In this way, ionizing electrons can be described more easily. Two different types of finite difference grid can be implemented:

(i) a standard grid, with uniform spacings between grid points, or

(ii) a scaled grid, with non-uniform spacings between grid points, in which the spacing in a small region around the molecule is smaller than elsewhere.

In both types of grid the origin, (0, 0, 0), is positioned at the centre of the grid. For the standard grid, the grid spacing is constant in each dimension. Working in a Cartesian coordinate system (with unit vectors $\hat{\boldsymbol{e}}_x = \hat{\boldsymbol{\imath}}$, $\hat{\boldsymbol{e}}_y = \hat{\boldsymbol{\jmath}}$, $\hat{\boldsymbol{e}}_z = \hat{\boldsymbol{k}}$ for the x, y, z coordinates respectively), the position vector in these unscaled coordinates is simply

$$\boldsymbol{r} = x\hat{\boldsymbol{\imath}} + y\hat{\boldsymbol{\jmath}} + z\hat{\boldsymbol{k}}. \tag{3.3}$$

Consider the x coordinate. Using N_x grid points along this direction, and a grid spacing of Δx, the grid spans the range $-x_{\text{max}} \leq x \leq x_{\text{max}}$, where

$$x_{\text{max}} = \frac{(N_x - 1) \times \Delta x}{2}. \tag{3.4}$$

The gridpoints themselves are defined as

$$x_i = -x_{\max} + (i-1)\Delta x, \tag{3.5}$$

for $i = 1, \ldots, N_x$. Similar expressions hold for the y and z coordinates.

If a high density of points is required near the origin (in the vicinity of the molecule), a scaled grid can be used. In this case the position vector is given by

$$\boldsymbol{r} = f(x)\hat{\boldsymbol{\imath}} + g(y)\hat{\boldsymbol{\jmath}} + h(z)\hat{\boldsymbol{k}}, \tag{3.6}$$

where $f(x)$, $g(y)$ and $h(z)$ are scaling functions. The volume element in these scaled coordinates is

$$\mathrm{d}\boldsymbol{r} = f'(x)g'(y)h'(z)\mathrm{d}x\mathrm{d}y\mathrm{d}z = |\boldsymbol{J}|\mathrm{d}x\mathrm{d}y\mathrm{d}z, \tag{3.7}$$

where $f'(x) = \frac{\partial f(x)}{\partial x}$, $g'(y) = \frac{\partial g(y)}{\partial y}$, $h'(z) = \frac{\partial h(z)}{\partial z}$, and $|\boldsymbol{J}| = \det(\boldsymbol{J})$ is the determinant of the Jacobian describing the transformation. For this orthogonal transformation the Jacobian is

$$\boldsymbol{J} = \begin{pmatrix} f'(x) & 0 & 0 \\ 0 & g'(y) & 0 \\ 0 & 0 & h'(z) \end{pmatrix}. \tag{3.8}$$

The gradient operator can then be written as [239]

$$\boldsymbol{\nabla} = \hat{\boldsymbol{\imath}}\frac{1}{f'}\frac{\partial}{\partial x} + \hat{\boldsymbol{\jmath}}\frac{1}{g'}\frac{\partial}{\partial y} + \hat{\boldsymbol{k}}\frac{1}{h'}\frac{\partial}{\partial z}, \tag{3.9}$$

while the Laplacian is [239]

$$\nabla^2 = \frac{1}{|J|}\left[\frac{\partial}{\partial x}\left(\frac{g'h'}{f'}\right)\frac{\partial}{\partial x} + \frac{\partial}{\partial y}\left(\frac{f'h'}{g'}\right)\frac{\partial}{\partial y} + \frac{\partial}{\partial z}\left(\frac{f'g'}{h'}\right)\frac{\partial}{\partial z}\right]. \tag{3.10}$$

In addition, the Kohn-Sham orbitals are transformed according to

$$\psi_j(\boldsymbol{r}, t) \to \frac{1}{\sqrt{|J|}}\psi_j(\boldsymbol{r}, t). \tag{3.11}$$

These expressions can then be substituted into the Lagrangian defined in Eq. (2.42) before taking the variation to obtain the TDKS equations. With this choice, the Laplacian

operator in the TDKS equations becomes

$$\nabla^2 = \frac{1}{\sqrt{f'}}\frac{\partial}{\partial x}\left(\frac{1}{f'}\right)\frac{\partial}{\partial x}\frac{1}{\sqrt{f'}} + \frac{1}{\sqrt{g'}}\frac{\partial}{\partial y}\left(\frac{1}{g'}\right)\frac{\partial}{\partial y}\frac{1}{\sqrt{g'}} + \frac{1}{\sqrt{h'}}\frac{\partial}{\partial z}\left(\frac{1}{h'}\right)\frac{\partial}{\partial z}\frac{1}{\sqrt{h'}}, \quad (3.12)$$

which will result in symmetric equations when central finite difference formulae are applied (see [220] for more details). This is important as it ensures that the resulting finite difference Hamiltonian is Hermitian, which in turn allows for the use of unitary time propagation schemes [240]. This expression for the Laplacian, given in terms of first derivatives, can be rewritten in terms of second derivatives for convenience, while maintaining the symmetry of the finite difference equations. Taking the term involving derivatives with respect to x as an example, we can write

$$\frac{1}{\sqrt{f'}}\frac{\partial}{\partial x}\left(\frac{1}{f'}\right)\frac{\partial}{\partial x}\frac{1}{\sqrt{f'}} = \frac{1}{2}\left[\frac{1}{(f')^2}\frac{\partial^2}{\partial x^2} + \frac{\partial^2}{\partial x^2}\frac{1}{(f')^2}\right] + \left[\frac{f'''}{2(f')^3} - \frac{7}{4}\frac{(f'')^2}{(f')^4}\right], \quad (3.13)$$

where f', f'' and f''' indicate successively higher derivatives of $f(x)$ with respect to x. The terms in Eq. (3.12) involving derivatives with respect to y and z can be rewritten in analogous forms.

To obtain a higher density of points close to the molecule, we apply the following transformation. For clarity, here we apply this to the x coordinate; similar expressions can be obtained for the y and z coordinates. In this case, we have

$$\begin{aligned} f(x) = 2x &+ \frac{1}{2}\left[(x - x_b)\mathrm{erf}(x - x_b) + \frac{e^{-(x-x_b)^2}}{\sqrt{\pi}}\right] \\ &- \frac{1}{2}\left[(x + x_b)\mathrm{erf}(x + x_b) - \frac{e^{-(x+x_b)^2}}{\sqrt{\pi}}\right]. \end{aligned} \quad (3.14)$$

Here x_b is the specified boundary between the inner region (high density of points) and outer region (low density of points), and

$$\mathrm{erf}(x) = \frac{2}{\sqrt{\pi}}\int_0^x e^{-t^2}\mathrm{d}t, \quad (3.15)$$

is the error function.

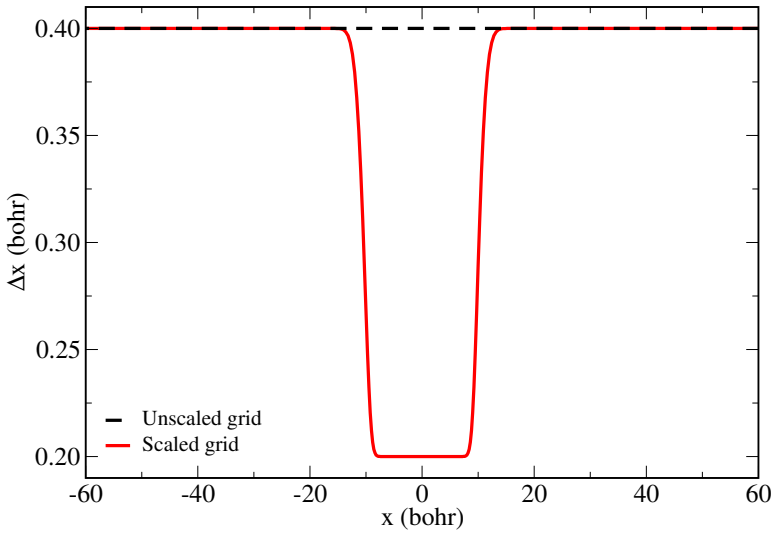

Figure 3.1: Grid spacings in the two different finite difference grids used in EDAMAME. In the unscaled grid, the grid spacing is constant ($0.4\,a_0$) throughout the grid. In the scaled grid, the grid spacing is $0.4\,a_0$ for most of the grid, but reduces to $0.2\,a_0$ near the centre of the grid. A smooth transition between the two regions occurs around $\pm 10\,a_0$. The x coordinate has been chosen here as an example; the y and z coordinates are scaled in the same manner.

The derivative terms appearing in Eq. (3.13) and elsewhere are therefore

$$f'(x) = 2 + \frac{1}{2}\left[\mathrm{erf}(x - x_b) - \mathrm{erf}(x + x_b)\right], \tag{3.16}$$

$$f''(x) = \frac{1}{\sqrt{\pi}}\left[e^{-(x-x_b)^2} - e^{-(x+x_b)^2}\right], \tag{3.17}$$

$$f'''(x) = \frac{2}{\sqrt{\pi}}\left[-(x - x_b)e^{-(x-x_b)^2} + (x + x_b)e^{-(x+x_b)^2}\right]. \tag{3.18}$$

From Eq. (3.7), the grid spacing in x will be related to the scale factor $f'(x)\Delta x$. Therefore, from Eq. (3.16), we obtain a finite difference grid with a grid spacing of Δx in the inner region, and $2\Delta x$ in the outer region, with a smooth transition between the two around x_b, as shown in Fig. 3.1.

3.2.2 Finite difference formulae for derivatives

Evaluation of the kinetic energy operator in Eqs. (3.12) and (3.13) requires approximations to second derivatives. Derivatives in EDAMAME are approximated using central difference formulae. For some function, $F(x)$, the first derivative at the point x_a can be

approximated as

$$F'(x_a) = \frac{1}{\Delta x} \sum_{\kappa=-N_{\text{fd}}}^{N_{\text{fd}}} d_1(x_{a+\kappa}) F(x_{a+\kappa}), \tag{3.19}$$

while the second derivative is approximated as

$$F''(x_a) = \frac{1}{(\Delta x)^2} \sum_{\kappa=-N_{\text{fd}}}^{N_{\text{fd}}} d_2(x_{a+\kappa}) F(x_{a+\kappa}), \tag{3.20}$$

where $d_1(x_{a+\kappa})$ and $d_2(x_{a+\kappa})$ are the finite difference coefficients at point $x_{a+\kappa}$. We refer to Eqs. (3.19)–(3.20) as $(2N_{\text{fd}}+1)$-point, or $(\mathcal{N}+1)$-point, finite difference rules, where $\mathcal{N} = 2N_{\text{fd}}$.

The finite difference coefficients can be derived in a number of different ways, including using the Taylor series or Lagrange interpolation. For the results presented in Chapter 4, the standard coefficients [241, 242] are used along with the unscaled grid described above. The work that will be described in Chapter 5 requires the use of the scaled grid described above. An undesired consequence of reducing the grid spacing is the associated requirement to also reduce the time step used in the propagation of the TDKS equations (see Section 3.2.8). This is due to the fact that the highest frequency modes supported by the finite difference grid increase as the grid spacing is reduced. The highest modes have energies beyond any physical energies associated with the system, but will result in errors in the calculation if not described correctly. Reducing the time step to accommodate the propagation of these states would be an added computational burden on top of that imposed by the need for a greater number of grid points when the scaled coordinates are used. Instead, we follow the approach taken in the development of an RMT (R-Matrix with time-dependence) code in Belfast [243], and alter the finite difference method used to one which suppresses the highest frequency components. Briefly, this approach proceeds as follows (further details and discussion of this approach can be found in [243]).

An arbitrary function, $F(x)$, can be approximated as a linear combination of $(\mathcal{N}+1)$ discrete orthogonal polynomials, $u_j(x)$, as

$$F(x) = \sum_{j=0}^{\mathcal{N}} c_j u_j(x) \qquad\qquad j = 0, \ldots, \mathcal{N}. \tag{3.21}$$

Here the expansion coefficients, c_j, are determined by projecting both sides of this equation onto an arbitrary polynomial. Noting the orthogonality of the polynomials, this gives

$$c_j = \frac{(F, u_j)}{(u_j, u_j)}, \tag{3.22}$$

where (F, G) denotes the weighted inner product of the functions $F(x)$ and $G(x)$ over the discrete points, x_k, $k = 0, \ldots, \mathcal{N}$, given by

$$(F, G) = \sum_{k=0}^{\mathcal{N}} w_k F(x_k) G(x_k), \tag{3.23}$$

with weights w_k. In this work Lorentzian weights are employed where

$$w_k = \left[1 + 2^{12} \left(\frac{x_k}{x_{\mathcal{N}}}\right)^2\right]^{-1} \qquad k = 0, \ldots, \mathcal{N}. \tag{3.24}$$

The set of $(\mathcal{N} + 1)$ discrete orthogonal polynomials are defined through the recurrence relation

$$u_0(x) = 1 \tag{3.25}$$

$$u_1(x) = x - \alpha_1 \tag{3.26}$$

$$u_j(x) = (x - \alpha_j) u_{j-1}(x) - \beta_j u_{j-2}(x) \qquad j = 2, \ldots, \mathcal{N}, \tag{3.27}$$

where

$$\alpha_j = \frac{(x\alpha_{j-1}, \alpha_{j-1})}{(\alpha_{j-1}, \alpha_{j-1})} \qquad j = 1, \ldots, \mathcal{N}, \tag{3.28}$$

and

$$\beta_j = \frac{(x\alpha_{j-1}, \alpha_{j-2})}{(\alpha_{j-2}, \alpha_{j-2})} \qquad j = 2, \ldots, \mathcal{N}. \tag{3.29}$$

We can therefore rewrite Eq. (3.21) as

$$F(x) = \sum_{j=0}^{\mathcal{N}} \frac{(F, u_j)}{(u_j, u_j)} u_j(x) = \sum_{k=0}^{\mathcal{N}} F(x_k) \left(w_k \sum_{j=0}^{\mathcal{N}} \frac{u_j(x_k)}{(u_j, u_j)} u_j(x) \right). \tag{3.30}$$

Expressions for the derivatives of $F(x)$ can then be obtained through differentiation of Eq. (3.30). For example, suppose we wish to approximate the second derivative of $F(x)$ at the point $x = x_a$. Here we could use an $(\mathcal{N} + 1)$-point central finite difference

scheme evaluated around the point $x_a = x_{\mathcal{N}/2}$. This scheme would use the value of the function at the discrete set of points $x_0, \ldots, x_{\mathcal{N}}$, where $\mathcal{N}$ is even. As an example, in the work described in this thesis, we use a 9-point central finite difference rule, meaning $\mathcal{N} = 8$. The central difference approximation to the second derivative can be found by differentiating Eq. (3.30), and evaluating the resulting equation at the midpoint, $x_{\mathcal{N}/2}$, giving

$$F''(x_{\mathcal{N}/2}) = \sum_{k=0}^{\mathcal{N}} F(x_k) \left(w_k \sum_{j=0}^{\mathcal{N}} \frac{u_j(x_k)}{(u_j, u_j)} u_j''(x_k) \right) = \sum_{k=0}^{\mathcal{N}} d_2^{(\mathcal{N})}(x_k) F(x_k). \tag{3.31}$$

In Eq. (3.31) the summations are taken over the complete set of $(\mathcal{N}+1)$ discrete orthogonal polynomials defined over $(\mathcal{N}+1)$ points. A sum of $(\mathcal{N}+1)$ orthogonal polynomials is an interpolating approximation, and so the coefficients $d_2^{(\mathcal{N})}(x_k)$ as defined in Eq. (3.31) are simply the standard central difference coefficients that one would obtain from a Taylor expansion [241, 242]. If instead, the summation is truncated to fewer than $(\mathcal{N}+1)$ polynomials, the result is a least-squares fit to the $(\mathcal{N}+1)$ points. By truncating the summation such that the highest-order polynomials are neglected, we can suppress the highest frequency components of $f(x)$. This approach, introduced by Parker [243], of truncating the summation in Eq. (3.31) at order $\mathcal{M} < \mathcal{N}$ results in a set of finite difference coefficients defined by

$$d_2^{(\mathcal{M})}(x_k) = w_k \sum_{j=0}^{\mathcal{M}} \frac{u_j(x_k)}{(u_j, u_j)} u_j''(x_k). \tag{3.32}$$

Comparisons of the eigenvalues calculated using a normal 9-point finite difference rule (i.e., Eq. (3.31) with $\mathcal{N} = 8$) with those calculated using a least-squares approximation (i.e., Eq. (3.32) with $\mathcal{M} = 7$) show that while the lowest eigenvalues for both cases agree, the maximum eigenvalue supported by the grid in the least-squares case is reduced. An example of these differences between eigenvalues calculated with $\mathcal{N} = 8$ and $\mathcal{N} = 7$, as well as between eigenvalues calculated on standard and scaled grids, is shown in Fig. 3.2 for the one-dimensional model Hamiltonian

$$H_{\text{model}} = -\frac{1}{2}\frac{\mathrm{d}^2}{\mathrm{d}x^2} - \frac{1}{\sqrt{x^2 + a}} \tag{3.33}$$

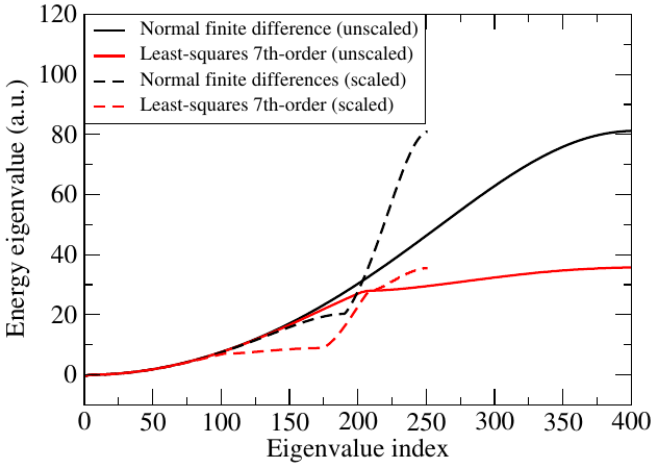

Figure 3.2: Eigenvalues of the one-dimensional Hamiltonian defined in Eq. (3.33), where the softcore parameter has been set to $a = 2.0$ to reproduce the ground state energy of the hydrogen atom (-0.5 Ha). Four cases are considered, using either the scaled or unscaled grids described in Section 3.2.1, and either the normal finite difference or least-squares finite difference methods. In the normal finite difference method, a 9-point finite difference rule is used (i.e., coefficients given by Eq. (3.31) with $\mathcal{N} = 8$). In the least-squares finite difference method, the function is approximated with a 7th-order polynomial (i.e., coefficients given by Eq. (3.32) with $\mathcal{M} = 7$).

where a is a softcore parameter that prevents singularities on the grid ($a = 2.0$ in this case). Here we see that, since the grid extent is the same in both scaled and unscaled grids, the number of grid points, and therefore the number of eigenvalues, is smaller when the scaled grid is used. However the maximum eigenvalue is the same in both scaled and unscaled grids. Comparing the normal finite difference and least-squares cases, we see that while the lowest eigenvalues are identical between the two cases, the maximum eigenvalue supported by the grid is reduced when the least-squares approximation is used, as desired.

In the work presented in Chapter 5, we use this least-squares approximation, with finite difference coefficients defined by Eq. (3.32) with $\mathcal{M} = 7$ (instead of $\mathcal{N} = 8$ that would reproduce the standard finite difference coefficients).

3.2.3 Calculation of the Hartree potential

The Hartree potential

$$V_{\mathrm{H}}(\boldsymbol{r}, t) = \int \frac{n(\boldsymbol{r}', t)}{|\boldsymbol{r} - \boldsymbol{r}'|} \mathrm{d}\boldsymbol{r}' \tag{3.34}$$

is the classical electrostatic potential due to the charge distribution $n(\boldsymbol{r},t)$. Evaluating this integral directly is computationally demanding, and becomes impractical for large grids. Therefore, we instead obtain $V_{\mathrm{H}}(\boldsymbol{r},t)$ by solving the corresponding Poisson equation

$$\nabla^2 V_{\mathrm{H}}(\boldsymbol{r},t) = -4\pi n(\boldsymbol{r},t). \tag{3.35}$$

As described previously for applying the Laplacian to the Kohn-Sham orbitals, we transform the Hartree potential as

$$V_{\mathrm{H}}(\boldsymbol{r},t) \rightarrow \frac{1}{\sqrt{|J|}} V_{\mathrm{H}}(\boldsymbol{r},t), \tag{3.36}$$

so that Eq. (3.35) can be rewritten as

$$\left[\frac{1}{\sqrt{f'}}\frac{\partial}{\partial x}\left(\frac{1}{f'}\right)\frac{\partial}{\partial x}\frac{1}{\sqrt{f'}} + \frac{1}{\sqrt{g'}}\frac{\partial}{\partial y}\left(\frac{1}{g'}\right)\frac{\partial}{\partial y}\frac{1}{\sqrt{g'}} + \frac{1}{\sqrt{h'}}\frac{\partial}{\partial z}\left(\frac{1}{h'}\right)\frac{\partial}{\partial z}\frac{1}{\sqrt{h'}}\right] V_{\mathrm{H}}(\boldsymbol{r},t) = -4\pi\sqrt{|J|}\, n(\boldsymbol{r},t). \tag{3.37}$$

This equation is then solved using a conjugate-gradient method on the finite difference grid. Since the systems in EDAMAME are non-periodic, it is necessary to impose some boundary conditions on the system. In the work presented in this thesis, two different boundary condition methods have been used, both involving a multipole expansion of the charge distribution. In the first of these methods, used for the work presented in Chapter 4, a single multipole expansion is taken around the centre of both the grid and the molecule (i.e., the origin). In the second method, used for the work presented in Chapter 5, the multicentre nature of the molecule is taken into account by taking multipole expansions of a number of charge distributions, each centred around the position of one of the N_n nuclei. This method is known as the fuzzy cell decomposition and multipole expansion method, and involves setting up Voronoi polyhedra to partition the grid and density into parts associated with each ion. Both of these methods are described in more detail in chapter 2 of [242].

3.2.4 Pseudopotential description of the electron-ion interactions

The external potential in Eq. (3.1), $V_{\mathrm{ext}}(\boldsymbol{r},\boldsymbol{R},t)$, accounts for both the Coulomb interaction between the electrons and the ions, $V_{\mathrm{ions}}(\boldsymbol{r},\boldsymbol{R},t)$, and the interaction between

the applied laser field and the electrons, $U_{\text{elec}}(\boldsymbol{r}, t)$, i.e.,

$$V_{\text{ext}}(\boldsymbol{r}, \boldsymbol{R}, t) = V_{\text{ions}}(\boldsymbol{r}, \boldsymbol{R}, t) + U_{\text{elec}}(\boldsymbol{r}, t). \tag{3.38}$$

These two terms will be dealt with in turn in this and the following subsection, beginning with $V_{\text{ions}}(\boldsymbol{r}, \boldsymbol{R}, t)$. EDAMAME employs the use of psuedopotentials to treat this term, as described below.

Describing the dynamics of an atomic or molecular system in principle requires the explicit treatment of all the electrons in the system. However, close to each ion the potential felt by the core electrons can be extremely steep. This would therefore require a very high density of gridpoints to accurately describe the rapidly oscillating wavefunction in this region. Considering the wavelengths of the laser pulses considered in this work however, we expect that the laser field will couple predominantly with the valence electrons, and that the core electrons will play little to no part in the laser-molecule interaction. In this case, it can be reasonable to replace the (all-electron) Coulomb potentials with pseudopotentials. Using these effective potentials has the effect of replacing the all-electron wavefunctions with pseudo-wavefunctions, which are identical to the true wavefunctions beyond some cut-off radius, but do not have as many (or any) nodes within the core region.

There are various forms that pseudopotentials can take. “Norm-conserving” pseudopotentials are one of the most commonly used forms, and it is these that are used in EDAMAME. Pseudopotentials of this type are constructed so as to satisfy four criteria:

1. The valence all-electron and pseudopotential eigenvalues must be equal;
2. The pseudo-wavefunctions should contain no nodes;
3. Beyond a given cut-off radius, the normalized radial pseudo-wavefunction with angular momentum l should be identical to the corresponding normalized radial all-electron wavefunction;
4. Within the cut-off radius, the norm of the pseudo- and all-electron wavefunctions should be equal (i.e., the charge inside the cut-off region should be equivalent in both cases).

The particular scheme used for generating the pseudopotentials used in EDAMAME, namely that of Troullier and Martins [244], sets a number of additional conditions, namely that the pseudo-wavefunction and its first four derivatives should be continuous at the cut-off radius, and that the screened pseudopotential should have zero curvature at the origin.

Norm-conserving pseudopotentials are non-local, meaning that the potential is different for each angular momentum (l) state. In 1982 however, Kleinman and Bylander showed that a non-local pseudopotential can be recast into a separable, fully non-local form [245]. Use of this form rather than a non-separable form requires significantly less computation, and as such is the form used in EDAMAME.

EDAMAME allows the core (1s) electrons in a molecule to be frozen through the use of norm-conserving Troullier-Martins pseudopotentials [244], implemented in their fully-separable Kleinman-Bylander form [245], so that V_{ions} can be written as

$$V_{\text{ions}}(\boldsymbol{r},\boldsymbol{R},t) = \sum_{K=1}^{N_n}\Bigg[V_{K,\text{ps}}^{l_{\text{loc}}}(\boldsymbol{x}_K) + \sum_{\substack{l=0\\ l\neq l_{\text{loc}}}}\sum_{m=-l}^{l}\frac{|\Delta V_{K,\text{ps}}^{l}(\boldsymbol{x}_K)\chi_{lm}^{K}(\boldsymbol{x}_K)\rangle\,\langle\Delta V_{K,\text{ps}}^{l}(\boldsymbol{x}_K)\chi_{lm}^{K}(\boldsymbol{x}_K)|}{\langle\chi_{lm}^{K}(\boldsymbol{x}_K)|\,\Delta V_{K,\text{ps}}^{l}(\boldsymbol{x}_K)\,|\chi_{lm}^{K}(\boldsymbol{x}_K)\rangle}\Bigg], \tag{3.39}$$

where l is the orbital angular momentum quantum number, m is the magnetic quantum number, $V_{K,\text{ps}}^{l_{\text{loc}}}(\boldsymbol{x}_K)$ and $\Delta V_{K,\text{ps}}^{l}(\boldsymbol{x}_K)$ are the local and non-local components respectively of the pseudopotential of ion K, $\chi_{lm}^{K}(\boldsymbol{x}_K)$ is the pseudo-wavefunction for the partial wave $|lm\rangle$, and $\boldsymbol{x}_K = \boldsymbol{r} - \boldsymbol{R}_K$. The non-local components are defined as

$$\Delta V_{K,\text{ps}}^{l}(\boldsymbol{x}_K) = V_{K,\text{ps}}^{l}(\boldsymbol{x}_K) - V_{K,\text{ps}}^{l_{\text{loc}}}(\boldsymbol{x}_K), \tag{3.40}$$

where $V_{K,\text{ps}}^{l}(\boldsymbol{x}_K)$ is the l angular momentum component of the non-local pseudopotential for ion K. The force acting on ion K due to this non-local pseudopotential is given by [220, 246]

$$\boldsymbol{F}_K = \int n(\boldsymbol{r})\boldsymbol{\nabla}V_{K,\text{ps}}^{l_{\text{loc}}}(\boldsymbol{x}_K)\mathrm{d}\boldsymbol{r} + \sum_{j=1}^{N}\sum_{\substack{l=0\\ l\neq l_{\text{loc}}}}\sum_{m=-l}^{l}\left(\frac{B_{lm}^{jK}}{A_{lm}^{K}}\right)\boldsymbol{\nabla}B_{lm}^{jK}, \tag{3.41}$$

where

$$A_{lm}^{K} = \langle \chi_{lm}^{K}(\boldsymbol{x}_K) | \, \Delta V_{K,\text{ps}}^{l}(\boldsymbol{x}_K) \, | \chi_{lm}^{K}(\boldsymbol{x}_K) \rangle \, , \tag{3.42}$$

and

$$B_{lm}^{jK} = \langle \Delta V_{K,\text{ps}}^{l}(\boldsymbol{x}_K) \chi_{lm}^{K}(\boldsymbol{x}_K) | \psi_j(\boldsymbol{r},t) \rangle \, . \tag{3.43}$$

The pseudopotentials used in EDAMAME were generated using the Atomic Pseudopotential Engine (APE) [247].

3.2.5 Laser interaction potential

The second contribution to the external potential, Eq. (3.38), is the interaction between the electrons and the applied laser field, $U_{\text{elec}}(\boldsymbol{r},t)$. In Section 2.5 it was shown how an applied laser pulse can be introduced to our calculations by describing it as a classical radiation field, resulting in a semiclassical treatment of the laser-molecule interaction. Specifically, in Eq. (2.69) we obtained an expression for the electron-laser interaction potential, $U_{\text{elec}}(\boldsymbol{r},t)$, namely

$$U_{\text{elec}}(\boldsymbol{r},t) = \boldsymbol{r} \cdot \boldsymbol{E}(t). \tag{3.44}$$

In EDAMAME, the exact form of the laser field comes from the definition of the vector potential, $\boldsymbol{A}(t)$, which for the linearly polarized pulses considered in this thesis is

$$\boldsymbol{A}(t) = A_0 f(t) \cos(\omega_L t + \phi) \hat{\boldsymbol{e}}_k, \tag{3.45}$$

where A_0 is the peak value of the vector potential, ω_L is the laser frequency, ϕ is the carrier-envelope phase, $f(t)$ is the pulse envelope, and $k = x, y, z$. A $\sin^2$ pulse envelope is used, i.e.,

$$f(t) = \begin{cases} \sin^2\left(\dfrac{\pi t}{T}\right) & \text{for } \; 0 \leq t \leq T, \\ 0 & \text{otherwise.} \end{cases} \tag{3.46}$$

The electric field vector is then obtained through the derivative of $\boldsymbol{A}(t)$

$$\boldsymbol{E}(t) = -\frac{\partial}{\partial t} \boldsymbol{A}(t). \tag{3.47}$$

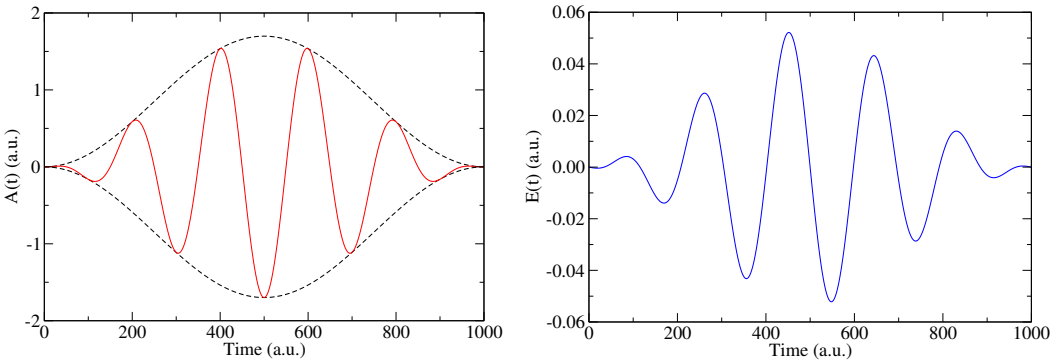

(a) A-field (b) E-field

Figure 3.3: Typical temporal profile of laser pulses used in EDAMAME calculations. In (a) the vector potential, $\boldsymbol{A}(t)$, is plotted along with the pulse envelope (dashed line), while the electric field vector, $\boldsymbol{E}(t)$, is plotted in (b). These plots correspond to a laser pulse with wavelength $\lambda = 1450\,\text{nm}$, peak intensity $1.0\times10^{14}\,\text{W/cm}^2$, and a duration of 5 cycles.

For all the calculations presented in this work, the carrier-envelope phase, ϕ, is set to zero, and so $\boldsymbol{E}(t)$ can be written as

$$\boldsymbol{E}(t) = \left[E_0 f(t)\sin(\omega_L t) - \frac{E_0}{\omega_L}\frac{\partial f}{\partial t}\cos(\omega_L t)\right]\hat{\boldsymbol{e}}_k. \tag{3.48}$$

The peak electric field strength in atomic units, E_0, is related to the peak intensity of the field in W/cm^2, I_0, through

$$E_0 = \sqrt{\frac{I_0}{I_{\text{au}}}}, \tag{3.49}$$

where I_{au} is the atomic unit of intensity, $I_{\text{au}} = 3.51\times10^{16}\,\text{W/cm}^2$. Figures 3.3(a) and 3.3(b) respectively show typical A-field and E-field profiles. In calculations in which two pulses are applied, each individual pulse will have the profile defined by the above equations, with the overall applied field then simply a sum of the two pulses, taking account of any chosen delay time between the two pulses.

3.2.6 Exchange-correlation potential

As discussed in Section 2.3.3, the exact form of the exchange-correlation potential, $V_{\text{xc}}(\boldsymbol{r},t)$, is unknown, and must be approximated. In EDAMAME, $V_{\text{xc}}(\boldsymbol{r},t)$ is described in the adiabatic local density approximation (ALDA), incorporating the Perdew-Wang parameterization of the correlation functional [176], and supplemented by the average-density self-interaction-correction (ADSIC) [182, 186]. A brief discussion around the

merits and failings of these approximations was previously given in Section 2.3.3, and will not be repeated here. The exchange and correlation components of the LDA potential, $V_{\text{xc}}^{\text{LDA}}(\boldsymbol{r},t)$, are treated separately, with the exchange component defined from the analytical form of the exchange-only energy of a homogeneous electron gas, Eqs. (2.24)–(2.25), as

$$V_{\text{x}}^{\text{LDA}}(\boldsymbol{r},t) = -\left(\frac{6}{\pi}\right)^{1/3} n^{1/3}(\boldsymbol{r},t). \tag{3.50}$$

Since analytical forms of the correlation part of the energy of a homogenous electron gas are only available in the high- and low-density limits, for $V_{\text{c}}^{\text{LDA}}(\boldsymbol{r},t)$ we use the parameterization of Perdew and Wang, given in [176].

To correct the self-interaction errors inherent in LDA, $V_{\text{xc}}^{\text{LDA}}(\boldsymbol{r},t)$ is supplemented by the average-density self-interaction-correction [182, 186], which we write as

$$V^{\text{ADSIC}}(\boldsymbol{r},t) = \int \frac{n(\boldsymbol{r}',t)/P(t)}{|\boldsymbol{r}-\boldsymbol{r}'|}\mathrm{d}\boldsymbol{r}' + \frac{\delta E_{\text{xc}}^{\text{LDA}}[n(\boldsymbol{r},t)/P(t)]}{\delta n(\boldsymbol{r},t)}, \tag{3.51}$$

where $P(t)$ is the total electronic population contained in the grid at time t. This is given simply by

$$P(t) = \int_V n(\boldsymbol{r},t)\mathrm{d}\boldsymbol{r}, \tag{3.52}$$

where the volume V is the total volume of the grid, such that $P(t) = 2N = N_e$ for $t = 0$, but where we may have that $P(t) < N_e$ for $t > 0$ in the presence of an applied field, due to the effect of the absorbing boundaries (see Section 3.2.9). The total form of the exchange-correlation potential is then given by

$$V_{\text{xc}}(\boldsymbol{r},t) = V_{\text{x}}^{\text{LDA}}(\boldsymbol{r},t) + V_{\text{c}}^{\text{LDA}}(\boldsymbol{r},t) - V^{\text{ADSIC}}(\boldsymbol{r},t). \tag{3.53}$$

3.2.7 Calculation of the initial state

With all the terms in Eq. (3.1) defined in the previous subsections, we now turn to the solution of the TDKS equations. The first step in an EDAMAME simulation is the calculation of the initial state of the system. For a given geometry, the initial state of the system is assumed to be the ground electronic state. Changing the geometry of the system will of course change the calculated ground state; Section 3.3.2 will describe how the geometry of a system can be relaxed using EDAMAME in order to calculate the

equilibrium geometry for the ground state.

The calculation of the initial state requires the self-consistent solution of the time-independent Kohn-Sham equations

$$H_{\text{KS}}\psi_j(\boldsymbol{r}) = E_j\psi_j(\boldsymbol{r}), \qquad j = 1, \ldots, N, \tag{3.54}$$

where H_{KS} is the Kohn-Sham Hamiltonian and E_j is the eigenstate energy of Kohn-Sham orbital $\psi_j(\boldsymbol{r})$.

Calculating the Kohn-Sham eigenpairs at every self-consistent cycle can create a bottleneck in the calculation of the ground state. To avoid this, we employ the Chebyshev filtered subspace iteration (CheFSI) method proposed by Zhou *et al.* [248, 249]. By emphasising the importance of eigenspaces rather than eigenpairs, this method removes the need to solve the eigenvalue problem at every self-consistent iteration. The CheFSI method is based on the fact that the electronic density $n(\boldsymbol{r}, t)$ can be calculated from the diagonal of the density matrix, Π, which is given by

$$\Pi = \Phi\Phi^{\dagger}, \tag{3.55}$$

where Φ is the matrix whose columns are the occupied Kohn-Sham orbitals. For any orthonormal matrix U of suitable dimension, we can write

$$\Pi = (\Phi U)(\Phi U)^{\dagger}, \tag{3.56}$$

which means that explicit eigenvectors are not required to calculate the density in Eq. (3.2); any orthonormal basis of the eigenspace corresponding to the occupied Kohn-Sham states will do [248]. In order to find this eigenspace, the Kohn-Sham Hamiltonian, H_{KS}, is used to create a Chebyshev filter of order m, $p_m(H_{\text{KS}})$. Chebyshev polynomials are chosen because they grow rapidly outside of the interval [-1,1]. By mapping only the unwanted part of the spectrum of the Hamiltonian into the interval [-1,1], these unwanted parts of the spectrum can be damped. Therefore, by iteratively applying this filter to the basis of Kohn-Sham orbitals, i.e, computing $p_m(H_{\text{KS}})\Phi$, one can obtain successively better approximations to the eigenspace of the occupied Kohn-Sham states. Once self-consistency is reached, the filtered subspace includes the

eigensubspace corresponding to the occupied states, and explicit eigenvectors can be obtained by a Rayleigh-Ritz refinement (subspace rotation) step [249].

Using the CheFSI method, the self-consistent solution to Eq. (3.54) is therefore obtained through the following procedure:

1. Get initial guess for Kohn-Sham orbitals $\psi_j(\boldsymbol{r})$, choosing a random vector for each orbital and then orthonormalising the set;
2. Calculate charge density $n(\boldsymbol{r})$, by Eq. (3.2);
3. Calculate effective potential $V_{\text{KS}}(\boldsymbol{r})$, as defined in Eq. (3.1);
4. Calculate new guess for Kohn-Sham orbitals. This is taken to be either a set of random orthonormal vectors, or the eigenvectors obtained from a single application of the Thick-Restart Lanczos method implemented in the TRLan library [250] to solve the time-independent Kohn-Sham equations, Eq. (3.54);
5. Calculate new charge density $\nu(\boldsymbol{r})$, again, by Eq. (3.2);
6. If convergence criteria $|\nu(\boldsymbol{r})$ - $n(\boldsymbol{r})| < \epsilon$ is satisfied:
   - Ground state calculated; stop.

   Else if convergence criteria not satisfied:
   - Mix densities;
   - Calculate new effective potential $V_{\text{KS}}(\boldsymbol{r})$, again, by Eq. (3.1);
   - Perform Chebyshev subspace iteration;
   - Go back to step 5;

Comparisons of the ground state obtained using the two methods for calculating an initial approximation to the eigenspace given in step 4 show good agreement. When the calculations presented in Chapter 4 were performed, the TRLan method was used for step 4. This was subsequently found to be slightly slower than using a set of random orthonormal vectors, and so the results presented in Chapter 5 are from calculations using random orthonormal vectors.

3.2.8 Time propagation

Once the initial state of the system is determined, the state at later times is determined by applying the unitary time evolution operator, $U(t+\Delta t)$, to the Kohn-Sham orbitals, so that ψ_j at time $t+\Delta t$ is given by

$$\psi_j(\boldsymbol{r}, t+\Delta t) = U(t+\Delta t)\psi_j(\boldsymbol{r}, t). \tag{3.57}$$

For $\Delta t \to 0$, this operator may be approximated as

$$U(t+\Delta t) \approx e^{-iH_{\text{KS}}\Delta t}. \tag{3.58}$$

Evaluating this exponential directly is impractical for the large Kohn-Sham Hamiltonian matrices of typical practical interest; instead iterative methods are generally used [251]. In EDAMAME we employ the unitary nth-order Arnoldi propagator [252, 253]. This is an explicit propagator based on successive operations of H_{KS} upon the Kohn-Sham orbitals. We begin by constructing a set of orthonormal vectors that span the Krylov subspace K_{m+1}

$$K_{m+1}(H_{\text{KS}}, \psi_j) = \{\psi_j, H_{\text{KS}}\psi_j, H_{\text{KS}}^2\psi_j, \ldots, H_{\text{KS}}^m\psi_j\}. \tag{3.59}$$

Gram-Schmidt orthonormalisation is then used to construct a set of $(m+1)$ orthonormal vectors, $[q_0, q_1, \ldots, q_m]$, that span the subspace K_{m+1}. Using these vectors to form the columns of matrix Q, we can write the Krylov subspace Hamiltonian, h, as

$$h = Q^\dagger H_{\text{KS}} Q. \tag{3.60}$$

We can then replace H_{KS} in the time evolution operator with the approximation

$$H_{\text{KS}} \approx \tilde{H}_{\text{KS}} = QhQ^\dagger, \tag{3.61}$$

The time evolution operator is therefore approximated as

$$U(t+\Delta t) \approx \tilde{U}(t+\Delta t) = e^{-i\tilde{H}_{\text{KS}}\Delta t} = Qe^{-ih\Delta t}Q^\dagger, \tag{3.62}$$

where we have used the fact that $(QhQ^\dagger)^m = Qh^mQ^\dagger$ to bring Q and $Q^\dagger$ outside of the exponentiation. Since the Krylov subspace Hamiltonian, h, is much smaller than the Kohn-Sham Hamiltonian, H_{KS}, and is a tridiagonal matrix (if H_{KS} is Hermitian), the exponential $e^{-ih\Delta t}$ can then be inexpensively evaluated through direct diagonalization of h. This unitary propagator $\tilde{U}(t + \Delta t)$ will be correct to order m in Δt [219]. One advantage of the Arnoldi propagator is that it permits the use of larger values of Δt compared to other propagators, such as the Taylor series propagator [251]. In the work described in this thesis, converged solutions are obtained using an 18th-order Arnoldi propagator with a time step of $\Delta t = 0.2$ a.u. (using the unscaled grid and normal finite difference method for the work presented in Chapter 4, and the scaled grid and least-squares finite difference method for the work presented in Chapter 5).

3.2.9 Absorbing boundaries

At the beginning of a calculation, the molecule under investigation will typically be located with its centre of mass at the centre of the grid, with the majority of the electronic density in close proximity. As a simulation in which a strong laser field applied progresses however, ionized electronic wavepackets can propagate far from the centre of the grid towards the edges. Upon reaching the grid boundary, these wavepackets could be reflected back and return to the centre, interfering with the molecule and the remaining electronic density in an unphysical manner. To prevent these reflections, absorbing boundaries are employed near the edges of the grid. This absorption is performed by applying a mask function, $M(\boldsymbol{r})$ which splits each Kohn-Sham orbital $\psi_j(\boldsymbol{r}, t)$ in to two parts:

$$\psi_j(\boldsymbol{r}, t) = M(\boldsymbol{r})\psi_j(\boldsymbol{r}, t) + [1 - M(\boldsymbol{r})]\psi_j(\boldsymbol{r}, t). \tag{3.63}$$

The first term here represents the non-ionized wavepackets which have remained near the centre of the grid, while the second term is associated with those wavepackets that have been ionized and are propagating far away from the molecule. Each time the mask function is applied, only the first term (the non-ionized parts of the wavefunction) is carried forward in the calculation. Discarding the second term of the above equation in this manner has the effect of reducing the electronic population in each Kohn-Sham orbital over time; this can be used as a measure of the amount of ionization occuring over time, as will be described in Section 3.5.1.

The exact form that the mask function should take is an important factor: it should decrease slowly enough towards the edges of the grid that reflections are kept to a minimum, but quickly enough that a very large absorbing region isn't required to ensure that the wavepackets are absorbed before reaching the edge of the grid.

The mask function is expressed in terms of independent functions in the x, y and z coordinates as

$$M(\boldsymbol{r}) = M_x(x)M_y(y)M_z(z). \tag{3.64}$$

Considering the x component of the mask function separately, it can be written as

$$M_x(x) = \begin{cases} 1 & |x| \leq x_m, \\ 1 - (1 - M_{\text{edge}})\dfrac{(|x| - x_m)^5}{(x_{\text{max}} - x_m)^5} & |x| > x_m, \end{cases} \tag{3.65}$$

where x_{max} is the maximum extent of the grid along the x coordinate, x_m is the point along the x coordinate where the absorbing boundary begins, and M_{edge} is the value chosen for the mask function at the edges of the grid (i.e., $M_{\text{edge}} = M_x(x_{\text{max}})$). The x component of a typical mask function used in the work described in this thesis is shown in Fig. 3.4. The y and z components of the mask function, $M_y(y)$ and $M_z(z)$, have similar forms to $M_x(x)$, although the grid extents and absorption start points can be different to those for the x coordinate.

3.2.10 Summary

In this section we have described how the TDKS equations are discretised on a finite difference grid and subsequently solved in EDAMAME. Each term in the Kohn-Sham Hamiltonian was discussed individually, followed by the techniques used to calculate the initial state of the system and how this is then propagated in time. In the next section we will see how the ionic equations of motion, Eq. (2.41), are described in EDAMAME.

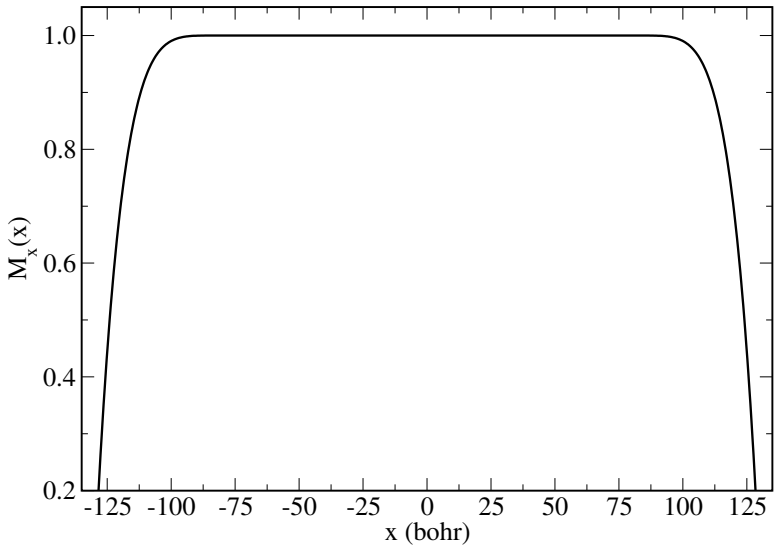

Figure 3.4: Example of the form of the mask function described by Eq. (3.65). $M_x(x)$ is plotted here for a grid with maximum extent in the x direction of $|x| = 128.4\,\mathrm{a_0}$, and where absorption begins at $\pm 80.0\,\mathrm{a_0}$, with a final $M_x(x)$ value of $M_{\mathrm{edge}} = 0.2$.

3.3 Ionic dynamics

In Section 2.4 in the previous chapter it was shown how a classical description of ionic motion could be combined with a quantum treatment of electronic dynamics in a quantum-classical molecular dynamics approach. This method has been implemented in EDAMAME, and enables calculations to be run with all ions free to move, all ions fixed in place, or a mixture of fixed and free ions. Unless otherwise specified, all the EDAMAME results presented in this thesis are from calculations where all the ions are free to move.

The dynamics of the ions during a simulation are calculated classically using Newton's equations of motion. For ion K we have

$$M_K \ddot{\boldsymbol{R}}_K = -\int \Big(n(\boldsymbol{r},t) \boldsymbol{\nabla}_K H_{\mathrm{KS}} \Big) \mathrm{d}\boldsymbol{r} - \boldsymbol{\nabla}_K \Big(V_{nn}(\boldsymbol{R}) + Z_K \boldsymbol{R}_K \cdot \boldsymbol{E}(t) \Big), \tag{3.66}$$

where $\boldsymbol{\nabla}_K$ is the gradient operator with respect to the ionic coordinates of ion K, $V_{nn}(\boldsymbol{R})$ is the Coulomb repulsion between the ions

$$V_{nn}(\boldsymbol{R}) = \frac{1}{2} \sum_{K=1}^{N_n} \sum_{\substack{L=1 \\ L \neq K}}^{N_n} \frac{Z_K Z_L}{|\boldsymbol{R}_K - \boldsymbol{R}_L|}, \tag{3.67}$$

and $Z_K \boldsymbol{R}_K \cdot \boldsymbol{E}(t)$ denotes the interaction between ion K and the laser field.

3.3.1 Time propagation

To propagate the classical ionic equations of motion in time, we use the velocity-Verlet algorithm [254]. With this algorithm, the position and velocity of ion K are evolved according to

$$\begin{aligned} \boldsymbol{R}_K(t+\Delta T) &= \boldsymbol{R}_K(t) + \dot{\boldsymbol{R}}_K(t)\Delta T + \frac{1}{2}\ddot{\boldsymbol{R}}_K(t)(\Delta T)^2, \\ \dot{\boldsymbol{R}}_K(t+\Delta T) &= \dot{\boldsymbol{R}}_K(t) + \frac{\ddot{\boldsymbol{R}}_K(t) + \ddot{\boldsymbol{R}}_K(t+\Delta T)}{2}\Delta T, \end{aligned} \tag{3.68}$$

where $\ddot{\boldsymbol{R}}_K(t)$ is given by Eq. (3.66) above. Note that the time step here for the ions, ΔT, need not be the same as the time step for the electrons, Δt (Section 3.2.8).

3.3.2 Geometry relaxation

The relaxed geometry of a molecule in its ground state will depend upon various numerical factors specific to the code used, including the choice of exchange-correlation potential approximation, the grid spacings, and the pseudopotentials. Therefore, before a molecule can be studied using EDAMAME, a geometry optimization is required in order to find the relaxed geometry specific to EDAMAME with the chosen calculation parameters.

Geometry relaxations for the systems studied in this work follow a simple relaxation scheme involving propagation in real time, based upon the idea of the variation in kinetic energy throughout the motion of a swinging pendulum. In a simple pendulum, the kinetic energy is greatest when the pendulum is passing through its equilibrium position, and zero when the pendulum is at a turning point. The geometry relaxation scheme in EDAMAME follows a similar logic. An initial guess of the ground state geometry is taken from experimental or other computational works, for example, from the NIST Chemistry WebBook [255]. Then, after calculating the initial state of the system (Section 3.2.7), the system is allowed to evolve in time with no external field applied, until the total kinetic energy of the ions reaches a maximum value. The geometry at this point is assumed to be a closer approximation to the relaxed ground state geometry,

and is used as input for a new geometry relaxation. These calculations are performed iteratively until the kinetic energy is reduced to an sufficiently low level, and the ions are effectively stationary (in the absence of an external field) over the duration of a typical calculation.

In previous versions of EDAMAME (as described in [220], for example), geometry optimization was performed using a quasi-Newton method known as the limited-memory BFGS (L-BFGS) algorithm [256]. However, previous studies using EDAMAME encountered a number of problems in trying to achieve convergence with this approach. The alternative approach described above was suggested for use in EDAMAME by researchers from Université Paul Sabatier in Toulouse, based on their experience working with this approach in their code, TELEMAN. As this is a somewhat unusual geometry optimization method however, it is unclear, for example, how well this approach will work for very large systems. As such, future work with EDAMAME should include more testing of the range of validity of this optimization technique, including how this approach compares (in terms of both accuracy and efficiency) with more common methods such as steepest decent or conjugate gradient. It would also be interesting to investigate the convergence behaviour of the L-BFGS approach when used with the recently implemented coordinate scaling and least-squares finite difference techniques described in Sections 3.2.1 and 3.2.2.

3.3.3 Summary

In this section we have outlined how the classical equations of motion for the nuclei are implemented in EDAMAME, and how the equilibrium geometry of a system can be calculated using a simple geometry relaxation scheme.

3.4 Parallelization

Solving the Kohn-Sham equations for molecules interacting with strong laser fields requires large grid extents in order to contain the ionizing wavepackets as they propagate in the field. For this reason it is necessary to parallelize the code so that the full finite difference grid is distributed over a number of processors. With this domain decomposition approach, each processor stores all the Kohn-Sham orbitals for a small spatial

region, and communication between processors is required when calculating the kinetic energy terms (using the central finite difference formulae described above) or calculating observables that require a summation over the full grid (e.g., ionization, as described in Section 3.5.1).

An alternative strategy for parallelizing the computation would be to parallelize over Kohn-Sham orbitals, i.e., each processor only stores a single Kohn-Sham orbital, but over the full grid extent. While this strategy has advantages in certain applications, for the typical work done with EDAMAME, it would have two main disadvantages. Firstly, a given system will only have a relatively small number of Kohn-Sham orbitals (e.g., fewer than 50 orbitals for the systems typically studied using EDAMAME). This would place an upper limit on the number of processors that could be used in a calculation where the parallelization was over Kohn-Sham orbitals (for comparison, in the work presented in this thesis, the number of Kohn-Sham orbitals never exceeds 35, whereas many of the calculations performed on ARCHER used over 3,500 cores). The second drawback of parallelizing over Kohn-Sham orbitals would arise during calculation of quantities that involve multiple orbtials, such as the density. In this case, whole orbitals would need to be transferred between processors, resulting in a large communication overhead. As we will see below, the communication required with spatial parallelization of the grid is substantially smaller.

The decomposition of the grid is carried out in each of the three spatial dimensions. The number of processors, N_k^{proc}, and the number of local points per processor, N_k^{loc}, can be varied for each dimension $k = x, y, z$, according to the size and shape of the molecule, and the parameters of any laser pulse involved in the calculation. The total number of gridpoints along dimension k is then simply given by $N_k = N_k^{\text{proc}} N_k^{\text{loc}}$, and the total number of processors by $N^{\text{proc}} = N_x^{\text{proc}} N_y^{\text{proc}} N_z^{\text{proc}}$.

The main communication overhead in EDAMAME is due to the application of the Laplacian operator. In order to calculate the derivatives using a $(2N_{\text{FD}} + 1)$-th order central finite difference formula, communication between neighbouring processors is required for points located near a boundary between processors. Since we are using central finite difference formulae, evaluating the derivatives of a function at any grid point requires the value of the function at the N_{FD} grid points to either side. Therefore, evaluating the

derivatives at a grid point at a processor boundary will require the communication of just N_{FD} grid points, since the other points required are local. In all cases described in this thesis, the number of points per processor is chosen to be large enough compared to the level of finite difference rule being used such that a given processor is never required to communicate with any processors other than its nearest neighbours.

3.5 Calculation of observables

In this section we will describe how several important observables are calculated in EDAMAME. In TDDFT, all observables are in principle defined as functionals of the electron density, $n(\boldsymbol{r}, t)$. However, the exact forms of the functionals for many observables are not known, and so these observables must be evaluated by other means.

3.5.1 Ionization

Ionization is one of the observables in TDDFT for which the exact form of the functional is unknown. For this reason measures of ionization in TDDFT are usually obtained using geometric properties of the time-dependent Kohn-Sham orbitals [192, 193]. In EDAMAME this is generally done through use of the mask function described in Section 3.2.9.

As well as preventing wavepacket reflections, use of the mask function near the edge of the grid also allows us to describe ionization from the system from geometric considerations. We define the (bound) electronic population of a Kohn-Sham orbital, ψ_j, at time t as

$$P_j(t) = 2\int_V |\psi_j(\boldsymbol{r}, t)|^2 \,\mathrm{d}\boldsymbol{r}, \qquad j = 1, \ldots, N, \tag{3.69}$$

where the volume V is the total volume of the grid, and the factor of two reflects the fact that we are neglecting spin effects as before (i.e., each orbital is initially doubly occupied). Then the total number of electrons contained in the grid at time t is

$$P(t) = \sum_{j=1}^{N} P_j(t) = 2\sum_{j=1}^{N}\int_V |\psi_j(\boldsymbol{r}, t)|^2 \,\mathrm{d}\boldsymbol{r} = \int_V n(\boldsymbol{r}, t)\mathrm{d}\boldsymbol{r}. \tag{3.70}$$

At time $t = 0$, $P(t) = 2N = N_e$, but as the calculation progresses, depending on the laser parameters and the specifics of the system, the norms of the Kohn-Sham orbitals

can decrease due to repeated applications of the mask function. This decrease of $P(t)$ over time can be considered a measure of the ionization of the system.

Equations (3.69) and (3.70) respectively define the orbital population and net population contained within the entire grid. On some occasions however, we may be more interested in the populations within a smaller region of the grid, for instance the volume around an atom or molecule. In this case we define the inner population in the same manner as the total populations defined above, but with the volume V now referring to the volume of a sphere of some chosen radius, centered at the origin of the grid.

3.5.2 High harmonic spectra

Calculation of HHG spectra is traditionally done by first calculating the time-dependent dipole moment of the system, $\boldsymbol{d}(t)$. However this is not the only approach: one could instead begin by calculating the dipole velocity, $\dot{\boldsymbol{d}}(t)$, or the dipole acceleration, $\ddot{\boldsymbol{d}}(t)$. The HHG spectrum is then calculated through a Fourier transform of the chosen dipole quantity. Several studies in recent years, for example [224, 237, 257], have compared the accuracy of using these three dipole quantities for computing the HHG spectra. The 2010 work by Han and Madsen [237] also compared the results obtained when the three forms were used in the length gauge and the velocity gauge. There they noted that while the forms of the dipole moment were identical in the length and velocity gauges, and similarly for the dipole acceleration, the forms of the dipole velocity were not.

Focusing on just the dipole and the dipole acceleration, the groups of Burnett *et al.* [257] and Bandrauk *et al.* [224] concluded that there were no significance differences (aside from a frequency scaling factor) between the results obtained using one dipole quantity or the other in the case of a long, weak laser pulse. This was not the case when a short, high intensity laser field was applied. In the strong-field case, where there is appreciable levels of ionization, non-zero final values of the dipole can result in increasing levels of background in the spectra obtained using from the dipole. For this reason, both groups conclude that use of the dipole acceleration rather than the dipole is a more robust method for calculating HHG spectra in the case of short, intense laser

fields.

This recommendation is followed in EDAMAME: the harmonic spectral density $S_k(\omega)$, along the direction $\hat{\boldsymbol{e}}_k$, is calculated as the squared magnitude of the Fourier transform of the dipole acceleration $\ddot{\boldsymbol{d}}(t)$

$$S_k(\omega) = \left| \int e^{i\omega t} \hat{\boldsymbol{e}}_k \cdot \ddot{\boldsymbol{d}}(t) \mathrm{d}t \right|^2, \tag{3.71}$$

where $k = x, y, z$, and where $\ddot{\boldsymbol{d}}(t)$ is calculated, via Ehrenfest's theorem, as

$$\begin{aligned} \ddot{\boldsymbol{d}}(t) &= \frac{d^2}{dt^2} \langle \boldsymbol{r} \rangle \\ &= -\int n(\boldsymbol{r}, t) \boldsymbol{\nabla} H_{\mathrm{KS}} \, \mathrm{d}\boldsymbol{r}. \end{aligned} \tag{3.72}$$

Rather than calculating the overall harmonic response, calculating the response for each individual Kohn-Sham orbital can also yield useful information [211]. The response for each orbital can be estimated by replacing the total dipole acceleration $\ddot{\boldsymbol{d}}(t)$ in Eq. (3.71) with the dipole acceleration for orbital j, $\ddot{\boldsymbol{d}}_j(t)$, calculated as

$$\begin{aligned} \ddot{\boldsymbol{d}}_j(t) &= -\int n_j(\boldsymbol{r}, t) \boldsymbol{\nabla} H_{\mathrm{KS}} \, \mathrm{d}\boldsymbol{r} \\ &= -2 \int |\psi_j(\boldsymbol{r}, t)|^2 \, \boldsymbol{\nabla} H_{\mathrm{KS}} \, \mathrm{d}\boldsymbol{r}, \qquad j = 1, \ldots, N. \end{aligned} \tag{3.73}$$

While this approach neglects interferences between different orbitals in the overall harmonic signal, it does give an indication of the contribution of that state to the overall harmonic response.

3.5.3 Time-frequency analysis

Equation (3.71) allows us to calculate the total harmonic response of a system to an applied field, but gives no information about the times at which different harmonics are emitted. In order to study HHG in more depth, we can retrieve this information by performing a time-frequency analysis (also known as a Gabor transformation). In this analysis, rather than Fourier transforming the entire dipole acceleration, we take a series of Fourier transforms of short time periods. This is done using Gaussian functions

as windows of the dipole acceleration

$$H_k(\omega, t) = \int_{-\infty}^{\infty} \left(e^{-(t-\tau)^2/\sigma^2} e^{-i\omega\tau} \hat{\boldsymbol{e}}_k \cdot \ddot{\boldsymbol{d}}(\tau) \right) \mathrm{d}\tau, \tag{3.74}$$

where $k = x, y, z$ as before, and where the parameter σ determines the width of the Gaussian window. This parameter is defined to be

$$\sigma = \frac{1}{3\omega_L}, \tag{3.75}$$

so that the Gaussian window has full width half maximum (FWHM) equal to 3 times the laser frequency.

3.5.4 Summary

In this section we have described how several important observables are calculated in EDAMAME. These observables will form the basis of much of the analysis of the results presented in Chapters 4 and 5.

3.6 Conclusions

In this chapter we have described the implementation of the quantum-classical molecular dynamics method in the Fortran2008 code EDAMAME. We began in Section 3.2 by describing how the TDKS equations are discretized and solved in EDAMAME. Discretizing the Kohn-Sham orbitals on a finite difference grid, parallelized over a large number of processors, allows us to efficiently simulate the large spatial extent required to accurately describe high harmonic generation. To describe molecules for which a high density of grid points is required around the nuclei, such as those studied in Chapter 5, a coordinate scaling has been implemented to allow a small grid spacing to be used close to the molecule while not drastically increasing the total number of gridpoints required. In Sections 3.2.2–3.2.6, the methods for calculating each of the terms in the Kohn-Sham Hamiltonian in EDAMAME were described. The remainder of Section 3.2 included a description of the Chebyshev filtering method used for calculating the initial state of the system, and the Arnoldi propagator used to propagate the Kohn-Sham orbitals in time.

Section 3.3 dealt with the implementation in EDAMAME of the classical equations of motion for the ions, describing how these are propagated in time, and how equilibrium ground state geometries of molecules are calculated. The parallelization scheme used in EDAMAME to allow the finite difference grid to be efficiently distributed across large numbers of processors was outlined in Section 3.4. Finally, in Section 3.5, we described how a number of observables quantities, such as ionization and harmonic generation, are calculated in EDAMAME.

In the remainder of this thesis we will present a series of results from calculations performed using EDAMAME: we begin in Chapter 4 by studying high harmonic generation in a small hydrocarbon molecule (acetylene), before moving on to study three molecules of biological relevance (uracil, thymine and 5-fluorouracil) in Chapter 5.

Chapter 4

High harmonic generation in acetylene and the role of excited states

---

4.1 Introduction

Acetylene, C_2H_2, also known as ethyne, is a small, linear, polyatomic molecule. It is one of the simplest hydrocarbons, and indeed is the simplest of the class of hydrocarbons known as alkynes (hydrocarbons with a C-C triple bond). For this reason it has historically been a useful molecule for both experimental and theoretical studies, helping to elucidate processes occurring in more complex hydrocarbons and biomolecules, or serving as a prototype for proof of concept demonstrations of new techniques [51, 258].

Related to acetylene's simple structure are two additional reasons for its popularity amongst experimentalists. Firstly, the majority of organic molecules and biomolecules are in the solid or liquid phase at room temperature [83], making them unsuitable for certain types of experiments, at least not without the addition of extra (sometimes complicated) experimental steps [57, 259]. Acetylene on the other hand, is readily (and cheaply) available in the gas phase at room temperature.

Secondly, due to its linear form and rigidity, acetylene is much more suitable for rotational alignment techniques [70] than other hydrocarbons and biomolecules [83]. This makes experimental studies of the kind of alignment-dependent effects presented in this chapter feasible.

In this chapter, we present results from a series of EDAMAME calculations studying the interaction of aligned acetylene molecules with mid infrared (mid-IR) laser pulses, with a particular focus on the high harmonic response. The chapter is arranged as follows. In Section 4.2 we provide a brief overview of previous experimental and theoretical work on acetylene. Our results begin in Section 4.3 with the ground state equilibrium properties of acetylene calculated using EDAMAME. Sections 4.4 and 4.5 present the main topic of interest in this chapter, namely the high harmonic spectra produced during the interaction of acetylene with a range of laser pulses. Finally, in Section 4.6, the effect of the motion of the ions is briefly addressed.

Unless otherwise specified, ionic motion is included in all the calculations described in this chapter (as discussed in Section 3.3). Some aspects of this work have previously been presented in [260] and [261].

4.2 Background

Acetylene is a linear molecule with equilibrium C-C and C-H bond lengths of 2.273 a_0 and 2.003 a_0 respectively. Its electronic ground state ($X^1\Sigma_g^+$) configuration is $(1\sigma_g)^2(1\sigma_u)^2(2\sigma_g)^2(2\sigma_u)^2(3\sigma_g)^2(1\pi_u)^4$, while the next lowest unoccupied orbitals are $(1\pi_g)^0(3\sigma_u)^0(4\sigma_g)^0$ [262]. The ionization potential to the ground state ($X^2\Pi_u$) of the acetylene cation is 0.419 Ha (11.4 eV), while to the first excited ($A^2\Sigma_g^+$), second excited ($B^2\Sigma_u^+$) and third excited ($C^2\Sigma_g^+$) states the ionization potentials are 0.614 Ha (16.7 eV), 0.691 Ha (18.8 eV), and 0.867 Ha (23.6 eV) respectively [263].

In this section we will provide a brief overview of some previous experimental and theoretical studies of acetylene. In particular we will focus our attention on studies of photoionization and HHG.

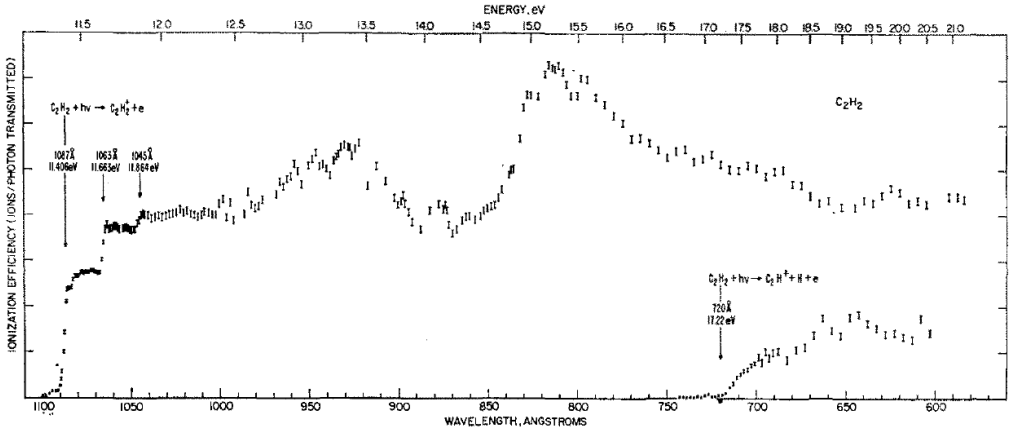

Figure 4.1: Photoionization-efficiency curve for $C_2H_2^+$ and C_2H^+ ions from the acetylene molecule, which exhibits a "double-hump" structure with peaks around 13.3 eV and 15.5 eV. Figure reproduced from [264].

4.2.1 Photoionization

Experimental work on acetylene from the 1960s through to the 1980s focused largely on measuring photoelectron spectra and attempting to assign specific peaks in the spectra to specific electronic transitions (see, for example, [264–268]). These experimental studies were supported by subsequent theoretical calculations [262, 263, 269–271] to explain the origin of peaks and satellite features seen in the experimental spectra.

An area of particular contention in these studies and related works was the origin of two features at $\sim$13.3 eV (0.4888 Ha) and $\sim$15.5 eV (0.5696 Ha) in the photoionization spectra; the so-called "double hump" structure, shown in Fig. 4.1 [264]. Different authors have proposed different origins for these features, but the general consensus is that the lower energy feature arises mainly from the $3\sigma_g \rightarrow 3\sigma_u$ transition or the $3\sigma_g \rightarrow 3p\sigma_u$ Rydberg transition, while the higher energy feature is associated with the $2\sigma_u \rightarrow 1\pi_g$ transition [262, 263, 270].

In recent years, several time-dependent studies of ionization of acetylene have been carried out. For example, in 2012, the group of Yamanouchi used a one-dimensional time-dependent Hartree-Fock (TDHF) model to investigate the effect of the C-H bond length on the ionization rate, with results suggesting an enhanced ionization mechanism when the C-H distances are symmetrically stretched to more than twice the equilibrium bond length [122, 272]. These calculations were subsequently extended to the three-dimensional case [117].

A number of time-dependent density functional theory (TDDFT) calculations on ionization of acetylene have also been performed. These have focused on alignment-dependent effects [273–275] in the ionization rate, as well as differences in the response to linearly or circularly polarized laser fields [276]. More recent TDDFT calculations have focused on the ionization enhancement studied previously with the TDHF models detailed above. This work showed that with strong laser pulses polarized parallel to the molecular axis, ionization was enhanced due to an increase in the coupling between σ states, and a "geometrically induced energy upshift of the orbitals" as the C-H bond lengths increase to 2-2.5 times the equilibrium distance [277, 278]. It should be noted that the laser intensities used in these studies are generally greater than those that we will consider in our calculations.

4.2.2 High harmonic generation

In recent years, several experimental studies of HHG in acetylene have been performed [50, 51, 66, 68, 279]. As well as acetylene, these experiments also considered other small hydrocarbons such as ethylene and allene. The focus of the first of these experiments [50, 66] was on alignment effects in the harmonic spectra, and how these could be used to infer the orbital structure of the molecules. These experiments used Ti:sapphire lasers ($\lambda = 780\,\text{nm}, 800\,\text{nm}$), split into two separate beams with a variable delay between them, to firstly induce some degree of molecular alignment in the sample gas, and subsequently generate high-order harmonics from it. The authors observed a "suppression of the HHG signal with increasing alignment" [66]; in other words, the harmonic signal increased as the angle between the molecular axis and the polarization direction of the laser field was increased. This observation was deemed to be indicative of the π structure of the highest occupied molecular orbital (HOMO), which has a nodal plane passing through the molecular axis (see Fig. 4.2(a)). When the laser field is polarized within this plane, the ionization and therefore high harmonic generation from the HOMO are suppressed; when the field is perpendicular to the nodal plane, ionization and HHG are at a maximum. This effect has previously been observed in other molecules, for example [65, 73, 220], while a similar effect in atomic species, in which the atomic polarization can play an important role in the HHG process, has been investigated in helium [280].

Subsequent studies [51, 68, 279] focused on achieving an extension to the harmonic plateau by using longer wavelength pulses to drive HHG. As before, a Ti:sapphire wavelength pulse was used for molecular alignment, but for the generating pulse, an optical parameter amplifier (OPA), pumped by the 800 nm pulse, was used to produce a mid-IR pulse of central wavelength $\lambda = 1450\,\text{nm}$.

An extended harmonic spectrum is essential for high harmonic spectroscopy, since the level of spatial resolution available is determined by the energy of the recolliding electrons, which is inherently linked to the extent of the plateau. According to the semiclassical three-step model, the energy that can be picked up by an ionized electron before recollision is determined by the ponderomotive energy U_p, given by Eq. (1.3). Since U_p scales with both the square of the amplitude of the applied electric field and the square of the wavelength of the applied pulse, increasing either the wavelength or the intensity of the driving pulse should result in an extension to the plateau. However, the ionization saturation intensity (an effective intensity beyond which increasing the intensity does not increase the ionization rate) of a molecule places an upper limit on the maximum intensity that can be applied. This upper limit is on the order of $10^{14}\,\text{W/cm}^2$ for many molecules, and lower still for organic molecules with low ionization potentials [281]. Therefore a limit is placed on the maximum energy of emitted harmonics (and consequently on the usefulness of HHG as a spectroscopic tool) when performing HHG studies of organic molecules using Ti:sapphire laser pulses.

The works cited above ([51, 68, 279]) sought to overcome this problem by increasing the wavelength of the driving field, rather than its intensity. Extension of the harmonic cutoff had previously been demonstrated experimentally in atomic gas targets, for example in argon [282]. However, as noted in these works, and investigated further elsewhere [283–286], this technique does have a major drawback: as the wavelength λ is increased, the intensity of the harmonic signal scales as λ^{-5} or λ^{-6}. This decrease is due to the increased time the ionized electron spends in the continuum between ionization and recombination. Increased time in the continuum leads to increased wavepacket spreading, which reduces the probability of recombination. So a balance must be struck between extending the cutoff energy and maintaining sufficient HHG generation efficiency.

With this technique, extended harmonic spectra were produced as desired in a range of small molecules [51, 68, 279]. For example, by using a driving pulse with a wavelength of 1300 nm rather than 800 nm, the observed cutoff in acetylene was extended from $\sim$40 eV to $\sim$60 eV, enabling the study of interference features at $\sim$46 eV [68]. Using a 1450 nm driving pulse, in a subsequent work, harmonics with energies as high as 70 eV were obtained for acetylene [51].

Although some of the experimental work cited above includes some form of theoretical accompaniment to their results (for example [66]), to our knowledge there have been few previous theoretical studies of HHG in acetylene beyond those performed within the Lewenstein model [287].

4.2.3 Summary

In this section we have provided a brief overview of the most relevant experimental and theoretical works on acetylene in the literature. Some of these works are provided merely as a general background on acetylene studies, while others are more directly relevant to our work and will be referred to in later sections of this chapter. In the next section we will show how acetylene is accurately modelled using EDAMAME.

4.3 Equilibrium ground state properties

In this work, acetylene is treated using our code, EDAMAME, as described in Chapter 3. Before the interaction of acetylene with a laser pulse can be considered, we must first ensure that we have a good description of the static properties of the molecule. To calculate the ground states properties, the molecule was aligned along the z-axis, with initial trial values for the bond lengths taken from the NIST Chemistry Webbook [255]. For all the calculations presented in this chapter, we use the standard (unscaled) finite difference grid described in Section 3.2.1, along with the standard finite difference formulae described in Section 3.2.2 (i.e., using the standard finite difference coefficients obtained from Eq. (3.31) with $\mathcal{N} = 8$). For these geometry relaxation calculations the grid extent was $\pm 32.8\,\mathrm{a}_0$ in all directions, with a uniform grid spacing of $0.4\,\mathrm{a}_0$ in each coordinate. With the exchange-correlation functional approximated using LDA-PW92-ADSIC, the system was then relaxed to find the equilibrium geometry, using the

Bond	Calculated Value/a_0	Experimental Value/a_0
C-C	2.207	2.273
C-H	2.045	2.003

Table 4.1: Equilibrium bond lengths in acetylene calculated using EDAMAME, compared with experimental values taken from [262].

geometry relaxation scheme described in Section 3.3.2. The resulting equilibrium bond lengths are given in Table 4.1, and show good agreement with experimental values.

From this equilibrium geometry, the initial Kohn-Sham states and energies are calculated. Since the innermost 4 electrons of acetylene are bound much more tightly than the others, we expect that, with the laser parameters considered in these simulations, they will not have a significant contribution to the dynamics. Therefore pseudopotentials are employed (as described in Section 3.2.4) to treat these inner electrons; only the remaining 10 electrons are dealt with explicitly (i.e., $N_e = 10$ in Eq. (3.2)). We therefore obtain the $N = N_e/2 = 5$ doubly occupied Kohn-Sham orbitals shown in Fig. 4.2(a). Figure 4.2(b) shows the calculated Kohn-Sham energies for these occupied orbitals along with those for a number of the lowest unoccupied orbitals; some of these are also given in Table 4.2 for reference. The symmetries of the occupied orbitals listed in this table can be clearly seen in Fig. 4.2(a). Note that HOMO(a) and HOMO(b) are the two forms of the degenerate HOMO.

By Koopmans' theorem, or rather, its DFT analogue, the magnitudes of occupied Kohn-Sham orbital energies can be considered as good approximations to the vertical ionization potentials of a system [289, 290]. Specifically, the magnitude of the HOMO energy of a neutral molecule can be considered an approximation of the ionization potential to the ground state of the cation, while the energies of the HOMO-1, HOMO-2, etc. can be considered approximations of the ionization potentials to the first, second, etc. excited states of the cation. Therefore we have also included experimental ionization potentials to the ground and first three excited states of the acetylene cation in Table 4.2 for reference.

The reader may observe from Table 4.2 that the magnitude of the LUMO+1 energy is smaller than that of the LUMO+2. This is a result of the numerics of the eigensolving algorithm, and the fact that the two states are very close in energy. The states have

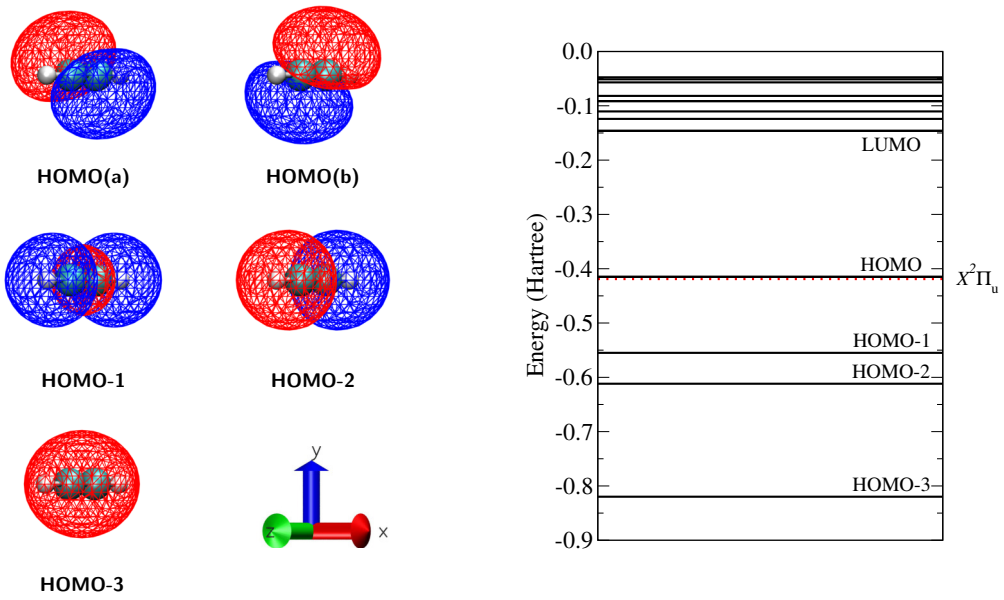

(a) Kohn-Sham orbitals

(b) Kohn-Sham orbital energies

Figure 4.2: Kohn-Sham orbitals and orbital energies of acetylene, calculated using EDAMAME. Panel (a) show isosurface plots of the 5 doubly-occupied orbitals. These plots were made using the VMD software package [288], with isosurface values of ± 0.03. Panel (b) shows the energies of the occupied and lowest unoccupied Kohn-Sham orbitals (solid lines) along with the negative of the experimental ionization potential (red dotted line), taken from [263].

been assigned in the order given in the table so the symmetries of the lowest Kohn-Sham states follow the order usually found in the literature [262].

4.3.1 Summary

In this section we have shown how the static properties of acetylene, namely the bond lengths and ionization potentials, are accurately described in the TDDFT framework implemented in the EDAMAME code. In the next three sections we will move beyond this static picture, and investigate the dynamics of acetylene when driven by a strong laser field.

4.4 Interaction of acetylene with a mid-IR pulse

We begin our time-dependent studies of acetylene by considering the response to a mid-IR laser pulse. In particular, we will focus on alignment effects in HHG. This will

Orbital	State	|Energy|/Ha	Experimental I_p/Ha
LUMO+2	$4\sigma_g$	0.1241	–
LUMO+1	$3\sigma_u$	0.1104	–
LUMO	$1\pi_g$	0.1469	–
HOMO	$1\pi_u$	0.4160	0.419 — $X^2\Pi_u$
HOMO-1	$3\sigma_g$	0.5543	0.614 — $A^2\Sigma_g^+$
HOMO-2	$2\sigma_u$	0.6112	0.691 — $B^2\Sigma_u^+$
HOMO-3	$2\sigma_g$	0.8187	0.867 — $C^2\Sigma_g^+$

Table 4.2: Kohn-Sham energies and states of the lowest-energy orbitals of acetylene, calculated using EDAMAME. Also included are the experimental ionization potentials to the ground and first three excited states of the acetylene cation, taken from [263]. By the DFT analogue of Koopmans' theorem, the magnitude of the Kohn-Sham energies can be considered as approximations to these ionization potentials (see text). Note that the $3\sigma_u$ and $4\sigma_g$ states have been reordered to follow the ordering usually found in the literature [262].

compliment the experimental work discussed in Section 4.2.2 ([51, 68, 279]). In Section 4.4.1 we set out the calculation details. This is followed in Section 4.4.2 by a qualitative look at the electronic dynamics during the interaction with the laser. Quantitative results are presented in Sections 4.4.3 and 4.4.4, in which we investigate the effect of molecular alignment on ionization and high harmonic generation, respectively.

4.4.1 Calculation parameters

The calculation parameters used throughout this work were chosen through specific convergence tests and experience from previous work [46, 220]. A crucial factor in our calculations is the extent of the finite difference grid, since it dramatically affects the accuracy of calculations and the resulting computational cost. The required grid extent is highly dependent on the laser parameters employed, so we address these first.

For our first set of calculations, laser parameters were chosen that were comparable to those used in the 2010 experimental work of Vozzi *et al.* [51]: we apply a 5-cycle, mid-IR pulse with a wavelength of $\lambda = 1450\,\text{nm}$ and a peak intensity of $I = 1.0\times10^{14}\,\text{W/cm}^2$. The pulse is linearly polarized, with the polarization direction along the z-axis. In all the work described in this chapter, the carrier-envelope phase is set to $\phi = 0$, and a $\sin^2$ pulse envelope is used, as described in Chapter 3.

Based on these laser parameters, converged results are obtained with the following grid extents: $x_{\text{max}} = y_{\text{max}} = \pm 90.8\,\text{a}_0$ and $z_{\text{max}} = \pm 146.8\,\text{a}_0$. The grid is much larger

Coordinate	Points per core	Number of cores	Grid spacing/a_0	|Grid extent|/a_0
x	35	13	0.4	90.8
y	35	13	0.4	90.8
z	35	21	0.4	146.8

Table 4.3: Grid parameters used in the majority of EDAMAME calculations described in this chapter, for simulating the interaction of acetylene with a mid-IR laser pulse. These calculations therefore require the use of 3549 cores on a parallel machine.

along the polarization direction since ionized wavepackets will predominantly propagate along this direction. As described in Section 3.2.9, absorbing boundaries are implemented near the edges of the grid, with absorption beginning at $x_m = y_m = \pm 60.0\,a_0$ and $z_m = \pm 100.0\,a_0$. Considering that the quiver amplitude, α_0, associated with these laser parameters is 54.1 a_0, we note that our grid extent along the laser polarization direction is $\sim 3\alpha_0$, with absorption beginning at $\sim 2\alpha_0$.

As in the static calculation in the previous section, the grid spacing is 0.4 a_0 in each coordinate, and is uniform across the entire grid. The grid is parallelized in x, y, and z over 13, 13 and 21 cores respectively, with 35 points per core in each direction. Thus the total number of cores used is 3549. These parameters are summarized in Table 4.3. Both the TDKS equations, Eq. (3.1), and the ionic equations of motion, Eq. (3.66), are propagated in time (as described in Sections 3.2.8 and 3.3.1) with a time step of 0.2 a.u..

In the static calculation, the molecule was orientated with the molecular axis aligned along the z-axis. In the time-dependent calculations described below, the orientation of the molecule will be varied. The molecular axis will always lie in the x-z plane, but the angle, θ, between the molecular axis and the z-axis will be varied. We refer to the molecule lying along the z-axis as the parallel orientation, or $\theta = 0°$. The perpendicular orientation refers to the $\theta = 90°$ case, in which the molecule is aligned along the x-axis.

4.4.2 Evolution of electronic density

Before we begin a proper quantitative treatment of our results, we present a number of 2D plots showing the evolution of the electronic density in the molecule during a typical interaction with a strong laser pulse, in order to qualitatively show the dynamics of the system. Figure 4.3 shows the 2D electronic density in the x-z plane at a number of

times during the interaction of acetylene with a 5-cycle laser pulse with a wavelength of $\lambda = 1450\,\text{nm}$ and a peak intensity of $I = 1.0\times10^{14}\,\text{W/cm}^2$. The total duration of the pulse is $T_{\text{IR}} = 999.8\,\text{a.u.} = 24.18\,\text{fs}$. The pulse is linearly polarized along the z-axis, while the molecular axis is aligned perpendicular to this (along the x-axis). In these figures the density plotted is obtained by integrating the full 3D density over the y-coordinate.

In Fig. 4.3(a), the ground state electronic density is plotted. In Fig. 4.3(b), as the intensity of the IR probe begins to increase, we see the electron cloud becoming distorted by the electric field. The electron cloud is behaving as a tightly bound oscillator, moving in antiphase to the field. Once the field has ramped up enough, we begin to see bursts of ionization around the peaks of the laser field, as in Fig. 4.3(c), which increase in intensity as the field ramps up further, as in Fig. 4.3(d). Following these ionization bursts, ionized wavepackets propagate away from the molecule, while also spreading in the x-direction, until the sign of the electric field reverses. At that point the ionized wavepackets slow and are driven back towards the molecule, as shown in Fig. 4.3(e). As the ionized wavepacket (in the negative z-direction) returns to the proximity of the molecule, Fig. 4.3(f) shows interference occurring between the ionized and bound parts of the wavefunction. At this point recombination occurs. Meanwhile, we see another burst of ionization in the positive z-direction. This pattern of tunnel ionization, propagation in the field, and recombination with the molecule continues as the field intensity begins to ramp down, as shown in Fig. 4.3(g). In this panel we see how interference between different ionized wavepackets, and between bound and ionized parts of the wavefunction cause the electronic density to obtain an increasingly complicated structure as the calculation progresses. At the end of the calculation, Fig. 4.3(h), as the strength of the laser field reduces again to zero, we see the system returning to a state somewhat resembling the initial state, although with some ionized wavepackets still propagating in the continuum. In addition, the grid now has an overall reduced electronic population due to absorption of ionized electrons at the edges of the grid.

4.4.3 Ionization dynamics

We begin a quantitative discussion of our results by considering ionization of acetylene during interaction with the laser pulse. As was described in the previous chapter,

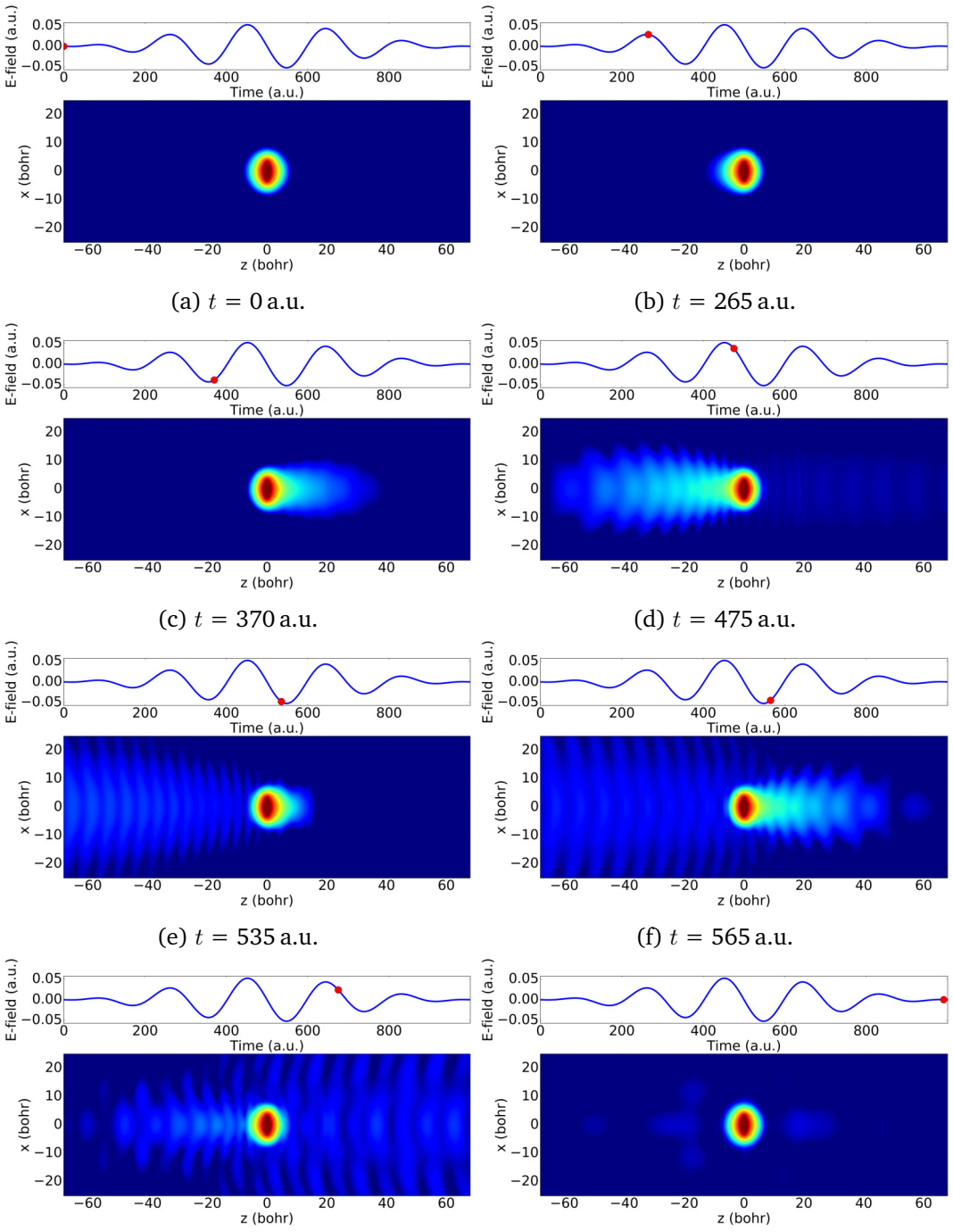

(a) $t = 0$ a.u. (b) $t = 265$ a.u.

(c) $t = 370$ a.u. (d) $t = 475$ a.u.

(e) $t = 535$ a.u. (f) $t = 565$ a.u.

(g) $t = 675$ a.u. (h) $t = 990$ a.u.

Figure 4.3: Electronic density of acetylene at various times during an interaction with a 5-cycle mid-IR laser pulse with wavelength $\lambda = 1450\,\text{nm}$ and a peak intensity of $I = 1.0\times10^{14}\,\text{W/cm}^2$. The laser pulse is linearly polarized along the z-axis, while the molecular axis is aligned along the x-axis. The densities presented in the x-z plane are obtained by integrating the full 3D densities over the y-coordinate. The densities are plotted on a logarithmic scale, with the lowest density clamped to 5×10^{-6}. The electric field strength is shown at the top of each panel, with the specific time indicated by the red marker.

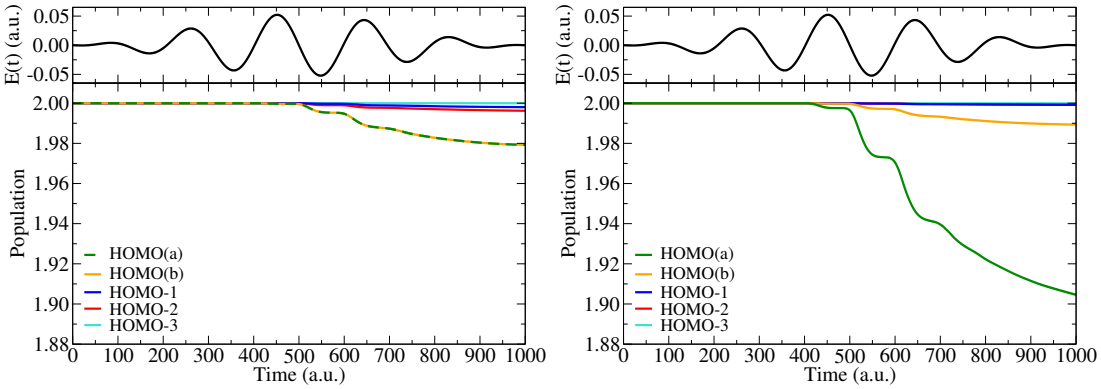

(a) Orbital populations, $\theta = 0°$

(b) Orbital populations, $\theta = 45°$

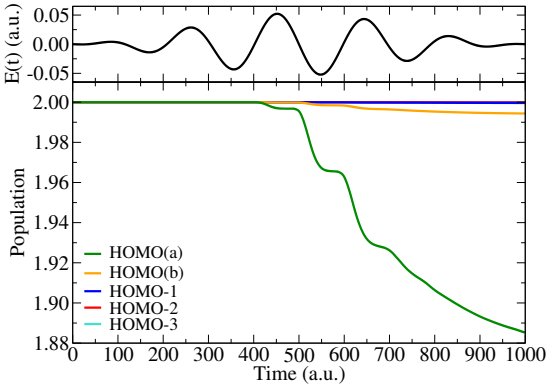

(c) Orbital populations, $\theta = 90°$

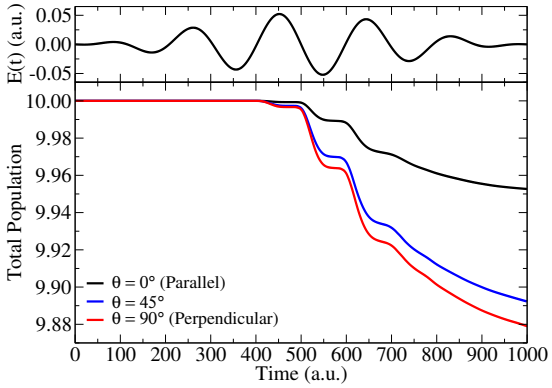

(d) Total populations, $\theta = 0°, 45°, 90°$

Figure 4.4: Electronic populations of the 5 occupied Kohn-Sham orbitals of acetylene during interaction with a 5-cycle mid-IR laser pulse with wavelength $\lambda = 1450\,\text{nm}$ and a peak intensity of $I = 1.0\times10^{14}\,\text{W/cm}^2$. The pulse is linearly polarized along the z-axis, while the angle between the molecular axis and the laser polarization direction is either (a) 0° (parallel orientation), (b) 45°, or (c) 90° (perpendicular orientation). In these plots, HOMO(a) and HOMO(b) refer to the two forms of the HOMO, shown in Fig. 4.2(a). (d) shows the total population in each of the three orientations, found by summing over the 5 orbitals in each case. The z-component of the E-field is shown at the top of each plot.

ionization is modelled in EDAMAME through the use of absorbing boundaries: as a simulation progresses, ionizing wavepackets may propagate away from the molecule towards the edges of the grid, where they are "absorbed", with the effect that the total electronic population in the grid decreases over time.

Figure 4.4 show the changes in electronic population in each of the 5 occupied Kohn-Sham orbitals during the interaction of acetylene with a linearly polarized, mid-IR pulse. Three orientations of the molecular axis with the laser polarization are considered: Figs. 4.4(a) and 4.4(c) respectively show the response when the laser pulse

is polarized parallel or perpendicular to the molecular axis, and Fig. 4.4(b) shows the intermediate case where the molecular axis is aligned at an angle of 45° to the laser polarization direction. Figure 4.4(d) shows the total population (i.e., summing over all 5 Kohn-Sham orbitals) in the grid for each orientation.

In each of these figures we can observe clear step-like decreases of the populations, resulting from the oscillations in $E(t)$ and the strong dependence of tunnel ionization on electric field strength. The reader may note that the steepest decreases in population do not coincide with the extreme values of $E(t)$ as may be expected. This is due to the fact that the decreases in population occur when an electronic wavepacket reaches the absorbing boundary, not at the actual ionization time; there will be some delay time between these two events, dependent on the size of the grid, the extent of the absorbing region, and the laser parameters. If we looked instead at the populations within a small region close to the molecule (not shown here), we would see similar behaviour to that observed in Fig. 4.4, with similar final populations, but with the population decreases coinciding with the extreme values of $E(t)$.

From these figures we can see that in the parallel orientation, the two forms of the HOMO, shown in Fig. 4.2(a), respond identically to the laser field, due to the symmetry of the orbitals with respect to the laser polarization direction (the z-axis). When this symmetry is broken by rotating the molecule with respect to the laser polarization direction, there is a clear difference between the responses of the two forms of the HOMO. These results also show that there is substantially more ionization when the molecular axis is perpendicular to the laser polarization direction than in the parallel case. This overall increase is due to the greatly increased amount of ionization from one form of the HOMO (the HOMO(a) in this case); ionization from the other form of the HOMO and the HOMO-1 and HOMO-2 decreases as the angle θ is increased, while ionization from the HOMO-3 is minimal, and varies little with angle. It is also notable that the response at $\theta = 45^\circ$ bears much more resemblance to the perpendicular response than to the parallel response. This effect of increased ionization at particular molecular orientations is a well-known phenomenon due to the symmetry of the molecular orbitals, and has been previously observed for a number of molecules [291–293], including acetylene [273, 275, 278].

We briefly note how the results in Fig. 4.4 compare with those of a previous TDDFT study of ionization in acetylene [273]. Although the laser intensities used in this earlier study by Russakoff *et al.* are much higher than those used in our work, our results are in qualitative agreement with the results for the lowest intensity and shortest duration pulse used in the Russakoff study ($I = 4.0\times10^{14}$ W/cm^2, 4.5 fs at FWHM). However, the behaviour observed by Russakoff *et al.* at higher intensities (7.0×10^{14} W/cm^2, 14.0×10^{14} W/cm^2) and longer pulse durations (15 fs, 25 fs) is different to what we see in Fig. 4.4. With these higher intensity or longer duration pulses, Russakoff *et al.* observed that the response of individual orbitals varied with increasing angle θ in the same manner as in our results (i.e., ionization from one form of the HOMO increases; ionization from the other orbitals decreases), but that the total ionization of the molecule was actually greatest in the parallel orientation. This was due to a much higher degree of ionization from the σ states in the parallel orientation than we see in Fig. 4.4(a), arising from an enhanced ionization mechanism that becomes important as the C-H bond length is stretched considerably. As we will show in Section 4.6, such significant bond stretching does not occur for the laser parameters considered in our calculations.

4.4.4 High harmonic generation

We now turn to the central topic of interest in this chapter: high harmonic generation in acetylene. As discussed in the previous chapter, we calculate harmonic spectra by taking the Fourier transform of the dipole acceleration along a given direction, as in Eq. (3.71). In the results presented here we have summed the spectral densities along the 3 coordinates (i.e., $S_x + S_y + S_z$). However, since the molecule is linear and the laser pulse is linearly polarized, the harmonic emission along the x- and y-directions (S_x, S_y) is negligible.

Figure 4.5 shows the harmonic spectra for acetylene interacting with the mid-IR laser pulse described above (5-cycle duration, $\lambda = 1450$ nm, $I = 1.0\times10^{14}$ W/cm^2, linearly polarized along the z-axis), in the three molecular orientations also described above ($\theta = 0^\circ, 45^\circ, 90^\circ$). In Fig. 4.5(a) the harmonic responses for the three orientations are plotted on separate axes for clarity. Fig. 4.5(b) shows the spectra together on a single set of axes to highlight the contrast between the three spectra, which will be discussed

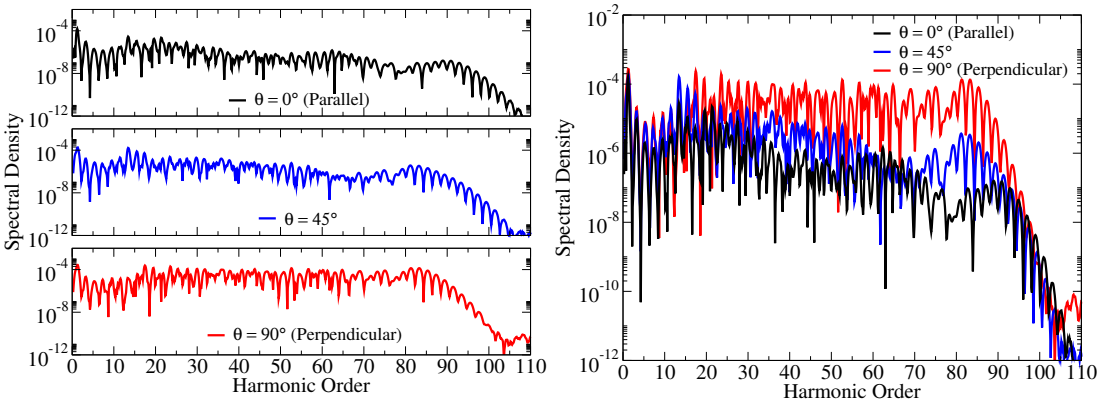

(a) $\theta = 0°, 45°, 90°$, plotted separately

(b) $\theta = 0°, 45°, 90°$, plotted together

Figure 4.5: Harmonic spectra from acetylene following interaction with a 5-cycle mid-IR laser pulse with wavelength $\lambda = 1450\,\text{nm}$ and a peak intensity of $I = 1.0\times10^{14}\,\text{W/cm}^2$. The pulse is linearly polarized along the z-axis, while the molecule is aligned either along the z-axis (parallel to the laser polarization direction), along the x-axis (perpendicular to the laser polarization direction), or at an angle of 45° to both the z- and x-axes. In panel (a), the three spectra are plotted on separate axes, for clarity. In panel (b), all three spectra are shown together, for ease of comparison.

presently.

The most striking feature of Fig. 4.5 is the large increase in the intensity of the emitted harmonics, across the entire spectrum, when the molecule is rotated away from the parallel orientation (increasing θ). Comparing the parallel and perpendicular spectra (Fig. 4.5(b)), we can see that the intensity of low-order harmonics in the perpendicular case is about an order of magnitude larger than in the parallel case. For higher-order harmonics close to the cutoff region, this enhancement can be greater than 3 orders of magnitude.

These results tie in with the increased ionization at large angles between the molecule and laser polarization direction that was observed in the previous section. Considering the three-step model of high harmonic generation, increased HHG follows naturally from increased levels of ionization. This effect of increased harmonic response at certain molecular orientations is a well-known effect, which has been seen in both experiments and calculations (see, for example, [65, 73, 220]). Considering acetylene in particular, this orientation-enhancement effect has previously been observed experimentally in [51, 66, 68].

Another notable feature of Fig. 4.5(b) is the difference in the position of the cutoff

Orbital	State	|Energy|/Ha	Cutoff harmonic
LUMO+2	$4\sigma_g$	0.1241	76.7
LUMO+1	$3\sigma_u$	0.1104	76.3
LUMO	$1\pi_g$	0.1469	77.4
HOMO	$1\pi_u$	0.4160	86.0
HOMO-1	$3\sigma_g$	0.5543	90.4
HOMO-2	$2\sigma_u$	0.6112	92.2
HOMO-3	$2\sigma_g$	0.8187	98.8

Table 4.4: Calculated energies of the lowest-energy Kohn-Sham orbitals of acetylene, and the cutoff harmonic associated with recombination to each state, as given by the semiclassical cutoff law, Eq. (1.14), for a laser pulse with wavelength $\lambda = 1450$ nm and a peak intensity of $I = 1.0\times10^{14}$ W/cm^2.

between the parallel and perpendicular spectra: around the 91st harmonic for the parallel orientation compared to around the 83rd harmonic for the perpendicular orientation. In the three-step model of HHG, it is generally assumed that the electron ionizes from and recombines back to the HOMO. In this case, the I_p term in the cutoff law, Eq. (1.14), refers to the ionization potential from the ground state of the neutral molecule to the ground state of the cationic molecule. However, the more tightly bound orbitals (HOMO-1, HOMO-2, etc.) can also play an important role in the high harmonic generation process [78, 79]. Recombination to one of these states will have a corresponding I_p value that is larger than for recombination to the HOMO, and consequently a higher cutoff harmonic will be predicted by the cutoff law. Using Eq. (1.14), we would expect that HHG with recombination to the HOMO would result in a cutoff around the 86th harmonic, whereas HHG involving recombination to the HOMO-1 or HOMO-2 would correspond to cutoffs around the 90th and 92nd harmonics respectively (see Table 4.4).

Considering the positions of the cutoffs in the spectra shown in Fig. 4.5, and the increase in ionization seen in Fig. 4.4, these results suggest that in the perpendicular orientation HHG arises mainly from the HOMO, while in the parallel orientation HHG occurs mainly from the HOMO-1 and HOMO-2. This interpretation is backed up if we consider the spectra obtained by taking the FFT of the dipole acceleration of individual Kohn-Sham states, using Eqs. (3.71) and (3.73), as shown in Figs. 4.6(a) and 4.6(b). As expected, these figures also show that the harmonic response of the two forms of the HOMO are identical in the parallel orientation, but significantly different in the perpendicular orientation.

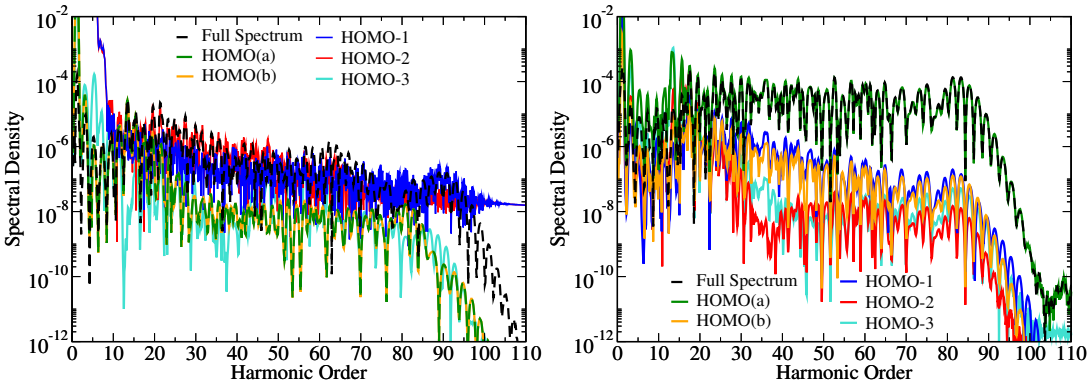

(a) $\theta = 0°$ (parallel) (b) $\theta = 90°$ (perpendicular)

Figure 4.6: Contributions of individual Kohn-Sham orbitals to the "parallel" and "perpendicular" harmonic spectra shown in Fig. 4.5, calculated using Eqs. (3.71) and (3.73), along with the full spectra from Fig. 4.5(b) for reference. In both cases the laser pulse is a 5-cycle pulse with wavelength $\lambda = 1450\,\text{nm}$ and a peak intensity of $I = 1.0\times10^{14}\,\text{W/cm}^2$, linearly polarized along the z-axis. In panel (a), the molecule is aligned parallel to the laser polarization direction, with the molecular axis along the z-axis, while in panel (b) it is aligned perpendicular to the polarization direction (along the x-axis). HOMO(a) and HOMO(b) refer to the two forms of the HOMO, shown in panels (i) and (ii) of Fig. 4.2(a) respectively.

The final feature of note in Fig. 4.5 is the presence of what appears to be a double plateau in the parallel spectrum. The inner plateau, with more intense harmonics, has a cutoff around harmonic 65, compared to an outer plateau cutoff of harmonic 91. Analogously to how the cutoff can be increased beyond that predicted by the semiclassical three-step model if the electron recombines to a more tightly bound state than the HOMO, we can also envisage a case where recombination occurs to a less tightly bound state. In this case we would expect the cutoff to decrease. Recombination to one of the initially unoccupied orbitals (the LUMO, LUMO+1, etc.) may therefore be the origin of the observed inner plateau region. However, calculating the expected cutoff for recombination to the LUMO, LUMO+1 or LUMO+2 (Table 4.4) does not match up with the observed inner plateau cutoff. This is also the case if recombination to higher orbitals is considered; recombination to any of these states will result in a cutoff of at least harmonic order 73, which would be the cutoff harmonic arising from Eq. (1.14) with $I_p = 0$. We will return to the explanation of the position of the inner plateau cutoff later, after investigating whether the inner plateau does indeed arise from recombination to one of the initially unoccupied Kohn-Sham states.

Recent work by Erattupuzha *et al.* investigating enhanced ionization of acetylene as the

	HOMO-3	HOMO-2	HOMO-1	HOMO(a)	HOMO(b)
HOMO-3 $(2\sigma_g)$	–	0.99	0	0	0
HOMO-2 $(2\sigma_u)$	0.99	–	2.18	0	0
HOMO-1 $(3\sigma_g)$	0	2.18	–	0	0
HOMO(a) $(1\pi_u)$	0	0	0	–	0
HOMO(b) $(1\pi_u)$	0	0	0	0	–
LUMO(a) $(1\pi_g)$	0	0	0	-1.27	0.00
LUMO(b) $(1\pi_g)$	0	0	0	-0.00	-1.27
LUMO+1 $(3\sigma_u)$	-0.01	0	0.66	0	0
LUMO+2 $(4\sigma_g)$	0	-0.11	0	0	0

(a) $\langle \phi_k(\boldsymbol{r}) | z | \phi_l(\boldsymbol{r}) \rangle$ (Parallel)

	HOMO-3	HOMO-2	HOMO-1	HOMO(a)	HOMO(b)
HOMO-3 $(2\sigma_g)$	–	0	0	0.72	0.42
HOMO-2 $(2\sigma_u)$	0	–	0	0	0
HOMO-1 $(3\sigma_g)$	0	0	–	0.20	0.12
HOMO(a) $(1\pi_u)$	0.72	0	0.20	–	0
HOMO(b) $(1\pi_u)$	0.42	0	0.12	0	–
LUMO(a) $(1\pi_g)$	0	-0.69	0	0	0
LUMO(b) $(1\pi_g)$	0	-0.40	0	0	0
LUMO+1 $(3\sigma_u)$	0	0	0	0	0
LUMO+2 $(4\sigma_g)$	0	0	0	-0.43	-0.25

(b) $\langle \phi_k(\boldsymbol{r}) | x | \phi_l(\boldsymbol{r}) \rangle$ (Perpendicular)

Table 4.5: Transition dipole matrix elements (in a.u.) for transitions between the 5 occupied Kohn-Sham orbitals of acetylene and each of the 9 lowest occupied and unoccupied orbitals, calculated using Eq. (4.1). The molecular axis is aligned along the z-axis. In (a) the matrix elements for parallel transitions are given (i.e., $\boldsymbol{r} = \hat{\boldsymbol{e}}_z$ in Eq. (4.1)), while the matrix elements for perpendicular transitions (i.e., $\boldsymbol{r} = \hat{\boldsymbol{e}}_x$) are given in (b).

molecule is stretched considered how the different Kohn-Sham states are coupled with each other in the presence of a strong laser pulse [278], and found that in a parallel alignment the states with σ-symmetry are strongly coupled when the C-H bonds are stretched. We have performed a similar analysis of the coupling between states in order to better understand the excitation and ionization mechanisms that result in the formation of the inner plateau region observed in Fig. 4.5.

We begin by calculating the transition dipole matrix elements for transitions between each of the occupied and lowest unoccupied Kohn-Sham orbitals. These are given by

$$\boldsymbol{d}_{kl} = \langle \phi_k(\boldsymbol{r}) | \boldsymbol{r} | \phi_l(\boldsymbol{r}) \rangle, \qquad k, l = 1, \ldots, M, \tag{4.1}$$

where $\phi_k(\boldsymbol{r})$ are the M ($M < N$) lowest-energy field-free eigenstates of the Kohn-Sham Hamiltonian (i.e., the lowest-energy Kohn-Sham orbitals, $\psi_j(\boldsymbol{r}, t)$, at time $t = 0$). The calculated values for transitions between the 5 occupied Kohn-Sham orbitals and each of the 9 lowest-energy orbitals are given in Table 4.5, with Tables 4.5(a) and 4.5(b) respectively showing the components parallel and perpendicular to the molecular axis. These tables show us which transitions between field-free states are allowed transitions, and which are dipole forbidden (those with elements equal to zero). For example, here we see that in the parallel case, Table 4.5(a), the allowed transitions are $\sigma_g \leftrightarrow \sigma_u$ and $\pi_u \leftrightarrow \pi_g$ transitions, whereas in the perpendicular case, Table 4.5(b), $\sigma_g \leftrightarrow \pi_u$ and $\sigma_u \leftrightarrow \pi_g$ are the allowed transitions.

We then calculate the overlap of the N time-dependent Kohn-Sham orbitals $\psi_j(\boldsymbol{r}, t)$ with the M lowest-energy occupied and unoccupied field-free Kohn-Sham orbitals, $\phi_k(\boldsymbol{r})$, namely

$$\eta_k(t) = 2\sum_{j=1}^{N} \left| \int \phi_k^*(\boldsymbol{r})\psi_j(\boldsymbol{r}, t)\mathrm{d}\boldsymbol{r} \right|^2, \qquad k = 1, \ldots, M. \tag{4.2}$$

The evolution of $\eta_k(t)$ over time can give us an better understanding of the coupling between the Kohn-Sham states, and the transitions between field-free states that are induced by the mid-IR pulse.

Figure 4.7 shows the calculated overlaps, $\eta_k(t)$, for the 9 lowest-energy Kohn-Sham states, in the parallel and perpendicular orientations. From Fig. 4.7(a) we can see that, noting the allowed transitions given in Table 4.5(a), in the parallel orientation the IR pulse seems to be exciting both the HOMO $\rightarrow$ LUMO ($1\pi_u \rightarrow 1\pi_g$) and HOMO-1 $\rightarrow$ LUMO+1 ($3\sigma_g \rightarrow 3\sigma_u$) transitions. Figure 4.7(b) is included here to show that the response is quite different in the perpendicular case. With this orientation we now see that, noting Table 4.5(b), the main transitions between the occupied and lowest unoccupied states are the HOMO $\rightarrow$ LUMO+2 ($1\pi_u \rightarrow 4\sigma_g$) and HOMO-2 $\rightarrow$ LUMO(a) ($2\sigma_u \rightarrow 1\pi_g$) transitions (note the difference in scale between upper and lower panels). This plot is simply included to highlight the difference in response between different orientations, and will not be discussed any further at this point.

Returning to the parallel case, and considering again the “inner plateau” observed in

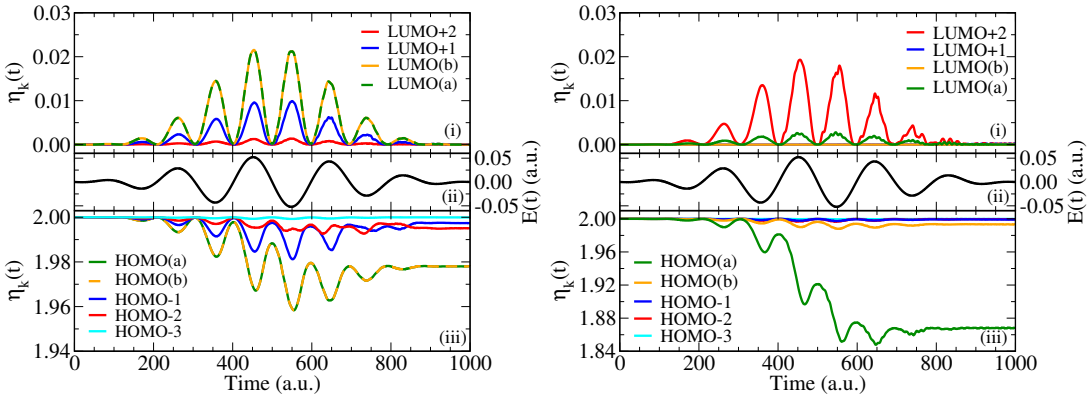

(a) $\theta = 0°$ (parallel) (b) $\theta = 90°$ (perpendicular)

Figure 4.7: Electronic population in each of the 9 lowest initial Kohn-Sham orbitals, $\phi_k(\boldsymbol{r})$, of acetylene, calculated using Eq. (4.2), during an interaction with a 5-cycle pulse with wavelength $\lambda = 1450\,\text{nm}$ and a peak intensity of $I = 1.0\times10^{14}\,\text{W/cm}^2$, linearly polarized along the z-axis. In panel (a), the molecule is aligned parallel to the laser polarization direction, with the molecular axis along the z-axis, while in panel (b) it is perpendicular to the polarization direction (along the x-axis). HOMO(a) and HOMO(b) refer to the two forms of the HOMO, shown in panels (i) and (ii) of Fig. 4.2(a) respectively. In both (a) and (b), the bottom and top sub-panels show the populations in the initially occupied and unoccupied Kohn-Sham orbitals respectively, while the middle sub-panel shows the z-component of the E-field.

Fig. 4.4.4, we might imagine that one of the HOMO $\rightarrow$ LUMO or HOMO-1 $\rightarrow$ LUMO+1 transitions could be related to the formation of this inner plateau. Although in Fig. 4.7(a) the HOMO $\rightarrow$ LUMO transition seems to be the dominant of the two transitions, we remember that when we examined the contributions of individual states to the parallel spectrum (Fig. 4.6(a)), the HOMO contribution was much less than the HOMO-1 and HOMO-2 contributions. To put it in terms of orbital symmetries, in the parallel orientation we saw that the harmonic response was dominated by σ states, whereas π states dominated in the perpendicular orientation. We therefore postulate that the existence of the inner plateau region in the harmonic spectrum is related to excitation of the HOMO-1 $\rightarrow$ LUMO+1 transition. The importance of this transition on the harmonic response will be the subject of Section 4.5.

4.4.5 Summary

In this section we have presented results for acetylene interacting with a mid-IR laser pulse. We have seen how the electronic density of the molecule changes during the interaction with the laser field, and how this can be investigated by studying the pop-

ulation loss from each Kohn-Sham orbital over time and the harmonic response of the system.

We have seen how the orientation of the molecule with respect to the laser polarization direction significantly affects the response. When the molecular axis is oriented perpendicular to the laser polarization direction, we see increased ionization and high harmonic generation compared to the case when the molecular axis and laser polarization direction are parallel to each other. In this parallel case, we also observe an extension to the harmonic cutoff, due to high harmonic generation from the HOMO-1 and HOMO-2 (rather than the HOMO), and the existence of an inner plateau region. By considering the transitions between the lowest field-free occupied and unoccupied orbitals, we suggested that this inner plateau is related to the excitation of the HOMO-1 $\rightarrow$ LUMO+1 transition. In the next section we will test this hypothesis, by introducing a second, lower intensity laser pulse, with the photon energy tuned to preferentially excite this transition.

4.5 HHG in acetylene with a VUV pump + mid-IR probe

In Section 4.4 it was proposed that the existence of the inner plateau seen in the parallel spectrum shown in Fig. 4.5 was related to excitation from the HOMO-1 ($3\sigma_g$ state) to the LUMO+1 ($3\sigma_u$ state). In order to investigate the role of this transition in the high harmonic generation process, we now directly excite this transition using a VUV pump pulse tuned to the energy gap between these two states before studying HHG with the mid-IR pulse.

As in the previous section, we apply a 5-cycle mid-IR pulse, with a wavelength of $\lambda =$ 1450 nm, an intensity of $I = 1.0\times10^{14}$ W/cm^2, and a duration of $T_{\text{IR}} = 999.8$ a.u. = 24.18 fs. Now, however, we precede this mid-IR pulse with an 8-cycle VUV pulse with a wavelength of $\lambda = 102$ nm, an intensity of $I = 1\times10^{12}$ W/cm^2, and a duration of T_{VUV} = 112.5 a.u. = 2.72 fs. This VUV wavelength is chosen as it corresponds to a photon energy of 0.4467 Ha, equivalent to the energy gap between the calculated HOMO-1 and LUMO+1 energies. Both the VUV and IR pulses are polarized parallel to the molecular axis, they both have $\sin^2$ pulse envelopes, and the IR pulse begins immediately after the VUV pulse has ended. It should be noted that the photon energy of this VUV pulse

is also large enough to directly ionize from the HOMO, and possibly also to excite the HOMO-2 $\rightarrow$ LUMO+2 transition (when the bandwidth of the pulse is taken into account).

Unless otherwise specified, in the calculations discussed in this section the molecular axis is aligned parallel to the polarization direction of both laser pulses (along the z-axis).

4.5.1 Ionization dynamics

As in the case of a single laser pulse (Section 4.4), we begin by considering how the populations in each of the Kohn-Sham orbitals vary over time. These are shown in Fig. 4.8 for three separate cases: Figs. 4.8(a) and 4.8(b) respectively show the response when just the VUV pump or just the IR probe are applied, while Fig. 4.8(c) shows the response when both pulses are applied sequentially. Note that the IR-only data has been shifted along the time-axis so that the IR pulse begins at the same time in all 3 cases.

We can see clearly from this figure that applying both pulses produces much more ionization than applying either pulse by itself. While from Fig. 4.8(a) we can see that the VUV pulse by itself doesn't cause any significant ionization from orbitals other than the HOMO (as expected due to the chosen photon energy), comparing Figs. 4.8(b) and 4.8(c) shows that combining the pulses produces a significant increase in ionization from the HOMO-1, as well as smaller increases from the other orbitals. Note also in that in the pump-probe case (Fig. 4.8(c)) we observe population depletion taking place much earlier in time than in the probe-only case (Fig. 4.8(b)), as the excitation by the VUV pump pulse increases the probability of tunnel ionization occurring at lower IR field strengths.

4.5.2 High harmonic generation

We now consider the harmonic response of the molecule to this pump-probe setup. Figure 4.9 shows the harmonic spectrum produced with this 2-pulse setup, with the parallel and perpendicular IR-only spectra included for comparison. With this combination of laser pulses, the addition of the VUV pulse clearly has a significant impact on

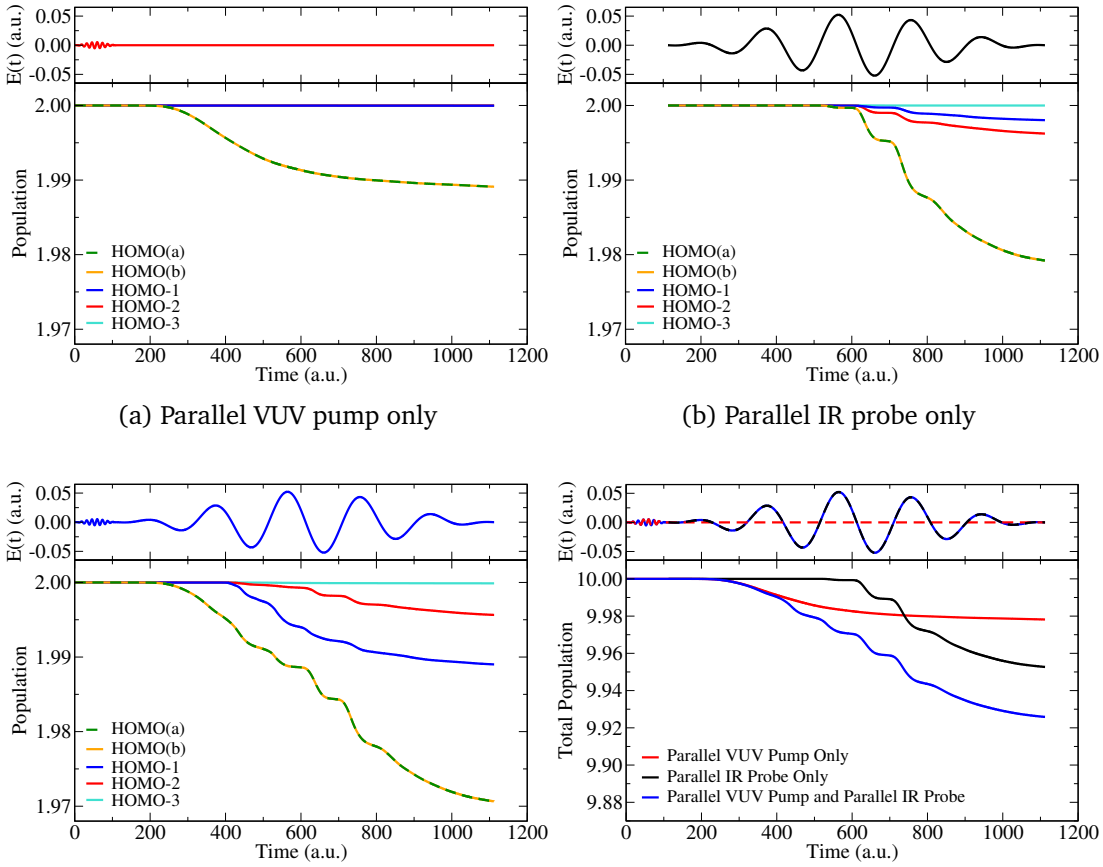

(a) Parallel VUV pump only

(b) Parallel IR probe only

(c) Parallel VUV pump and parallel IR probe

(d) Total Populations

Figure 4.8: Electronic populations of the 5 doubly occupied Kohn-Sham orbitals of acetylene during interactions with different setups of laser pulses. The IR probe pulse is a 5-cycle pulse with wavelength $\lambda = 1450\,\text{nm}$ and a peak intensity of $I = 1.0\times10^{14}\,\text{W/cm}^2$, while the VUV pump pulse is an 8-cycle pulse with wavelength $\lambda = 102\,\text{nm}$ and a peak intensity of $I = 1.0\times10^{12}\,\text{W/cm}^2$. Both pulses are linearly polarized along the z-axis. HOMO(a) and HOMO(b) refer to the two forms of the HOMO, shown in Fig. 4.2(a). In panel (a), the VUV pulse is applied, following which the system is allowed to propagate with zero applied field for the duration of the IR pulse. In panel (b), only the IR pulse is applied, and the times have been shifted so that the IR pulse begins at the same time in all three panels. In panel (c), the VUV pump pulse and IR probe pulse are applied sequentially. Panel (d) shows the total population in each of the three setups shown in the other panels. The z-component of the E-field is shown at the top of each plot.

the harmonic generation process: the intensities of the plateau harmonics (specifically the inner plateau harmonics) are enhanced by several orders of magnitude compared to those in the parallel IR-only case, although the inner plateau cutoff remains around harmonic 65. The intensities of the harmonics in this inner plateau are now comparable to the intensities seen in the spectrum produced in the perpendicular orientation with only the IR pulse. Beyond the inner plateau cutoff, the addition of the VUV pulse

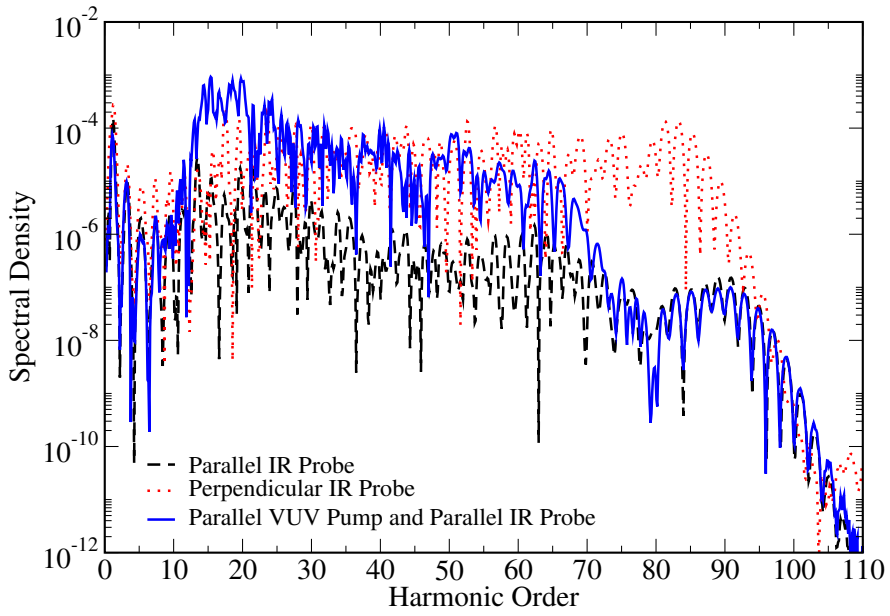

Figure 4.9: High harmonic generation in acetylene following interactions with different laser pulse setups. The IR probe pulse is a 5-cycle pulse with wavelength $\lambda = 1450\,\text{nm}$ and a peak intensity of $I = 1.0\times10^{14}\,\text{W/cm}^2$, while the VUV pump pulse is an 8-cycle pulse with wavelength $\lambda = 102\,\text{nm}$ and a peak intensity of $I = 1.0\times10^{12}\,\text{W/cm}^2$. In the pump-probe case, the IR probe begins immediately following the end of the VUV pump. The pulses in all cases are linearly polarized along the z-axis, while the molecular axis is aligned along the z-axis in the parallel cases, and along the x-axis in the perpendicular case.

has little effect on the spectrum, with just a slight reduction in the intensities of the outer cutoff harmonics. The outer plateau cutoff remains around harmonic 91.

As was done with the spectra produced with the IR pulse, we also consider the contributions of individual Kohn-Sham orbitals to the overall spectrum for this pump-probe case; these contributions are shown in Fig. 4.10. From this figure we can see that the enhancement of the inner plateau harmonics is due to an increased harmonic response from the HOMO-1. The exact processes behind the enhancement will be investigated further in the next subsection. In the remainder of this subsection, we will briefly discuss some of the previous investigations of enhancement of harmonic spectra, and the mechanisms at work in each of these.

Enhancement of harmonic spectra has previously been observed in a number of studies. In many of these, the enhancement effect is centred on a single harmonic or a narrow band of harmonics, due to a specific resonant transition in the system. For example, in a previous study of HHG in an indium plasma, the 13th harmonic was

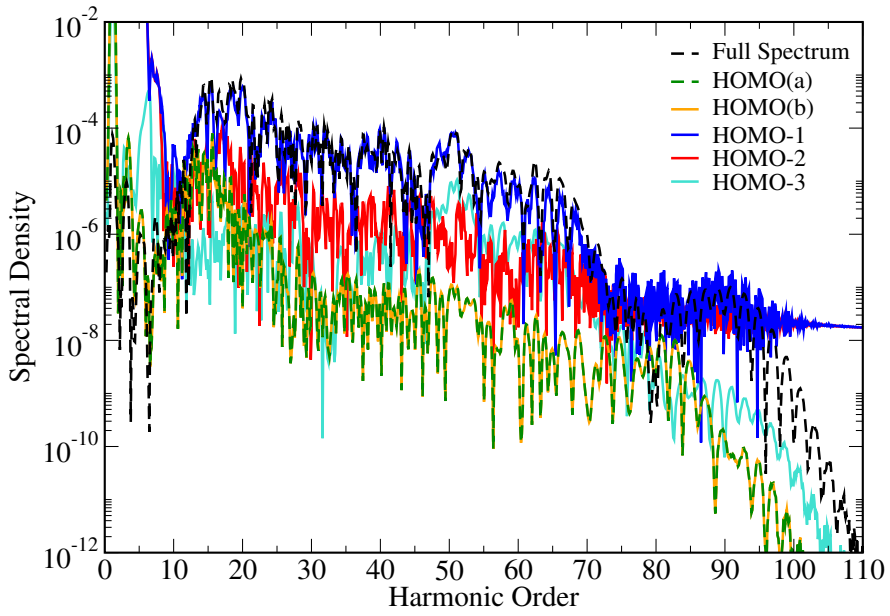

Figure 4.10: Contributions of individual Kohn-Sham orbitals to the pump-probe harmonic spectrum shown in Fig. 4.9, calculated using Eqs. (3.71) and (3.73), along with the full pump-probe spectrum from Fig. 4.9 for reference. The IR probe pulse is a 5-cycle pulse with wavelength $\lambda = 1450\,\text{nm}$ and a peak intensity of $I = 1.0\times10^{14}\,\text{W/cm}^2$, while the VUV pump pulse is an 8-cycle pulse with wavelength $\lambda = 102\,\text{nm}$ and a peak intensity of $I = 1.0\times10^{12}\,\text{W/cm}^2$. Both pulses are linearly polarized along the z-axis, along which the molecular axis is also aligned, and the IR probe begins immediately following the end of the VUV pump. HOMO(a) and HOMO(b) refer to the two forms of the HOMO, shown in panels (i) and (ii) of Fig. 4.2(a) respectively.

observed to be almost two orders of magnitude greater than neighbouring harmonics [294]. This was attributed to a resonant ionic transition. Smaller enhancements of individual harmonics were later observed in the spectra of other materials [295]. This resonant enhancement effect has been described by the development of a "four-step" model of HHG (replacing the standard three-step model), in which an electron tunnel ionizes and propagates in the field (as in the three-step model), but then, rather than radiatively recombining to the ground state, it is captured into an autoionizing state, from which it relaxes back to the ground state with the emission of a photon of energy equal to the energy gap between the ground and autoionizing states [296].

A different enhancement mechanism was reported in calculations on HHG in asymmetric diatomic molecules [297] and experimental observations of HHG in argon [298]. In these works, features in the harmonic spectra that were not explained by the usual three-step model was attributed to a mechanism in which electrons are ionized from an excited state of the molecule and recombine to the ground state (similar to the

mechanism proposed in a theoretical work in 1996 [299]).

The use of a two-pulse setup has been studied theoretically [300] and experimentally [301] in helium. In these works, the intensity across a wide range of harmonics is increased by applying a high harmonic pulse along with the driving pulse (in the experimental setup, this is achieved by using the driving pulse to generate "booster" harmonics from xenon, which then combine with the driving pulse to affect the HHG process in helium). The target systems are such that the driving pulse alone causes little ionization (and therefore little HHG). With the addition of the high harmonic pulse however, the ionization rate is significantly increased, which leads to a subsequent enhancement of high harmonics throughout the plateau region.

Having seen a number of potential harmonic enhancement mechanisms, we now return to the dramatic inner plateau enhancement seen in Fig. 4.9, and, in the next section, we investigate its origin.

4.5.3 Origin of inner plateau enhancement

In the previous section we saw that an increased harmonic response from the HOMO-1 is responsible for the enhancement of the inner plateau harmonics when the VUV pump is added. However, as was seen in the discussion surrounding Fig. 4.7, during the interaction with the laser pulse the field-free Kohn-Sham states are coupled together. This means that the as the field intensity increases, the time-dependent HOMO-1 is no longer the same state as the field-free HOMO-1, and is instead a superposition of field-free (mainly σ) states. A similar point is true for the other time-dependent Kohn-Sham states. So to understand the mechanism behind the observed harmonic enhancement, it would be beneficial to know which field-free states play an important role in the dynamics.

In Section 4.4.4, we investigated the changes in the populations of the field-free states by calculating the overlaps between the lowest time-dependent and field-free Kohn-Sham orbitals. We now apply the same analysis to the pump-probe setup. The results of these calculations are shown in Fig. 4.11(b), while Fig. 4.11(a) shows the parallel probe-only overlaps again for comparison (the data has been shifted so the IR pulse begins at the same time in both plots).

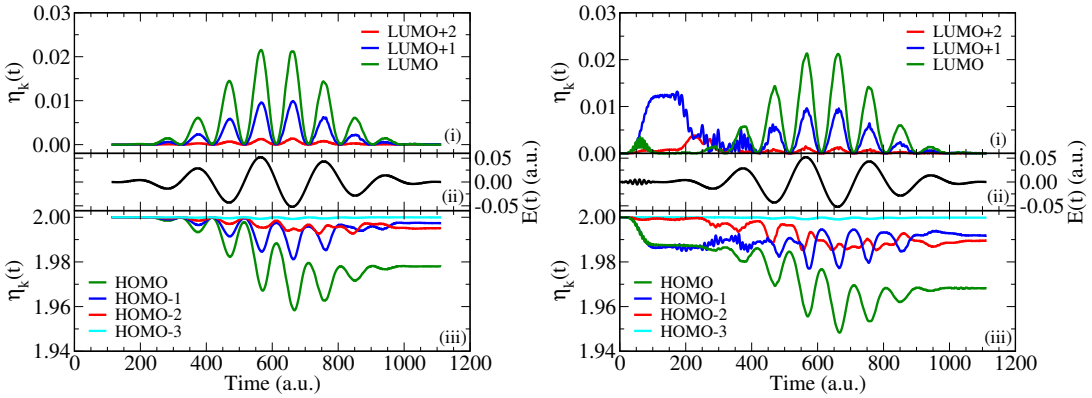

(a) Parallel IR Probe (b) Parallel VUV Pump and Parallel IR Probe

Figure 4.11: Electronic population in each of the 9 lowest initial Kohn-Sham orbitals, $\phi_k(\boldsymbol{r})$, of acetylene, calculated using Eq. (4.2), during interactions with different setups of laser pulses. In both panels a 5-cycle IR pulse with wavelength $\lambda = 1450\,\text{nm}$ and a peak intensity of $I = 1.0\times10^{14}\,\text{W/cm}^2$ is applied. In panel (b), this pulse is preceded by an 8-cycle VUV pulse with wavelength $\lambda = 102\,\text{nm}$ and a peak intensity of $I = 1.0\times10^{12}\,\text{W/cm}^2$. Both pulses are linearly polarized along the z-axis, along which the molecular axis is also aligned. The data in panel (a) has been shifted in time so that the IR pulse begins at the same time in both panels. In both (a) and (b), the bottom and top sub-panels show the populations in the initially occupied and unoccupied Kohn-Sham orbitals respectively, while the middle sub-panel shows the z-component of the E-field. For brevity, only one form of each of the HOMO and LUMO are shown.

In Fig. 4.11 the effect of the VUV pump in exciting the $3\sigma_g \rightarrow 3\sigma_u$ (HOMO-1 $\rightarrow$ LUMO+1) transition is evident. We also note that the excited population remains in the LUMO+1 for some time following the end of the VUV pulse (duration = 112.5 a.u.); the LUMO+1 population only decreases when the IR field strength has increased sufficiently. Comparing Figs. 4.11(a) and 4.11(b), we can see that the VUV pulse also causes some population loss from the HOMO, but does not significantly affect the HOMO's subsequent response to the IR field.

The most striking differences between Figs. 4.11(a) and 4.11(b) are in the first half of the calculation, i.e., during and immediately after the VUV pump pulse, but before the IR probe pulse has reached its maximum intensity. In order to better understand how these differences result in the large harmonic enhancement observed in Fig. 4.9, we can compare the times at which harmonics of specific energies are produced in the IR-only and VUV-IR simulations. Figures 4.12(a) and 4.12(b) show time-frequency analysis plots for the IR-only and VUV-IR cases respectively, calculated using Eq. (3.74) as described in Section 3.5.3.

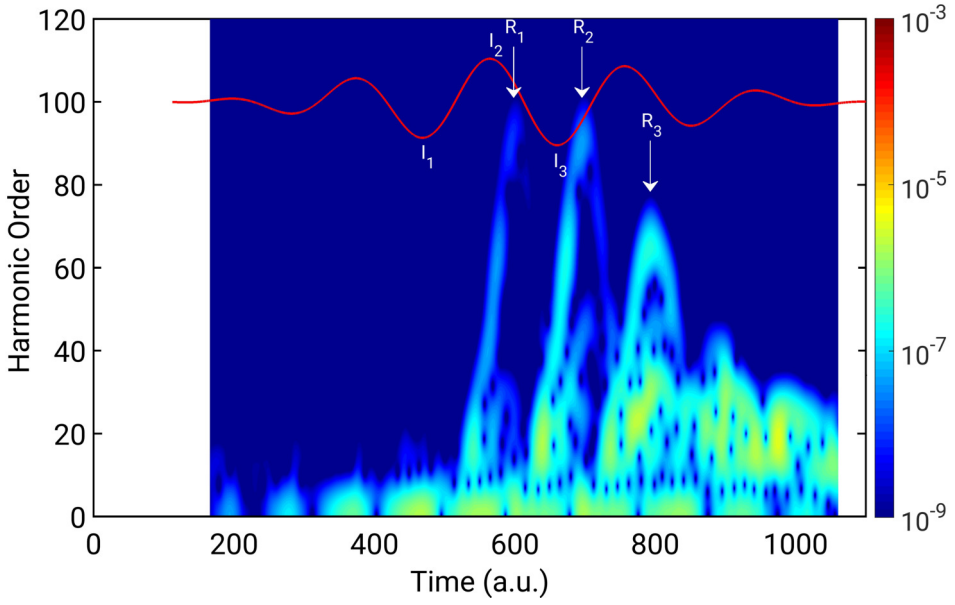

(a) Parallel IR Probe

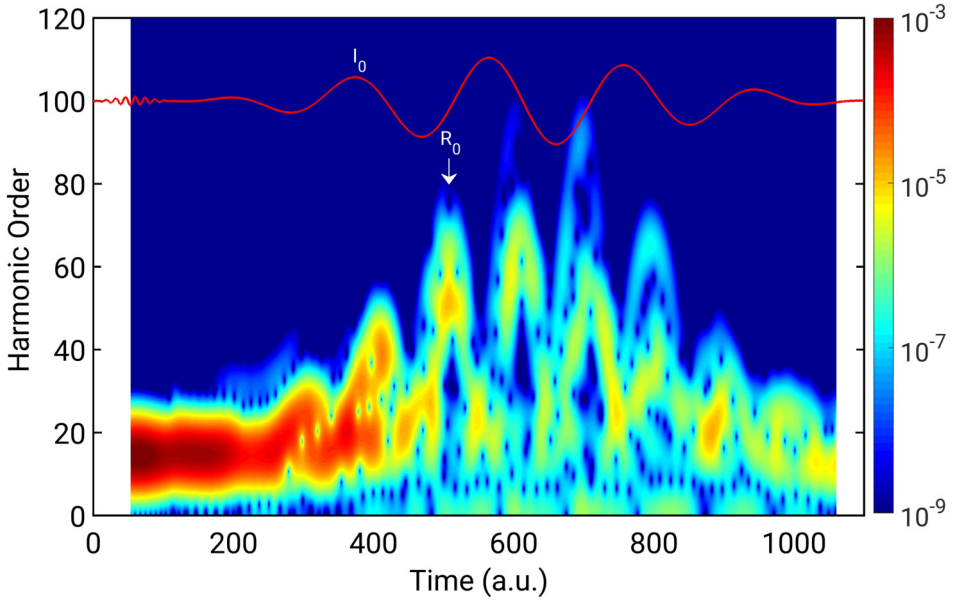

(b) Parallel VUV Pump and Parallel IR Probe

Figure 4.12: Time-frequency analyses of the two "parallel" HHG spectra shown in Fig. 4.9. In both panels a 5-cycle IR pulse with wavelength $\lambda = 1450\,\text{nm}$ and a peak intensity of $I = 1.0\times10^{14}\,\text{W/cm}^2$ is applied. In panel (b), this pulse is preceded by an 8-cycle VUV pulse with wavelength $\lambda = 102\,\text{nm}$ and a peak intensity of $I = 1.0\times10^{12}\,\text{W/cm}^2$. The data in panel (a) has been shifted in time so that the IR pulse begins at the same time in both panels. Both pulses are linearly polarized along the z-axis, along which the molecular axis is also aligned. The red lines denote the z-component of the electric field. The arrows highlight the emission times of some of the highest harmonics, originating from ionization around times indicated by I_j and recombination at times R_j, as described in text.

In the probe-only case (Fig. 4.12(a)), we can see the semiclassical three-step model at work: for the first $\sim$1/3 of the pulse, we see no plateau harmonics generated (only low-order harmonics due to bound-bound harmonic generation) since the field strength is initially too low to cause tunnel ionization. As the field strength ramps up, tunnel ionization occurs around the peaks and troughs of the oscillating field. These ionized wavepackets then propagate in the field, and can be driven back towards the core where they can recombine producing the high-order harmonics evident in this figure. From the three-step model, the harmonics near the cutoff should be emitted approximately two thirds of a pulse cycle after ionization: indeed we see cutoff harmonics emitted around 599 a.u. and 695 a.u. (indicated by arrows R_1 and R_2), corresponding to bursts of ionization around 466 and 562 a.u. respectively (I_1 and I_2 in Fig. 4.12(a)). We also note that the peak around 793 a.u. (arrow R_3) has a lower harmonic order than the preceding two peaks. Again, this is what we expect from the three-step model, noting that the applied field is lower due to the pulse envelope. This means that an electron ionized around 660 a.u. (I_3) will experience a less intense field during its time in the continuum than an electron ionized at 466 or 562 a.u., meaning it will gain less kinetic energy and therefore result in the emission of lower energy harmonics.

Looking now at the pump-probe case (Fig. 4.12(b)), we see that the situation is dramatically different. We see intense emission of harmonics in a window centred around harmonic 15 beginning during the VUV pulse, and continuing until around the 2nd cycle of the IR pulse. As emission of harmonics from this window ceases, we see higher energy harmonics begin to be emitted, much earlier than was seen in Fig. 4.12(a). Towards the end of the IR pulse, the low-order harmonics are emitted again, although less strongly than at the beginning of the pulse.

Comparing these two figures, we can see that the addition of the VUV pulse causes the enhancement seen in Fig. 4.9 in two ways:

1. Following excitation by the VUV pulse, low-order harmonics are emitted as the molecule relaxes back to its ground state. A transition from the LUMO+1 back to the HOMO-1 will involve the emission of a photon with energy 0.4439 Ha, corresponding to harmonic 15. Considering that the VUV pump may populate other excited states than just the LUMO+1, with a number of subsequent transi-

tions possible between different states, we therefore attribute the enhancement of harmonics 11-21 to an increase in bound-bound transitions. As the intensity of the IR field increases, ionization will occur from the excited states, reducing the number of bound-bound transitions. Only when the IR field strength has reduced to near zero at the end of the pulse do we see any significant number of these transitions occurring again. However, the bound-bound harmonics emission is much less intense now than it was at the beginning of the calculation, due to the relatively small excited state population (evident when comparing the beginning (0 - 200 a.u.) and the end (900 - 1100 a.u.) of the upper panel of Fig. 4.11(b)).

2. The excitation of the molecule by the VUV pulse allows tunnel ionization, the first step of the HHG process, to begin earlier in the IR pulse, before the intensity has ramped up fully. This is evidenced by the fact that we see emission of the inner plateau harmonics (up to around harmonic order 65) occurring at much earlier times in Fig. 4.12(b) than in Fig. 4.12(a). For example, we see a peak in Fig. 4.12(b) around 507 a.u. (indicated by arrow R_0). Emission of high-order harmonics at this time corresponds to ionization occurring at time $\sim$ 374 a.u. (I_0), when the IR field is still relatively weak. These earlier ionization times indicate that the tunnel ionization step of the harmonic generation process is occurring from an excited state. Combining this with the fact that only the inner plateau harmonics are affected by the addition of the VUV pump pulse (the harmonics beyond harmonic order $\sim$80 are comparable in the two parallel spectra in Fig. 4.9), we can conclude that the inner plateau harmonics are a result of ionization from and recombination back to an excited state of the molecule, specifically the LUMO+1.

To summarize, from the results presented up to this point we have drawn several conclusions regarding harmonic generation in acetylene in the parallel orientation. Firstly, the harmonic spectrum consists of two distinct plateau regions: an outer plateau, where high harmonic generation is a result of ionization from and recombination to the HOMO-1/HOMO-2, and an inner plateau, where high harmonic generation is a result of excitation from the HOMO-1 to the LUMO+1, followed by ionization from and recombination to the LUMO+1. Secondly, exciting the HOMO-1 $\rightarrow$ LUMO+1 transition by applying a suitably tuned VUV pump pulse before the IR pulse produces a large

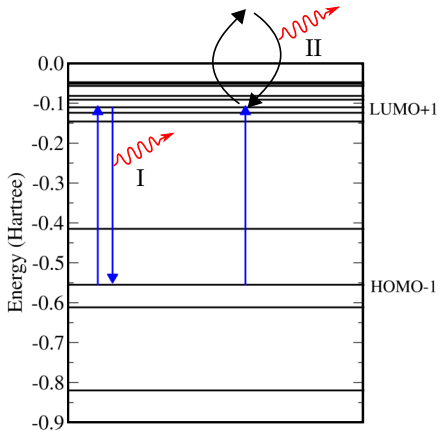

Figure 4.13: Schematic representation of the two enhancement mechanisms responsible for the increased intensity in the harmonic spectrum of acetylene when a VUV pump pulse precedes the driving IR pulse, as seen in Fig. 4.9. The left set of arrows (labelled I) represents the increase in bound-bound transitions, following excitation of the HOMO-1 $\rightarrow$ LUMO+1 transition by the VUV pump pulse, that is responsible for the enhancement of harmonics 11-21. The right set of arrows (labelled II), represents the mechanism responsible for the enhancement of the inner plateau harmonics: following excitation of the HOMO-1 $\rightarrow$ LUMO+1 transition by the VUV pump pulse, electrons are ionized from the LUMO+1 by the IR field, propagate in the continuum gaining kinetic energy, and then recombine back to the LUMO+1.

enhancement to the inner plateau harmonics. This enhancement is due to two separate mechanisms: a number of low-order harmonics (11-21) are enhanced due to increased bound-bound transitions between the initially unoccupied and occupied states, while high harmonic generation from the LUMO+1 is enhanced due to increased population in this state at the beginning of the IR pulse. Figure 4.13 presents these two enhancement mechanisms schematically.

However, as was noted earlier, the cutoff harmonic for the inner plateau is inconsistent with what is expected from the three-step model considering recombination to the LUMO+1. This discrepancy will now be addressed.

4.5.4 Position of inner plateau cutoff

Returning to the inner plateau seen in the spectrum shown for the parallel orientation in Fig. 4.5 and, more prominently, in the pump-probe spectrum in Fig. 4.9, we again note that the cutoff predicted by the semiclassical three-step model for HHG with recombination to the LUMO+1 would be around harmonic 77, far from the observed

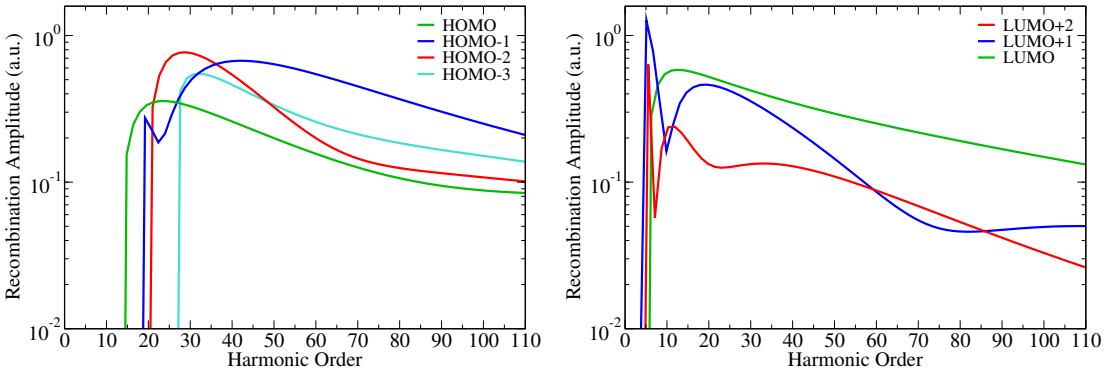

(a) Highest occupied orbitals (b) Lowest unoccupied orbitals

Figure 4.14: Dipole recombination matrix elements for a continuum electron recombining back to one of the lowest Kohn-Sham states of acetylene, calculated via Eq. (4.3). The energy of the free electron and the ionization potentials of the individual Kohn-Sham states are related to a given harmonic order, n, using the classical formula $n\omega_L = k^2/2 + I_p$, where ω_L is the frequency of the IR field, k is the magnitude of the momentum of the free electron, and I_p is the ionization potential of the Kohn-Sham state. Here the IR field has a wavelength of $\lambda = 1450\,\text{nm}$ (i.e., $\omega_L = 0.0314\,\text{Ha}$), and the I_p values are taken as the negatives of the Kohn-Sham energies given in Table 4.2. Panels (a) and (b) show the recombination elements for the field-free occupied and unoccupied orbitals respectively.

inner plateau cutoff around harmonic 65. There appears to be a suppression of harmonics near the expected cutoff.

There are a number of effects that can result in minima in harmonic spectra and suppression of particular harmonic orders, including multichannel interference [302–304] and structural interference [72, 74, 304, 305]. We can investigate structural interference effects by calculating recombination matrix elements [306, 307]. The recombination matrix element of an ionized electron to a bound state of a molecule can be written as

$$\boldsymbol{d}_{\text{rec}}(\boldsymbol{k}) = \left\langle \chi(\boldsymbol{k},\boldsymbol{r}) \middle| \boldsymbol{r} \middle| \Psi(\boldsymbol{r}) \right\rangle , \tag{4.3}$$

where $\chi(\boldsymbol{k},\boldsymbol{r})$ is a plane wave describing a free electron with momentum $\boldsymbol{k}$, and $\Psi(\boldsymbol{r})$ is the wavefunction of the bound state to which the free electron will recombine. We consider the amplitude of $\boldsymbol{d}_{\text{rec}}$ along the laser polarization direction, and integrate over all angular variables to calculate the recombination matrix elements as a function of the electron's momentum, $\boldsymbol{k}$. This momentum is then related to a given harmonic order, n, through the formula $n\omega_L = k^2/2 + I_p$, where ω_L is the frequency of the laser field (the IR probe) and I_p is the ionization potential of the bound state $\Psi(\boldsymbol{r})$.

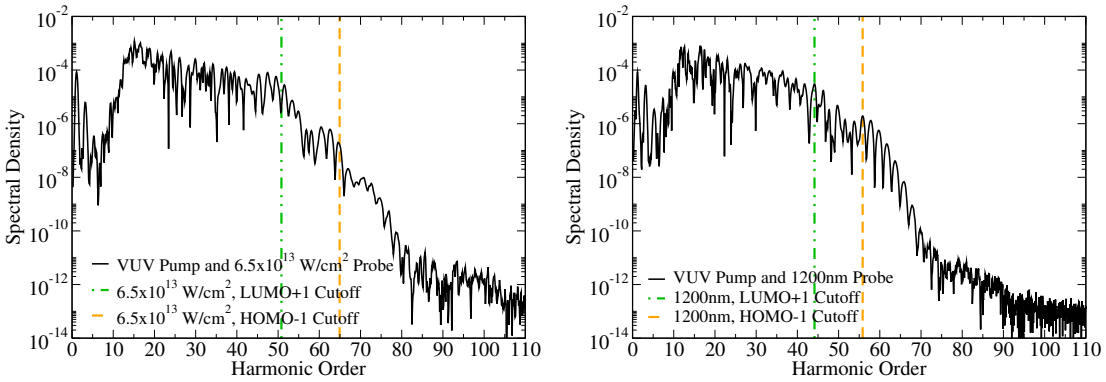

(a) $\lambda = 1450\,\text{nm}$, $I = 6.5\times10^{13}\,\text{W/cm}^2$ (b) $\lambda = 1200\,\text{nm}$, $I = 1.0\times10^{14}\,\text{W/cm}^2$

Figure 4.15: High harmonic spectra from acetylene following interactions with different setups of laser pulses. In all cases the VUV pump pulse is an 8-cycle pulse with wavelength $\lambda = 102\,\text{nm}$ and a peak intensity of $I = 1.0\times10^{12}\,\text{W/cm}^2$. In panel (a), the IR probe is a 5-cycle pulse with wavelength $\lambda = 1450\,\text{nm}$ and a peak intensity of $I = 6.5\times10^{13}\,\text{W/cm}^2$. In panel (b), the IR probe is a 6-cycle pulse with wavelength $\lambda = 1200\,\text{nm}$ and a peak intensity of $I = 1.0\times10^{14}\,\text{W/cm}^2$. The vertical lines indicate the harmonic cutoffs predicted by the semiclassical cutoff law, Eq. (1.14), for recombination to either the LUMO+1 or HOMO-1.

Taking this bound state to be one of the lowest field-free Kohn-Sham states, $\phi_k(\boldsymbol{r})$, of the molecule (and I_p the magnitude of the energy of the state), we have calculated the recombination matrix elements of an ionized electron recombining to various states of acetylene in the parallel orientation (see Appendix A for further details about how these are calculated). These are shown in Fig. 4.14, where recombination to field-free occupied and unoccupied states are shown separately in Figs. 4.14(a) and 4.14(b) respectively, for clarity. We highlight in particular the LUMO+1 recombination matrix element, noting the presence of a minimum around harmonic 81: close to the predicted inner plateau cutoff.

To test if this minimum in the LUMO+1 recombination matrix element is responsible for the discrepancy between the expected and observed inner plateau cutoffs, we now consider replacing the probe pulse in our pump-probe setup with one of two different probe pulses. In the first case, we reduce the probe intensity to $I = 6.5\times10^{13}\,\text{W/cm}^2$, keeping the wavelength at $\lambda = 1450\,\text{nm}$. In the second case, we keep the probe intensity at $I = 1.0\times10^{14}\,\text{W/cm}^2$, but reduce the wavelength to $\lambda = 1200\,\text{nm}$. As was discussed in Section 4.2.2, the predicted cutoff is dependent on both the wavelength and intensity of the driving pulse. With these two new probe pulses we expect the inner plateau cutoffs to be reduced to around harmonic 51 and harmonic 44, for the lower

intensity and lower wavelength cases respectively. These cutoff values are far below the minimum in the recombination matrix element for the LUMO+1 seen in Fig. 4.14(b). The harmonic spectra produced in pump-probe setups with these two choices of probe pulse (the pump pulse remains the same as above) are shown in Fig. 4.15. In both cases, we see that the inner plateau cutoff matches what is predicted by the three-step model cutoff law for recombination to the LUMO+1. We also note that with these varied laser parameters, the outer plateau cutoff remains in agreement with the cutoff expected for recombination to the HOMO-1 (harmonic 65 and harmonic 56 in Figs. 4.15(a) and 4.15(b) respectively).

These results support our conclusions drawn above, and the idea that the discrepancy in the inner plateau cutoff is due to a minimum in the recombination matrix element for the LUMO+1. In the next section we will test our conclusions further, by now considering alternative pump pulses.

4.5.5 Effect of varying VUV pump wavelength

If our conclusion, that the enhancement of the plateau harmonics originates from HOMO-1 $\rightarrow$ LUMO+1 excitation followed by HHG from the LUMO+1, is correct, the enhancement effect should be sensitive to the wavelength (i.e., the photon energy) of the pump pulse. To investigate this wavelength-sensitivity, three additional pump-probe calculations were performed. In all three cases the pump wavelength is changed from $\lambda = 102\,\text{nm}$ to one of the following:

(a) $\lambda = 160\,\text{nm}$ (0.285 Ha): In this case the photon energy is too small to excite the HOMO-1 $\rightarrow$ LUMO+1 or HOMO-2 $\rightarrow$ LUMO+2 transitions with a single photon;

(b) $\lambda = 82\,\text{nm}$ (0.556 Ha): In this case the photon energy is equal to the energy required to ionize directly from the HOMO-1;

(c) $\lambda = 65\,\text{nm}$ (0.701 Ha): In this case the photon energy is large enough to ionize directly from the HOMO, HOMO-1 and HOMO-2.

These photon energies are shown schematically in Fig. 4.16. The number of VUV pulse cycles is varied between the different cases, in order to keep the total VUV pulse duration approximately constant in all calculations ($T_{\text{VUV}} \approx 110\,\text{a.u.} = 2.66\,\text{fs}$). The

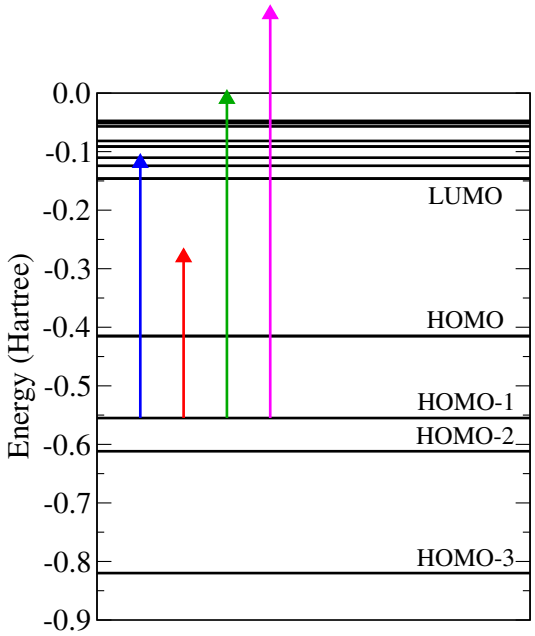

Figure 4.16: Schematic representation of the four VUV pump pulse wavelengths described in the text and associated with the harmonic spectra shown in Fig. 4.17. The length of the arrows correspond to the photon energies associated with the following wavelengths: blue $\rightarrow \lambda = 102\,\text{nm}$; red $\rightarrow \lambda = 160\,\text{nm}$; green $\rightarrow \lambda = 82\,\text{nm}$; magenta $\rightarrow \lambda = 65\,\text{nm}$.

harmonic spectra produced from acetylene interacting with these pump pulses followed in each case by the 5-cycle ($T_{\text{IR}} = 999.8\,\text{a.u.} = 24.18\,\text{fs}$), $\lambda = 1450\,\text{nm}$, $I = 1.0\times10^{14}\,\text{W/cm}^2$ probe pulse are shown in Fig. 4.17.

Clearly from these plots we see that the inner plateau enhancement mechanism is highly sensitive to the VUV photon energy. With a VUV pulse tuned to the HOMO-1 $\rightarrow$ LUMO+1 transition, as in Fig. 4.17(a), we see a large enhancement of the inner plateau harmonics, as presented in previous sections. Increasing the wavelength of the VUV pulse (reducing the photon energy), as in the spectrum shown in Fig. 4.17(b), we see the enhancement effect disappear across the inner plateau, since the VUV pulse is no longer able to excite the HOMO-1 $\rightarrow$ LUMO+1 transition with a single photon. The only enhancement we observe compared to the probe-only spectrum is at a few peaks at low harmonic orders, due to bound-bound transitions (since the VUV photon energy is still large enough to excite the HOMO $\rightarrow$ LUMO transition).

Reducing the wavelength of the VUV pulse (i.e., increasing the photon energy), as in Figs. 4.17(c) and 4.17(d), we observe two changes. Firstly, when the VUV photon energy is increased so that it is just large enough to ionize directly from the HOMO-1

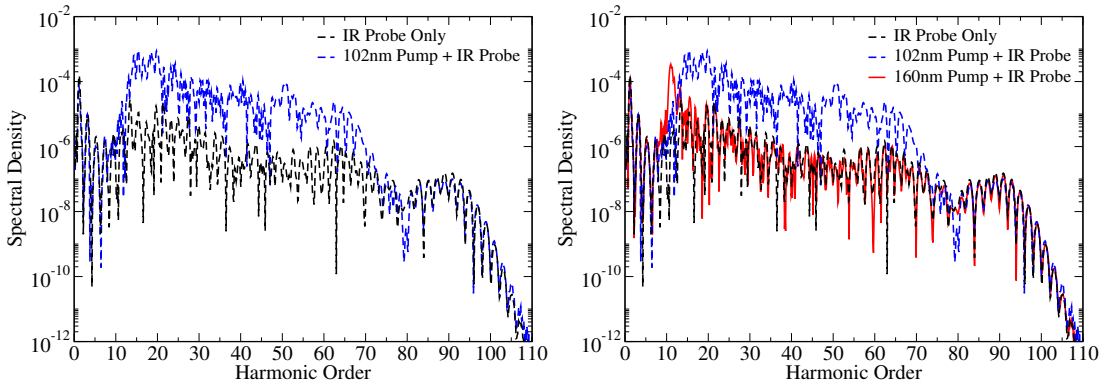

(a) $\lambda = 102\,\text{nm}$

(b) $\lambda = 160\,\text{nm}$

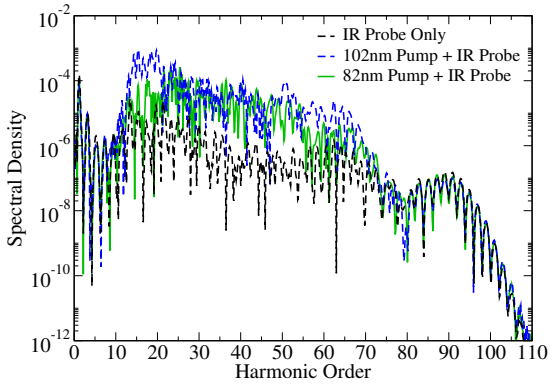

(c) $\lambda = 82\,\text{nm}$

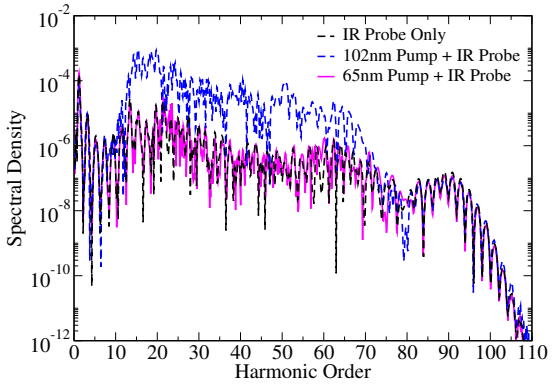

(d) $\lambda = 65\,\text{nm}$

Figure 4.17: High harmonic spectra from acetylene following interactions with different setups of laser pulses. The IR probe pulse is a 5-cycle pulse with wavelength $\lambda = 1450\,\text{nm}$ and a peak intensity of $I = 1.0\times10^{14}\,\text{W/cm}^2$, while the VUV pump pulse is varied between panels. The pulses in all cases are linearly polarized along the z-axis, and the molecular axis also lies along the z-axis. Panel (a) presents the two parallel spectra from Fig. 4.9; for comparison, these two spectra are also shown in the other three panels. The VUV pulse in all cases has a peak intensity of $I = 1.0\times10^{12}\,\text{W/cm}^2$, and the following wavelengths and number of cycles: (a) $\lambda = 102\,\text{nm}$, 8 cycles (duration = 112.5 a.u.); (b) $\lambda = 160\,\text{nm}$, 5 cycles (duration = 110.3 a.u.); (c) $\lambda = 82\,\text{nm}$, 10 cycles (duration = 113.0 a.u.); (d) $\lambda = 65\,\text{nm}$, 12 cycles (duration = 107.6 a.u.).

with a single photon, as in Fig. 4.17(c), we see a reduction in the enhancement of the window of bound-bound harmonics seen with a $\lambda = 102\,\text{nm}$ VUV pump pulse. This is due to the fact that the higher photon energy of a $\lambda = 82\,\text{nm}$ pulse will less efficiently populate the LUMO+1 than a $\lambda = 102\,\text{nm}$ pulse, with a subsequent reduction in bound-bound transitions. However, this choice of VUV pump pulse can populate some higher-lying (near-threshold) states, from which HHG may occur, and so we still see some enhancement of the inner plateau harmonics. Secondly, when the VUV wavelength is reduced further, as in Fig. 4.17(d), so that the photon energy is significantly greater than the energy required to ionize directly from the HOMO-1, we again observe no

inner plateau enhancement.

4.5.6 Effect of pump-probe delay

In experimental pump-probe setups, the main "control knob" that can be varied is the time delay between the two pulses. Following this train of thought, several additional calculations were performed on the parallel VUV pump ($\lambda = 102\,\text{nm}$, $I = 1.0\times10^{12}\,\text{W/cm}^2$) + parallel IR probe ($\lambda = 1450\,\text{nm}$, $I = 1.0\times10^{14}\,\text{W/cm}^2$) setup described above, but in which the time delay between the two pulses was varied.

Figure 4.18 shows the spectrum from one such calculation in which the VUV pulse is applied during the IR pulse, beginning after 2 IR pulse cycles (we will refer to this as the overlapping pulses setup). Also shown in this figure for comparison are the previously shown spectra for the case in which the probe pulse begins immediately after the pump pulse has ended (the sequential pulses setup) and the case in which only the IR probe is applied (the probe-only setup). All pulses are polarized parallel to the molecular axis.

Comparing the 3 spectra in Fig. 4.18, we see that while applying the pump pulse during the probe pulse produces an enhancement of the inner plateau harmonics relative to the probe-only spectrum, the level of enhancement is less than in the spectrum obtained when the pulses are applied sequentially. This is because a VUV pulse applied to the ground state molecule before the IR pulse is much more effective at exciting the HOMO-1 $\rightarrow$ LUMO+1 transition than one applied during the IR pulse, when the system has already been excited.

Looking at the window of low-order harmonics we previously associated with bound-bound transitions, we see that overlapping the pump and probe pulses causes a broadening and enhancement of the harmonic peaks in this window, compared to the sequential pulses setup. This is again due to the state of the system when the VUV pump pulse is applied. In the sequential pulses setup, the molecule is in its ground state when the VUV pulse is applied. During the interaction of the pump pulse with the molecule, the LUMO+1 is populated, and the subsequent transitions back to the ground state produce relatively well defined harmonics. In the overlapping pulses setup, the VUV pulse is applied when the molecule has already been distorted by the strong IR pulse, which may have already excited some transitions to the LUMO+1. Now the VUV pulse

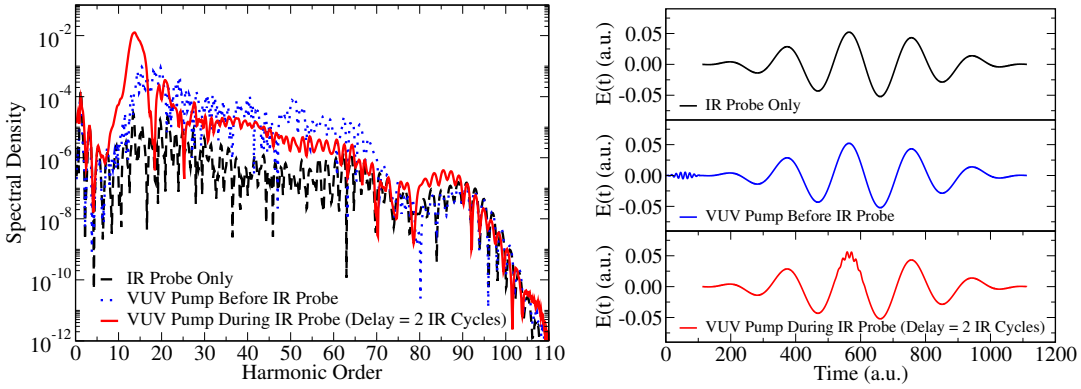

(a) Harmonic spectra

(b) Electric fields

Figure 4.18: Effect of pump-probe delay on enhancement of harmonic spectrum. (a) High harmonic spectra from acetylene following interactions with different setups of laser pulses. The IR probe pulse is a 5-cycle pulse with wavelength $\lambda = 1450\,\text{nm}$ and a peak intensity of $I = 1.0\times10^{14}\,\text{W/cm}^2$, while the VUV pump pulse is an 8-cycle pulse with wavelength $\lambda = 102\,\text{nm}$ and a peak intensity of $I = 1.0\times10^{12}\,\text{W/cm}^2$. The pulses in all cases are linearly polarized along the z-axis, and the molecular axis also lies along the z-axis. The dashed black line is the spectrum when only the IR probe pulse is applied. The dotted blue line is the spectrum when the IR probe pulse begins immediately after the VUV pump pulse has ended. The solid red line is the spectrum when the IR probe pulse begins first, with the VUV pump pulse beginning after 2 cycles of the IR pulse. (b) The z-components of the three electric fields, where the top and bottom pulses have been shifted in time so the IR pulse begins at the same time in all three panels.

can excite more transitions to the LUMO+1, as before, but can also stimulate the emission of the low-order (bound-bound) harmonics. The broadening of the peak reflects the distorted nature of the molecule and the associated shifting of energy levels at the time when the VUV pulse is applied.

4.5.7 Effect of VUV pump at different molecular orientations

In Section 4.4 it was shown how the orientation of the molecular axis relative to the laser polarization direction had a significant effect on the response of the system, specifically on the ionization rate and harmonic response. In the pump-probe calculations described thus far, both pulses have always been polarized along the molecular axis. We now consider the harmonic response in the pump-probe setup when the angle between the molecular axis and the laser polarization direction is varied. Figure 4.19 presents the spectra obtained in three different orientations: Fig. 4.19(a) shows the previously shown spectrum for the case where both pulses are polarized parallel to the molecular

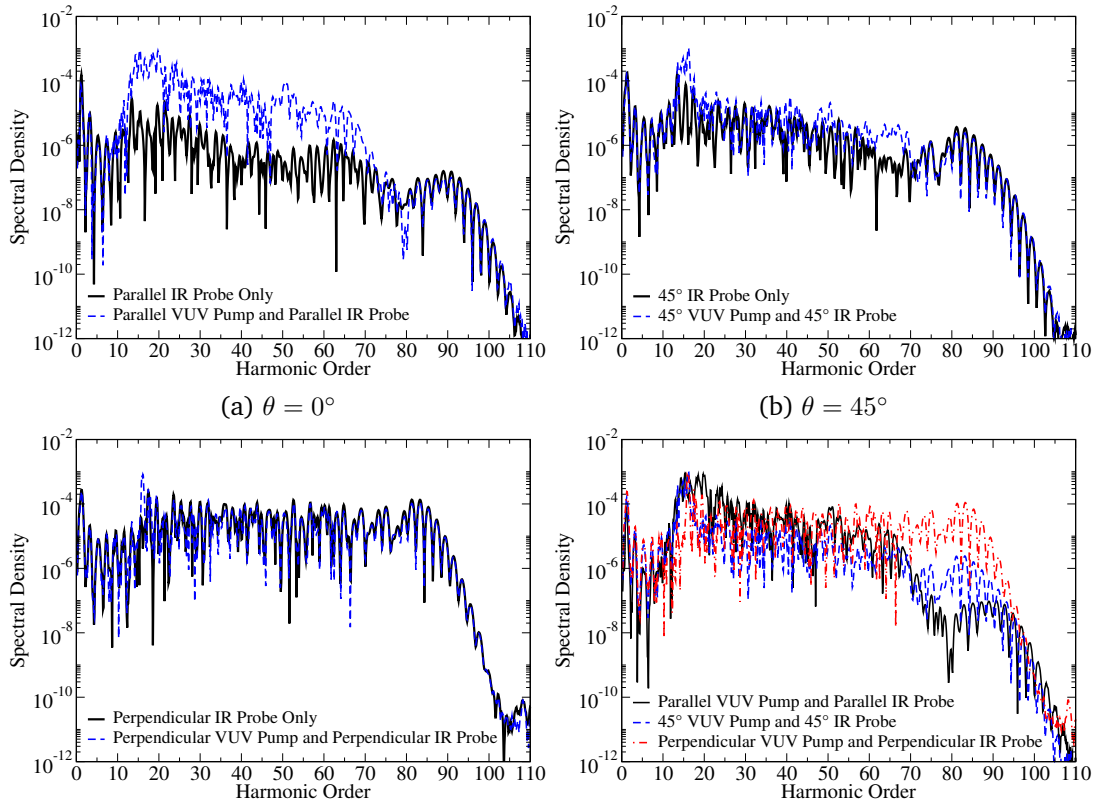

(a) $\theta = 0°$ (b) $\theta = 45°$

(c) $\theta = 90°$ (d) Pump-probe, $\theta = 0°, 45°, 90°$

Figure 4.19: High harmonic spectra from acetylene following interaction with a VUV pump pulse and a mid-IR probe pulse, for three different orientations of the molecule with respect to the laser polarization direction. The IR probe pulse is a 5-cycle pulse with wavelength $\lambda = 1450\,\text{nm}$ and a peak intensity of $I = 1.0\times10^{14}\,\text{W/cm}^2$, while the VUV pump pulse is an 8-cycle pulse with wavelength $\lambda = 102\,\text{nm}$ and a peak intensity of $I = 1.0\times10^{12}\,\text{W/cm}^2$. The pulses in all cases are linearly polarized along the z-axis, while the molecule is aligned in one of three ways: panels (a) and (c) correspond to the cases where the molecular axis lies along the z-axis and x-axis respectively; panel (b) corresponds to the intermediate case in which the molecular axis is at an angle of 45° to both the z- and x-axes. The spectra for the three pump-probe cases are compared directly in panel (d).

axis; Fig. 4.19(b) shows the spectrum when the molecular axis is at angle of $\theta = 45°$ to the polarization direction of the two pulses; Fig. 4.19(c) shows the spectrum for the perpendicular case, in which the molecular axis is at an angle of $\theta = 90°$ to the laser polarization direction. In each case both the probe-only and pump-probe spectra are shown.

These figures show that the plateau enhancement due to the addition of the VUV pump pulse is greatest when both pump and probe pulses are polarized along the molecular axis. In addition, when both pulses are polarized perpendicular to the molecular axis,

no harmonic enhancement is observed, with the exception of a single peak due to a bound-bound transition. Looking specifically at some individual peaks in the spectrum, we see that the addition of the VUV pulse can actually causes a slight reduction in the harmonic intensity.

As was shown in Fig. 4.12 for the parallel orientation, Fig. 4.20 presents time-frequency analyses of the two harmonic spectra from the perpendicular orientation shown in Fig. 4.19(c). We immediately see a much higher intensity of harmonics in the probe-only case than was seen in the parallel probe-only case (Fig. 4.12(a)), as expected from the results and discussion of Section 4.4. Comparing now Figs. 4.20(a) and 4.20(b), we see that while the addition of the VUV pump clearly affects the harmonic response, the effect is much less pronounced than in the parallel orientation, since the harmonic response in the perpendicular probe-only case is already strong. Indeed, comparing Figs. 4.20(a) and 4.20(b) for times greater than 600 a.u., we see that the harmonic responses with or without the pump pulse are almost indistinguishable.

To explain these results, we again consider the symmetries of the Kohn-Sham orbitals, the allowed and forbidden transitions given in Table 4.5(b), and the overlaps of the time-dependent states with the initial, field-free, orbitals. These calculated overlaps for the perpendicular pump-probe setup are shown in Fig. 4.21(a). From this figure we see that in the perpendicular orientation, the VUV pump is ineffective at exciting the HOMO-1 $\rightarrow$ LUMO+1 transition. Instead, during the VUV pulse we see some excitation from the HOMO-2 to the LUMO(a) (although the LUMO(a) is less effectively populated by this pump pulse than the LUMO+1 pulse was in the parallel case, due to the chosen photon energy). Considering that the photon energy is slightly larger than the energy required to ionize directly from the HOMO, the VUV pump likely also populates a number of high-lying (near-threshold) states, for which the overlaps with the time-dependent orbitals have not been calculated. During the IR pulse, we see HOMO-2 $\rightarrow$ LUMO(a) transitions as well as HOMO $\rightarrow$ LUMO+2 transitions, with similar magnitudes as in the probe-only case shown in Fig. 4.7(b).

We can therefore explain the lack of enhancement of the harmonic spectrum when the combined pump-probe setup is applied to acetylene aligned in the perpendicular orientation as a result of the symmetries of the orbitals, and the selection rules gov-

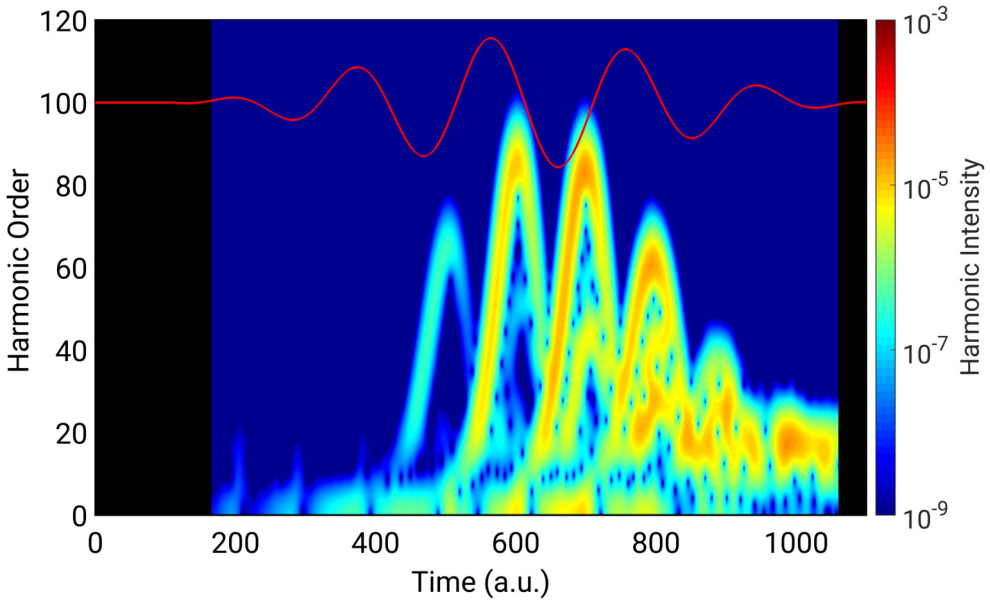

(a) Perpendicular IR Probe

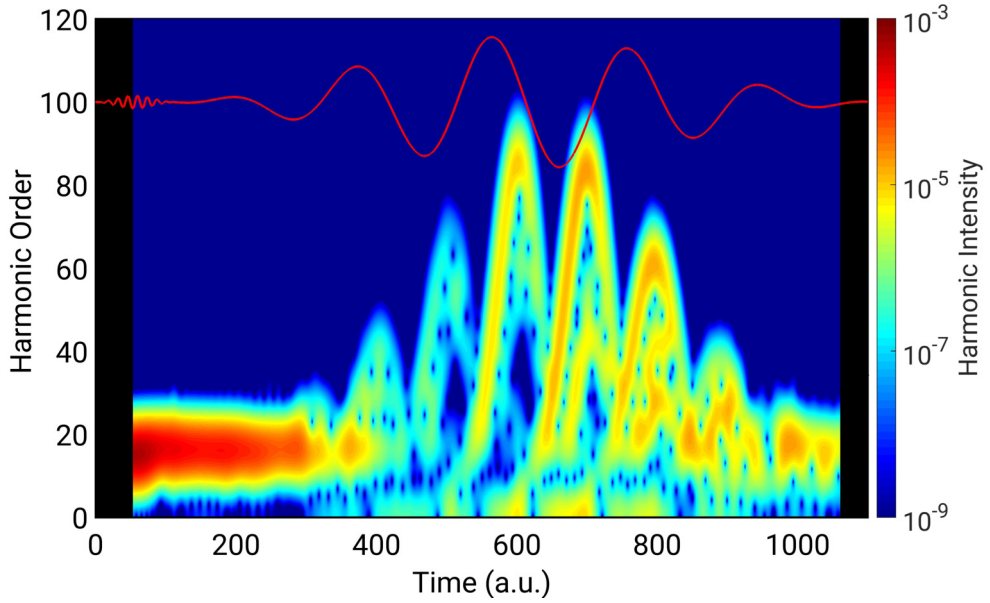

(b) Perpendicular VUV Pump and Perpendicular IR Probe

Figure 4.20: Time-frequency analyses of the two "perpendicular" HHG spectra shown in Fig. 4.19(c). In both panels a 5-cycle IR pulse with wavelength $\lambda = 1450\,\text{nm}$ and a peak intensity of $I = 1.0\times10^{14}\,\text{W/cm}^2$ is applied. In panel (b), this pulse is preceded by an 8-cycle VUV pulse with wavelength $\lambda = 102\,\text{nm}$ and a peak intensity of $I = 1.0\times10^{12}\,\text{W/cm}^2$. The data in panel (a) has been shifted in time so that the IR pulse begins at the same time in both panels. Both pulses are linearly polarized along the z-axis, while the the molecular axis is aligned perpendicular to this, along the x-axis. The red lines denote the z-component of the electric field.

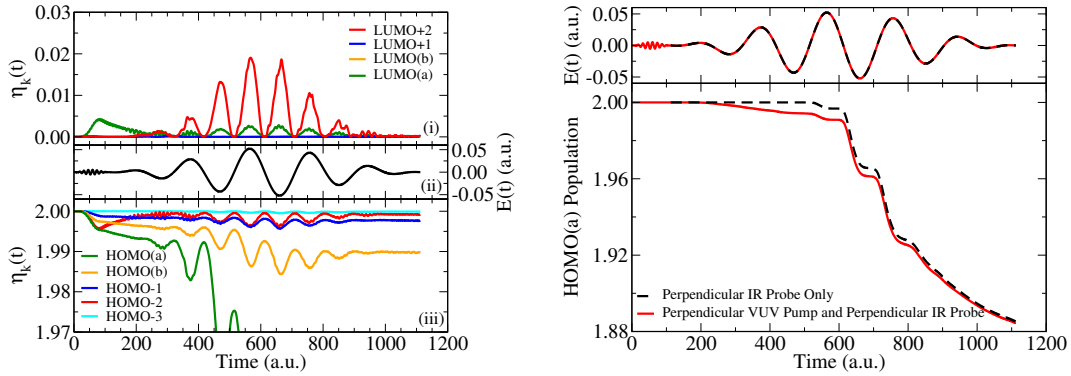

(a) Population in field-free orbitals

(b) Population in time-dependent HOMO(a)

Figure 4.21: Response of different initial and time-dependent Kohn-Sham orbitals to different setups of laser pulses, when the molecular axis is aligned perpendicular to the laser polarization direction. In panel (a), Eq. (4.2) has been used to calculate the electronic population in each of the 9 lowest initial Kohn-Sham orbitals $\phi_k(\boldsymbol{r})$, for the perpendicular pump-probe setup. In panel (b) the populations of the time-dependent HOMO(a), calculated using Eq. (3.69), are shown for the perpendicular pump-probe and perpendicular probe-only cases. In both laser setups, a 5-cycle IR pulse with wavelength $\lambda = 1450\,\text{nm}$ and a peak intensity of $I = 1.0\times10^{14}\,\text{W/cm}^2$ is applied. In the pump-probe setup, the IR pulse is preceded by an 8-cycle VUV pulse with wavelength $\lambda = 102\,\text{nm}$ and a peak intensity of $I = 1.0\times10^{12}\,\text{W/cm}^2$. Both pulses are linearly polarized along the z-axis, while the the molecular axis is aligned perpendicular to this, along the x-axis.

erning the transitions between them. In the parallel orientation considered previously, the HOMO-1 $\rightarrow$ LUMO+1 transition was efficiently excited by a parallel VUV pump, following which the σ-type LUMO+1 was ionized by a parallel probe pulse, initiating the HHG process. In the perpendicular orientation on the other hand, the HOMO-1 $\rightarrow$ LUMO+1 transition is not efficiently excited by the perpendicular VUV pump. Instead the HOMO-2 $\rightarrow$ LUMO(a) transition is excited. The excited population does not remain in the LUMO(a) for a significant length of time however, as the LUMO+1 population did in the parallel case. The effect of this is that while bound-bound transitions from the LUMO(a) result in the enhancement of a single peak in the harmonic spectrum, the population excited to the LUMO(a) by the VUV pump does not play a significant role in the subsequent HHG process. In addition, from Fig. 4.21(b) we see that the VUV pump pulse causes ionization from the HOMO(a) to occur earlier in the calculation than in the perpendicular probe-only case; this has the effect of reducing the population available for tunnel ionization during the IR pulse, and subsequently can lead to a small reduction in the intensities of some of the high harmonics in Fig. 4.19(c).

Finally, we note that since the addition of the VUV pump pulse in the parallel orientation increases the intensity of the inner plateau harmonics to a level comparable to that of the plateau harmonics in the perpendicular probe-only case, and since the addition of the VUV pump has little effect on the harmonic response in the perpendicular orientation, the addition of a VUV pump pulse could prove useful in boosting the overall harmonic response of an unaligned sample of molecules.

4.5.8 Summary

In this section we have investigated the role of the HOMO-1 $\rightarrow$ LUMO+1 transition in the high harmonic generation process in acetylene. We showed first that when the molecular axis is aligned parallel to the laser polarization direction, by applying a VUV pump pulse tuned to the HOMO-1 $\rightarrow$ LUMO+1 energy gap before the IR probe pulse is applied, the high harmonic response in acetylene can be dramatically enhanced. This enhancement was shown to be due to two separate mechanisms. Firstly, after the VUV pump pulse is applied and has promoted some electronic population to excited states, the molecule begins to relax back to its ground state, with associated bound-bound transitions occurring. The VUV pump increases the population of the LUMO+1, which leads to an increase in these bound-bound transitions, and the observed enhancement of a window of low-order harmonics. Secondly, the population of the LUMO+1 by the VUV pump pulse allows tunnel ionization and subsequent high harmonic generation to occur earlier in the IR probe pulse, due to the lower ionization potential of the LUMO+1 than the HOMO, HOMO-1, etc.. Increased ionization from and recombination back to the LUMO+1 results in the observed enhancement of the inner plateau harmonics.

In Section 4.5.4, we addressed the issue of the discrepancy between the observed inner plateau cutoff and the cutoff predicted by the three-step model for HHG with recombination back to the LUMO+1. The lower than predicted cutoff was shown to be due to a minimum near the expected cutoff harmonic in the dipole recombination matrix element for a continuum electron recombining to the LUMO+1. When the IR wavelength or intensity are reduced, so that the predicted cutoff is far below this minimum, it was shown that the position of the cutoff is as expected for recombination back to the LUMO+1.

Finally in Sections 4.5.5, 4.5.6 and 4.5.7, we considered the response of the system when various aspects of the laser setup were varied, namely the VUV wavelength, the timing of the VUV pulse relative to the IR pulse, and the polarization direction of the pulses relative to the orientation of the molecular axis. In each of these sections we showed how the observed effects fit with our explanation of the enhancement mechanism outlined above.

In the next section, we will conclude our investigations of acetylene by briefly considering the effect of the ionic motion on the dynamics of the system.

4.6 Effect of ionic motion

In an earlier work using EDAMAME to study HHG in benzene [46], it was found that ionic motion had a large influence on the calculated harmonic spectra. Specifically, it was found that allowing the ions to move during the calculation resulted in an enhanced harmonic response compared to when they were fixed in their initial positions throughout the calculation. The pulse in this case was circularly polarized, in the plane of the molecule. This increased harmonic response for moving nuclei was explained as being due to a mechanism in which an electron is tunnel ionized from one atom, but can recombine at an adjacent atomic site, due to the circularly polarized field causing the ionized electron to spiral. It was shown that when the ions were allowed to move, they traced out circular or elliptical trajectories. If the displacement of an ion from its equilibrium position was sufficiently increased, the probability of an ionized electron recombining at that atomic site was also increased, with such an increase leading naturally to the observed increased intensity of plateau harmonics. While linearly polarized pulses were studied elsewhere in this paper, the effect of ionic motion in the case of linear polarization was not specifically discussed.

In all the calculations presented on acetylene in the above sections, ionic motion has been included. As a calculation progresses, the position of each ion is output, which allows us to plot the ionic trajectories. Two illustrative examples of these trajectories are shown in Fig. 4.22, for the probe-only cases discussed in Section 4.4. In Fig. 4.22(a), the trajectories of the ions when the pulse is polarized along the molecular axis are shown, while the trajectories for the perpendicular case are shown in Fig. 4.22(b). In

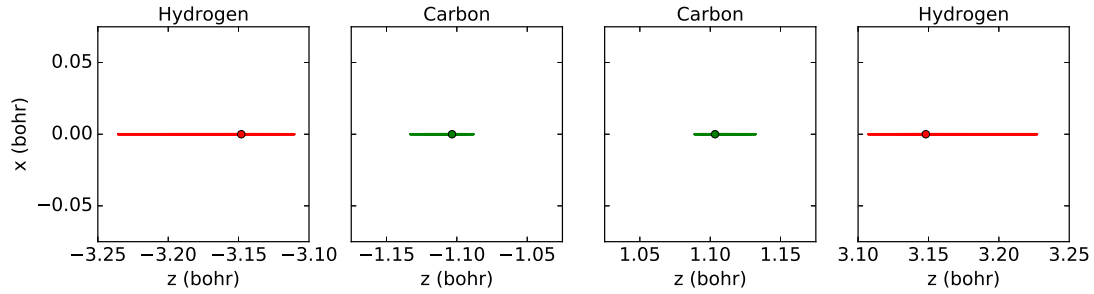

(a) $\theta = 0°$ (parallel)

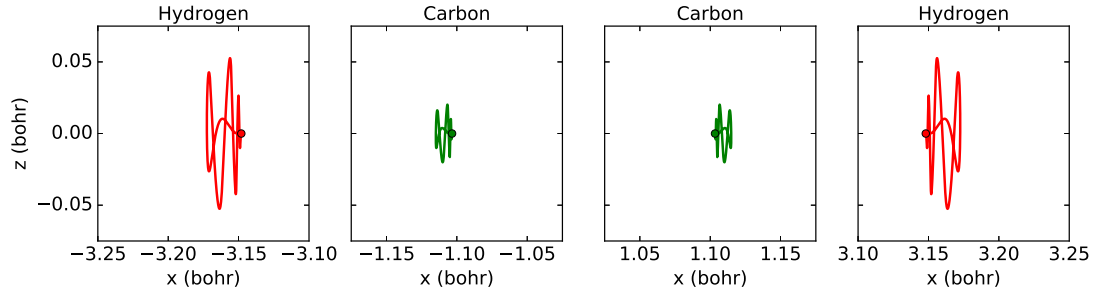

(b) $\theta = 90°$ (perpendicular)

Figure 4.22: Trajectories of the individual ions of acetylene during interaction with a 5-cycle laser pulse with wavelength $\lambda = 1450\,\text{nm}$ and a peak intensity of $I = 1.0\times10^{14}\,\text{W/cm}^2$. The pulse is linearly polarized along the z-axis, while the molecular axis is aligned along either the z-axis ($\theta = 0°$, parallel orientation; panel (a)) or the x-axis ($\theta = 90°$, parallel orientation; panel (b)). The circle markers indicate the initial positions of the ions.

each of these figures, the trajectory of each ion is plotted on a separate set of axes, since the displacements are small relative to the size of the molecule. In the parallel case, Fig. 4.22(a), we see that the motion is confined entirely along the laser polarization direction (the z-axis), due to the symmetrical nature of the molecule about this axis. In the perpendicular case, Fig. 4.22(b), we see a different behaviour. Now, although the motion is mainly along the laser polarization direction (the z-axis), there is also some motion perpendicular to this, along the molecular axis (along the x-axis). In both parallel and perpendicular orientations, we see that the hydrogen ions respond much more strongly to the field than the heavier carbon ions. However, in all cases, we note again that the ions move a relatively small distance during the calculation.

When considering the ionization from different Kohn-Sham orbitals due to a single IR pulse in Section 4.4.3, we briefly commented on the comparison of our results to the results of Russakoff *et al.* [273]. This work, and a subsequent work [278], reported

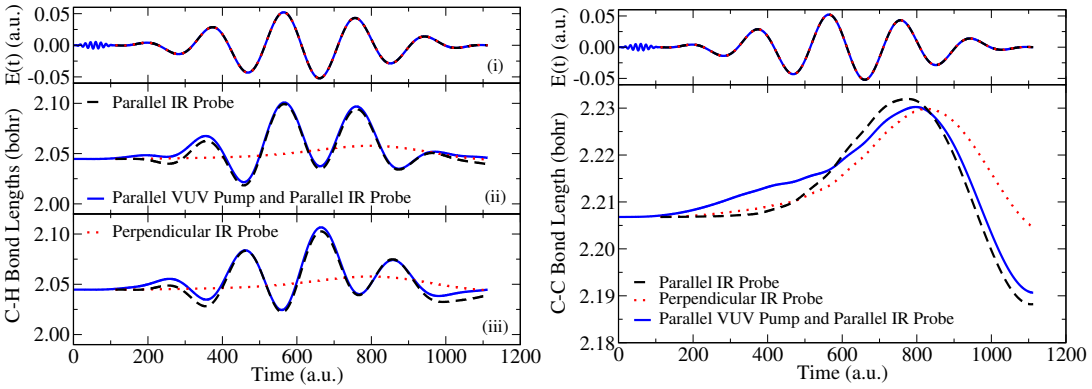

(a) C-H bond lengths

(b) C-C bond length

Figure 4.23: Variations in bond lengths in acetylene during the interaction with different setups of laser pulses. The IR probe pulse is a 5-cycle pulse with wavelength $\lambda = 1450\,\text{nm}$ and a peak intensity of $I = 1.0\times10^{14}\,\text{W/cm}^2$, while the VUV pump pulse is an 8-cycle pulse with wavelength $\lambda = 102\,\text{nm}$ and a peak intensity of $I = 1.0\times10^{12}\,\text{W/cm}^2$. The pulses in all cases are linearly polarized along the z-axis, while the molecule is aligned along the z-axis in the parallel cases, and along the x-axis in the perpendicular case. Panels (a) and (b) show the C-H and C-C bond lengths respectively. The z-component of the E-field is shown in the top sub-panel in both cases. In panel (a), the middle sub-panel corresponds to the C-H bond between the carbon and hydrogen ions positioned on the positive side of the z-axis (in the parallel orientation) or the x-axis (in the perpendicular orientation), while the bottom sub-panel corresponds to the C-H bond between the carbon and hydrogen ions positioned on the negative side.

a significant enhancement of ionization from the HOMO-1 and HOMO-2 when the C-H bonds are stretched to beyond twice the equilibrium distance. From Fig. 4.22 it is already quite clear that the laser parameters used in our work do not cause such significant bond stretching. This point is illustrated explicitly in Fig. 4.23, in which we have plotted the changes in the C-H and C-C bond lengths over time, for three different laser setups (the C-H bond lengths are shown in Fig. 4.23(a) while the C-C bond length is shown Fig. 4.23(b)). From these figures we can assume that the bond stretching and associated ionization enhancement mechanism reported in [273, 278] will not be an important factor in the work reported in this chapter.

In order to investigate further whether or not this ionic motion is an important factor in the dynamics of the molecule with these laser parameters, we repeated several of our simulations but now keeping the ions fixed. The results of these calculations are illustrated in Fig. 4.24. Figures 4.24(a) and 4.24(b) show the harmonic spectra for the parallel and perpendicular probe-only setups, respectively, with and without ionic motion. Figure 4.24(c) shows the total populations in the grid for these four different

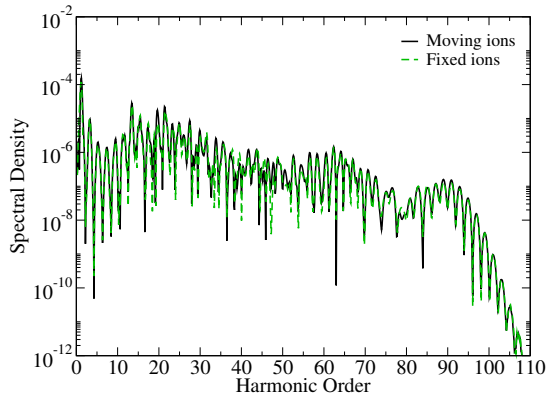

(a) HHG, $\theta = 0°$

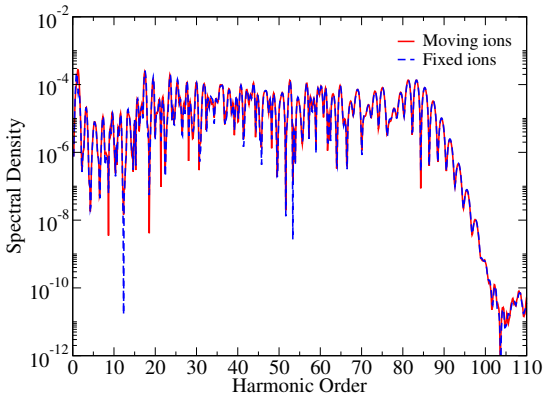

(b) HHG, $\theta = 90°$

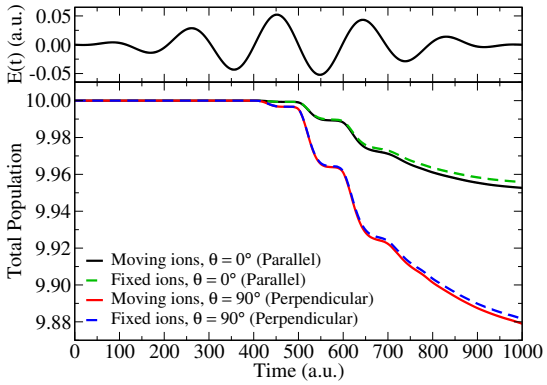

(c) Ionization, $\theta = 0°, 90°$

Figure 4.24: Effect of ionic motion on the response of acetylene to a 5-cycle laser pulse with wavelength $\lambda = 1450\,\text{nm}$ and a peak intensity of $I = 1.0\times10^{14}\,\text{W/cm}^2$. The pulse is linearly polarized along the z-axis, while the molecular axis is aligned along either the z-axis ($\theta = 0°$, parallel orientation) or the x-axis ($\theta = 90°$, parallel orientation). Panel (a) shows the harmonic spectra produced in the parallel orientation when the ions are allowed to move or are fixed in place. Panel (b) shows the same as (a), but for the perpendicular orientation. Panel (c) shows the changes in the total electronic population in the grid over time for the four different cases.

cases. Looking at the ionization with or without ionic motion included (Fig. 4.24(c)), we see that allowing the ions to move increases the total population depletion, although the effect is very small. Considering now the harmonic spectra, the effect of the ionic motion is even less obvious, with the moving ions and fixed ions spectra nearly identical in both parallel and perpendicular cases. In the parallel case, there are some slight changes in individual peak intensities between the moving ions and fixed ions spectra; in the perpendicular case there is near perfect agreement between the two spectra.

While only the probe-only cases are shown explicitly here for brevity, we have also checked the effect of the ionic motion on the dynamics of the pump-probe setup of

Section 4.5. In this case the result is similar to that shown above for the probe-only cases: the ionic motion has only a minimal effect on the ionization and high harmonic generation, for the chosen pulse parameters.

4.7 Conclusions

In this chapter we have presented results from a series of simulations of acetylene interacting with a variety of laser pulses. In Section 4.2 we discussed some of the most relevant experimental and theoretical work on acetylene from the literature. In Section 4.3 we presented results showing how EDAMAME can accurately reproduce the static properties of acetylene, such as the bond lengths and ionization potentials.

Section 4.4 focused on the dynamics of acetylene interacting with a linearly polarized mid-IR laser pulse. The effects of the molecular orientation relative to the laser polarization direction were investigated by studying the ionization from the Kohn-Sham orbitals and the harmonic response of the system. Both ionization and high harmonic generation were found to increase as the angle between the laser polarization direction and the molecular axis was increased from a parallel to a perpendicular orientation. This was shown to be a result of an increased response of one form of the degenerate HOMO in the perpendicular orientation. In the parallel orientation, it was shown that the main contributor to the high harmonic spectrum was not the HOMO, but the HOMO-1 and HOMO-2. The existence of an inner plateau in the parallel spectrum was also discussed. By considering how the populations of the field-free occupied and unoccupied orbitals varied over time, it was suggested that the origin of the inner plateau region was related to the excitation of the HOMO-1 $\rightarrow$ LUMO+1 transition.

This HOMO-1 $\rightarrow$ LUMO+1 transition, and its role in the high harmonic generation process, was investigated further in Section 4.5 by preceding the IR probe pulse with a lower intensity VUV pump pulse, with a photon energy chosen to match the HOMO-1 $\rightarrow$ LUMO+1 energy gap. In the parallel orientation, the addition of such a VUV pump pulse was found to dramatically enhance the intensity of the inner plateau harmonics, while having little to no effect on the harmonics beyond the inner plateau cutoff. By again considering the populations of the field-free states, and by performing time-frequency analyses of the probe-only and pump-probe harmonic spectra, the origin of

this inner plateau enhancement was shown to be due to increased excitation of the HOMO-1 $\rightarrow$ LUMO+1 transition, followed by ionization from and recombination back to the LUMO+1. A discrepancy between the inner plateau cutoff and the cutoff predicted by the three-step model cutoff law was found to be due to a minimum in the recombination matrix element for the LUMO+1. Harmonic spectra from several other pump-probe setups were also shown, and these results were discussed in the context of our understanding of the observed enhancement mechanisms. Finally, in Section 4.6, the (small) effect of ionic motion on the ionization and harmonic response of the system was briefly discussed.

In the next chapter, we will turn our attention to the study of high harmonic generation in three larger molecules, namely uracil, thymine and 5-fluorouracil. These molecules are of great interest due to their biological significance, but their large size and increased complexity compared to acetylene make them much more challenging to describe computationally.

Chapter 5

High harmonic generation in nucleobases and radiosensitisers

5.1 Introduction

In the previous chapter, we studied the dynamic response of acetylene, a linear hydrocarbon with 14 electrons, to an intense mid-IR laser pulse. The linearity and small size of this molecule enabled us to conduct an in-depth investigation of the response of acetylene to a range of laser wavelengths, intensities and polarization directions. Understanding the response of a relatively simple molecule such as acetylene is an essential first step towards understanding the response of more complex molecules. One such class of molecules of particular interest is that of biological molecules.

In this chapter we study the response of three biologically relevant molecules to intense, mid-IR laser pulses. These molecules are: uracil ($C_4H_4N_2O_2$), thymine (also known as 5-methyluracil, $C_5H_6N_2O_2$), and 5-fluorouracil ($C_4H_3FN_2O_2$). These three molecules are all pyrimidine derivatives, and differ only in what is bonded to the 5th carbon atom: in uracil, this is a hydrogen atom, in thymine a methyl group, and in 5-fluorouracil a fluorine atom. Uracil and thymine are nucleobases in RNA and DNA respectively, while 5-fluorouracil (5-FU) is a radiosensitiser molecule that is used in cancer therapies. A radiosensitiser molecule in general is a molecule which is used to enhance the killing

of tumour cells during radiotherapy, while reducing the effect on normal tissue [308]. Since it has a similar structure to thymine, 5-fluorouracil can be used as a replacement for thymine in DNA, with the resulting radiosensitised-DNA suffering increased lethal damage when exposed to radiation [309]. In healthy DNA, thymine pairs with the nucleobase adenine, whereas with 5-FU, tautomerization can result in mispairing with guanine. Ionization has been found to increase this mispairing [310]. This link between ionization, ionic rearrangement, and ultimately increased lethal DNA damage implies that understanding the radiosensitising role of 5-FU requires an understanding of the combined electronic and ionic dynamics of the molecule.

Due to their biological significance, these molecules (in particular uracil and thymine) have been the focus of numerous experimental and theoretical studies. These include photoionization studies [311–313], as well as investigations of fragmentation and relaxation dynamics following excitation or ionization by a UV pump pulse [309, 314, 315]. However, there have been few studies carried out investigating the interaction of these molecules with intense laser pulses, due in part to the significant technical challenge of producing a gas-phase sample of intact (unfragmented) molecules. This challenge is exasperated in HHG experiments, in which a relatively high density of intact molecules is required in order to give a measurable HHG signal.

To our knowledge the only example of experimental measurements of HHG in these molecules is that of Hutchison *et al.* in 2013 [57]. In this work, the technique of laser ablation [58, 316, 317] was used to produce weakly ionized plasma plumes from solid samples of uracil and thymine. The harmonic responses of the two molecules were then investigated by applying driving laser pulses of 1300 nm or 780 nm to the plasma plumes. While high harmonic spectra were obtained from the uracil plume, no high harmonic signal was detected from the thymine plume, as shown in Fig. 5.1(a). The authors of this study attributed the large difference between the non-linear responses of uracil and thymine to differences in the ion composition of the ablation plumes of the two molecules. Specifically, by analysing the composition of the ablation plumes using time of flight mass spectrometry (TOFMS), the authors observed that the thymine molecules experienced a much higher degree of fragmentation during the creation of the ablation plume than the uracil molecules. This was evidenced in the two mass spectra, shown in Fig. 5.1(b), by the significantly lower intensity of the peak corresponding

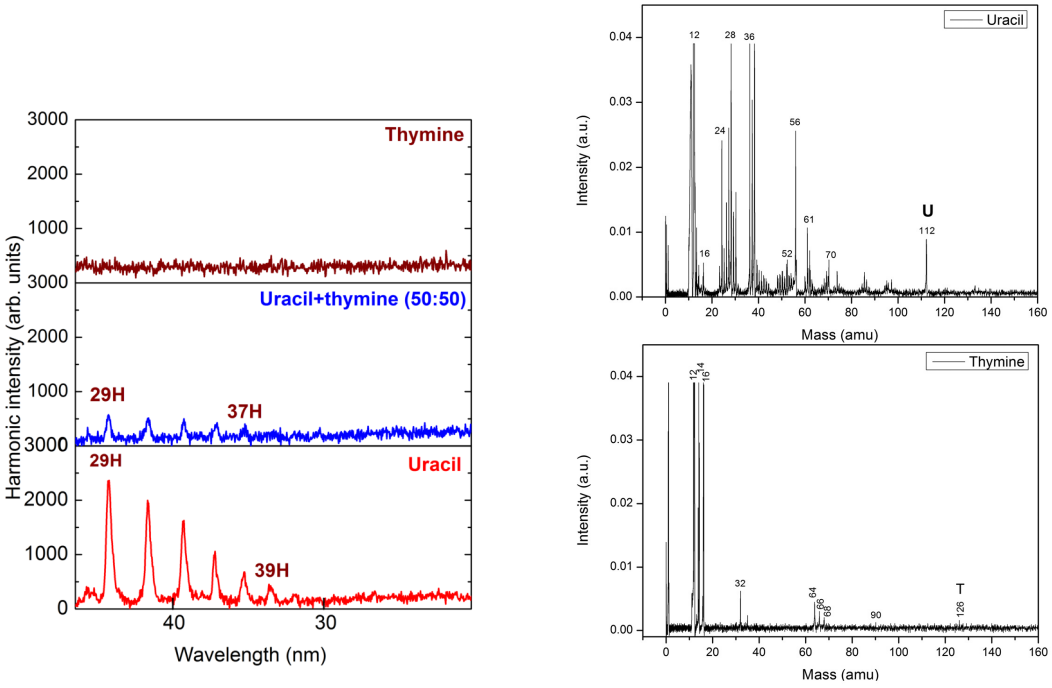

(a) HHG spectra (b) Mass spectra

Figure 5.1: HHG spectra and mass spectra from an experimental study of HHG in uracil and thymine. (a) Experimental HHG results measured under identical conditions in uracil, thymine, and an equal mixture of uracil and thymine, with a 1300 nm driving pulse. In the pure uracil case a strong harmonic signal is observed, which is reduced by a factor of ≈ 4 in the uracil+thymine mixture. No signal is observed in the pure thymine case. (b) Time of flight mass spectra showing the composition of the ablation plumes for uracil and thymine. The parent ions are indicated by the labels U and T. Figures reproduced from [57].

to the parent thymine ion than the corresponding peak for the parent uracil ion. These mass spectra also demonstrated how, even in the case of uracil, the ablation plume contained a large number of fragments of the parent ion. Such fragmentation makes it difficult to determine whether the measured HHG signal originated from the parent uracil ions or from some fragment ions [83]. We are not aware of any corresponding theoretical calculations of HHG in biologically relevant molecules.

In this chapter we present the first results from a series of calculations using EDAMAME to study uracil, thymine and 5-fluorouracil. The chapter is arranged as follows. We begin in Section 5.2 by setting out the ground state equilibrium properties of the molecules as calculated using EDAMAME. In Sections 5.3 and 5.4 we consider the response of each of these three molecules, in three different orientations, to an intense, mid-IR laser pulse. In Section 5.3 we compare the ionization and high harmonic

responses of the two nucleobases uracil and thymine, drawing comparison with the experimental work of Hutchison *et al.* described above. In Section 5.4, we investigate the differences between the responses of the nucleobase thymine and its radiosensitising replacement in DNA, 5-fluorouracil, again in terms of ionization and high harmonic generation.

Ionic motion is included in all the calculations described in this chapter (as discussed in Section 3.3).

5.2 Equilibrium ground state properties

Before we can consider the interaction of a mid-IR laser pulse with uracil, thymine and 5-fluorouracil, we must calculate the equilibrium ground states of the three molecules in EDAMAME. Due to the size and complexity of these molecules compared to acetylene, obtaining their ground state configurations was not as straightforward as in the work described in the previous chapter. In this section we will first discuss the changes to EDAMAME that were required to calculate equilibrium ground states for uracil, thymine and 5-fluorouracil. The calculated static properties of the molecules in these ground states, namely the bond lengths, orbital energies, and Kohn-Sham orbitals, will then be presented.

5.2.1 Equilibrium geometries

In order to obtain relaxed geometries for uracil, thymine and 5-fluorouracil, it was found that the grid spacings used in the acetylene work described in the previous chapter, $\Delta x = \Delta y = \Delta z = 0.4\,\mathrm{a_0}$, were too large. A much finer grid was required, with grid spacings of $\Delta x = \Delta y = \Delta z = 0.2\,\mathrm{a_0}$. However, such a reduction in grid spacing would require the use of eight times as many grid points to produce the same grid extent. Additionally, a smaller grid spacing would necessitate the use of a smaller time step ($\Delta t = 0.1$ a.u., compared to $\Delta t = 0.2$ a.u. as used in Chapter 4) due to the higher frequencies supported by a finer grid. Taken together, these two computational increases would result in calculations many times more computationally expensive than those for acetylene, if the same finite difference methods were employed. To circumvent such a computational burden, the finite difference methods in EDAMAME were adapted to

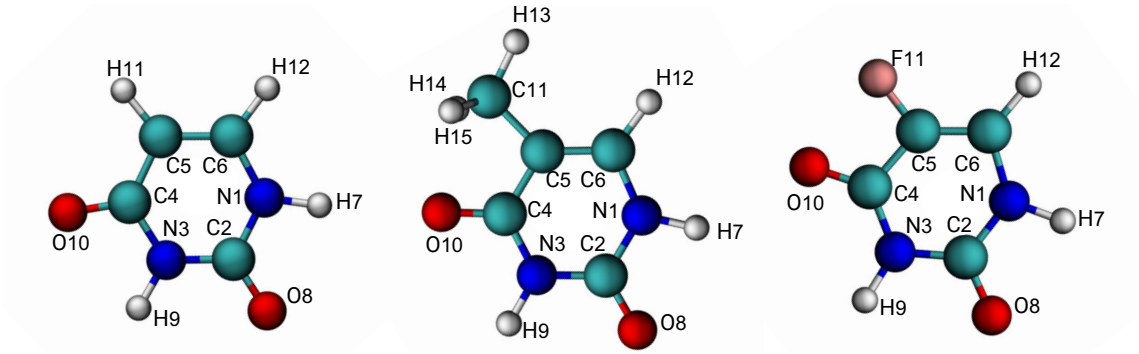

(a) Uracil (b) Thymine (c) 5-fluorouracil

Figure 5.2: Relaxed geometries of (a) uracil, (b) thymine, and (c) 5-fluorouracil, calculated using EDAMAME. The labels N1, C2, etc. indicate the atom type and numbering system used, with the corresponding bond lengths given in Table 5.1. Atoms are coloured according to: white = hydrogen, turquoise = carbon, blue = nitrogen, red = oxygen, pink = fluorine.

incorporate a coordinate scaling of the standard Cartesian grid. In this scheme, which was described in Section 3.2.1, the grid is divided into two regions, with a finer grid used in the inner region, and a coarser grid in the outer region. In addition, the finite difference method was altered so as to suppress the highest frequency components on the grid, by deriving the finite difference coefficients from a least-squares procedure (see Section 3.2.2). Suppressing these unphysical frequencies allows for the use of a larger time step.

In this work we use this new coordinate scaling in EDAMAME to set up a finite difference grid with a grid spacing of $\Delta x = \Delta y = \Delta z = 0.2\,\mathrm{a}_0$ close to the molecule. We use the scaling function defined in Eq. (3.14) for each coordinate with $x_b = y_b = z_b = 10\,\mathrm{a}_0$, after which the grid spacings gradually increase to $\Delta x = \Delta y = \Delta z = 0.4\,\mathrm{a}_0$ (with a grid extent of $x_{\mathrm{max}} = y_{\mathrm{max}} = z_{\mathrm{max}} = \pm 34.8\,\mathrm{a}_0$). Here the coordinate scaling allows us to obtain this grid extent with 225 grid points in each coordinate, compared to the 349 grid points in each coordinate that would be required to obtain the same grid extent with an unscaled grid with $\Delta x = \Delta y = \Delta z = 0.2\,\mathrm{a}_0$. The benefit of using the scaled grid will be much greater for the larger grids employed in the laser-molecule calculations presented in Sections 5.3 and 5.4. We also use the least-squares finite difference method described in Section 3.2.2, and truncate the summation in Eq. (3.32) at $\mathcal{M} = 7$ (rather than $\mathcal{M} = 8$ as in the standard 9-point finite difference scheme). This truncation allows us to keep the time step at $\Delta t = 0.2\,\mathrm{a.u.}$, despite the effective reduction in grid spacing.

Bond	Bond lengths/a_0					
	Uracil		Thymine		5-fluorouracil	
	EDAMAME	PDB	EDAMAME	PDB	EDAMAME	PDB
N1–C6	2.567	2.610	2.583	2.591	2.599	2.646
N1–C2	2.519	2.619	2.545	2.596	2.543	2.636
C2–N3	2.471	2.608	2.506	2.608	2.528	2.608
N3–C4	2.520	2.615	2.503	2.608	2.494	2.591
C4–C5	2.673	2.731	2.656	2.727	2.649	2.729
C5–C6	2.604	2.544	2.568	2.538	2.539	2.534
N1–H7	2.036	1.928	2.040	1.928	2.039	1.929
C2–O8	2.267	2.315	2.286	2.305	2.286	2.319
N3–H9	2.027	1.926	2.032	1.926	2.033	1.928
C4–O10	2.297	2.296	2.304	2.330	2.275	2.324
C5–X11	2.172	2.084	2.773	2.835	2.379	2.470
C6–H12	2.186	2.086	2.189	2.084	2.180	2.084
C11-H13	–	–	2.224	2.107	–	–
C11-H14	–	–	2.239	2.107	–	–
C11-H15	–	–	2.239	2.109	–	–

Table 5.1: Equilibrium bond lengths in uracil, thymine and 5-fluorouracil calculated using EDAMAME, compared with those from the experimental model geometries given in the Protein Data Bank entries for the three molecules [321–324]. The atom labels of N1, C2, etc. are those shown in Fig. 5.2, where the atom X11 is a hydrogen atom in uracil, a carbon atom in thymine, and a fluorine atom in 5-fluorouracil.

Using these grid parameters, the geometries of the each of the three molecules were relaxed using the relaxation scheme described in Section 3.3.2, with initial trial geometries taken from the NIST Chemistry Webbook [255] and the PubChem Substance and Compound [320] databases. The exchange-correlation potential approximation used is the same as in Chapter 4: LDA-PW92-ADSIC. The resulting equilibrium geometries are shown in Fig. 5.2, with the bond lengths set out in Table 5.1.

5.2.2 Orientation of molecules

In Section 5.2.3, we will present the initial Kohn-Sham states and energies calculated for the three molecules in these equilibrium geometries. Firstly however, we will take a moment to describe the different orientations of the molecules that will be considered in the calculations involving an applied laser field that will be discussed later in this chapter. This will allow us to present isosurface plots of the various Kohn-Sham orbitals in the three different orientations, which will aid discussion of the results in Sections 5.3 and 5.4.

To calculate the equilibrium geometries of the molecules, the orientation of the molecule with respect to x-, y-, or z-axes is unimportant, provided that the grid is large enough and the grid spacing small enough. However, in Sections 5.3 and 5.4, we will discuss the results of calculations in which an intense, linearly polarized laser field is applied. In such calculations, the orientation of the molecule relative to the laser polarization direction can be very important, as was discussed in Chapter 4.

With acetylene, the molecular axis provided a natural reference for aligning the molecule relative to the laser polarization direction. With uracil, thymine and 5-fluorouracil however, the structure and asymmetric nature of the molecules mean that we must choose some other reference for specifying the orientations of the molecules. In this work we specify molecular orientations by aligning the permanent dipole moments of the molecules along the x-, y-, or z-axes. The dipole moment, $\boldsymbol{d}(t)$, is calculated in EDAMAME as

$$\boldsymbol{d}(t) = \int \boldsymbol{r} n(\boldsymbol{r}, t) \mathrm{d}\boldsymbol{r}, \tag{5.1}$$

with the permanent dipole moment given by $\boldsymbol{d}(t = 0)$. In all the time-dependent calculations presented later in this chapter, the applied laser field is polarized in the x-direction, and we refer to the orientation of the molecule by two angles:

(i) θ_{mol}: the angle between the laser polarization direction and the plane of the molecule[1];

(ii) θ_{dip}: the angle between the laser polarization direction and the permanent dipole moment of the molecule.

The three orientations considered in this work are:

(1) $\theta_{\text{mol}} = 0^\circ$, $\theta_{\text{dip}} = 0^\circ$: The molecule lies in the x-y plane, oriented so that the dipole moment is aligned along the x-axis. In this orientation the laser field is polarized in the plane of the molecule, and parallel to the dipole moment;

(2) $\theta_{\text{mol}} = 0^\circ$, $\theta_{\text{dip}} = 90^\circ$: The molecule lies in the x-y plane, oriented so that the dipole

[1]While uracil and 5-fluorouracil are planar molecules, the presence of the methyl group in thymine means that it is non-planar. Throughout this chapter references to the "molecular plane" refer to the plane containing the ring of the molecule.

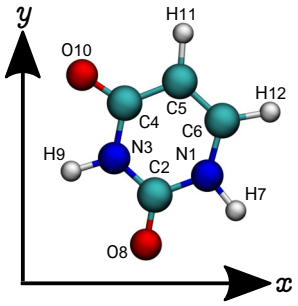

(a) $\theta_{\text{mol}} = 0°$, $\theta_{\text{dip}} = 0°$
Uracil

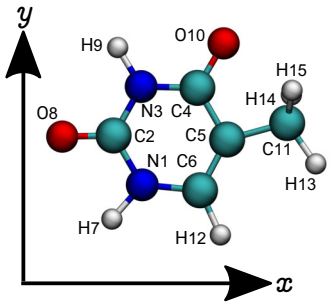

(b) $\theta_{\text{mol}} = 0°$, $\theta_{\text{dip}} = 0°$
Thymine

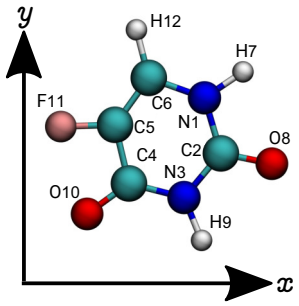

(c) $\theta_{\text{mol}} = 0°$, $\theta_{\text{dip}} = 0°$
5-fluorouracil

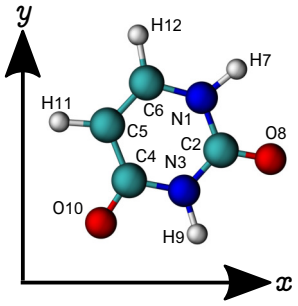

(d) $\theta_{\text{mol}} = 0°$, $\theta_{\text{dip}} = 90°$
Uracil

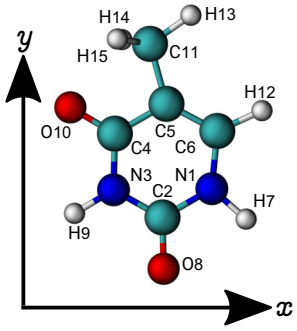

(e) $\theta_{\text{mol}} = 0°$, $\theta_{\text{dip}} = 90°$
Thymine

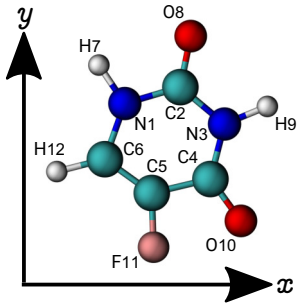

(f) $\theta_{\text{mol}} = 0°$, $\theta_{\text{dip}} = 90°$
5-fluorouracil

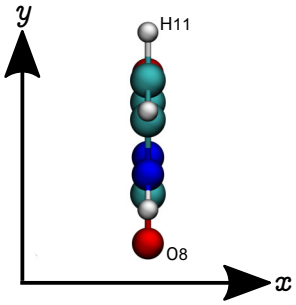

(g) $\theta_{\text{mol}} = 90°$, $\theta_{\text{dip}} = 90°$
Uracil

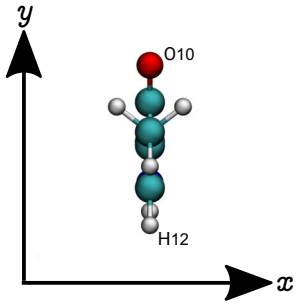

(h) $\theta_{\text{mol}} = 90°$, $\theta_{\text{dip}} = 90°$
Thymine

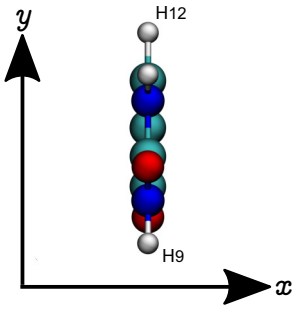

(i) $\theta_{\text{mol}} = 90°$, $\theta_{\text{dip}} = 90°$
5-fluorouracil

Figure 5.3: Relaxed geometries of uracil, thymine and 5-fluorouracil, in the three orientations considered in this work. Molecules are oriented so that the calculated dipole moment is aligned along: (a)–(c) the x-axis; (d)–(f) the y-axis; (g)–(i) the z-axis (perpendicular to the page). The angle θ_{mol} is the angle between the laser polarization direction (the x-axis) and the plane containing the ring of the molecule, while θ_{dip} is the angle between the laser polarization direction and the permanent dipole moment of the molecule, $\boldsymbol{d}$. Atoms are coloured according to: white = hydrogen, turquoise = carbon, blue = nitrogen, red = oxygen, pink = fluorine. Note that the placement of the axes in the bottom left corner is for clarity; the origin in each case is located at the centre of mass of each molecule.

moment is aligned along the y-axis. In this orientation the laser field is polarized in the plane of the molecule, and perpendicular to the dipole moment;

(3) $\theta_{\text{mol}} = 90^\circ$, $\theta_{\text{dip}} = 90^\circ$: The molecule lies in the y-z plane, oriented so that the dipole moment is aligned along the z-axis. In this orientation the laser field is polarized perpendicular to the plane of the molecule, and perpendicular to the dipole moment.

These three orientations, for each of the three molecules, are shown in Fig. 5.3.

5.2.3 Kohn-Sham states

From the equilibrium geometries detailed above, the initial Kohn-Sham states and energies of the three molecules are calculated. For each molecule, as with acetylene, the inner electrons are treated using pseudopotentials, as we do not expect them to contribute to the dynamics for an applied field with the mid-IR wavelength considered here. We therefore solve the TDKS equations for 21 doubly occupied orbitals (42 electrons) for uracil, and for 24 doubly occupied orbitals (48 electrons) for both thymine and 5-fluorouracil. The calculated Kohn-Sham energies for each of these orbitals are given in Table 5.2. Here we note that for every Kohn-Sham state (HOMO, HOMO-1 etc.), the magnitude of the energy of the state in thymine is lower than that in both uracil and 5-fluorouracil.

By Koopmans' theorem, we can consider the magnitude of the HOMO energy of a neutral molecule as an approximation to the vertical ionization potential to the ground state of the cation. In Table 5.3 we compare our calculated values of the HOMO energies with experimental values for the ionization potentials of the three molecules. Here we can see that the calculated ionization potentials are lower than the experimental values. While differences between the relaxed geometry in EDAMAME and the experimental geometry may account for some of this difference, comparisons of the ionization potentials calculated with relaxed and unrelaxed geometries suggests that the differences in Table 5.3 are not due to differences in geometry alone. This may be an indication that the electronic structures of these molecules are not as well described by the LDA-PW92-ADSIC exchange-correlation potential approximation as other molecules previously studied with EDAMAME. Use of other exchange-correlation

	Uracil		Thymine		5-fluorouracil	
Orbital	Sym.	Energy/Ha	Sym.	Energy/Ha	Sym.	Energy/Ha
HOMO	σ	-0.3007	π	-0.2963	π	-0.3014
HOMO-1	π	-0.3196	σ	-0.3029	σ	-0.3127
HOMO-2	σ	-0.3430	σ	-0.3275	σ	-0.3348
HOMO-3	π	-0.3466	π	-0.3419	π	-0.3579
HOMO-4	σ	-0.4368	π	-0.3899	σ	-0.4119
HOMO-5	π	-0.4388	σ	-0.3904	π	-0.4214
HOMO-6	σ	-0.4456	σ	-0.4127	σ	-0.4484
HOMO-7	σ	-0.4702	σ	-0.4392	σ	-0.4664
HOMO-8	π	-0.4740	π	-0.4427	π	-0.4730
HOMO-9	σ	-0.4924	σ	-0.4555	σ	-0.5187
HOMO-10	σ	-0.5640	π	-0.4790	π	-0.5271
HOMO-11	π	-0.5674	σ	-0.4886	σ	-0.5490
HOMO-12	σ	-0.6057	π	-0.5568	π	-0.5814
HOMO-13	σ	-0.6357	σ	-0.5600	σ	-0.5835
HOMO-14	σ	-0.6996	σ	-0.5856	σ	-0.6405
HOMO-15	σ	-0.7446	σ	-0.6067	σ	-0.6519
HOMO-16	σ	-0.8356	σ	-0.6850	σ	-0.7047
HOMO-17	σ	-0.9430	σ	-0.7032	σ	-0.7515
HOMO-18	σ	-0.9940	σ	-0.7498	σ	-0.8198
HOMO-19	σ	-1.0443	σ	-0.8439	σ	-0.9664
HOMO-20	σ	-1.1207	σ	-0.9448	σ	-0.9909
HOMO-21			σ	-0.9779	σ	-1.0487
HOMO-22			σ	-1.0388	σ	-1.1145
HOMO-23			σ	-1.1049	σ	-1.2066

Table 5.2: Kohn-Sham energies of the occupied orbitals of uracil, thymine and 5-fluorouracil, calculated using EDAMAME. The entries σ and π in the 'Sym.' columns refer to the symmetry properties of each Kohn-Sham orbital.

approximations or self-interaction-correction schemes may yield HOMO energies closer to the experimental I_p values; this would be an interesting avenue of further work with EDAMAME, but is beyond the scope of this thesis. However we do see in Table 5.3 that EDAMAME does correctly reproduce the fact that while the ionization potentials of uracil and 5-fluorouracil are almost identical, the ionization potential of thymine is lower.

The Kohn-Sham orbitals themselves are plotted in Figs. 5.4–5.6. In these three figures we show isosurface plots of the Kohn-Sham orbitals for the three molecules aligned in each of the orientations shown in Fig. 5.3, with each orientation in a separate figure for clarity and ease of discussion in later sections of this chapter. In Fig. 5.4 the Kohn-Sham orbitals are plotted for the molecules oriented with the dipole moment along the x-axis

	|HOMO Energy|/Ha	Experimental I_p/Ha
Uracil	0.3007	0.353
Thymine	0.2963	0.338
5-fluorouracil	0.3014	0.351

Table 5.3: Calculated energies of the highest occupied Kohn-Sham orbitals of uracil, thymine and 5-fluorouracil, compared with experimental ionization potentials. Experimental values were taken from [318] for uracil and thymine, and from [319] for 5-fluorouracil.

($\theta_{\text{mol}} = 0^\circ$, $\theta_{\text{dip}} = 0^\circ$); in Figs. 5.5 and 5.6, the molecules are oriented with the dipole moments along the y-axis ($\theta_{\text{mol}} = 0^\circ$, $\theta_{\text{dip}} = 90^\circ$) and z-axis ($\theta_{\text{mol}} = 90^\circ$, $\theta_{\text{dip}} = 90^\circ$) respectively.

From Fig. 5.6 in particular, the symmetries of the Kohn-Sham orbitals can be clearly seen. These are also given in Table 5.2 for reference. In all three molecules, the majority of states are σ-type orbitals, with only 5/21 orbitals in uracil and 6/24 orbitals in thymine and 5-fluorouracil having π-symmetry (in which the Kohn-Sham wavefunction has a nodal plane in the plane of the molecule). We also note that the HOMO in uracil is a σ-type orbital, whereas it is a π-type orbital in 5-fluorouracil and thymine. As we will see in Sections 5.3 and 5.4, these symmetries are important when considering the response of the different Kohn-Sham states to an applied laser field.

To conclude this section, we note several features that are common to a number of the Kohn-Sham orbitals in all three molecules. Firstly, the four highest lying states consist of two σ states and two π states. In the two σ states (HOMO and HOMO-2 in uracil, HOMO-1 and HOMO-2 in thymine and 5-fluorouracil), the Kohn-Sham wavefunctions have relatively large densities in lobes on either side of the oxygen atoms (O8, O10). In the two π states (HOMO-1 and HOMO-3 in uracil, HOMO and HOMO-3 in thymine and 5-fluorouracil), the Kohn-Sham wavefunctions are localised around a number of different atomic sites on either side of the molecular plane. Finally, we note the similarity between the lowest lying π state in each molecule (HOMO-11 in uracil, HOMO-12 in thymine and 5-fluorouracil). In these states, the Kohn-Sham wavefunctions (which have a nodal plane in the plane of the molecule) are dispersed over a large extent of the molecule compared to the other π states, in which the wavefunctions are generally more localised around a number of different sites.

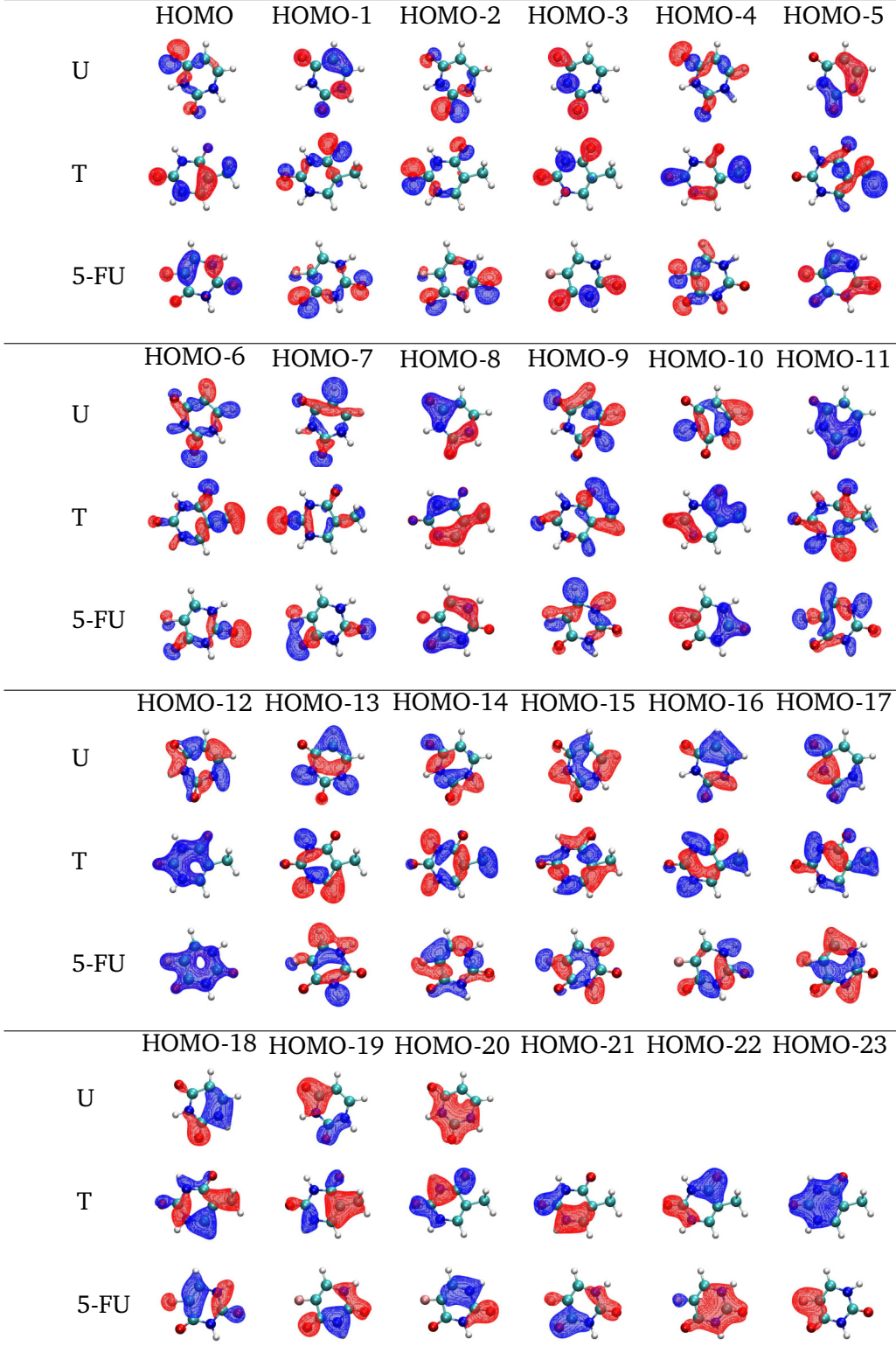

Figure 5.4: Isosurface plots of the doubly-occupied Kohn-Sham orbitals of uracil (U), thymine (T) and 5-fluorouracil (5-FU), calculated using EDAMAME. The axes and molecules are aligned as in the ($\theta_{\text{mol}} = 0°$, $\theta_{\text{dip}} = 0°$) orientation shown in Figs. 5.3(a), 5.3(b) and 5.3(c), with the dipole moment of each molecule aligned along the x-axis. These plots were produced using the VMD software package [288], with isosurface values of 0.05 (blue mesh) and -0.05 (red mesh).

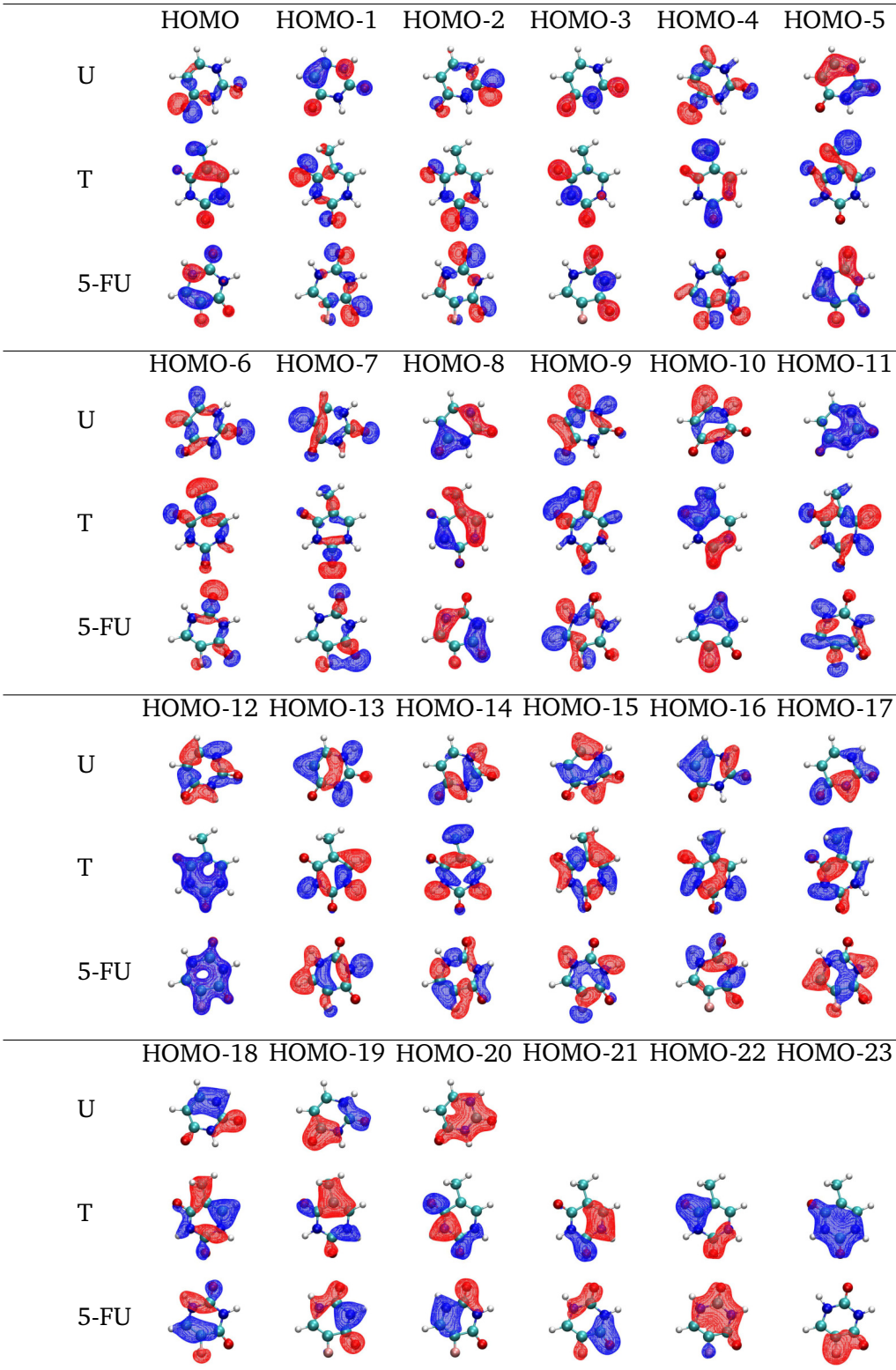

Figure 5.5: Isosurface plots of the doubly-occupied Kohn-Sham orbitals of uracil (U), thymine (T) and 5-fluorouracil (5-FU), calculated using EDAMAME. The axes and molecules are aligned as in the ($\theta_{\text{mol}} = 0°$, $\theta_{\text{dip}} = 90°$) shown in Figs. 5.3(d), 5.3(e) and 5.3(f), with the dipole moment of each molecule aligned along the y-axis. These plots were produced using the VMD software package [288], with isosurface values of 0.05 (blue mesh) and -0.05 (red mesh).

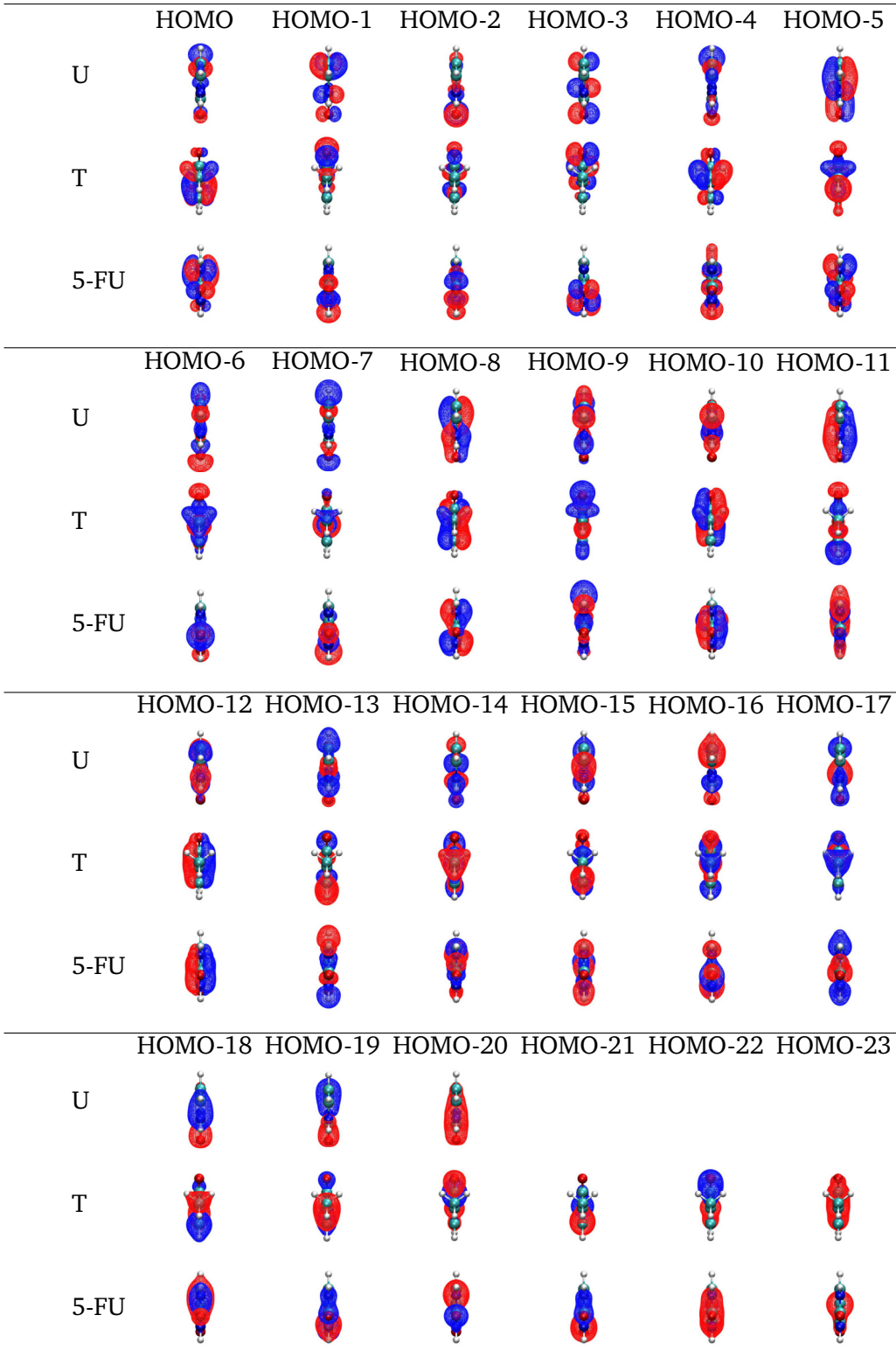

Figure 5.6: Isosurface plots of the doubly-occupied Kohn-Sham orbitals of uracil (U), thymine (T) and 5-fluorouracil (5-FU), calculated using EDAMAME. The axes and molecules are aligned as in the ($\theta_{\text{mol}} = 90°$, $\theta_{\text{dip}} = 90°$) orientation shown in Figs. 5.3(g), 5.3(h) and 5.3(i), with the dipole moment of each molecule aligned along the z-axis. These plots were produced using the VMD software package [288], with isosurface values of 0.05 (blue mesh) and -0.05 (red mesh).

5.2.4 Summary

In this section we have described how the ground state properties of uracil, thymine and 5-fluorouracil are calculated using EDAMAME. The complexity of these molecules compared to molecules previously studied using EDAMAME meant that the standard finite difference approach with equally spaced grid points was no longer adequate, unless much smaller grid spacings and time steps were used. To avoid the huge increase in computational cost that such a reduction in grid spacings and time steps would entail, the finite difference routines in EDAMAME were modified to allow for: (i) coordinate scaling, resulting in a grid with non-uniform grid spacings, in which the density of grid points is much higher in a small region of space surrounding the molecule than elsewhere in the grid; (ii) a least-squares approximation to the finite difference operators, which has the effect of suppressing unphysical, high frequency eigenstates supported by the finer grid, and allows for the use of a larger time step than if the standard finite difference coefficients were used.

These new finite difference approaches implemented in EDAMAME were used to relax the geometries of the three molecules, and calculate their equilibrium ground state properties. These properties, specifically the bond lengths and Kohn-Sham orbitals and orbital energies, were presented and compared against experimental values. While the agreement between the calculated and experimental values for the bond lengths and ionization potentials of the three molecules is not as good as in a similar comparison for acetylene (Section 4.3), the static properties of uracil, thymine and 5-fluorouracil are still reasonably well described in EDAMAME.

With the ground state properties calculated, we are now able to investigate the dynamics of the three molecules during interactions with an intense, mid-IR laser field. In the next section we begin by considering the differences between the responses of the nucleobases uracil and thymine, for three different orientations of the molecules. Then, in Section 5.4, we examine the differences between the response of the nucleobase thymine and its radiosensitising replacement in DNA, 5-fluorouracil.

5.3 Response of uracil and thymine to a mid-IR field

We begin our investigation of the dynamics of uracil, thymine and 5-fluorouracil when exposed to an intense, mid-IR laser pulse by first focusing on the responses of the two nucleobases: uracil and thymine. These two molecules were the subject of the 2013 study by Hutchison *et al.* [57], which was the first attempt to "analyse differences in structural molecular properties through plasma ablation-induced HHG spectroscopy", but in which the authors were unable to obtain a HHG signal in thymine due to excessive fragmentation. This section is arranged as follows. In Section 5.3.1 we set out the calculation parameters that are used in the laser-molecule calculations described in this section and in Section 5.4. Then in Section 5.3.2 we compare the ionization response of each molecule, for the three different orientations described in Section 5.2.2. Finally in Section 5.3.3 the differences in high harmonic response between the molecules and orientations are examined.

5.3.1 Calculation parameters

As in the calculations described in Chapter 4, here we consider the interaction of the molecules with an intense, linearly polarized, mid-IR pulse. For this work, the applied field is a 5-cycle pulse with a wavelength of $\lambda = 1300\,\text{nm}$ and a peak intensity of $I = 1.0\times10^{14}\,\text{W/cm}^2$. The pulse is linearly polarized along the x-axis, and has a duration of 896.2 a.u. = 21.7 fs. As in Chapter 4, the pulse has a $\sin^2$ envelope, and the carrier-envelope phase is set to $\phi = 0$.

This wavelength of $\lambda = 1300\,\text{nm}$ was chosen to match the mid-IR wavelength used in the work of Hutchison *et al.* [57]. The shortening of the wavelength compared to the $\lambda = 1450\,\text{nm}$ pulse used throughout Chapter 4 also has the benefit of reducing the associated quiver amplitude, given by Eq. (1.4), and consequently the grid extent required to contain ionized wavepackets. For these laser parameters, converged results are obtained with the following grid extents: $x_{\text{max}} = \pm128.4\,\text{a}_0$, and $y_{\text{max}} = z_{\text{max}} = \pm75.6\,\text{a}_0$. The absorbing boundary begins at $x_m = \pm80.0\,\text{a}_0$ and $y_m = z_m = \pm50.0\,\text{a}_0$. As in the geometry relaxation calculations described in the previous section, the grid spacing in the inner region (which extends to $\approx x_b = y_b = z_b = \pm10.0\,\text{a}_0$) is $0.2\,\text{a}_0$. Beyond $\approx \pm10.0\,\text{a}_0$ in each direction, the grid spacing increases to $0.4\,\text{a}_0$, and then remains con-

stant. The grid is parallelized over 21 cores in x, and 13 cores in both y and z (3549 cores in total), with 33 points per core in each direction. Here the advantage of working with a scaled finite difference grid is clear. Using the coordinate scaling, we require 693 grid points in the x coordinate and 429 points in both the y and z coordinates to obtain the stated grid extents; with an unscaled grid with $\Delta x = \Delta y = \Delta z = 0.2\,\mathrm{a_0}$, we would require 1285 grid points in x and 757 points in y and z, and therefore the use of 20,631 cores in total. As in the geometry relaxation calculations described in Section 5.2.1, we use the least-squares finite difference method described in Section 3.2.2, with the summation in Eq. (3.32) truncated at $\mathcal{M} = 7$. Using this approach, both the TDKS equations, Eq. (3.1), and the ionic equations of motion, Eq. (3.66), are propagated in time with a time step of 0.2 a.u., as in the acetylene calculations of Chapter 4.

Three orientations of each molecule are considered, as described in Section 5.2.2. In all orientations the laser field polarization is fixed along the x-axis.

5.3.2 Ionization response

We begin our time-dependent studies of uracil and thymine by considering the total ionization from each molecule in each of the three orientations shown in Fig. 5.3, following interaction with the 1300 nm laser pulse described above. These total ionizations, I_{total}, are calculated as

$$I_{\text{total}} = N_e - P(T) \tag{5.2}$$

where N_e is the number of active electrons (N_e = 42 for uracil, N_e = 48 for thymine, since the core electrons are described using pseudopotentials), and $P(T)$ is the total electronic population, given by Eq. (3.70), in the grid at the end of the pulse ($t = T$). The total ionizations for the six calculations (three orientations for each of the two molecules) are shown in Fig. 5.7.

The first feature of note in this figure is that in both molecules, we see a much greater degree of ionization (approximately twice as much) when the laser field is polarized in the plane of the molecule ($\theta_{\text{mol}} = 0^\circ$) than perpendicular to it ($\theta_{\text{mol}} = 90^\circ$). Secondly, we note the differences in ionization between the two $\theta_{\text{mol}} = 0^\circ$ orientations, in which the laser field is polarized in the plane of the molecule (i.e., the dipole is aligned along either the x- or y-axes). In uracil, there is significantly more ionization in the $\theta_{\text{dip}} = 0^\circ$

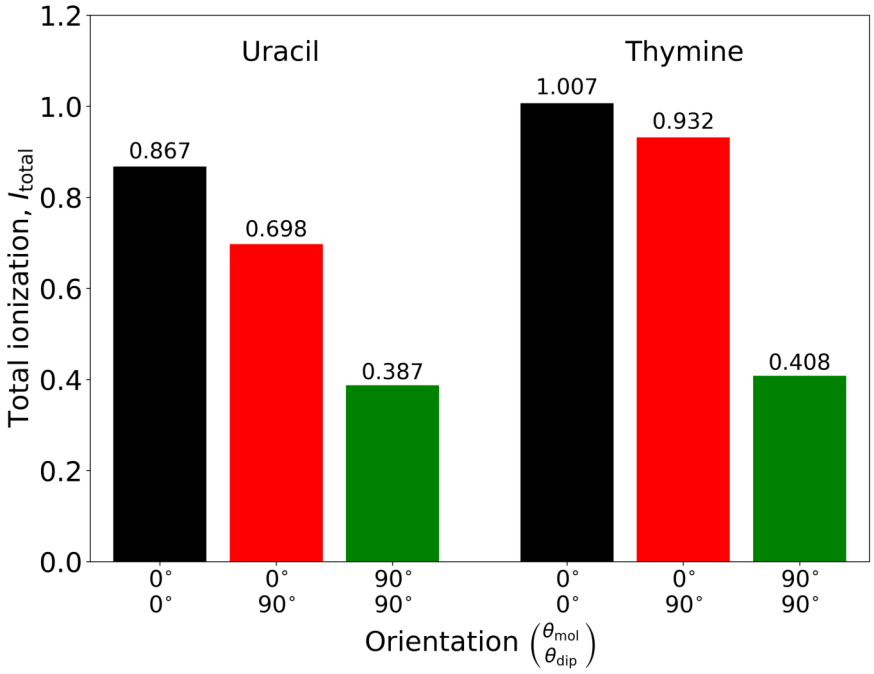

Figure 5.7: Total ionization I_{total}, given by Eq. (5.2), for three different orientations of uracil and thymine, following interaction with a 5-cycle mid-IR laser pulse with wavelength $\lambda = 1300\,\text{nm}$ and a peak intensity of $I = 1.0\times10^{14}\,\text{W/cm}^2$. The pulse is linearly polarized along the x-axis, and the molecules are aligned in the orientations shown in Fig. 5.3. The angles θ_{mol} and θ_{dip} respectively refer to the angle between the laser polarization direction and the plane of the molecule, and the angle between the laser polarization direction and the initial dipole moment of the molecule.

orientation than the $\theta_{\text{dip}} = 90°$ orientation. In thymine, the difference in ionization between these two orientations is smaller than in uracil, with the total ionization in the $\theta_{\text{dip}} = 0°$ orientation only slightly larger than in the $\theta_{\text{dip}} = 90°$ case. Finally, in all orientations we see greater ionization from thymine than from uracil, as we might expect considering the slightly lower ionization potential of thymine. To understand the origins of these differences in the ionization response of the molecules in these different orientations, we can consider individually the ionization from each of the Kohn-Sham orbitals.

In Fig. 5.8 we show the ionization from each Kohn-Sham orbital in uracil and thymine, for three different orientations of the molecules with respect to the laser polarization direction. Due to the large number of orbitals in these molecules compared to in acetylene, to analyse the ionization from each orbital in the following we plot only the population loss at the end of the pulse, rather than the variations in population over time as in Chapter 4. In Fig. 5.8 we consider the orbital depletions, D_j, from the HOMO-j,

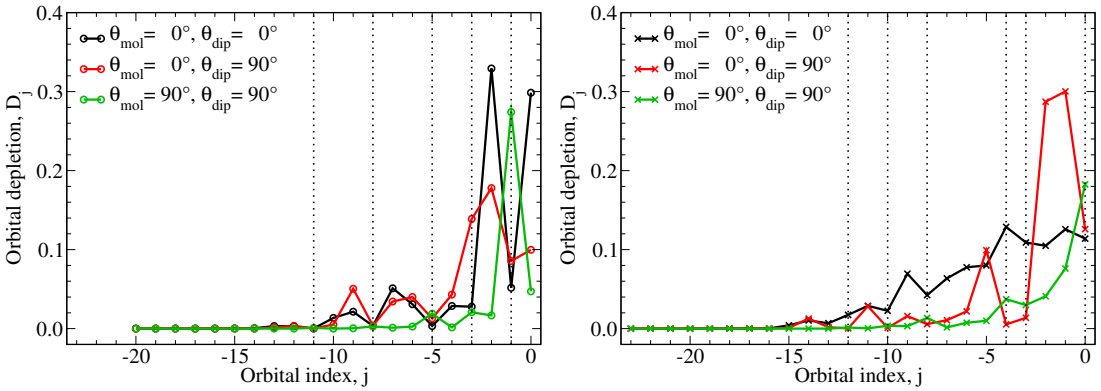

(a) Uracil (b) Thymine

Figure 5.8: Orbital depletions, D_j, defined by Eq. (5.3), from each Kohn-Sham orbital for three different orientations of (a) uracil and (b) thymine, following interaction with a 5-cycle mid-IR laser pulse with wavelength $\lambda = 1300$ nm and a peak intensity of 1.0×10^{14} W/cm^2. The pulse is linearly polarized along the x-axis, and the molecules are aligned in the orientations shown in Fig. 5.3. The angles θ_{mol} and θ_{dip} respectively refer to the angle between the laser polarization direction and the plane of the molecule, and the angle between the laser polarization direction and the initial dipole moment of the molecule. We consider the orbital depletions, D_j, from the HOMO-j, where $j = 0, \ldots, N-1$ (i.e., $j = 0 \rightarrow$ HOMO-0 = HOMO, $j = 1 \rightarrow$ HOMO-1, $j = 2 \rightarrow$ HOMO-2, etc.). The vertical dotted lines indicate the Kohn-Sham states of π symmetry.

where $j = 0, \ldots, N-1$ (i.e., $j = 0 \rightarrow$ HOMO-0 = HOMO, $j = 1 \rightarrow$ HOMO-1, $j = 2 \rightarrow$ HOMO-2, etc.). These orbital depletions are defined as

$$D_j = 2 - P_{N-j}(T), \tag{5.3}$$

for $j = 0, \ldots, N-1$, where $P_{N-j}(T)$ is the population of Kohn-Sham orbital ψ_{N-j}, given by Eq. (3.69), and evaluated at the end of the pulse ($t = T$).

For both molecules the importance of the orbital symmetries is evident in Fig. 5.8. When the molecule is aligned so that the laser polarization is in the plane of the molecule ($\theta_{\text{mol}} = 0°$, black and red curves), ionization from the π orbitals (indicated by the vertical dotted lines) is suppressed in most cases. On the other hand, when the molecule is aligned perpendicular to the laser polarization direction ($\theta_{\text{mol}} = 90°$, green curves), we generally see enhanced ionization from the π orbitals compared to the nearest σ orbitals. This symmetry dependence leads to the large difference seen in Fig. 5.7 between total ionizations in the $\theta_{\text{mol}} = 0°$ and $\theta_{\text{mol}} = 90°$ orientations. In the $\theta_{\text{mol}} = 0°$ orientations, the ionization response is dominated by several of the highest-lying σ states (e.g., the HOMO and HOMO-2 in uracil for $\theta_{\text{mol}} = 0°$, $\theta_{\text{dip}} = 0°$),

with smaller contributions from lower-lying σ states. In the $\theta_{\text{mol}} = 90^\circ$ orientation on the other hand, ionization from a single π state (the HOMO-1 in uracil, the HOMO in thymine) dominates the response of each molecule. The larger number of significantly ionized states in the $\theta_{\text{mol}} = 0^\circ$ orientations than in the $\theta_{\text{mol}} = 90^\circ$ case leads directly to the differences in total ionization between the $\theta_{\text{mol}} = 0^\circ$ and $\theta_{\text{mol}} = 90^\circ$ orientations.

Considering now the differences in total ionization observed in Fig. 5.7 between the ($\theta_{\text{mol}} = 0^\circ$, $\theta_{\text{dip}} = 0^\circ$) and ($\theta_{\text{mol}} = 0^\circ$, $\theta_{\text{dip}} = 90^\circ$) orientations, we focus our attention on the two highest-lying σ states of each molecule (HOMO and HOMO-2 in uracil, HOMO-1 and HOMO-2 in thymine). Looking at the response of these states in uracil, we see in Fig. 5.8 that ionization from these two states in uracil is maximized in the ($\theta_{\text{mol}} = 0^\circ$, $\theta_{\text{dip}} = 0^\circ$) orientation. As can be seen in Figs. 5.4 and 5.5, the Kohn-Sham wavefunctions for these states in all three molecules have relatively high densities around around the two oxygen atoms. Looking again at the orientations shown in Fig. 5.3, we can see that in this ($\theta_{\text{mol}} = 0^\circ$, $\theta_{\text{dip}} = 0^\circ$) orientation, the C2–O8 bond is aligned almost perpendicular to the laser polarization direction. In the ($\theta_{\text{mol}} = 0^\circ$, $\theta_{\text{dip}} = 90^\circ$) orientation on the other hand, in which we see reduced ionization from the HOMO and HOMO-2, the C2–O8 bond is aligned almost parallel to the laser polarization direction. For the other carbon–oxygen bond (C4–O10), the angle between the laser polarization direction and the bond is similar in both $\theta_{\text{mol}} = 0^\circ$ orientations. From these observations, we might imagine that there may be some connection between the orientation of these carbon–oxygen bonds relative to the laser polarization direction and the response of these highest-lying σ states. However further calculations would be required to investigate this more thoroughly; these will be discussed in the context of possible future work at the end of this thesis.

In thymine, while we see that ionization from the HOMO-1 and HOMO-2 is increased in the ($\theta_{\text{mol}} = 0^\circ$, $\theta_{\text{dip}} = 90^\circ$) orientation (in which the C2–O8 bond is almost perpendicular to the laser polarization direction), ionization from almost all of the other Kohn-Sham orbitals is larger in the ($\theta_{\text{mol}} = 0^\circ$, $\theta_{\text{dip}} = 0^\circ$) orientation. Indeed, in this ($\theta_{\text{mol}} = 0^\circ$, $\theta_{\text{dip}} = 0^\circ$) orientation of thymine the symmetries of the Kohn-Sham orbitals have considerably less bearing on the ionization response than in the other orientations for both thymine and uracil. For example, looking at the depletions of the five highest lying orbitals in this this orientation, we see very little variation between orbitals,

despite three of these having π symmetry and two having σ symmetry. We note that in this orientation the bond between the ring of the molecule and the methyl group (C5–C11) is aligned almost parallel to the laser polarization direction; this may have some bearing on the ionization dynamics. Again, this could be the subject of future work, and will be discussed later.

The final point we noted in reference to Fig. 5.7 was that in all orientations, the ionization from thymine was greater than from uracil. We might expect that this is a result of increased ionization in thymine from the most ionized states than from the equivalent states in uracil. However, comparing the response of the most ionized states in the two molecules for a given orientation, we see that this is not always the case. While in the ($\theta_{\text{mol}} = 0^\circ$, $\theta_{\text{dip}} = 90^\circ$) orientation (red curves), the ionization from the most ionized orbitals in thymine is significantly larger than from those in uracil, in the other two orientations (black and green curves) the reverse is true: ionization from the most ionized orbitals in thymine is smaller than from those in uracil. In these two orientations, the increased overall ionization in thymine than in uracil arises instead due to greater ionization from lower lying orbitals. This is not surprising, considering that the magnitudes of all the energies of the Kohn-Sham states in thymine are smaller than those of the equivalent Kohn-Sham states in uracil (Table 5.2).

Considering again the study of uracil and thymine by Hutchison *et al.* [57] described previously, we remind the reader that in this experimental work, the authors were unable to obtain any high harmonic signal from the thymine ablation plume. They attributed this to a much greater degree of fragmentation during the creation of the thymine ablation plume than the uracil ablation plume (from which a strong high harmonic signal was measured). While the duration of our calculations (21.7 fs) is too short to allow for any significant fragmentation of the molecules, the significantly higher ionization observed in thymine than in uracil, in all orientations considered (around 20% greater on average), could be a precursor to greater fragmentation of thymine than uracil, as in the Hutchison study.

In the work of Hutchison *et al.*, the large degree of fragmentation in the thymine sample hindered the attempt to study differences in the high harmonic spectra of uracil and thymine. An advantage of studying the single molecule response on the short

timescales considered in our work is that we do not encounter such a difficulty, and are able to calculate the harmonic spectra from intact (unfragmented) parent molecules.

5.3.3 High harmonic generation

We now consider high harmonic generation in uracil and thymine following interaction with the 5-cycle, mid-IR laser pulse described previously ($\lambda = 1300\,\text{nm}$, $I = 1.0\times10^{14}\,\text{W/cm}^2$). As in the previous section, we consider three orientations for each of the molecules, with the laser field polarized along the x-axis in all cases. In Fig. 5.9 we plot the harmonic spectra for these six cases. As described in Section 3.5.2, we calculate these harmonic spectra by taking the Fourier transform of the dipole acceleration along x, y or z, as in Eq. (3.71). In Fig. 5.9 we have plotted the sum of the spectral densities in the three directions, i.e., $S_x(\omega) + S_y(\omega) + S_z(\omega)$, as was the case in Chapter 4. Unlike with acetylene however, in which the harmonic emission in directions other than the laser polarization direction was negligible, the increased size and reduced symmetry of the molecules studied in this chapter mean that the spectral density can be significant in more than one direction. In general though, the spectral density along the laser polarization direction, S_x, is still larger than the spectral densities in the other two directions, S_y and S_z. For simplicity all spectra plotted in this chapter are the combined spectra, $S_x + S_y + S_z$.

Returning now to Fig. 5.9, the most obvious feature of note is the difference in intensities between the spectra produced in different orientations. For both molecules, we see that the intensities of the harmonic spectra vary with orientation in approximately the same manner as the total ionization varied in the previous section; as we would expect from the three-step model of HHG. In both molecules the spectral density is much smaller (approximately one order of magnitude) when the molecules are oriented with the laser field polarized perpendicular to the plane of the molecule ($\theta_{\text{mol}} = 90^\circ$) than with the laser field polarized in the plane of the molecule ($\theta_{\text{mol}} = 0^\circ$). In uracil, the greatest harmonic response is observed for the ($\theta_{\text{mol}} = 0^\circ$, $\theta_{\text{dip}} = 0^\circ$) orientation. In thymine, the harmonic spectra produced in the ($\theta_{\text{mol}} = 0^\circ$, $\theta_{\text{dip}} = 0^\circ$) and ($\theta_{\text{mol}} = 0^\circ$, $\theta_{\text{dip}} = 90^\circ$) orientations are of comparable intensity.

While the intensities of the harmonic spectra produced for molecules in the $\theta_{\text{mol}} =$

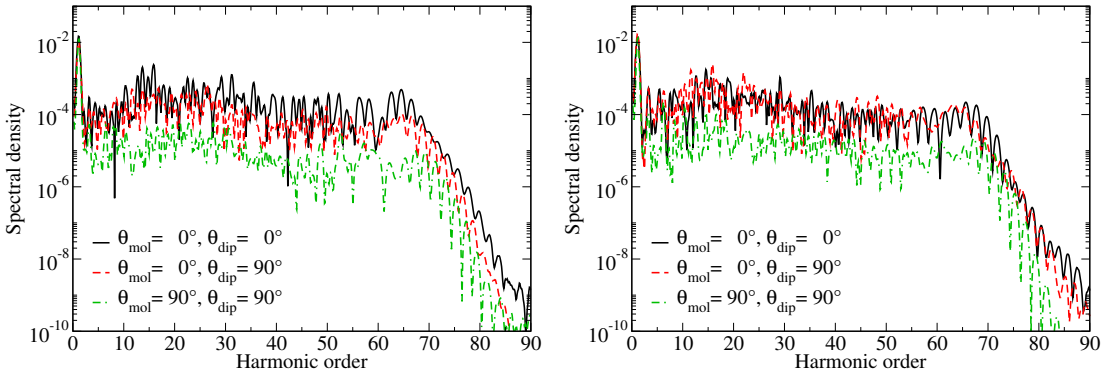

(a) Uracil (b) Thymine

Figure 5.9: High harmonic generation in (a) uracil and (b) thymine, following interaction with a 5-cycle mid-IR laser pulse with wavelength $\lambda = 1300\,\text{nm}$ and a peak intensity of $I = 1.0\times10^{14}\,\text{W/cm}^2$. The pulse is linearly polarized along the x-axis, and the molecules are aligned in the orientations shown in Fig. 5.3. The angles θ_{mol} and θ_{dip} respectively refer to the angle between the laser polarization direction and the plane of the molecule, and the angle between the laser polarization direction and the initial dipole moment of the molecule.

90° orientation are lower than those for molecules in the $\theta_{\text{mol}} = 0^\circ$ orientations, we note from Fig. 5.9 that the harmonic plateaus extend slightly further in the $\theta_{\text{mol}} = 90^\circ$ spectra. For example, in uracil the cutoff in the $\theta_{\text{mol}} = 0^\circ$ orientations is around the 65th harmonic, whereas in the $\theta_{\text{mol}} = 90^\circ$ orientation the cutoff is around the 68th harmonic. We also note that the intensities of the cutoff harmonics decrease more sharply in the $\theta_{\text{mol}} = 90^\circ$ orientation than in the other two orientations. We can investigate both of these differences in cutoff harmonics by examining the contributions of individual Kohn-Sham orbitals to the overall HHG spectra.

As an example, in Fig. 5.10 we show the contributions of a number of Kohn-Sham orbitals to two of the HHG spectra from thymine plotted in Fig. 5.9(b). As described previously, these state-spectra are calculated by taking the FFT of the dipole acceleration of individual Kohn-Sham states, given by Eq. (3.73). Due to the large number of Kohn-Sham states, here we only plot the spectra from states with the largest spectral densities, particularly those with high intensities around the cutoff region.

Considering first the ($\theta_{\text{mol}} = 0^\circ$, $\theta_{\text{dip}} = 90^\circ$) orientation, in Fig. 5.10(a) we see that when thymine is oriented in this way (with the laser field polarized in the plane of the molecule) the high harmonic response is dominated by the response of the two highest-lying σ states: the HOMO-1 and HOMO-2. This is to be expected considering

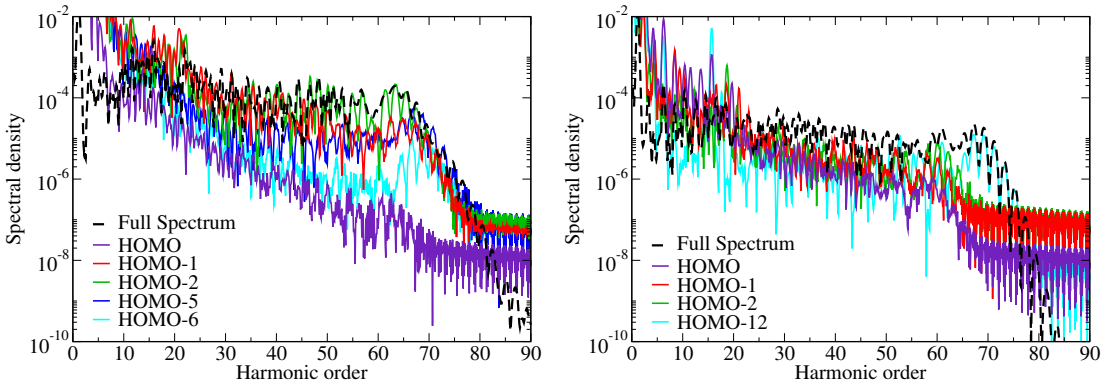

(a) Thymine, $\theta_{\text{mol}} = 0°$, $\theta_{\text{dip}} = 90°$ (b) Thymine, $\theta_{\text{mol}} = 90°$, $\theta_{\text{dip}} = 90°$

Figure 5.10: Contributions of a number of individual Kohn-Sham orbitals to two of the harmonic spectra shown in Fig. 5.9(b), calculated using Eqs. (3.71) and (3.73), along with the full spectra from Fig. 5.9(b) for reference. In all cases the laser pulse is a 5-cycle pulse with wavelength $\lambda = 1300$ nm and a peak intensity of $I = 1.0\times10^{14}$ W/cm^2, linearly polarized along the x-axis. The molecule, thymine, is aligned with the dipole aligned along (a) the y-axis and (b) the z-axis, as shown in Fig. 5.3. Due to the large number of Kohn-Sham orbitals, only those with the largest spectral densities are shown here.

what was seen in the ionization response in the previous section. The next highest σ states, the HOMO-5 and HOMO-6, contribute to the overall HHG spectra to a lesser degree in the plateau region, but increase in significance around the cutoff region. Here the difference in Kohn-Sham energies (effective ionization potentials) of the different orbitals means that the cutoffs associated with recombination to the four states shown are slightly different, and results in a broadening of the cutoff region in the overall harmonic spectrum. A similar behaviour is observed when the state contributions to the thymine spectrum for the ($\theta_{\text{mol}} = 0°$, $\theta_{\text{dip}} = 0°$) orientation are examined (not presented here), although in this case the HOMO-1 and HOMO-2 contributions are much less dominant, since the ionization in this orientation comes from a larger number of states, as seen in Fig. 5.8(b). Overall, the state contributions to the full harmonic spectrum in Fig. 5.10(a) are not surprising considering the three-step model and the observations previously made concerning the ionization from each Kohn-Sham orbital.

In the $\theta_{\text{mol}} = 90°$ orientation however, the picture is quite different, as shown in Fig. 5.10(b). In this orientation, while the plateau harmonics arise from recombination to a number of the highest occupied orbitals, the cutoff harmonics are associated with recombination to a relatively low lying orbital (the HOMO-12). Noting the difference in Kohn-Sham energies between the HOMO-12 and the highest occupied states

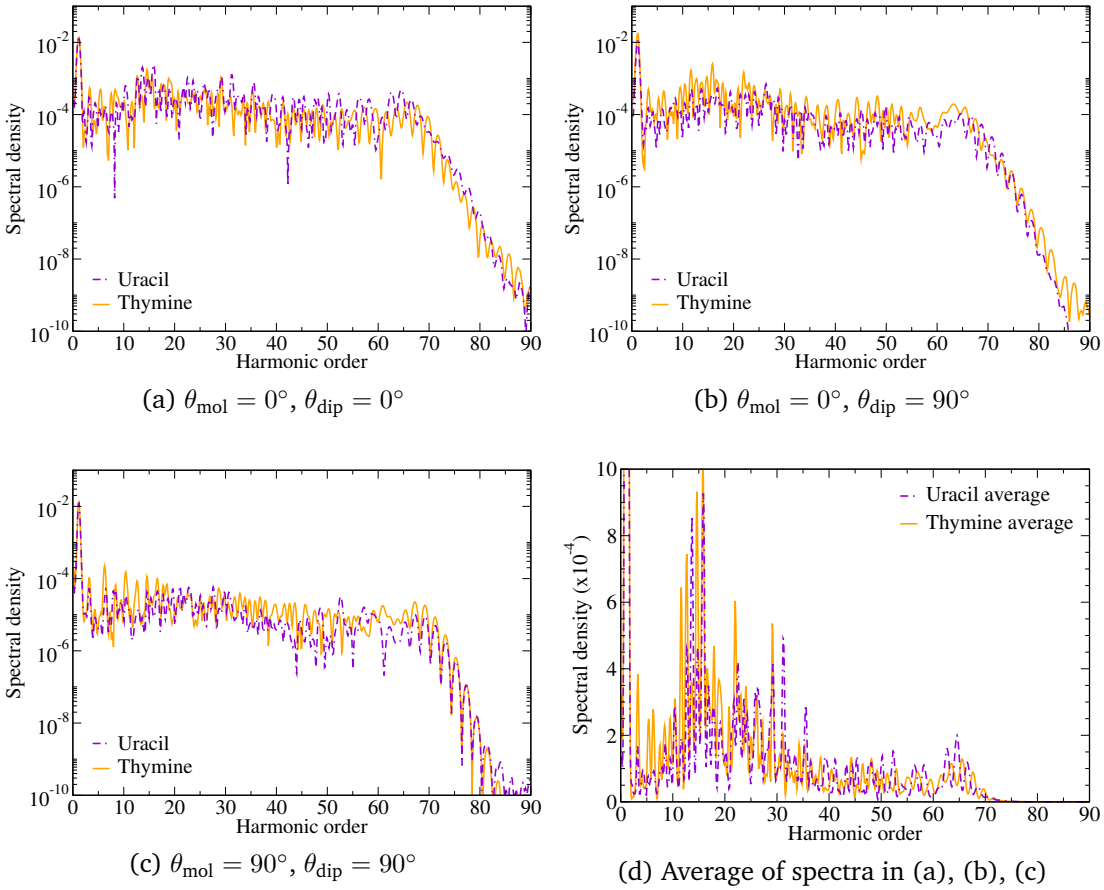

(a) $\theta_{\text{mol}} = 0°$, $\theta_{\text{dip}} = 0°$

(b) $\theta_{\text{mol}} = 0°$, $\theta_{\text{dip}} = 90°$

(c) $\theta_{\text{mol}} = 90°$, $\theta_{\text{dip}} = 90°$

(d) Average of spectra in (a), (b), (c)

Figure 5.11: High harmonic generation in uracil and thymine, following interaction with a 5-cycle mid-IR laser pulse with wavelength λ = 1300 nm and a peak intensity of I =1.0×10^{14} W/cm^2. The pulse is linearly polarized along the x-axis, and the molecules are aligned in the orientations shown in Fig. 5.3. The angles θ_{mol} and θ_{dip} respectively refer to the angle between the laser polarization direction and the plane of the molecule, and the angle between the laser polarization direction and the initial dipole moment of the molecule. Note that in panel (d), the spectral density is plotted on a linear rather than a logarithmic scale.

(Table 5.2), recombination to such a low lying orbital explains the extended cutoff observed in the spectra for $\theta_{\text{mol}} = 90°$ orientation compared to those for the $\theta_{\text{mol}} = 0°$ orientations. We see a similar picture when we examine the contributions of individual states to HHG in uracil (not shown here): in the $\theta_{\text{mol}} = 0°$ orientations, the HOMO and HOMO-2 dominate the spectrum; in the $\theta_{\text{mol}} = 90°$ orientation, the cutoff harmonics are dominated by the response of the lowest-lying π state (the HOMO-11).

To conclude this section we wish to compare the harmonic spectra for the two molecules, in each orientation. To this end, in Fig. 5.11 we re-plot the spectra shown in Fig. 5.9, but now directly comparing the spectra for uracil and for thymine. In Fig. 5.11 we see

that while in all three orientations the spectra for uracil and for thymine have similar shapes in general, with similar cutoff harmonics and a number of minima common to the spectra for both molecules (although other minima appear in only one spectrum), there are some clear differences.

In terms of the overall intensities of the spectra, we see from Figs. 5.11(b) and 5.11(c) that in the ($\theta_{\text{mol}} = 0^\circ$, $\theta_{\text{dip}} = 90^\circ$) and ($\theta_{\text{mol}} = 90^\circ$, $\theta_{\text{dip}} = 90^\circ$) orientations, the intensities of the thymine spectra are in general larger than the uracil spectra. This is not surprising, considering that we saw greater ionization from thymine than from uracil in Fig. 5.7. The same is not true, however, for the spectra produced in the ($\theta_{\text{mol}} = 0^\circ$, $\theta_{\text{dip}} = 0^\circ$) orientation. In Fig. 5.11(a) we see that the greater ionization from thymine than from uracil in this orientation does not lead to a greater harmonic response, as is the case in the other two orientations. We recall that in this ($\theta_{\text{mol}} = 0^\circ$, $\theta_{\text{dip}} = 0^\circ$) orientation for thymine, the ionization response was not dominated by one or two Kohn-Sham orbitals; instead we saw similar levels of ionization from a large number of the highest lying orbitals, of both σ and π symmetries.

From Fig. 5.11 we note that in none of the orientations considered do we see a large difference between HHG efficiency in uracil and thymine, as was observed in the uracil and thymine ablation plumes studied in the work of Hutchison *et al.* [57]. Considering the averages of the spectra for the three different orientations, as shown in Fig. 5.11(d), we might expect that for unaligned samples of unfragmented molecules, one would obtain harmonic spectra with broadly similar intensities from the two molecules. The largest differences in intensity between the two average spectra shown in Fig. 5.11(d) are generally localised to individual harmonic orders, and are most prominent among the lower-order harmonics where bound-bound transitions dominate the harmonic response.

5.3.4 Summary

In this section, we have investigated the response of the nucleobases uracil and thymine to an intense, mid-IR laser pulse. Three orientations of each molecule relative to the polarization direction of the linearly polarized laser pulse were considered, for each of which we calculated the ionization and the high harmonic spectra. For both molecules,

significantly more ionization and high harmonic generation were observed when the molecule was oriented such that the laser polarization direction was in the plane of the molecule than perpendicular to it. These differences were shown to be due to differences in the response of orbitals with σ symmetry and those with π symmetry. In the $\theta_{\text{mol}} = 0^\circ$ orientations, we observed significant ionization and high harmonic generation from a number of the highest-lying σ orbitals. In the $\theta_{\text{mol}} = 90^\circ$ orientation, ionization was observed mainly from a single orbital (the highest-lying π state), while the high harmonic spectra was dominated by contributions from a number of orbitals in the plateau region, and the lowest-lying π orbital near the cutoff.

Considering differences in response between the two $\theta_{\text{mol}} = 0^\circ$ orientations (in which the laser field is polarized in the plane of the molecule), in uracil we observed a significant increase in ionization and high harmonic generation in the ($\theta_{\text{mol}} = 0^\circ$, $\theta_{\text{dip}} = 0^\circ$) orientation compared to the ($\theta_{\text{mol}} = 0^\circ$, $\theta_{\text{dip}} = 90^\circ$) orientation, and showed that this was largely due to increased response of the two highest-lying σ states. In thymine, although the response of the two highest-lying σ states also increases in the ($\theta_{\text{mol}} = 0^\circ$, $\theta_{\text{dip}} = 90^\circ$) orientation, the total ionization is actually greatest in the ($\theta_{\text{mol}} = 0^\circ$, $\theta_{\text{dip}} = 0^\circ$) orientation. This was seen to be a slightly special case, in which a large number of orbitals, of both σ and π symmetry, contributed to the total ionization. We noted that in this orientation the bond between the methyl group and the ring of the thymine molecule was aligned parallel to the laser polarization direction. In terms of HHG in thymine, the value of θ_{dip} was seen to have little effect on the intensity of the harmonic spectrum.

Finally, in terms of differences between the two molecules, in all orientations we observed more ionization from thymine than from uracil. This greater ionization from thymine than from uracil was seen to lead to greater HHG in some orientations, but not in the ($\theta_{\text{mol}} = 0^\circ$, $\theta_{\text{dip}} = 0^\circ$) orientation. The average intensity of the harmonic spectra across the three orientations was seen to be comparable for the two molecules, with large differences in intensity generally localised to individual harmonic orders.

5.4 Response of thymine and 5-fluorouracil to a mid-IR field

Having observed a number of differences in the responses of the two nucleobases, uracil and thymine, to an applied mid-IR field in the previous section, we now consider the differences between thymine and the radiosensitising molecule used as a replacement for thymine in DNA, 5-fluorouracil. Understanding the differences in the responses of these two molecules is important for gaining a better understanding of the radiosensitising nature of 5-fluorouracil.

In this section all the calculation parameters are identical to those set out previously in Section 5.3.1.

5.4.1 Ionization response

As in Section 5.3, we begin by considering the total ionization from each molecule in each of the three orientations shown in Fig. 5.3, following interaction with the 1300 nm laser pulse described above (i.e., the pulse has a peak intensity of $I = 1.0\times10^{14}$ W/cm^2, a duration of 896.2 a.u. = 21.7 fs, and is linearly polarized along the x-axis). These total ionizations, I_{total}, are calculated using Eq. (5.2) as before (with $N_e = 48$ for both thymine and 5-fluorouracil).

From Fig. 5.12 we can see that the comparison of the total ionization from thymine and 5-fluorouracil is similar to the equivalent comparison between uracil and thymine presented in Fig. 5.7, with three main features of note. Firstly, there is significantly more ionization from both molecules when the laser pulse is polarized in the plane of the molecule ($\theta_{\text{mol}} = 0^\circ$) than perpendicular to it ($\theta_{\text{mol}} = 90^\circ$). Secondly, in all orientations, we see greater ionization from thymine than from 5-fluorouracil. However we note that in the ($\theta_{\text{mol}} = 0^\circ$, $\theta_{\text{mol}} = 90^\circ$) orientation, there is only a small difference between the total ionization from thymine and from 5-fluorouracil. Finally, in 5-fluorouracil there is a substantial difference in total ionization between the two $\theta_{\text{mol}} = 0^\circ$ orientations, as was the case in uracil; in thymine on the other hand, this difference is much smaller.

As in Section 5.3.2, we now examine the ionization response further by considering the ionization from each individual Kohn-Sham orbital. In Fig. 5.13 we show the ionization

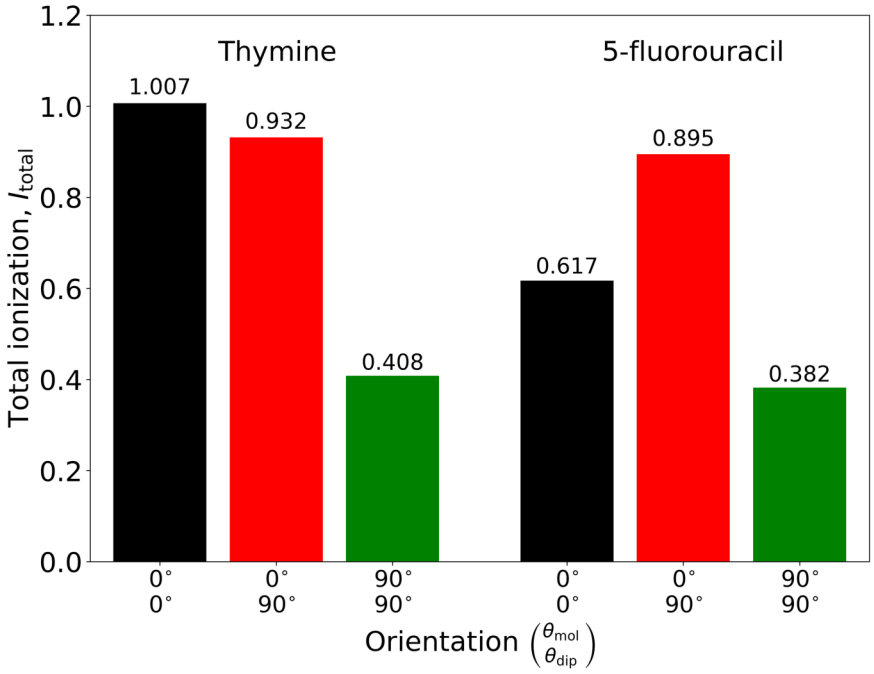

Figure 5.12: Total ionization, given by Eq. (5.2), from three different orientations of thymine and 5-fluorouracil, following interaction with a 5-cycle mid-IR laser pulse with wavelength $\lambda = 1300\,\text{nm}$ and a peak intensity of $I = 1.0\times10^{14}\,\text{W/cm}^2$. The pulse is linearly polarized along the x-axis, and the molecules are aligned in the orientations shown in Fig. 5.3. The angles θ_{mol} and θ_{dip} respectively refer to the angle between the laser polarization direction and the plane of the molecule, and the angle between the laser polarization direction and the initial dipole moment of the molecule.

from each orbital in thymine and 5-fluorouracil, for three different orientations of the molecules with respect to the laser polarization direction, calculated using Eq. (5.3) as before. Many of the features of this figure are similar to those described previously for Fig. 5.8, and so we will only describe them briefly here.

Firstly, we see from Fig. 5.13 that in 5-fluorouracil in all orientations, the ionization from a particular Kohn-Sham orbital is strongly dependent on whether the orbital has σ or π symmetry; such dependence is also observed in thymine, with the exception of the ($\theta_{\text{mol}} = 0°$, $\theta_{\text{dip}} = 0°$) orientation. Secondly, in a given orientation the orbital depletion from the most ionized orbital in 5-fluorouracil is greater than the depletion from the most ionized orbital in thymine; the greater total ionization from thymine than from 5-fluorouracil in each orientation (Fig. 5.12) is a result of significant ionization from a larger number of orbitals in thymine than in 5-fluorouracil. A clear example of this is in the ($\theta_{\text{mol}} = 0°$, $\theta_{\text{dip}} = 90°$) orientation (red curves): in both molecules, ionization comes mainly from the HOMO-1 and HOMO-2. In thymine however, there

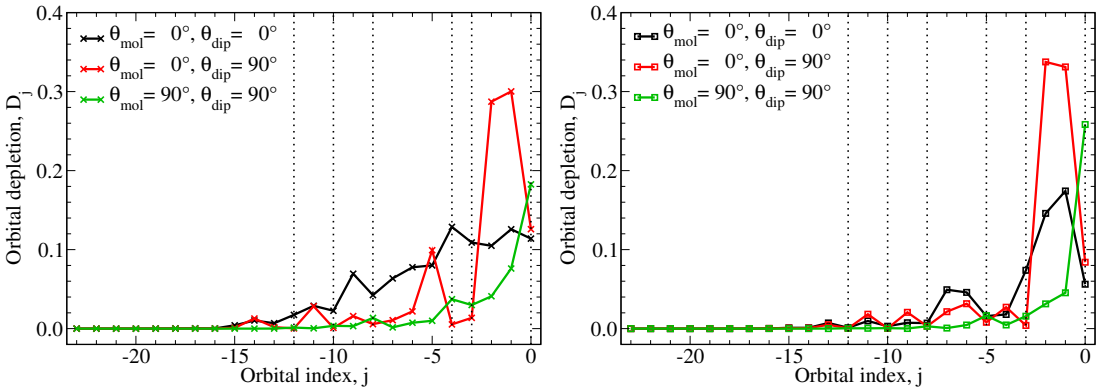

(a) Thymine (b) 5-fluorouracil

Figure 5.13: Orbital depletions, D_j, defined by Eq. (5.3), from each Kohn-Sham orbital for three different orientations of (a) thymine and (b) 5-fluorouracil, following interaction with a 5-cycle mid-IR laser pulse with wavelength $\lambda = 1300\,\text{nm}$ and a peak intensity of $1.0\times10^{14}\,\text{W/cm}^2$. The pulse is linearly polarized along the x-axis, and the molecules are aligned in the orientations shown in Fig. 5.3. The angles θ_{mol} and θ_{dip} respectively refer to the angle between the laser polarization direction and the plane of the molecule, and the angle between the laser polarization direction and the initial dipole moment of the molecule. We consider the orbital depletions, D_j, from the HOMO-j, where $j = 0, \ldots, N-1$ (i.e., $j = 0 \rightarrow$ HOMO-0 = HOMO, $j = 1 \rightarrow$ HOMO-1, $j = 2 \rightarrow$ HOMO-2, etc.). The vertical dotted lines indicate the Kohn-Sham states of π symmetry.

is also significant ionization from the HOMO-5. In 5-fluorouracil on the other hand, the other orbitals only exhibit minor ionization. Finally we note that in 5-fluorouracil, the greatest ionization is observed in the ($\theta_{\text{mol}} = 0°$, $\theta_{\text{dip}} = 90°$) orientation, due to the increased response of the two highest-lying σ states (the HOMO-1 and HOMO-2).

Having seen the differences in ionization between thymine and 5-fluorouracil, we now wish to see how the high harmonic response varies between the two molecules.

5.4.2 High harmonic generation

We consider high harmonic generation in thymine and 5-fluorouracil following interaction with the 5-cycle, mid-IR laser pulse described previously ($\lambda = 1300\,\text{nm}$, $I = 1.0\times10^{14}\,\text{W/cm}^2$, linearly polarized along the x-axis). The harmonic spectra for the two molecules, in the three different orientations, are plotted in Fig. 5.14.

As was the case with the uracil spectra shown in Fig. 5.9(a), we see in Fig. 5.14(a) that the intensities of the spectra for 5-fluorouracil vary in the manner one would expect from the three-step model, considering the differences in ionization response observed

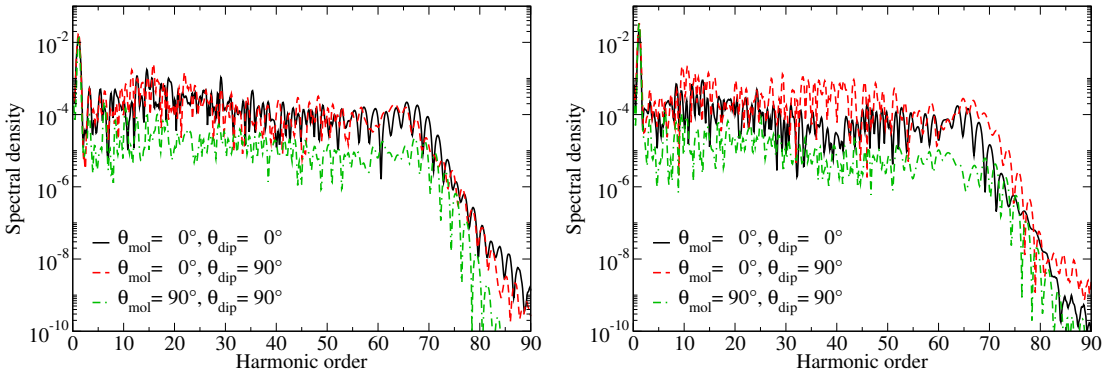

(a) Thymine (b) 5-fluorouracil

Figure 5.14: High harmonic generation in (a) thymine and (b) 5-fluorouracil, following interaction with a 5-cycle mid-IR laser pulse with wavelength $\lambda = 1300$ nm and a peak intensity of $I = 1.0\times10^{14}$ W/cm^2. The pulse is linearly polarized along the x-axis, and the molecules are aligned in the orientations shown in Fig. 5.3. The angles θ_{mol} and θ_{dip} respectively refer to the angle between the laser polarization direction and the plane of the molecule, and the angle between the laser polarization direction and the initial dipole moment of the molecule.

above. The difference between the spectra for the ($\theta_{\text{mol}} = 0°$, $\theta_{\text{dip}} = 0°$) and ($\theta_{\text{mol}} = 0°$, $\theta_{\text{dip}} = 90°$) orientations is particularly striking between harmonics 33 and 50, in which we see up to an order of magnitude enhancement of the spectrum between these two orientations. In 5-fluorouracil, we again see that the spectrum for the $\theta_{\text{mol}} = 90°$ orientation extends slightly further than the spectra for the $\theta_{\text{mol}} = 0°$ orientations.

As in the previous section, we can investigate the harmonic response further by examining the contributions of individual orbitals to the full spectra. These contributions for the three orientations of 5-fluorouracil are shown in Fig. 5.15. Here we see that, as was the case in thymine, in the $\theta_{\text{mol}} = 0°$ orientations (Figs. 5.15(a), 5.15(b)) the spectrum is dominated by contributions from the highest-lying σ states (the HOMO-1 and HOMO-2), whereas in the $\theta_{\text{mol}} = 90°$ orientation (Fig. 5.15(c)) the spectrum around the cutoff is dominated by contributions from a low-lying orbital (mainly the HOMO-12). Thus we observe a slight extension to the spectrum in the $\theta_{\text{mol}} = 90°$ orientation. In Fig. 5.15(d) we compare directly the HOMO-1 and HOMO-2 contributions in the two $\theta_{\text{mol}} = 0°$ orientations. Here we observe a large increase in the spectral densities for both the HOMO-1 and HOMO-2 contributions in the ($\theta_{\text{mol}} = 0°$, $\theta_{\text{dip}} = 90°$) orientation compared to the ($\theta_{\text{mol}} = 0°$, $\theta_{\text{dip}} = 0°$) orientation.

We can also investigate the presence of minima in the harmonic spectra, and whether

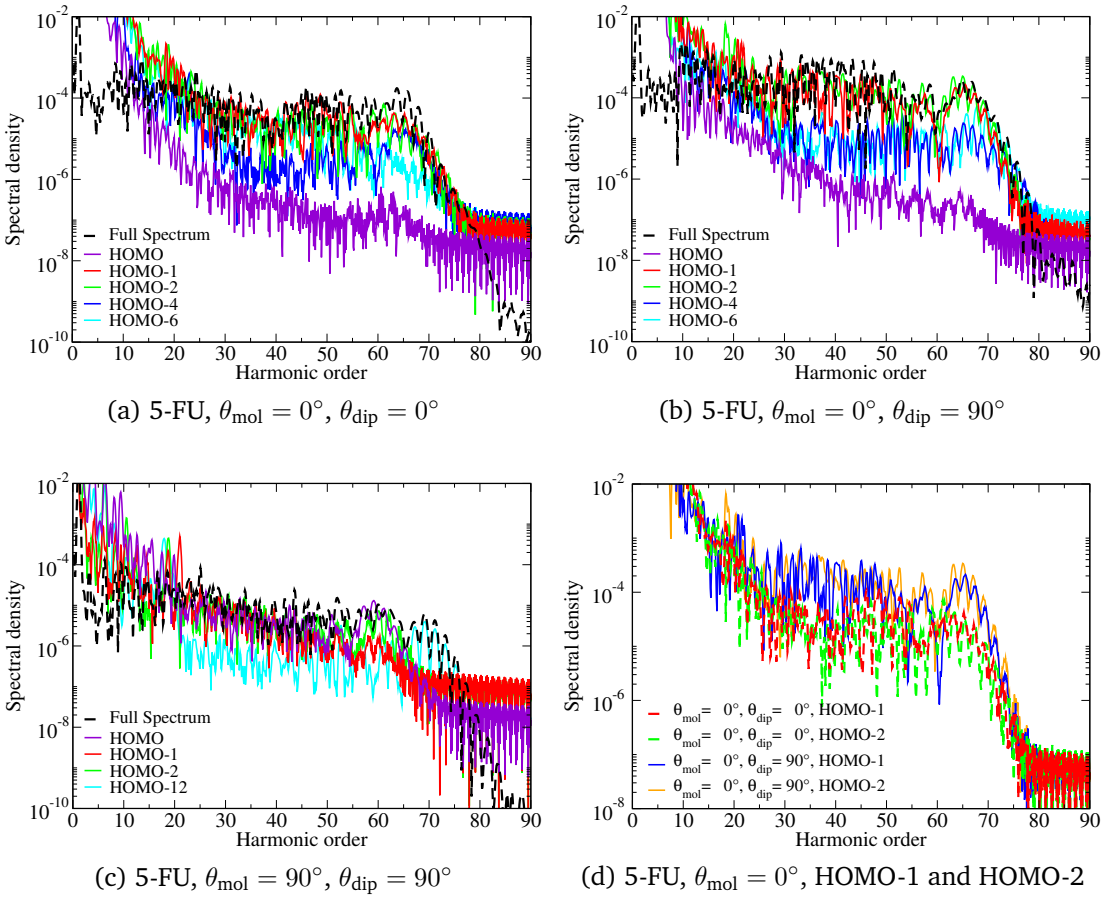

(a) 5-FU, $\theta_{\text{mol}} = 0°$, $\theta_{\text{dip}} = 0°$

(b) 5-FU, $\theta_{\text{mol}} = 0°$, $\theta_{\text{dip}} = 90°$

(c) 5-FU, $\theta_{\text{mol}} = 90°$, $\theta_{\text{dip}} = 90°$

(d) 5-FU, $\theta_{\text{mol}} = 0°$, HOMO-1 and HOMO-2

Figure 5.15: Contributions of a number of individual Kohn-Sham orbitals to the harmonic spectra shown in Fig. 5.14(b), calculated using Eqs. (3.71) and (3.73), along with the full spectra from Fig. 5.14(b) for reference. In all cases the laser pulse is a 5-cycle pulse with wavelength $\lambda = 1300$ nm and a peak intensity of $I = 1.0\times10^{14}$ W/cm^2, linearly polarized along the x-axis. The molecule, 5-fluorouracil, is aligned with the dipole aligned along (a) the x-axis, (b) the y-axis and (c) the z-axis, as shown in Fig. 5.3. Due to the large number of Kohn-Sham orbitals, only those with the largest spectral densities are shown here. In panel (d) the contributions of the HOMO-1 and HOMO-2 in the two $\theta_{\text{mol}} = 0°$ orientations are compared directly.

they are the result of structural interference, by calculating the recombination matrix elements for recombination to the various Kohn-Sham orbitals (see Section 4.5.4 and Appendix A for more details). These have been calculated for recombination to a number of the highest-lying states in each molecule for each orientation. As an example, in Fig. 5.16 we show the recombination amplitudes for recombination to the two highest-lying σ states in 5-fluorouracil (the HOMO-1 and HOMO-2) for the two $\theta_{\text{mol}} = 0°$ orientations. Comparing Figs. 5.16(a) and 5.16(b), we see that the recombination matrix elements for these two states exhibit quite different behaviours in the two $\theta_{\text{mol}} = 0°$ orientations. In the ($\theta_{\text{mol}} = 0°$, $\theta_{\text{dip}} = 0°$) orientation, Fig. 5.16(a), there are a number

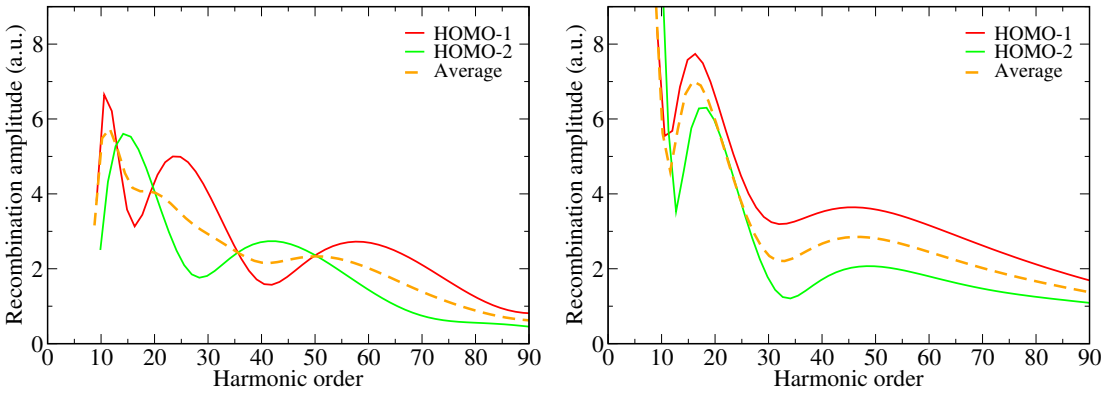

(a) 5-fluorouracil, ($\theta_{\text{mol}} = 0°$, $\theta_{\text{dip}} = 0°$)

(b) 5-fluorouracil, ($\theta_{\text{mol}} = 0°$, $\theta_{\text{dip}} = 90°$)

Figure 5.16: Dipole recombination matrix elements for a continuum electron recombining back to one of the two highest-lying occupied σ states of 5-fluorouracil, calculated via Eq. (4.3). The energy of the free electron and the ionization potentials of the individual Kohn-Sham states are related to a given harmonic order, n, using the classical formula $n\omega_L = k^2/2 + I_p$, where ω_L is the frequency of the IR field, k is the magnitude of the momentum of the free electron, and I_p is the ionization potential of the Kohn-Sham state. Here the IR field has a wavelength of $\lambda = 1300\,\text{nm}$ (i.e., $\omega_L = 0.0350\,\text{Ha}$), and the I_p values are taken as the negatives of the Kohn-Sham energies given in Table 5.2. The molecule, 5-fluorouracil, is aligned with the dipole aligned along (a) the x-axis and (b) the y-axis, as shown in Fig. 5.3. Recombination amplitudes are plotted as solid lines for recombination to the HOMO-1 and HOMO-2, while the averages of these two recombinations amplitudes are indicated with dashed lines.

of minima and maxima in the recombination amplitudes for the two states, appearing at different harmonic orders for the two states. However, taking an average of the recombination amplitudes for the two states, we see a minima around harmonic 41, which matches fairly well with what we see in the harmonic spectrum for this orientation shown in Fig. 5.14(b) (black spectrum). In the ($\theta_{\text{mol}} = 0°$, $\theta_{\text{dip}} = 90°$) orientation on the other hand, Fig. 5.16(b), we see that the recombination amplitudes for the two states follow similar shapes, with a minima around harmonic 32. Again, this matches fairly well with what we see in the harmonic spectrum for this orientation shown in Fig. 5.14(b) (red spectrum). In addition, we note that the recombination amplitudes across much of the spectrum are larger in the ($\theta_{\text{mol}} = 0°$, $\theta_{\text{dip}} = 90°$) orientation than in the ($\theta_{\text{mol}} = 0°$, $\theta_{\text{dip}} = 0°$) orientation, particularly so for the HOMO-1 in the region in which we observed the large harmonic enhancement in Fig. 5.14(b) (between harmonic 33 and harmonic 50).

Returning now to Fig. 5.14, comparing Figs. 5.14(a) and 5.14(b) we see that in the $\theta_{\text{mol}} = 0°$ orientations, thymine is much less sensitive to the value of θ_{dip} than 5-

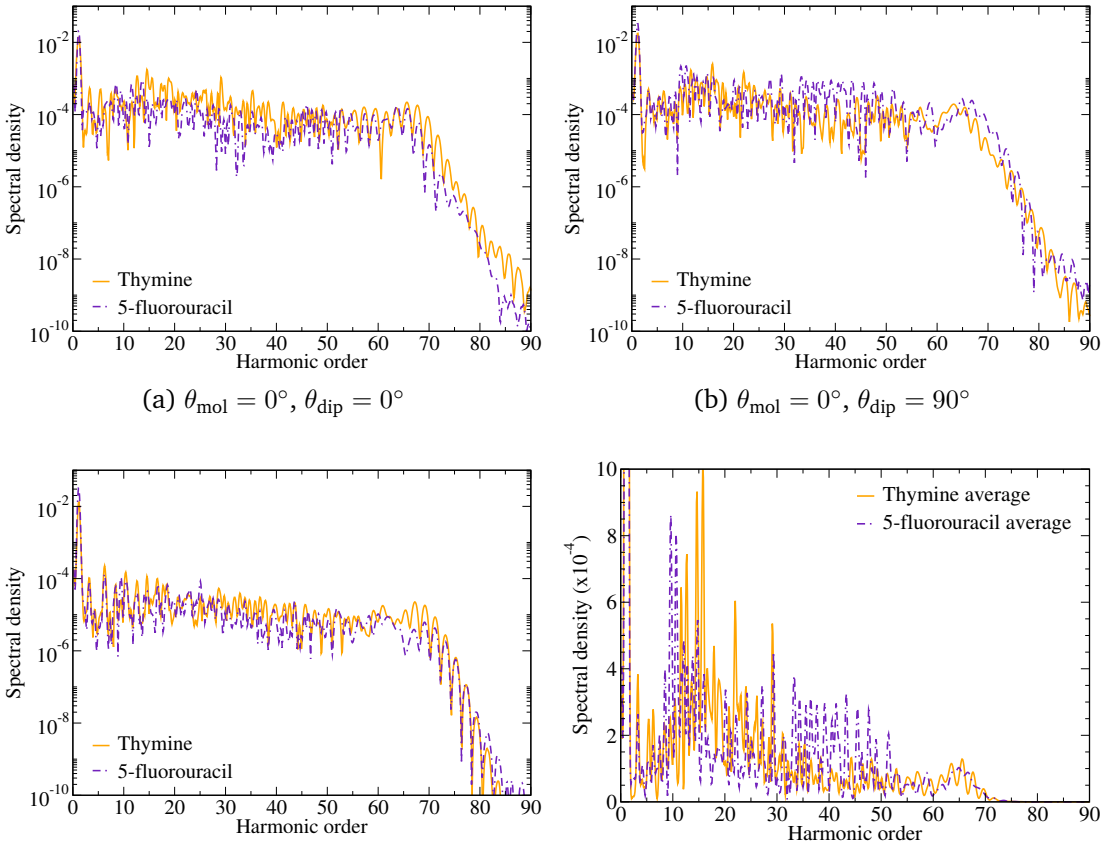

(a) $\theta_{\text{mol}} = 0°$, $\theta_{\text{dip}} = 0°$

(b) $\theta_{\text{mol}} = 0°$, $\theta_{\text{dip}} = 90°$

(c) $\theta_{\text{mol}} = 90°$, $\theta_{\text{dip}} = 90°$

(d) Average of spectra in (a), (b), (c)

Figure 5.17: High harmonic generation in thymine and 5-fluorouracil, following interaction with a 5-cycle mid-IR laser pulse with wavelength $\lambda = 1300\,\text{nm}$ and a peak intensity of $I = 1.0\times10^{14}\,\text{W/cm}^2$. The pulse is linearly polarized along the x-axis, and the molecules are aligned in the orientations shown in Fig. 5.3. The angles θ_{mol} and θ_{dip} respectively refer to the angle between the laser polarization direction and the plane of the molecule, and the angle between the laser polarization direction and the initial dipole moment of the molecule. Note that in panel (d), the spectral density is plotted on a linear rather than a logarithmic scale.

fluorouracil, as was the case with the total ionizations shown in Fig. 5.12. As in Section 5.3, in order to directly compare the thymine spectra with the 5-fluorouracil spectra we re-plot the spectra for each orientation; these comparisons are shown in Fig. 5.17.

In the ($\theta_{\text{mol}} = 0°$, $\theta_{\text{dip}} = 0°$) orientation, in which there is significantly more ionization from thymine than from 5-fluorouracil ($>$ 60% greater in thymine), we see that the spectral density in the lower half of the harmonic spectrum (up to $\approx$ harmonic 40) is in general larger in the thymine spectrum than in the spectrum for 5-fluorouracil. Above harmonic 40 however, the intensities of the two spectra are very similar. In the ($\theta_{\text{mol}} = 0°$, $\theta_{\text{dip}} = 90°$) orientation, in which the difference between ionization

from thymine and 5-fluorouracil is smaller ($<$ 5% greater in thymine), we see that in general the intensity of the 5-fluorouracil spectrum is comparable to or greater than the spectrum for thymine, with a particularly clear difference in the enhanced region between harmonics 33 and 50. In both of these orientations, considering the greater ionization seen in thymine than in 5-fluorouracil (Section 5.4.1), from a simple interpretation of the three-step model we would expect that the corresponding harmonic spectra from thymine would be greater than, or at least comparable to, the spectra from 5-fluorouracil; in Figs. 5.17(a) and 5.17(b), the intensities of the thymine spectra are smaller compared to the 5-fluorouracil than we might expect. In the ($\theta_{\text{mol}} = 90^\circ$, $\theta_{\text{dip}} = 90^\circ$) orientation on the other hand, in which we saw slightly more ionization from thymine than from 5-fluorouracil ($>$ 5% greater in thymine), the intensities of the harmonics in the thymine spectrum are consistently larger than those 5-fluorouracil spectrum.

Finally, in Fig. 5.17(d) we compare the averages of the spectra for the three different orientations of the two molecules. Here we see that the enhancement of harmonics 33–50 in 5-fluorouracil in the ($\theta_{\text{mol}} = 0^\circ$, $\theta_{\text{dip}} = 90^\circ$) orientation results in a noticeable difference between the two average spectra; in this region of harmonics we see that the average spectral density for 5-fluorouracil is 2–3 times as large as the average spectral density for thymine. While larger differences in spectral densities are seen for individual peaks in the spectra of the two molecules (particularly among the low-order harmonics), this region between harmonics 33 and 50 is interesting in that the average spectrum for 5-fluorouracil is consistently more intense than the average spectrum for thymine over a fairly wide range of harmonic orders. In addition, we note that the average spectra for thymine and 5-fluorouracil exhibit a much larger difference than the average spectra for uracil and thymine (Fig. 5.11(d)).

5.4.3 Summary

In this section, we have investigated the response of the nucleobase thymine and the radiosensitiser 5-fluorouracil to an intense, mid-IR laser pulse. Three different orientations of each molecule relative to the polarization direction of the linearly polarized laser pulse were considered, for each of which we calculated the ionization and the high harmonic spectra. To our knowledge these represent the first calculations of HHG

in these molecules.

In all three orientations, we observed greater ionization from thymine than from 5-fluorouracil. In addition, for both molecules we saw much greater ionization in the two $\theta_{\text{mol}} = 0^\circ$ orientations (in which the laser field is polarized in the plane of the molecule) than in the $\theta_{\text{mol}} = 90^\circ$ orientation (in which the laser field is polarization perpendicular to the plane of the molecule), as was seen with uracil in the previous section. In both molecules this resulted in a significantly less intense harmonic spectrum in the $\theta_{\text{mol}} = 90^\circ$ orientation than in the $\theta_{\text{mol}} = 0^\circ$ orientations.

In the $\theta_{\text{mol}} = 0^\circ$ orientations, a large difference was observed between the $\theta_{\text{dip}} = 0^\circ$ and $\theta_{\text{dip}} = 90^\circ$ orientations in the response of 5-fluorouracil, but not in the response of thymine. In other words, for a laser field linearly polarized in the plane of the molecule, the orientation of the molecule within the plane has a significant effect on the response of 5-fluorouracil, but not on the response of thymine. In 5-fluorouracil, we saw significantly more ionization in the ($\theta_{\text{mol}} = 0^\circ$, $\theta_{\text{dip}} = 90^\circ$) orientation than in the ($\theta_{\text{mol}} = 0^\circ$, $\theta_{\text{dip}} = 0^\circ$) orientation, which we attributed to enhanced ionization from the two highest-lying σ orbitals, as described previously for uracil. In this ($\theta_{\text{mol}} = 0^\circ$, $\theta_{\text{dip}} = 90^\circ$) orientation of 5-fluorouracil, this increase in ionization resulted in an increase in the intensity of the high harmonic spectrum, with particularly strong enhancement observed between harmonics 33 and 50.

Finally, we compared the harmonic spectra between the two molecules, for the three different orientations, and saw that increased ionization from thymine than from 5-fluorouracil did not always result in a more intense high harmonic spectrum. For instance, in the two $\theta_{\text{mol}} = 0^\circ$ orientations, the higher-order plateau harmonics in the spectra for 5-fluorouracil were of comparable or greater intensity to those in the spectra for thymine. Considering the average spectra over the three different orientations, we saw that while a number of the low-order harmonics had much greater intensity in thymine, the region of the plateau between harmonics 33 and 50 was significantly more intense in 5-fluorouracil, due to the enhancement in the ($\theta_{\text{mol}} = 0^\circ$, $\theta_{\text{dip}} = 90^\circ$) orientation.

5.5 Conclusions

In this chapter, we have presented results from the first set of TDDFT calculations of ionization and high harmonic generation in uracil, thymine and 5-fluorouracil, during interaction with an intense, linearly polarized, mid-IR laser pulse. The computationally demanding grid parameters required to describe these molecules in EDAMAME in an tractable way led to the development of new finite difference functionality in the EDAMAME code.

In Section 5.2 we showed how, using these new finite difference methods, the ground state properties of uracil, thymine and 5-fluorouracil are reproduced adequately well in EDAMAME. Although the calculated ionization potentials of the molecules are lower than the experimental values, the differences between calculated and experimental values are approximately the same for all three molecules, which gives us more confidence in making comparisons between the three molecules.

In Section 5.3 we investigated the response of the nucleobases uracil and thymine to an intense, linearly polarized, mid-IR pulse, for three different orientations of each molecule. These two molecules were the focus of an experimental study in 2013 by Hutchison *et al.*, which aimed to obtain the first measurements of HHG in uracil and thymine ablation plumes. While they were able to obtain a HHG signal in uracil, no signal was measured in thymine due to excessive fragmentation during the creation of the ablation plume. In our investigation of the response of uracil and thymine to a mid-IR pulse, we observed significantly more ionization from thymine than from uracil, although the duration of our calculations were too short to allow for fragmentation to occur. While in individual orientations the intensities of the harmonic spectra from uracil and thymine were noticeably different, averaging the spectral densities over the three different orientations produced harmonic spectra of similar intensities between the two molecules.

In Section 5.4 we extended our investigation to consider the differences in response to a mid-IR pulse between the nucleobase thymine and its radiosensitising replacement in DNA, 5-fluorouracil. Here we observed that ionization from thymine was also greater than that from 5-fluorouracil. In the high harmonic response however, we saw that

an enhancement of a window of high harmonics in one orientation of 5-fluorouracil led to a larger difference between the "orientation-averaged" spectra for thymine and 5-fluorouracil than between the "orientation-averaged" spectra for uracil and thymine.

In all three molecules considered here, the orientation of the plane of the molecule relative to the laser polarization direction was the most significant factor in determining the overall response. In all molecules we observed a significant reduction in ionization and HHG when the applied field was polarized perpendicular to the plane of the molecule, rather than in the plane. With the field polarized in the plane of the molecule, the molecules differed in the importance of the orientation of the molecule within this plane (specified by the angle θ_{dip} in this work). In uracil and 5-fluorouracil, we observed a strong dependence of both ionization and high harmonic generation on the angle θ_{dip}. This was seen to be largely due to changes in the responses of the two highest-lying σ states (HOMO and HOMO-2 in uracil, HOMO-1 and HOMO-2 in 5-fluorouracil). In thymine on the other hand, the total ionization and high harmonic generation varied only slightly with changing angle θ_{dip}, although the responses of individual orbitals did vary.

The work described in this chapter will hopefully form the first step in a larger study of the dynamics of these molecules, and potentially other biologically relevant molecules. Some of the possible future avenues of research in this area will be outlined at the end of this thesis. In addition, the coordinate scaling and least-squares finite difference approximation methods developed for this work should increase the range of systems that can be studied using EDAMAME.

Conclusions and future work

In this thesis we have investigated the dynamics of small organic molecules and biological molecules during interactions with intense laser fields. Using a mixed quantum-classical approach, in which the electrons are described using time-dependent density functional theory while the motion of the ions is treated classically, we have studied the response of four different molecules to intense, linearly polarized, mid-infrared laser pulses. In Chapter 1 we began with an overview of a number of the physical processes that can occur during the interaction of molecules with intense laser pulses, focusing in particular on ionization and harmonic generation processes. In Chapter 2 we introduced a number of theoretical methods used to described strong-field laser-molecule interactions, with a particular focus on the time-dependent density functional theory (TDDFT) and quantum-classical molecular dynamics methods used in this thesis. In Chapter 3 we described how these two methods are implemented in the Fortran2008 code EDAMAME.

In Chapter 4 we presented results from a series of calculations investigating the response of acetylene (C_2H_2) to a linearly polarized, mid-IR laser pulse. The aim of this project area was to perform one of the first in-depth theoretical studies of HHG in acetylene, focusing initially on the effect of varying the alignment of the molecule relative to the laser polarization direction. This molecular alignment effect was investigated by performing calculations for three different orientations of the molecule. Both ionization and high harmonic generation were found to increase as this angle was increased from a parallel to a perpendicular orientation, due to an increased response from the highest occupied molecular orbital (HOMO), which dominates the response of the molecule in the perpendicular orientation. In the parallel orientation, it was shown that the main

contributor to the high harmonic spectrum was not the HOMO, but the HOMO-1 and HOMO-2.

The second aim of this part of the project was to study differences in the response of the system when exposed to one of a number of different pump-probe laser pulse setups. The majority of Chapter 4 was dedicated to the discussion of these type of calculations, in which the pump-probe setup was used as a tool for investigating the origin of a double plateau structure observed in the harmonic spectrum produced in the parallel orientation. By preceding the mid-IR pulse with a shorter, lower intensity VUV pump pulse, we showed that the intensity of the inner plateau in the harmonic spectrum produced in the parallel orientation could be dramatically enhanced. While enhancement of harmonic spectra has previously been observed in other systems, these enhancements have generally been centred on a single harmonic or a narrow band of harmonics; in acetylene we see enhancement across the entire inner plateau. By varying the pulse parameters, performing time-frequency analyses of the harmonic response, and examining the electronic populations in each of the initial Kohn-Sham orbitals, we showed that the observed inner plateau is the result of high harmonic generation in which electronic population is ionized from and recombines back to an excited state (namely, the LUMO+1). A discrepancy between the observed inner plateau cutoff and that predicted by the semiclassical three-step model was resolved by calculating the recombination matrix element for recombination from the continuum to the LUMO+1, which exhibits a minimum near the predicted cutoff harmonic. To conclude this chapter we considered a number of variations on the pump-probe scheme, showing how the results of these are in agreement with our understanding of the HHG mechanism at work, and briefly considered the (minimal) role of ionic motion in the dynamic response of the molecule to the chosen laser pulses. Overall, the aims of this part of the project (as outlined in the Introduction) have been achieved.

In Chapter 5 we presented results from a series of calculations investigating the response of uracil, thymine and 5-fluorouracil to a mid-IR laser field. Describing these molecules in EDAMAME in a tractable way required the implementation of new finite difference methods in the code, namely coordinate scaling and a least-squares approximation to the central finite difference formulae. Using these new finite difference methods enabled the interaction of a mid-IR pulse with the three molecules of interest

to be studied at a manageable computational cost. For each molecule, we considered three different orientations with respect to the laser polarization direction, and investigated differences between molecules and between molecular orientations by studying the ionization and high harmonic generation in each case.

We first compared the response of the two nucleobases, uracil and thymine, as these molecules were the subject of a previous experimental study; as far as we know the only experimental study of HHG in these molecules to date. We then considered differences between the response of thymine and its radiosensitising replacement in DNA, 5-fluorouracil. In both of these comparisons (uracil and thymine on the one hand, thymine and 5-fluorouracil on the other) we observed a number of differences between orientations and between molecules.

Firstly, in all three molecules we observed a significant reduction in ionization and HHG when the laser field was polarized perpendicular to the plane of the molecule, rather than in the plane. Secondly, with the field polarized in the plane of the molecule, we found that in uracil and 5-fluorouracil the alignment of the molecule within this plane had a significant effect on the overall ionization and high harmonic generation. This was seen to be largely due to changes in the responses of the two highest-lying σ-type orbitals (HOMO and HOMO-2 in uracil, HOMO-1 and HOMO-2 in 5-fluorouracil). In both molecules the increased response of these orbitals in a particular orientation dominated the overall response of the molecules, and led to increased total ionization and an enhanced HHG signal. In thymine however, the difference between the response in the two orientations in which the laser field was polarized in the plane of the molecule was much smaller: while in one of these orientations we observed increased ionization from the two highest-lying σ orbitals (HOMO-1 and HOMO-2), in the other orientation we observed significant ionization from a larger number of orbitals, of both σ and π symmetries. The result is that while the orientation of the plane of the molecule relative to the laser polarization direction has a significant effect on the response in all three molecules, the exact orientation of the molecule when the laser field is polarized in the plane of the molecule is significant in uracil and 5-fluorouracil, but much less so in thymine.

Finally, in terms of the relative responses of the three molecules, in all three orientations

we observed greater ionization from thymine than from uracil or 5-fluorouracil. However, this was not always accompanied by more intense HHG in thymine than in the other two molecules. Considering the average intensities of the harmonic spectra over the three orientations, we saw that the "orientation-averaged" spectra for uracil and thymine were largely similar in intensity, while those for thymine and 5-fluorouracil were more noticeably different, due to a window of enhanced harmonics in the spectrum for one orientation of 5-fluorouracil.

Overall, the aims of this part of the project (as outlined in the Introduction) have been partially met. With regards to the first aim (which was to determine the extent to which EDAMAME can accurately and efficiently describe larger and more complicated molecules than those previously studied with the code), it was found that the finite different methods previously used in EDAMAME calculations would be inadequate for molecules as large and complex as the three molecules studied in Chapter 5. With the introduction of the new finite difference techniques described above, we saw that EDAMAME can describe the ground state properties of these molecules reasonably well, although with larger differences between calculated and experimental ionization potentials and bond lengths than observed in smaller and more simple molecules; as such this is an area that would warrant further investigation (as discussed in Future Work below). The second aim of this part of the project was to perform the first calculations of HHG in uracil, thymine and 5-fluorouracil, and to investigate the effect of the molecular alignment relative to the laser polarization direction on the harmonic response. This aim has been achieved, in the sense that these calculations were performed successfully, and a number of differences between the responses of the molecules in different orientations were noted. However, the origins of a number of the effects observed in these calculations were unclear, and will require further study (also discussed in Future Work below). The final aim of this part of the project involved making comparisons between the responses of uracil and thymine on the one hand, and thymine and 5-fluorouracil on the other. This aim has been achieved, with several differences observed between the responses of the molecules. In terms of how the calculated harmonic responses of uracil and thymine compared with the results of the only experimental study of HHG in these molecules to date, we found no significant differences between HHG in the two molecules, suggesting that the large differences observed experimentally were indeed

due to differences in the compositions of the ablation plumes of the two molecules, as the authors of that experimental study had proposed.

Future work

The work presented in Chapter 5 on the interaction of nucleobase and radiosensitiser molecules to a mid-IR laser pulse will hopefully be the first step in a larger study of these molecules, and potentially other biologically relevant molecules. There are a number of obvious avenues of follow-up work to the results presented in Chapter 5.

There were two effects observed in the results presented in Chapter 5 that were flagged as requiring further investigation. The first of these was a possible connection between the orientation of the carbon–oxygen bonds in the three molecules relative to the laser polarization direction and the response of the two highest-lying σ states. The second was specific to thymine, in which we noted a possible connection between ionization from individual Kohn-Sham orbitals and the orientation of the bond between the methyl group and the ring of the molecule: when this bond was aligned almost parallel to the laser polarization direction, we observed significant ionization from a larger number of orbitals than in other cases, with the symmetry of the orbital (σ or π) having little effect on the orbital depletion. One approach for investigating these two factors in the responses of molecules would be to examine variations in ionization and HHG around different atomic sites. This could be done in a number of ways.

One relatively straightforward approach would be to make use of the Voronoi polyhedra set up in the fuzzy cell decomposition used in the calculation of the Hartree potential within EDAMAME (see Section 3.2.3). These polyhedra provide a convenient way of partitioning the grid into regions around each atom. With a few modifications to the code, we should be able to calculate the electron density in each of these regions, and follow how these vary when a laser field is applied. The ability to observe, and quantify to some degree, the changes in electron density around different locations in the molecules should aid our understanding of the ionization dynamics in the different molecules and orientations. Going a step further, we could envisage calculating HHG in the region around each atom. Again making use of the fuzzy cell decomposition, calculating the dipole acceleration via Eq. (3.72) but considering only the electron density

within each Voronoi polyhedra, we could obtain an idea of whether or not recombination was occurring at some atomic sites more than others, and if so at which sites. Combined with the time-frequency analyses described in Section 3.5.3 (examples of which were presented in Chapter 4), this would enable us to investigate both when and where harmonics were generated.

In all the calculations described in Chapter 5, only a single laser pulse (a mid-IR pulse) was applied. An obvious extension to these calculations would be to consider pump-probe schemes, using a VUV pump pulse to excite or ionize the molecule in advance of the mid-IR probe, similar to the pump-probe setups used in Chapter 4. Such calculations could provide insights into both the HHG process (as in Chapter 4), and the different relaxation or fragmentation pathways of the molecules. However, calculations involving an intense, linearly polarized, mid-IR pulse are computationally expensive due to the large quiver amplitude and therefore large grid size required. As such, the range of pump-probe setups that could be studied could be quite severely limited by the availability of supercomputer time. One could of course reduce the wavelength of the applied field to reduce the grid size required, but this would also reduce the extent of the harmonic spectra, unless the laser intensity was increased to compensate (although possible increases in intensity would be limited by the low ionization potentials of these biological molecules).

Such large grid extents would not be required if we were to consider the response to just a lower intensity VUV laser pulse by itself. A number of interesting avenues of inquiry could be followed with just a VUV pulse applied. One such focus of study would be the calculation of the photoelectron spectra in different molecules, using the time-dependent surface flux method (t-SURFF) which has been implemented in the POpSiCLE (PhOtoelectron SpeCtrum library for Laser-matter intEractions) library [325, 326]. This library was developed at QUB, and was designed to interface with a number of laser-molecule codes, including EDAMAME. POpSiCLE and EDAMAME have previously been used together to calculate photoelectron spectra (including angularly-resolved photoelectron spectra) in acetylene due to the interaction with a number of the VUV pulses considered in Chapter 4 [260]. Following excitation or ionization by a VUV pulse, we could also consider propagating the Kohn-Sham equations for some time in the absence of any applied field, which would enable us to study the onset of

fragmentation in the molecules. Note however that in both of these types of studies, the calculations involved will not necessarily be significantly computationally cheaper than the mid-IR calculations presented in this thesis, despite the less demanding grid requirements. In the case of photoelectron spectra calculations, the use of t-SURFF as implemented in POpSiCLE requires the interpolation of the wavefunction (described in EDAMAME in Cartesian coordinates) onto a spherical shell, which introduces an computational overhead to the propagation of the Kohn-Sham equations. The study of fragmentation processes on the other hand may require the propagation of the Kohn-Sham equations for much longer durations than those considered in the mid-IR calculations.

In Chapter 5 we considered three orientations of each molecule, and briefly considered an average over the orientations when comparing high harmonic spectra between different molecules. While these three orientations certainly allowed us to observe differences in response between different orientations, three orientations are not sufficient to provide a full picture. For a more robust study of the orientation-averaged response, we could consider making use of the results of a series of studies on orientation-averaging performed by the groups of Eric Suraud and Paul-Gerhard Reinhard [62, 327, 328]. In these studies, which focused on the calculation of photoelectron angular distributions (PADs), an analytical scheme was developed for one-photon processes, which requires only 6 calculations, in properly chosen reference orientations, to compute the orientation-averaged PAD. For more general cases, in the non-perturbative regime, the authors investigated direct orientation-averaging (in which one considers a sphere around the molecule, divided into segments around selected sampling directions) and found that converged results for the orientation-averaged PADs were obtained with 30 different reference orientations, while 18 reference orientations represented a "a good compromise between expense and averaging". The number of reference orientations required may be reduced further still if the molecule of interest has structural symmetries. Considering the computational expense of some of our calculations, taking advantage of orientation-averaging schemes such as these and molecular symmetries will be crucial to managing the cost of future studies.

In the future work described above, we have still considered the interaction of an applied field with a single, isolated molecule. However, treating a single molecule in isolation is an idealised scenario, particularly when considering biological molecules such

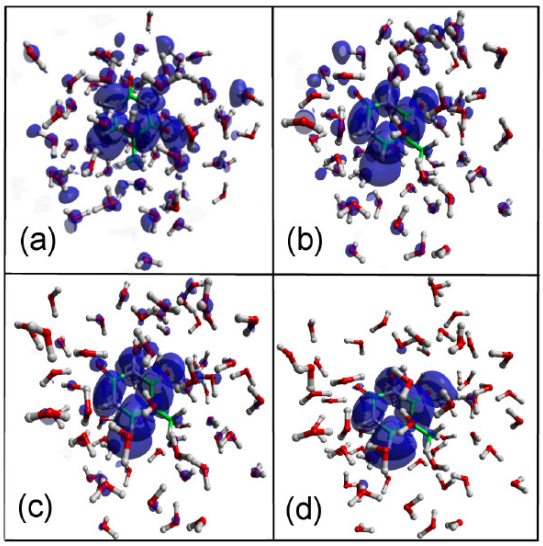

Figure 6: Evolution of the total spin density in solvated thymine, following vertical electron attachment, calculated using first-principles molecular dynamics. The panels show the system at times: (a) 0 fs, (b) 5 fs, (c) 10 fs and (d) 25 fs. Figure reproduced from [331].

as these. To simulate a more realistic biological environment, we could consider adding several water molecules to our systems, similar to a number of previous DFT studies [329–333]. For example, in [331], the authors studied the localisation of an excess electron in solvated DNA bases, and found that an initially delocalised electron localises around the nucleobase within a 15 fs timescale (as shown in Fig. 6 for thymine). These calculations were performed within the adiabatic approximation, in which the electron density follows the nuclear dynamics instantaneously. With EDAMAME, we would be able to describe the dynamics of the solvated system non-adiabatically. While the addition of numerous water molecules (enough to be representative of a liquid phase, e.g. five molecules as in [332]) would increase the computational cost of our calculations, it would be interesting to see what effect such an addition has on, for example, HHG in the system, or the ionization and fragmentation dynamics of the biological molecules. However, one potential challenge with working with such an ensemble of molecules may be accurately calculating the relaxed ground state geometry.

Considering more general future work, there are a number of changes to EDAMAME itself that could be implemented. One obvious example would be to investigate the use of different exchange-correlation approximations and/or self-interaction-correction schemes. The LDA-PW92-ADSIC approximation used in this work is a powerful approx-

imation, but as was seen in Section 5.2, it has its limitations. In addition, if we were to consider calculations in which the molecules under investigation undergo significant fragmentation, it is unclear how well or badly the LDA-PWD92-ADSIC approximation would describe the fragmenting molecule.

In the ADSIC scheme currently implemented in EDAMAME, we remove the self-interaction in the system in an orbital-independent way, by subtracting the interaction due to the average density. Alternatively, we could correct the self-interaction on an orbital-by-orbital basis. This is the approach taken in the widely-used SIC scheme introduced by Perdew and Zunger [183]. However, this Perdew-Zunger SIC scheme suffers from two major drawbacks. Firstly, the SIC functional depends explicitly on the orbitals, rather than the density. Secondly, it is not invariant under unitary transformation of the orbitals. These issues can be dealt with using the generalized OEP (optimized effective potential) scheme for self-interaction-correction developed by Kümmel *et al.* [181, 334, 335]. In this scheme, which aims to take advantage of the unitary variance of Perdew-Zunger-SIC, the Kohn-Sham orbitals are complemented by a second set of orbitals. These are obtained though a unitary transformation of the Kohn-Sham orbitals designed to minimize the instantaneous SIC energy, while reproducing the density given by the Kohn-Sham orbitals. Implementing the generalized OEP SIC scheme in EDAMAME would be considerably more computationally demanding than using ADSIC, but this orbital-specific self-interaction-correction may provide more accurate ionization potentials and bond lengths than the average-density self-interaction-correction currently used.

As with any computational study, we are restricted in the systems we can currently investigate using EDAMAME by the availability of supercomputer time. Increases in supercomputing power and availability in the coming years will hopefully allow us to investigate larger and more complex molecules with EDAMAME, and study laser-molecule interactions over longer timescales.

Appendix A

Calculation of recombination matrix elements

The recombination matrix element of an ionized electron to a bound state of a molecule can be written, in the length gauge, as

$$\boldsymbol{d}_{\mathrm{rec}}(\boldsymbol{k}) = \left\langle \chi(\boldsymbol{k},\boldsymbol{r}) \middle| \boldsymbol{r} \middle| \Psi(\boldsymbol{r}) \right\rangle, \tag{A.1}$$

where $\chi(\boldsymbol{k},\boldsymbol{r})$ is a plane wave describing a free electron with momentum $\boldsymbol{k}$,

$$\chi(\boldsymbol{k},\boldsymbol{r}) = \frac{1}{\left(\sqrt{2\pi}\right)^3} e^{i\boldsymbol{k}\cdot\boldsymbol{r}}, \tag{A.2}$$

while $\Psi(\boldsymbol{r})$ is the wavefunction of the bound state to which the free electron will recombine. In the work described in this thesis, we are interested in the recombination of the free electron to one of the field-free Kohn-Sham orbitals, meaning that we have $\Psi(\boldsymbol{r}) = \psi_j(\boldsymbol{r}, t=0)$ (in the following we will write $\psi_j(\boldsymbol{r}, t=0) = \psi_j(\boldsymbol{r})$ for brevity).

To calculate the recombination matrix elements within EDAMAME, for recombination to the Kohn-Sham orbital $\psi_j(\boldsymbol{r})$, we use an adapted version of the surface flux (t-SURFF) method [336, 337] as implemented in the POpSiCLE (PhOtoelectron SpeCtrum for Laser-matter intEractions) library [325, 326]. This method and library were designed for calculation of photoelectron spectra, but many of the routines used are

easily transferable to the calculation of recombination matrix elements, especially since POpSiCLE was developed to interface with EDAMAME (along with a number of other codes).

Due to the spherical nature of the problem, the t-SURFF method is generally implemented in spherical coordinates when describing a three-dimensional system; the implementation of t-SURFF in POpSiCLE is no different. We define sets of spherical coordinates in real-space (r, θ, ϕ) and momentum-space (k_r, k_θ, k_ϕ) such that

$$\boldsymbol{r} = (r\sin\theta\cos\phi)\,\hat{\boldsymbol{e}}_x + (r\sin\theta\sin\phi)\,\hat{\boldsymbol{e}}_y + (r\cos\theta)\,\hat{\boldsymbol{e}}_z, \tag{A.3}$$

$$\boldsymbol{k} = (k_r\sin k_\theta\cos k_\phi)\,\hat{\boldsymbol{e}}_x + (k_r\sin k_\theta\sin k_\phi)\,\hat{\boldsymbol{e}}_y + (k_r\cos k_\theta)\,\hat{\boldsymbol{e}}_z. \tag{A.4}$$

Working in these spherical coordinates, the plane wave $\chi(\boldsymbol{k}, \boldsymbol{r})$ can easily be expressed as a multipole expansion,

$$e^{i\boldsymbol{k}\cdot\boldsymbol{r}} = 4\pi\sum_{l=0}^{\infty}\sum_{m=-l}^{l} i^l j_l(\boldsymbol{k}\cdot\boldsymbol{r})Y_{lm}(k_\theta, k_\phi)Y^*_{lm}(\theta,\phi), \tag{A.5}$$

where $Y_{lm}(\theta,\phi)$ are spherical harmonics, for orbital angular momentum quantum number l and magnetic quantum number m, and $j_l(\boldsymbol{k}\cdot\boldsymbol{r})$ are spherical Bessel functions of the first kind.

The Kohn-Sham wavefunctions however, are defined in EDAMAME in terms of Cartesian coordinates. We therefore require a method of interpolating the Kohn-Sham wavefunctions from the Cartesian grid (x, y, z) to the spherical grid (r, θ, ϕ). This is achieved using tricubic interpolation (see [101, 338] for a description of how this method works).

In spherical coordinates, we can then rewrite Eq. (A.1) as

$$\boldsymbol{d}_{\text{rec}}(k_r, k_\theta, k_\phi) = \frac{1}{\left(\sqrt{2\pi}\right)^3}\int\int\int \psi_j(r,\theta,\phi)\boldsymbol{r}e^{-i\boldsymbol{k}\cdot\boldsymbol{r}}\mathrm{d}r\mathrm{d}\theta\mathrm{d}\phi. \tag{A.6}$$

Evaluating Eq. (A.6) along a given direction (e.g., along the laser polarization direction) and integrating over the momentum-space angular variables, k_θ and k_ϕ, we therefore obtain the dipole recombination matrix amplitude as a function of the momentum of the recolliding electron. In order to compare this calculated amplitude with high har-

monic spectra (as in Chapter 4), we can then relate the momentum of the returning electron, k_r, to the harmonic order, n, via the expression

$$n\omega_L = \frac{k_r^2}{2} + I_p, \tag{A.7}$$

where ω_L is the frequency of the applied laser field, and I_p is the ionization potential of the state to which the electron recombines (i.e., the magnitude of the energy of the Kohn-Sham orbital $\psi_j(\boldsymbol{r})$.)

References

[1] E. Muybridge, *The Horse in motion. "Sallie Gardner," owned by Leland Stanford; running at a 1:40 gait over the Palo Alto track, 19th June 1878*. http://www.loc.gov/pictures/resource/cph.3a45870/

[2] B. London and J. Upton, *Photography*, 6th ed. (Longman, 1997). http://goshootit.net/2015/04/15/convenience-and-spontaneity-of-zone-focusing/

[3] F. Krausz and M. Ivanov, Rev. Mod. Phys. **81**, 163, (2009).

[4] S. R. Leone *et al.*, Nat. Photonics **8**, 162, (2014).

[5] T. Gaumnitz, A. Jain, Y. Pertot, M. Huppert, I. Jordan, F. Ardana-Lamas and H. J. Wörner, Opt. Express **25**, 027506, (2017).

[6] F. Lépine, G. Sansone and M. J. J. Vrakking, Chem. Phys. Lett. **578**, 1, (2013).

[7] M. Nisoli, P. Decleva, F. Calegari, A. Palacios and F. Martín, Chem. Rev. **117**, 10760, (2017).

[8] T. H. Maiman, Nature, **187**, 493, (1960).

[9] G. Mourou, J. A. Wheeler and T. Tajima, Europhysics News **46**, 31, (2015).

[10] P. Agostini and L. F. DiMauro, Rep. Prog. Phys. **67**, 813, (2004).

[11] M. Protopapas, C. H. Keitel and P. L. Knight, Rep. Prog. Phys. **60**, 389, (1997).

[12] F. J. McClung and R. W. Hellwarth, J. Appl. Phys. **33**, 828, (1962).

[13] T. Brabec and F. Krausz, Rev. Mod. Phys. **72**, 545, (2000).

[14] H. A. Haus, IEEE J. Sel. Top. Quantum Electron. **6**, 1173, (2000).

[15] D. Strickland and G. Mourou, Opt. Commun. **56**, 219, (1985).

[16] M. D. Perry and G. Mourou, Science, **264**, 917, (1994).

[17] Wikipedia, *Chirped pulse amplification - Wikipedia, The Free Encyclopeda*. https://en.wikipedia.org/wiki/Chirped_pulse_amplification

[18] M. Perry, Science & technology review / Lawrence Livermore National Laboratory, (1995).

[19] A. H. Zewail, J. Phys. Chem. A **104**, 5660, (2000).

[20] Press release: The Nobel Prize in Physics 2018. https://www.nobelprize.org/prizes/physics/2018/press-release/

[21] A. Einstein, Ann. d. Physik **17**, 132, (1905).

[22] M. Göppert-Mayer, Ann. d. Physik **9**, 273, (1931).

[23] W. Kaiser and C. G. B. Garrett, Phys. Rev. Lett. **7**, 229, (1961).

[24] L. A. Lompre, G. Mainfray, C. Manus and J. Thebault, Phys. Rev. A **15**, 1604, (1977).

[25] P. Agostini, F. Fabre, G. Mainfray, G. Petiti and N. K. Rahman, Phys. Rev. Lett. **42**, 1127, (1979).

[26] Y. Gontier and M. Trahin, J. Phys. B: At. Mol. Phys. **13**, 4383, (1980).

[27] L. V. Keldysh, Sov. Phys. JETP **20**, 1307, (1965).

[28] D. M. Volkov, Z. Phys. **94**, 250, (1935).

[29] P. Agostini and L. F. DiMauro, Contemp. Phys. **49**, 179, (2008).

[30] F. H. M. Faisal, J. Phys. B: At. Mol. Phys. **6**, L89, (1973).

[31] H. R. Reiss, Phys. Rev. A **22**, 1786, (1980).

[32] M. V. Ammosov, N. B. Delone and V. P. Kraĭnov, Sov. Phys. JETP **64**, 1191, (1986).

[33] X. M. Tong, Z. X. Zhao and C. D. Lin, Phys. Rev. A **66**, 033402, (2002).

[34] F. Grasbon, G. G. Paulus, H. Walther, P. Villoresi, G. Sansone, S. Stagira, M. Nisoli and S. De Silvestri, Phys. Rev. Lett. **91**, 173003, (2003).

[35] P. B. Corkum, Phys. Rev. Lett. **71**, 1994, (1993).

[36] T. Kreibich, M. Lein, V. Engel and E. K. U. Gross, Phys. Rev. Lett. **87**, 103901, (2001).

[37] A. McPherson, G. Gibson, H. Jara, U. Johann, T. S. Luk, I. A. McIntyre, K. Boyer and C. K. Rhodes, J. Opt. Soc. Am. B **4**, 595, (1987).

[38] M. Ferray, A. L'Huillier, X. F. Li, L. A. Lompré, G. Mainfray and C. Manus, J. Phys. B: At. Mol. Opt. Phys. **21**, L31, (1988).

[39] C. Winterfeldt, C. Spielmann and G. Gerber, Rev. Mod. Phys. **80**, 117, (2008).

[40] K. Midorikawa, Jpn. J. Appl. Phys. **50**, 090001, (2011).

[41] J. L. Krause, K. J. Schafer and K. C. Kulander, Phys. Rev. Lett. **68**, 3535, (1992).

[42] J. J. Macklin, J. D. Kmetec and C. L. Gordon III, Phys. Rev. Lett. **70**, 766, (1993).

[43] J. P. Marangos, S. Baker, N. Kajumba, J. S. Robinson, J. W. G. Tisch and R. Torres, Phys. Chem. Chem. Phys. **10**, 35, (2008).

[44] O. E. Alon, V. Averbukh and N. Moiseyev, Phys. Rev. Lett. **80**, 3743, (1998).

[45] V. Averbukh, O. E. Alon and N. Moiseyev, Phys. Rev. A **64**, 033411, (2001).

[46] A. Wardlow and D. Dundas, Phys. Rev. A **93**, 023428, (2016).

[47] G. Sansone *et al.*, Science, **314**, 443, (2006).

[48] M. Lewenstein, Ph. Balcou, M. Yu. Ivanov, A. L'Huillier and P. B. Corkum, Phys. Rev. A **49**, 2117, (1994).

[49] S. Baker, J. S. Robinson, C. A. Haworth, H. Teng, R. A. Smith, C. C. Chirilă, M. Lein, J. W. G. Tisch and J. P. Marangos, Science, **312**, 424, (2006).

[50] R. Torres *et al.*, Phys. Rev. Lett. **98**, 203007, (2007).

[51] C. Vozzi, Appl. Phys. Lett. **97**, 241103, (2010).

[52] A.-T. Le, H. Wei, C. Jin and C. D. Lin, J. Phys. B: At. Mol. Opt. Phys. **49**, 053001, (2016).

[53] A.-T. Le, R. R. Lucchese, S. Tonzani, T. Morishita and C. D. Lin, Phys. Rev. A **80**, 013401, (2009).

[54] C. D. Lin, A.-T. Le, C. Jin and H. Wei, J. Phys. B: At. Mol. Opt. Phys. **51**, 104001, (2018).

[55] N. Hay, R. Velotta, M. Lein, R. de Nalda, E. Heesel, M. Castillejo and J. P. Marangos, Phys. Rev. A **65**, 053805, (2002).

[56] F. McGrath, A. S. Johnson, D. R. Austin, P. Hawkins, D. Wood, L. Miseikis, E. R. Simpson, M. Castillejo, R. Torres, S. Parker, T. Siegel and J. P. Marangos, Rev. Sci. Instrum. **88**, 103108, (2017).

[57] C. Hutchison *et al.*, Phys. Chem. Chem. Phys. **15**, 12308, (2013).

[58] C. Hutchison, Ph.D. thesis, Imperial College London, 2013.

[59] P.-C. Li and S.-I. Chu, Phys. Rev. A **88**, 053415, (2013).

[60] C. B. Madsen, A. S. Mouritzen, T. K. Kjeldsen and L. B. Madsen, Phys. Rev. A **76**, 035401, (2007).

[61] C. B. Madsen and L. B. Madsen, Phys. Rev. A **76**, 043419, (2007).

[62] P. Wopperer, B. Faber, P. M. Dinh, P.-G. Reinhard and E. Suraud, Phys. Lett. A **375**, 39, (2010).

[63] A. L. Lytle, Ph.D. thesis, University of Colorado, 2008.

[64] T. Pfeifer, C. Spielmann and G. Gerber, Rep. Prog. Phys. **69**, 443, (2006).

[65] R. de Nalda, E. Heesel, M. Lein, N. Hay, R. Velotta, E. Springate, M. Castillejo and J. P. Marangos, Phys. Rev. A **69**, 031804(R), (2004).

[66] N. Kajumba *et al.*, New. J. Phys. **10**, 025008, (2008).

[67] E. P. Fowe and A. D. Bandrauk, Phys. Rev. A **81**, 023411, (2010).

[68] R. Torres *et al.*, Opt. Express **18**, 3174, (2010).

[69] R. Torres, R. de Nalda and J. P. Marangos, Phys. Rev. A **72**, 023420, (2005).

[70] H. Stapelfeldt and T. Seideman, Rev. Mod. Phys. **75**, 543, (2003).

[71] S. Haessler, J. Caillat and P. Salières, J. Phys. B: At. Mol. Opt. Phys. **44**, 203001, (2011).

[72] T. Kanai, S. Minemoto and H. Sakai, Nature, **435**, 470, (2005).

[73] J. Itatani, J. Levesque, D. Zeidler, H. Niikura, H. Pépin, J. C. Kieffer, P. B. Corkum and D. M. Villeneuve, Nature, **432**, 867, (2004).

[74] M. Lein, T. Kreibich, E. K. U. Gross and V. Engel, Phys. Rev. A **65**, 033403, (2002).

[75] S. Baker, J. S. Robinson, M. Lein, C. C. Chirilă, R. Torres, H. C. Bandulet, D. Comtois, J. C. Kieffer, D. M. Villeneuve, J. W. G. Tisch and J. P. Marangos, Phys. Rev. Lett. **101**, 053901, (2008).

[76] R. M. Lock, X. Zhou, W. Li, M. M. Murnane and H. C. Kapteyn, Chem. Phys. **366**, 22, (2009).

[77] W. Li, X. Zhou, R. Lock, S. Patchkovskii, A. Stolow, H. C. Kapteyn and M. M. Murnane, Science, **322**, 1207, (2008).

[78] B. K. McFarland, J. P. Farrell, P. H. Bucksbaum and M. Gühr, Science, **322**, 1232, (2008).

[79] O. Smirnova, Y. Mairesse, S. Patchkovskii, N. Dudovich, D. Villeneuve, P. Corkum and M. Y. Ivanov, Nature, **460**, 972, (2009).

[80] M. Lein, Phys. Rev. Lett. **94**, 053004, (2005).

[81] C. C. Chirilă and M. Lein, J. Phys. B: At. Mol. Opt. Phys. **39**, S437, (2006).

[82] M. Lein, J. Phys. B: At. Mol. Opt. Phys. **40**, R135, (2007).

[83] J. P. Marangos, J. Phys. B: At. Mol. Opt. Phys. **49**, 132001, (2016).

[84] P. M. Paul, E. S. Toma, P. Breger, G. Mullot, F. Augé, Ph. Balcou, H. G. Muller and P. Agostini, Science, **292**, 1689, (2001).

[85] Y. Mairesse *et al.*, Science, **302**, 1540, (2003).

[86] P. Tzallas, D. Charalambidis, N. A. Papadogiannis, K. Witte and G. D. Tsakiris, Nature, **426**, 267, (2003).

[87] B. Shan, S. Ghimire and Z. Chang, J. Mod. Opt. **52**, 277, (2005).

[88] F. Calegari, M. Lucchini, M. Negro, C. Vozzi, L. Poletto, O. Svelto, S. De Silvestri, G. Sansone, S. Stagira and M. Nisoli, J. Phys. B: At. Mol. Opt. Phys. **45**, 074002, (2012).

[89] K. Zhao, Q. Zhang, M. Chini, Y. Wu, X. Wang and Z. Chang, Opt. Lett. **37**, 3891, (2012).

[90] J. Li *et al.*, Nat. Commun. **8**, 186, (2017).

[91] E. Goulielmakis, V. S. Yakovlev, A. L. Cavalieri, M. Uiberacker, V. Pervak, A. Apolonski, R. Kienberger, U. Kleineberg and F. Krausz, Science, **317**, 769, (2007).

[92] F. Calegari, G. Sansone, S. Stagira, C. Vozzi and M. Nisoli, J. Phys. B: At. Mol. Opt. Phys. **49**, 062001, (2016).

[93] A.-T. Le, R. R. Lucchese and C. D. Lin, J. Phys. B: At. Mol. Opt. Phys. **42**, 211001, (2009).

[94] J. H. Shirley, Phys. Rev. **138**, B979, (1965).

[95] S.-I. Chu and W. P. Reinhardt, Phys. Rev. Lett. **39**, 1195, (1977).

[96] P. G. Burke, J. Colgan, D. H. Glass and K. Higgins, J. Phys. B: At. Mol. Opt. Phys. **33**, 143, (2000).

[97] A. Giusti-Suzor, F. H. Mies, L. F. DiMauro, E. Charron and B. Yang, J. Phys. B: At. Mol. Opt. Phys. **28**, 309, (1995).

[98] I. Kawata, H. Kono and Y. Fujimura, J. Chem. Phys. **110**, 11152, (1999).

[99] D. Dundas, K. J. Meharg, J. F. McCann and K. T. Taylor, Eur. Phys. J. D **26**, 51, (2003).

[100] L. Peng, J. F. McCann, D. Dundas, K. T. Taylor and I. D. Williams, J. Chem. Phys. **120**, 10046, (2004).

[101] A. de la Calle, Ph.D. thesis, Queen's University Belfast, 2017.

[102] M. Born and J. R. Oppenheimer, Ann. d. Physik **84**, 457, (1927).

[103] S. Barmaki, H. Bachau and M. Ghalim, Phys. Rev. A **69**, 043403, (2004).

[104] A. Palacios, H. Bachau and F. Martín, Phys. Rev. Lett. **96**, 143001, (2006).

[105] F. Martín *et al.*, Science, **315**, 629, (2007).

[106] T. Niederhausen, U. Thumm and F. Martín, J. Phys. B: At. Mol. Opt. Phys. **45**, 105602, (2012).

[107] L. R. Moore, M. A. Lysaght, L. A. A. Nikolopoulos, J. S. Parker, H. W. van der Hart and K. T. Taylor, J. Mod. Opt. **58**, 1132, (2011).

[108] J. Wragg, J. S. Parker and H. W. van der Hart, Phys. Rev. A **92**, 022504, (2015).

[109] A. C. Brown and H. W. van der Hart, Phys. Rev. Lett. **117**, 093201, (2016).

[110] K. R. Hamilton, H. W. van der Hart and A. C. Brown, Phys. Rev. A **95**, 013408, (2017).

[111] C. Ó. Broin and L. A. A. Nikolopoulos, Phys. Rev. A **92**, 063428, (2015).

[112] C. Ó. Broin and L. A. A. Nikolopoulos, J. Phys. B: At. Mol. Opt. Phys. **50**, 033001, (2017).

[113] P. Ehrenfest, Z. Phys. **45**, 455, (1927).

[114] J. Kohanoff, *Electronic Structure Calculations for Solids and Molecules*, (Cambridge, New York, 2006).

[115] D. R. Hartree, Proc. Cambridge. Phil. Soc. **24**, 89, (1928).

[116] J. C. Slater, Phys. Rev. **32**, 339, (1928).

[117] E. Lötstedt, T. Kato and K. Yamanouchi, J. Chem. Phys. **138**, 104304, (2013).

[118] K. C. Kulander, Phys. Rev. A **36**, 2726, (1987).

[119] K. C. Kulander, Phys. Rev. A **38**, 778, (1988).

[120] M. S. Pindzola, F. Robicheaux and P. Gavras, Phys. Rev. A **55**, 1307, (1997).

[121] X. Li, S. M. Smith, A. N. Markevitch, D. A. Romanov, R. J. Levis and H. Bernhard Schlegel, Phys. Chem. Chem. Phys. **7**, 233, (2005).

[122] E. Lötstedt, T. Kato and K. Yamanouchi, Phys. Rev. A **85**, 041402(R), (2012).

[123] R. J. Bartlett and M. Musiał, Rev. Mod. Phys. **79**, 291, (2007).

[124] D. Cremer, Wiley Interdiscip. Rev.: Comput. Mol. Sci. **1**, 509, (2011).

[125] P. W. Atkins and R. S. Friedman, *Molecular Quantum Mechanics*, 3rd ed. (Oxford University Press, New York, 1997).

[126] I. Shavitt, Mol. Phys. **94**, 3, (1998).

[127] P. Krause, T. Klamroth and P. Saalfrank, J. Chem. Phys. **123**, 074105, (2005).

[128] H. Bernhard Schlegel, S. M. Smith and X. Li, J. Chem. Phys. **126**, 244110, (2007).

[129] J. A. Sonk, M. Caricato and H. Bernhard Schlegel, J. Phys. Chem. A **115**, 4678, (2011).

[130] E. Luppi and M. Head-Gordon, Mol. Phys. **110**, 909, (2012).

[131] A. F. White, C. J. Heide, P. Saalfrank, M. Head-Gordon and E. Luppi, Mol. Phys. **114**, 947, (2016).

[132] S. Pabst, A. Sytcheva, O. Geffert and R. Santra, Phys. Rev. A **94**, 033421, (2016).

[133] T. Kato and H. Kono, Chem. Phys. Lett. **392**, 533, (2004).

[134] J. Caillat, J. Zanghellini, M. Kitzler, O. Koch, W. Kreuzer and A. Scrinzi, Phys. Rev. A **71**, 012712, (2005).

[135] M. Nest, T. Klamroth and P. Saalfrank, J. Chem. Phys. **122**, 124012, (2005).

[136] D. Hochstuhl, C. M. Hinz and M. Bonitz, Eur. Phys. J. Special Topics **223**, 177, (2014).

[137] G. Jordan, J. Caillat, C. Ede and A. Scrinzi, J. Phys. B: At. Mol. Opt. Phys. **39**, S341, (2006).

[138] T. Kato and H. Kono, J. Chem. Phys. **128**, 184102, (2008).

[139] D. Hochstuhl and M. Bonitz, J. Chem. Phys. **134**, 084106, (2011).

[140] D. J. Haxton, K. V. Lawler and C. W. McCurdy, Phys. Rev. A **86**, 013406, (2012).

[141] M. Nest, R. Padmanaban and P. Saalfrank, J. Chem. Phys. **126**, 214106, (2007).

[142] T. Klamroth and M. Nest, Phys. Chem. Chem. Phys. **11**, 349, (2009).

[143] J. Zanghellini, Ch. Jungreuthmayer and T. Brabec, J. Phys. B: At. Mol. Opt. Phys. **39**, 709, (2006).

[144] G. Jordan and A. Scrinzi, New. J. Phys. **10**, 025035, (2008).

[145] P. V. Redkin and R. A. Ganeev, Phys. Rev. A **81**, 063825, (2010).

[146] M. Nest, Chem. Phys. Lett. **472**, 171, (2009).

[147] D. J. Haxton, K. V. Lawler and C. W. McCurdy, Phys. Rev. A **83**, 063416, (2011).

[148] H.-D. Meyer, U. Manthe and L. S. Cederbaum, Chem. Phys. Lett. **165**, 73, (1990).

[149] U. Manthe, H.-D. Meyer and L. S. Cederbaum, J. Chem. Phys. **97**, 3199, (1992).

[150] U. Manthe, H.-D. Meyer and L. S. Cederbaum, J. Chem. Phys. **97**, 9062, (1992).

[151] C. Meier and U. Manthe, J. Chem. Phys. **115**, 5477, (2001).

[152] G. Pasin, C. Iung, F. Gatti, F. Richter, C. Léonard and H.-D. Meyer, J. Chem. Phys. **129**, 144304, (2008).

[153] M. H. Beck, A. Jäckle, G. A. Worth and H.-D. Meyer, Phys. Rep. **324**, 1, (2000).

[154] M. Ruberti, V. Averbukh and P. Decleva, J. Chem. Phys. **141**, 164126, (2014).

[155] M. Ruberti, Ph.D. thesis, Imperial College London, 2016.

[156] M. Ruberti, R. Yun, K. Gokhberg, S. Kopelke, L. S. Cederbaum, F. Tarantelli and V. Averbukh, J. Chem. Phys. **140**, 184107, (2014).

[157] S. P. Neville, V. Averbukh, S. Patchkovskii, M. Ruberti, R. Yun, M. Chergui, A. Stolow and M. S. Schuurman, Faraday Discuss. **194**, 117, (2016).

[158] M. Ruberti, P. Decleva and V. Averbukh, Phys. Chem. Chem. Phys. **20**, 8311, (2018).

[159] E. Lötstedt, T. Kato and K. Yamanouchi, in *Progress in Ultrafast Intense Laser Science XIII*, edited by K. Yamanouchi, W. T. Hill and G. G. Paulus (Springer, New York, 2017).

[160] W. Kohn, Rev. Mod. Phys. **71**, 1253, (1999).

[161] Kieron Burke and friends, *The ABC of DFT*, (2007) http://dft.uci.edu/research.php.

[162] *Density Functional Theory*, edited by E. K. U. Gross and R. M. Dreizler (Plenum, New York, 1995).

[163] P. Hohenberg and W. Kohn, Phys. Rev. **136**, B864, (1964).

[164] W. Kohn and L. J. Sham, Phys. Rev. **140**, A1133, (1965).

[165] P. J. Hasnip, K. Refson, M. I. J. Probert, J. R. Yates, S. J. Clark and C. J. Pickard, Phil. Trans. R. Soc. A **372**, 20130270, (2014).

[166] D. J. Cole and N. D. M. Hine, J. Phys.: Condens. Matter **28**, 393001, (2016).

[167] K. Burke, J. Chem. Phys. **136**, 150901, (2012).

[168] A. D. Becke, J. Chem. Phys. **140**, 18A301, (2014).

[169] R. O. Jones, Rev. Mod. Phys. **87**, 897, (2015).

[170] E. Runge and E. K. U. Gross, Phys. Rev. Lett. **52**, 997, (1984).

[171] E. K. U. Gross and K. Burke, in *Time-Dependent Density Functional Theory*, edited by M. A. L. Marques, C. A. Ullrich, F. Nogueira, A. Rubio, K. Burke and E. K. U. Gross (Springer-Verlag, Berlin Heidelberg, 2006).

[172] M. A. L. Marques and E. K. U. Gross, Annu. Rev. Phys. Chem. **55**, 427, (2004).

[173] M. Lein and S. Kümmel, Phys. Rev. Lett. **94**, 143003, (2005).

[174] N. T. Maitra, in *Time-Dependent Density Functional Theory*, edited by M. A. L. Marques, C. A. Ullrich, F. Nogueira, A. Rubio, K. Burke and E. K. U. Gross (Springer-Verlag, Berlin Heidelberg, 2006).

[175] R. G. Parr and W. Yang, *Density-functional theory of atoms and molecules* (Oxford University Press, New York, 1989).

[176] J. P. Perdew and Y. Wang, Phys. Rev. B **45**, 13244, (1992).

[177] J. P. Perdew and K. Burke, Int. J. Quantum Chem. **57**, 309, (1996).

[178] C. A. Ullrich, U. J. Gossmann and E. K. U. Gross, Phys. Rev. Lett. **74**, 872, (1995).

[179] S. Kümmel and J. P. Perdew, Phys. Rev. B **68**, 035103, (2003).

[180] *Time-Dependent Density Functional Theory*, edited by M. A. L. Marques, C. A. Ullrich, F. Nogueira, A. Rubio, K. Burke and E. K. U. Gross (Springer-Verlag, Berlin Heidelberg, 2006).

[181] T. Körzdörfer, S. Kümmel and M. Mundt, J. Chem. Phys. **129**, 014110, (2008).

[182] C. Legrand, E. Suraud and P.-G. Reinhard, J. Phys. B: At. Mol. Opt. Phys. **35**, 1115, (2002).

[183] J. P. Perdew and A. Zunger, Phys. Rev. B **23**, 5048, (1981).

[184] T. Tsuneda and K. Hirao, J. Chem. Phys. **140**, 18A513, (2014).

[185] J. B. Krieger, Y. Li and G. J. Iafrate, Phys. Rev. A **45**, 101, (1992).

[186] I. Ciofini, C. Adamo and H. Chermette, Chem. Phys. **309**, 67, (2005).

[187] A. J. Krueger and N. T. Maitra, Phys. Chem. Chem. Phys. **11**, 4655, (2009).

[188] A. S. de Wijn, M. Lein and S. Kümmel, EPL **84**, 43001, (2008).

[189] D. Dundas and J. M. Rost, Phys. Rev. A **71**, 013421, (2005).

[190] P. Wopperer, U. De Giovannini and A. Rubio, Eur. Phys. J. B **90**, 51, (2017).

[191] C. A. Ullrich and A. D. Bandrauk, in *Time-Dependent Density Functional Theory*, edited by M. A. L. Marques, C. A. Ullrich, F. Nogueira, A. Rubio, K. Burke and E. K. U. Gross (Springer-Verlag, Berlin Heidelberg, 2006).

[192] C. A. Ullrich, J. Mol. Struct.: Theochem **501-502**, 315, (2000).

[193] A. Crawford-Urunga *et al.*, Phys. Rev. A **90**, 033412, (2014).

[194] S. Kurth, G. Stefanucci, C.-O. Almbladh, A. Rubio and E. K. U. Gross, Phys. Rev. B **72**, 035308, (2005).

[195] C.-L. Cheng, J. S. Evans and T. Van Voorhis, Phys. Rev. B **74**, 155112, (2006).

[196] U. Saalmann and R. Schmidt, Phys. Rev. Lett. **80**, 3213, (1998).

[197] Z. Wang, S.-S. Li and L.-W. Wang, Phys. Rev. Lett. **114**, 063004, (2015).

[198] R. Seraide, M. A. Bernal, G. Brunetto, U. de Giovannini and A. Rubio, J. Phys. Chem. B **121**, 7276, (2017).

[199] M. A. L. Marques, X. López, D. Varsano, A. Castro and A. Rubio, Phys. Rev. Lett. **90**, 258101, (2003).

[200] G. Onida, L. Reining and A. Rubio, Rev. Mod. Phys. **74**, 601, (2002).

[201] T. Kunert and R. Schmidt, Eur. Phys. J. D **25**, 15, (2003).

[202] M. Uhlmann, T. Kunert, F. Grossmann and R. Schmidt, Phys. Rev. A **67**, 013413, (2003).

[203] S. Chelkowski, T. Zuo, O. Atabek and A. D. Bandrauk, Phys. Rev. A **52**, 2977, (1995).

[204] M. A. L. Marques, A. Castro, G. F. Bertsch and A. Rubio, Comp. Phys. Comm. **151**, 60, (2003).

[205] A. Castro, M. A. L. Marques, J. A. Alonso, G. F. Bertsch and A. Rubio, Eur. Phys. J. D **28**, 211, (2004).

[206] H. Haberland, A. Hofmann and B. v. Issendorff, J. Chem. Phys. **103**, 3450, (1995).

[207] C.-Z. Gao, P. M. Dinh, P.-G. Reinhard and E. Suraud, Phys. Chem. Chem. Phys. **19**, 19784, (2017).

[208] X. Chu and S.-I. Chu, Phys. Rev. A **64**, 063404, (2001).

[209] L. Cui, J. Zhao, Y. J. Hu, Y. Y. Teng, X. H. Zeng and B. Gu, Appl. Phys. Lett. **89**, 211103, (2006).

[210] D. A. Telnov and S.-I. Chu, Phys. Rev. A **80**, 043412, (2009).

[211] X. Chu and G. C. Groenenboom, Phys. Rev. A **93**, 013422, (2016).

[212] J. Heslar, D. Telnov and S.-I. Chu, Phys. Rev. A **83**, 043414, (2011).

[213] E. P. Fowe and A. D. Bandrauk, Phys. Rev. A **84**, 035402, (2011).

[214] A. Crawford-Uranga, U. De Giovannini, D. J. Mowbray, S. Kurth and A. Rubio, J. Phys. B: At. Mol. Opt. Phys. **47**, 124018, (2014).

[215] T. Kreibich and E. K. U. Gross, Phys. Rev. Lett. **86**, 2984, (2001).

[216] R. van Leeuwen and E. K. U. Gross, in *Time-Dependent Density Functional Theory*, edited by M. A. L. Marques, C. A. Ullrich, F. Nogueira, A. Rubio, K. Burke and E. K. U. Gross (Springer-Verlag, Berlin Heidelberg, 2006).

[217] O. Butriy, H. Ebadi, P. L. de Boeij, R. van Leeuwen and E. K. U. Gross, Phys. Rev. A **76**, 052514, (2007).

[218] T. Kreibich, R. van Leeuwen and E. K. U. Gross, Phys. Rev. A **78**, 022501, (2008).

[219] D. Dundas, J. Phys. B: At. Mol. Opt. Phys. **37**, 2883, (2004).

[220] D. Dundas, J. Chem. Phys. **136**, 194303, (2012).

[221] T. N. Todorov, J. Phys.: Condens. Matter **13**, 10125, (2001).

[222] A. Abedi, N. T. Maitra and E. K. U. Gross, Phys. Rev. Lett. **105**, 123002, (2010).

[223] I. Tavernelli, B. F. E. Curchod and U. Rothlisberger, Phys. Rev. A **81**, 052508, (2010).

[224] A. D. Bandrauk, S. Chelkowski, S. Kawai and H. Lu, Phys. Rev. Lett. **101**, 153901, (2008).

[225] B. F. E. Curchod, U. Rothlisberger and I. Tavernelli, Chem. Phys. Chem. **14**, 1314, (2013).

[226] S. Meng and E. Kaxiras, J. Chem. Phys. **129**, 054110, (2008).

[227] A. D. Bandrauk, in *Molecules in Laser Fields*, edited by A. D. Bandrauk (Dekker, New York, 1992).

[228] T. W. B. Kibble and F. H. Berkshire, *Classical Mechanics*, 4th ed. (Addison Wesley Longman, Essex, 1996).

[229] C. J. Joachain and N. J. Kylstra, Phys. Scr. **68**, C72, (2003).

[230] A. D. Bandrauk, F. Fillion-Gourdeau and E. Lorin, J. Phys. B: At. Mol. Opt. Phys. **46**, 153001, (2013).

[231] K. J. Meharg, J. S. Parker and K. T. Taylor, J. Phys. B: At. Mol. Opt. Phys. **38**, 237, (2005).

[232] S. Selstø and M. Førre, Phys. Rev. A **76**, 023427, (2007).

[233] M. W. Walser, C. H. Keitel, A. Scrinzi and T. Brabec, Phys. Rev. Lett. **85**, 5082, (2000).

[234] A. D. Bandrauk and H. Z. Lu, Phys. Rev. A **73**, 013412, (2006).

[235] A. Staudt and C. H. Keitel, Phys. Rev. A **73**, 043412, (2006).

[236] R. Eisberg and R. Resnick, *Quantum Physics*, 2nd ed. (Wiley, 1985).

[237] Y.-C. Han and L. B. Madsen, Phys. Rev. A **81**, 063430, (2010).

[238] ARCHER UK National Supercomputing Service (http://www.archer.ac.uk).

[239] G. B. Arfken, H. J. Weber and F. E. Harris, *Mathematical Methods for Physicists: A Comprehensive Guide*, 7th ed. (Elsevier, 2013).

[240] A. Castro and M. A. L. Marques, in *Time-Dependent Density Functional Theory*, edited by M. A. L. Marques, C. A. Ullrich, F. Nogueira, A. Rubio, K. Burke and E. K. U. Gross (Springer-Verlag, Berlin Heidelberg, 2006).

[241] J. R. Chelikowsky, N. Troullier, K. Wu and Y. Saad, Phys. Rev. B **50**, 11355, (1994).

[242] K. Hirose, T. Ono, Y. Fujimoto and S. Tsukamoto, *First-Principles Calculations in Real-Space Formalism*, (Imperial College Press, 2005).

[243] J. S. Parker, *Optimization of the MPI parallel RMT code for HECToR and likely successors*, project summary report (2011). http://www.hector.ac.uk/cse/distributedcse/reports/rmt/

[244] N. Troullier and J. L. Martins, Phys. Rev. B **43**, 1993, (1991).

[245] L. Kleinman and D. M. Bylander, Phys. Rev. Lett. **48**, 1425, (1982).

[246] X. Jing, N. Troullier, D. Dean, N. Binggeli, J. R. Chelikowsky, K. Wu and Y. Saad, Phys. Rev. B **50**, 12234, (1994).

[247] M. J. T. Oliveira and F. Nogueira, Comp. Phys. Comm. **178**, 524, (2008).

[248] Y. Zhou, Y. Saad, M. L. Tiago and J. R. Chelikowsky, J. Comp. Phys. **219**, 172, (2006).

[249] Y. Zhou, Y. Saad, M. L. Tiago and J. R. Chelikowsky, Phys. Rev. E **74**, 066704, (2006).

[250] K. Wu, A. Canning, H. D. Simon and L.-W. Wang, J. Comp. Phys. **154**, 156, (1999).

[251] A. Castro, M. A. L. Marques and A. Rubio, J. Chem. Phys. **121**, 3425, (2004).

[252] E. S. Smyth, J. S. Parker and K. T. Taylor, Comp. Phys. Comm. **114**, 1, (1998).

[253] W. E. Arnoldi, Q. App. Math. **9**, 17, (1951).

[254] D. Frenkel and B. Smit, *Understanding Molecular Simulation: From Algorithms to Applications*, 2nd ed. (Elsevier, 2002).

[255] National Institute of Standards and Technology (NIST) Chemistry WebBook, http://webbook.nist.gov/chemistry

[256] D. C. Liu and J. Nocedal, Math. Program. **45**, 503, (1989).

[257] K. Burnett, V. C. Reed, J. Cooper and P. L. Knight, Phys. Rev. A **45**, 3347, (1992).

[258] H. Ibrahim *et al.*, Nat. Commun. **5**, 4422, (2014).

[259] J. B. Greenwood, J. Miles, S. De Camillis, P. Mulholland, L. Zhang, M. A. Parkes, H. C. Hailes and H. H. Fielding, J. Phys. Chem. Lett. **5**, 3588, (2014).

[260] D. Dundas, P. Mulholland, A. Wardlow and A. de la Calle, Phys. Chem. Chem. Phys. **19**, 19619, (2017).

[261] P. Mulholland and D. Dundas, Phys. Rev. A **97**, 043428, (2018).

[262] T. Yasuike and S. Yabushita, Chem. Phys. Lett. **316**, 257, (2000).

[263] M. Wells and R. R. Lucchese, J. Chem. Phys. **111**, 6290, (1999).

[264] R. Botter, V. H. Dibeler, J. A. Walker and H. M. Rosenstock, J. Chem. Phys. **44**, 1271, (1966).

[265] C. Baker and D. W. Turner, Proc. Roy. Soc. A **308**, 19, (1968).

[266] R. G. Cavell and D. A. Allison, J. Chem. Phys. **69**, 159, (1978).

[267] D. M. P. Holland, J. B. West, A. C. Parr, D. L. Ederer, R. Stockbauer, R. D. Buff and J. L. Dehmer, J. Chem. Phys. **78**, 124, (1983).

[268] J. C. Han, Chao Ye, Masako Suto and L. C. Lee, J. Chem. Phys. **90**, 4000, (1989).

[269] D. Lynch, M.-T. Lee, R. R. Lucchese and V. McKoy, J. Chem. Phys. **80**, 1907, (1984).

[270] H. Hattori, Y. Hikosaka, T. Hikida and K. Mitsuke, J. Chem. Phys. **106**, 4902, (1997).

[271] M. Wells and R. R. Lucchese, J. Chem. Phys. **110**, 6365, (1999).

[272] E. Lötstedt, T. Kato and K. Yamanouchi, Phys. Rev. A **86**, 023401, (2012).

[273] A. Russakoff, S. Bubin, X. Xie, S. Erattupuzha, M. Kitzler and K. Varga, Phys. Rev. A **91**, 023422, (2015).

[274] A. Russakoff, S. Bubin and K. Varga, J. Phys.: Conf. Ser. **574**, 012055, (2015).

[275] K. Doblhoff-Dier, M. Kitzler and S. Gräfe, Phys. Rev. A **94**, 013405, (2016).

[276] A. Russakoff and K. Varga, Phys. Rev. A **92**, 053413, (2015).

[277] S. Erattupuzha *et al.*, J. Phys.: Conf. Ser. **875**, 032012, (2017).

[278] S. Erattupuzha *et al.*, J. Phys. B: At. Mol. Opt. Phys. **50**, 125601, (2017).

[279] M. Negro, Faraday Discuss. **171**, 133, (2014).

[280] V. Averbukh, Phys. Rev. A **69**, 043406, (2004).

[281] S. M. Hankin, D. M. Villeneuve, P. B. Corkum and D. M. Rayner, Phys. Rev. Lett. **84**, 5082, (2000).

[282] B. Shan and Z. Chang, Phys. Rev. A **65**, 011804(R), (2001).

[283] J. Tate, T. Auguste, H. G. Muller, P. Salières, P. Agostini and L. F. DiMauro, Phys. Rev. Lett. **98**, 013901, (2007).

[284] K. Schiessl, K. L. Ishikawa, E. Persson and J. Burgdörfer, Phys. Rev. Lett. **99**, 253903, (2007).

[285] M. V. Frolov, N. L. Manakov and A. F. Starace, Phys. Rev. Lett. **100**, 173001, (2008).

[286] A. D. Shiner, C. Trallero-Herrero, N. Kajumba, H.-C. Bandulet, D. Comtois, F. Légaré, M. Giguère, J-C. Kieffer, P. B. Corkum and D. M. Villeneuve, Phys. Rev. Lett. **103**, 073902, (2009).

[287] V.-H. Le, A.-T. Le, R.-H. Xie and C. D. Lin, Phys. Rev. A **76**, 013414, (2007).

[288] W. Humphrey, A. Dalke and K. Schulten, J. Mol. Graph. **14**, 33, (1996).

[289] D. P. Chong, O. V. Gritsenko and E. J. Baerends, J. Chem. Phys. **116**, 1760, (2002).

[290] O. V. Gritsenko, Chem. Phys. Lett. **691**, 178, (2018).

[291] I. V. Litvinyuk, K. F. Lee, P. W. Dooley, D. M. Rayner, D. M. Villeneuve and P. B. Corkum, Phys. Rev. Lett. **90**, 233003, (2003).

[292] T. K. Kjeldsen, C. Z. Bisgaard, L. B. Madsen and H. Stapelfeldt, Phys. Rev. A **71**, 013418, (2005).

[293] D. Pavičić, K. F. Lee, D. M. Rayner, P. B. Corkum and D. M. Villeneuve, Phys. Rev. Lett. **98**, 243001, (2007).

[294] R. A. Ganeev, M. Suzuki, M. Baba, H. Kuroda and T. Ozaki, Opt. Lett. **31**, 1699, (2006).

[295] R. A. Ganeev, P. A. Naik, H. Singhal, J. A. Chakera and P. D. Gupta, Opt. Lett. **32**, 65, (2007).

[296] V. Strelkov, Phys. Rev. Lett. **104**, 123901, (2010).

[297] X.-B. Bian and A. D. Bandrauk, Phys. Rev. Lett. **105**, 093903, (2010).

[298] S. Beaulieu *et al.*, Phys. Rev. Lett. **117**, 203001, (2016).

[299] J. B. Watson, A. Sanpera, X. Chen and K. Burnett, Phys. Rev. A **53**, R1962, (1996).

[300] K. Ishikawa, Phys. Rev. Lett. **91**, 043002, (2003).

[301] E. J. Takahashi, T. Kanai, K. L. Ishikawa, Y. Nabekawa and K. Midorikawa, Phys. Rev. Lett. **99**, 053904, (2007).

[302] O. Smirnova, S. Patchkovskii, Y. Mairesse, N. Dudovich, D. Villeneuve, P. Corkum and M. Y. Ivanov, Phys. Rev. Lett. **102**, 063601, (2009).

[303] S. Haessler *et al.*, Nat. Phys. **6**, 200, (2010).

[304] H. J. Wörner, J. B. Bertrand, P. Hockett, P. B. Corkum and D. M. Villeneuve, Phys. Rev. Lett. **104**, 233904, (2010).

[305] C. Vozzi *et al.*, Phys. Rev. Lett. **95**, 153902, (2005).

[306] M. F. Ciappina, A. Becker and A. Jarón-Becker, Phys. Rev. A **76**, 063406, (2007).

[307] A. Etches, M. B. Gaarde and L. B. Madsen, Phys. Rev. A **84**, 023418, (2011).

[308] P. Wardman, Clin. Oncol. **19**, 397, (2007).

[309] P. Çarçabal, D. Descamps, S. Petit, Y. Mairesse, V. Blanchet and R. Cireasa, Faraday Discuss. **194**, 407, (2016).

[310] H. Yu, R. Eritja, L. B. Bloom and M. F. Goodman,J. Biol. Chem. **268**, 15935, (1993).

[311] M. Schwell and M. Hochlaf, Top. Curr. Chem. **355**, 155, (2014).

[312] A. B. Trofimov, J. Schirmer, V. B. Kobychev, A. W. Potts, D. M. P. Holland and L. Karlsson, J. Phys. B: At. Mol. Opt. Phys. **39**, 305, (2006).

[313] D. Toffoli, P. Decleva, F. A. Gianturco and R. R. Lucchese, J. Chem. Phys. **127**, 234317, (2007).

[314] S. Matsika, M. Spanner, M. Kotur and T. C. Weinacht, J. Phys. Chem. A **117**, 12796, (2013).

[315] O. Ghafur, S. W. Crane, M. Ryszka, J. Bockova, A. Rebelo, L. Saalbach, S. De Camillis, J. B. Greenwood, S. Eden and D. Townsend, J. Chem. Phys. **149**, 034301, (2018).

[316] R. A. Ganeev, Opt. Spectrosc. **117**, 605, (2014).

[317] Z. Abdelrahman, Ph.D. thesis, Imperial College London, 2015.

[318] D. Dougherty, K. Wittel, J. Meeks, S. P. McGlynn, J. Am. Chem. Soc. **98**, 3815, (1976).

[319] D. M. P. Holland, A. W. Potts, L. Karlsson, I. L. Zaytseva, A. B. Trofimov and J. Schirmer, Chem. Phys. **352**, 205, (2008).

[320] S. Kim *et al.*, Nucleic Acids Research, **44** (Database issue), D1202, (2016).

[321] H. M. Berman, J. Westbrook, Z. Feng, G. Gilliland, T. N. Bhat, H. Weissig, I. N. Shindyalov and P. E. Bourne, Nucleic Acids Research, **28**, 235, (2000).

[322] Ligand Expo, PDB Chemical Component URA, http://ligand-expo.rcsb.org/reports/U/URA/index.html

[323] Ligand Expo, PDB Chemical Component URF, http://ligand-expo.rcsb.org/reports/U/URF/index.html

[324] Ligando Expo, PDB Chemical Component TDR, http://ligand-expo.rcsb.org/reports/T/TDR/index.html

[325] POpSiCLE library, https://ccpforge.cse.rl.ac.uk/gf/project/popsicle/

[326] POpSiCLE: A photoelectron spectrum library for laser-matter interactions, http://www.archer.ac.uk/community/eCSE/eCSE04-03/eCSE04-03.php

[327] P. Wopperer, B. Faber, P. M. Dinh, P.-G. Reinhard and E. Suraud, Phys. Rev. A **82**, 063416, (2010).

[328] P. Wopperer, P. M. Dinh, E. Suraud and P.-G. Reinhard, Phys. Rev. A **85**, 015402, (2012).

[329] M.-P. Gaigeot and M. Ghmoi, J. Phys. Chem. B **105**, 5007, (2001).

[330] T. Gustavsson, Á. Bányász, E. Lazzarotto, D. Markovitsi, G. Scalmani, M. J. Frisch, V. Barone and R. Improta, J. Am. Chem. Soc. **128**, 607, (2006).

[331] M. Smyth and J. Kohanoff, Phys. Rev. Lett. **106**, 238108, (2011).

[332] M. Smyth, J. Kohanoff and I. I. Fabrikant, J. Chem. Phys. **140**, 184313, (2014).

[333] M. McAllister, M. Smyth, B. Gu, G. A. Tribello and J. Kohanoff, J. Phys. Chem. Lett. **6**, 3091, (2015).

[334] D. Hofmann, T. Körzdörfer and S. Kümmel, Phys. Rev. Lett. **108**, 146401, (2012).

[335] D. Hofmann, S. Klüpfel, P. Klüpfel and S. Kümmel, Phys. Rev. A **85**, 062514, (2012).

[336] L. Tao and A. Scrinzi, New. J. Phys. **14**, 013021, (2012).

[337] A. Scrinzi, New. J. Phys. **14**, 085008, (2012).

[338] F. Lekien and J. Marsden, Int. J. Numer. Meth. Engng. **63**, 455, (2005).